2019

Microstructure and mechanical properties of Ni-Cu alloys fabricated using wire arc additive manufacturing

Olexandra Marenych
University of Wollongong

University of Wollongong

School of Mechanical, Materials, Mechatronic and Biomedical Engineering

University of Wollongong, Australia

Microstructure and mechanical properties of Ni-Cu alloys fabricated using wire arc additive manufacturing

By

Olexandra Marenych, M.Sc.

This thesis is presented as part of the requirement

for the Award of the Degree of

Doctor of Philosophy

from

University of Wollongong

2019

Thesis certification

I, Olexandra Marenych, declare that this thesis, submitted in fulfilment of the requirements for the award of Doctor of Philosophy, in the School of Mechanical, Materials, Mechatronic and Biomedical Engineering, University of Wollongong, is wholly my own work unless otherwise referenced or acknowledged. The document has not been submitted for qualifications at any other academic institution.

Olexandra Marenych

2019

Abstract

Ni-Cu alloys, also known as Monel alloys, are widely used in marine industry due to their high corrosion resistance and good mechanical properties. Submarine propeller shafts, diesel engine piston rods and centrifugal pump shafts are examples of application of these alloys. Despite their good mechanical and corrosion resistant properties, Ni-Cu components may fail in operation via sliding wear, galling and pitting corrosion. Since the Ni-base alloys are expensive, repair is often an economic choice than replacement.

A possibility to use wire arc additive manufacturing (WAAM) technology for fabrication of new and repair of used Ni-Cu components was assessed in this thesis. Two Ni-Cu wires with various Ti, Mn, Al and C contents were deposited on a Ni-Cu substrate with a wide range of welding parameters (travel speed, wire feed rate). The solute atom concentrations and particle number density values were modified using various post processing heat treatment schedules. A comprehensive study of the microstructure, mechanical properties, wear and corrosion resistance of the Ni-Cu alloy components fabricated using WAAM has been conducted. Microstructure characterisation, in particular a detailed study of the precipitate's parameters (size, number density and chemical composition) was carried out using optical, scanning, transmission and atomic resolution electron microscopy. Mechanical properties were assessed using hardness, tensile testing to fracture, wear and corrosion resistance.

For similar deposition and heat treatment conditions, an alloy with higher C and Al, and lower Mn contents exhibited a higher number density of >20 nm TiC particles, higher number density of <20 nm γ'-Ni_3(Al, Ti) particles, and, associated with these, superior hardness, tensile strength, strain hardening rate, toughness and wear resistance. The effects of alloy composition and heat treatment on the microstructure-properties relationship in the studied Ni-Cu alloys are discussed. The hot-rolled Ni-Cu plate was used as a reference for mechanical properties, wear and corrosion resistance of the fabricated samples. The results showed that, although the strength of the deposited alloys was lower than this of the plate, the toughness, wear and corrosion resistance of depositions were higher almost in all conditions than this of the base plate.

A welding repair simulation by WAAM was performed by depositing the wire on a machined cylindrical rod. The chemical composition of the wire was chosen to match the composition of the component. The microstructure and mechanical properties

(hardness) of the deposition-component interface was analysed for three post-processing heat treatment conditions. Due to the difference in initial microstructure of the deposition (cast microstructure) and base metal (deformed microstructure), the hardness of the deposition was by 35% lower than this of base metal in as-welded condition. However, heat treatment reduced this difference down to 14%, which could be related to the precipitation of nano-sized TiC and γ' - $Ni_3(Al,Ti)$ particles in the depositions, as was observed in fabricated by WAAM plates and walls after age-hardening heat treatment.

Acknowledgement

I would like to express my sincere gratitude to my supervisors Prof. Huijun Li, A/Prof. Zengxi Pan and A/Prof. Stephen van Duin for giving me the opportunity to conduct a PhD research at the University of Wollongong. I am very grateful for their continuous support, constant encouragement and well directed guidance.

This study would be impossible without financial support of the Defence Materials Technology Centre (DMTC), which covered my scholarship and organisation of experiments. I am grateful to DMTC student training program, especially to Mr. Miles Kenyon, a program leader in education, for organisation of workshops and annual conferences, which by a considerable amount helped to improve my writing and presenting skills. I would also like to thank Ms. Bronwynne McPherson, an executive coordinator, for flawless organisation of trips and conferences and always pleasant communication and assistance.

I am grateful to MacTaggart Scott Australia, in particular to Mr. Matthew Leigh, for providing valuable industrial support and test materials.

I sincerely appreciate the help and support of my colleagues in the Faculty of Engineering and Information Sciences, in particular, Dr. Donghong Ding for his help with modification of a wire arc additive manufacturing system and producing the samples, which made the foundation of this research; to Dr. Chen Shen for his time and effort in arranging the heat treatment, and training in conducting tensile tests; Dr. Sina Jamali for his patience in training in corrosion testing and guidance in the data analysis. Thanks are extended to Dr. Mitchel Nancarrow for training on a scanning electron microscope; to Dr. Gilberto Casillas for training on transmission electron microscope and his assistance in conducting atomic resolution microscopy.

Words cannot express the depth of gratitude and love I feel to my family. To my role models - my parents and grandparents, for leading me to the path of engineering career. And to my sources of never-ending inspiration, energy and optimism – my husband Andrew and daughter Elizabeth, for being by my side every day.

The wire arc additive manufacturing was carried out in the UOW Welding and Industrial Automation Research Centre. The JEOL JEM-ARM200F, JEOL JEM-2011 and JEOL JSM-7001F FEG-SEM used in this work for microstructure characterisation were funded by the Australian Research Council grants LE120100104, LE0237478 and LE0882613.

Table of contents

List of figures

List of tables

List of publications

1. Effect of chemical composition on microstructure, strength and wear resistance of wire deposited Ni-Cu alloys, O.O. Marenych, D. Ding, Z. Pan, A.G. Kostryzhev, H. Li, S. van Duin, Additive Manufacturing 24 (2018), pp. 30-36

2. Precipitation strengthening in Ni-Cu alloys fabricated using wire arc additive manufacturing technology, O.O. Marenych, A.G. Kostryzhev, C. Shen, Z. Pan, H. Li, S. van Duin, Metals 9 (2019), paper 105.

3. Comparative effect of Mn/Ti solute atoms and TiC/Ni3(Al,Ti) nano-particles on work hardening behaviour in Ni-Cu alloys fabricated by wire arc additive manufacturing, O.O. Marenych, A.G. Kostryzhev, Z. Pan, H. Li, S. van Duin, Materials Science and Engineering A 753 (2019), pp. 262-275.

The results of this work were presented at the following conferences:

Annual Electron Microscopy HDR student competition, oral presentation, 7th Sept 2016. Innovation Campus, Wollongong, NSW, Australia.

DMTC (The Defence Materials Technology Centre) annual conferences, poster presentations in 2017 (28-29 March), 2018 (20-21 March) and 2019 (26-27 March), Canberra, ACT, Australia.

DMTC (The Defence Materials Technology Centre) student conferences, oral presentations in 2017 (11th October) and 2018 (9th October), Melbourne, VIC, Australia.

APICAM 2017 (Asia-Pacific International Conference on Additive Manufacturing), oral presentation, 4-6 Dec. 2017, Melbourne, VIC, Australia.

THERMEC 2018 (10th International Conference on Processing & Manufacturing of Advanced Materials Processing, Fabrication, Properties, Applications), poster presentation, 8-13 July 2018, Paris, France.

CAMS 2018 (Advancing Materials and Manufacturing), oral presentation, 27-29 November 2018, Wollongong, NSW, Australia.

1. INTRODUCTION

1.1. Background

Nickel has good mechanical properties and excellent resistance to various corrosive environments. It is the “base” for the Ni-base alloys families, which are amongst the most important classes of engineering materials. Ni-base alloys retain austenitic matrix from solidification to absolute zero that is why they can be used both at cryogenic temperatures and at temperatures approaching 1200 °C. They sustain high strength, ductility and toughness in this whole temperature range. Ni-base alloys have a higher tolerance for alloying elements in solid solution than stainless steels and other iron-base alloys but maintain good metallurgical stability. These factors have resulted in development of Ni-base alloys with multiple alloying additions to provide wide variety of properties. Major additions of copper (28-34%) provide solid solution strengthening and improve the resistance of Ni to nonoxidizing acids.

The Ni - Cu system has complete solid solubility, which allows production of single-phase alloys over the entire composition range. The 70Ni-30Cu system forms the basis for the Monel alloys. Monel alloys family has high room temperature strength, in comparison to some Ni-Cr alloys and low-alloy precipitation hardening steels, and are resistant to a wide range of corrosive media, including rapidly flowing seawater. Due to their excellent properties, Monel alloys have a wide area of applications, including marine industry, where they are used to produce propeller shafts, valves, marine fixtures and fasteners, electrical and electronic components.

The strength of cast Monel alloys can be increased by work hardening, solid solution strengthening (non-heat treatable alloys) and precipitation strengthening (heat-treatable alloys). The ability to significantly increase strength of Ni-Cu alloys by precipitation strengthening became one of the most prominent discoveries of the Ni alloy industry in the 20^{th} century. Additions of Al and Ti to Ni - Cu matrix help to produce a much stronger version of the 70Ni - 30Cu alloy, if a proper heat treatment is applied. The microstructure of age-hardened alloy may contain the following intermetallic precipitates: $Ni_3(Al,X)$, where X can be Cu, Mn, Ti or Si, known as gamma prime precipitates (γ'), Ni_3Ti and $Ni,Fe_3(Al,Fe)$.

γ′ has an ordered fcc crystal structure that has a very good crystallographic matching with the Ni fcc matrix (1% or less mismatch). The Al atoms reside in the cube corners while the Ni ones reside on the face centres. In commercial alloys, elements such as Co and Fe can substitute Ni, while Cu, Mn and Si have a tendency to substitute Al. γ′ precipitates nucleate homogeneously, remain spherical in shape and coherent with the matrix even after prolonged ageing. No tendency for precipitate alignment or for preferred nucleation at dislocations has been reported. The good crystallographic matching between the γ matrix and γ′ precipitates leads to a very low interface energy that, in turn, leads to very low coarsening rates of the precipitates. The γ′ solvus temperature for the solution treated and quenched samples is between 700 and 750 °C. This upper temperature limit for the γ + γ' phase field is rather low compared with those for most of the commercial γ'-hardened Ni-base superalloys in which the total amount of precipitate-forming elements such as Al, Ti, Nb and Ta is generally quite larger than the total Al and Ti content in Monel K500. The stable form of Ni_3Ti phase, often designated as eta (η), exhibits a hexagonal closed packed crystal structure and forms at the specific stoichiometric composition of 75Ni - 25Ti (at. %). The η phase can form the ordered metastable fcc structure at lower temperatures, it typically appears as coarse platelets and does not provide significant strengthening. Thus, the γ′ - Ni_3(Al,Ti) phase is preferred in this system.

In many Ni-base alloys with significant C levels, various types of carbides can form. Composition of the carbides and their amount depend on the alloy composition, processing route and service history. The MC-type carbide is the principal carbide phase in Monel alloys. It is identified as a titanium-rich MC-type phase, coarse particles of which are distributed in a non-uniform manner within the grains or along the grain boundaries. MC-type carbides exhibit the fcc crystal structure and typically form at the end of solidification of the alloy by eutectic-type reactions with γ matrix.

Historically, Ni-Cu alloys were produced by casting, followed by hot rolling and cold rolling process. Additive manufacturing is a novel rapidly developing alternative to traditional fabricating methods. It has a capacity to produce complex lightweight parts by adding material layers directly from 3D CAD model. In addition, it can be implemented as a repair technology of components that failed after being in service. Namely, Ni-Cu alloys are often used for manufacturing of machine parts with mating metal surfaces, thus wear is one of the key failure origins. Not only this directly affects

equipment life, especially when operated in corrosion environment, but also it may endanger an entire mechanical system if a critical part is damaged. Pitting corrosion, which is extremely localized corrosion leading to the creation of small holes on the surface, is another form of failure of Ni-Cu components. Since Ni-base alloys are expensive, repair is often a more economic choice than replacement.

Additive manufacturing of metals can be classified into two large groups with respect to a feedstock material type: powder-based and wire-based. Powder-based processes, such as selective laser melting, selective laser sintering or electron-beam melting are capable of producing complex parts with high geometrical accuracy. A typical layer thickness in powder-based fabrication is 20-100 μm, the dimensional accuracy can be up to ±0.05mm and the surface roughness is about 9-16 μm. However, powder-based process has significant downsides: porosity, low deposition rates (0.1-0.2 kg/h), limited size of the fabricated parts, high cost of powder and the inert gas required for the process.

In contrast, the wire-based additive manufacturing is a relatively simple and cheap process. Compared to powder, metal wires are lower in cost and readily available. The wire-feed processes are more environmentally friendly and have a higher material usage efficiency with up to 100% of melted wire material deposited to build a component. Compared to the powder-based methods, the deposition rates of wire-based methods are much higher (up to 12 kg/h), which allows to economically produce larger size components, although the complexity and accuracy of the fabricated part may be sacrificed. Depending on the energy source used for wire melting, wire-feed additive manufacturing can be classified into three groups, namely: laser-based, electron beam-based and arc welding-based. Laser-based methods are advantageous due to their precision; however, they have very poor energy efficiency of 2–5%. Electron beam-based methods have a slightly higher energy efficiency of 15–20 %, but they require a high vacuum working environment. On another hand, the energy efficiency of the arc welding processes can be up to 90 % in some circumstances. Additionally, the cost of the traditional arc welding equipment is relatively low, compared to the laser or electron beam equipment.

Wire arc additive manufacturing (WAAM) is a popular rapidly developing wire-based additive manufacturing technology. It employs an electric arc as a heat source and a wire as a feedstock and utilizes either gas metal arc welding (GMAW), gas tungsten

arc welding (GTAW) or plasma arc welding (PAW). The wire is deposited layer by layer perpendicularly on the substrate to manufacture a new component or repair an old component reducing material wastage and production/repair time. This process combines all the advantages of the wire-based methods (e.g. high deposition rates, high energy efficiency, readily available feedstock), in addition, WAAM can be applied using off the shelf welding machinery: welding power sources, torches and wire feeding systems. Moreover, it has potentially unlimited build volume, which allows to fabricate large machinery parts. WAAM has already been successfully applied to produce components from stainless steel, low carbon steel, Fe intermetallics, Ti-base, Al-base, Cu-base, and Ni-Cr-base alloys. In spite of significant number of works dedicated to the analysis of technology-properties relationships, detailed microstructural characterisation of WAAM components is rarely conducted, which slows down the properties optimisation. The key dependences observed up-to-date are as follows. An increase in deposition rate may result in smaller grain sizes, fracture void sizes and higher toughness. In multi-phase materials, such as Fe intermetallics and Ti-base alloys, interpass temperature should be controlled, as it may affect the room temperature phase balance and related to it combination of strength and ductility. In both single phase and multi-phase alloys the tensile properties have been reported to depend on test direction, which is related to the temperature and cooling rate gradient through the deposited object. Stress relief, homogenisation and age-hardening heat treatments improve mechanical properties. In particular, homogenisation may result in less disordered crystal structure, lower segregation, finer grain size and increased strength and ductility. Age-hardening leads to particle precipitation and may increase strength and toughness.

1.2 Thesis aim and objectives

Based on the analysis of previously published work, the following aim was set for this thesis: to develop for the first time a wire arc additive manufacturing technology for fabrication and repair of Ni-Cu components.

To achieve this aim the following objectives were defined:

1. To investigate the effect of welding parameters (torch travel speed, wire feed rate) on mechanical properties of depositions (strength, wear and corrosion resistance).

2. To study the effect of wire alloy chemistry on microstructure (in particular, precipitation of hard nano-particles) and mechanical properties of depositions;
3. To develop the post processing heat treatment procedure (temperature range, holding time, cooling rate) to assure stress relief and optimal combination of strength, toughness, wear and corrosion resistance.

1.3 Major contributions

The research presented in this thesis has shown a feasibility to fabricate Ni-Cu alloys using wire arc additive manufacturing. An opportunity for the wire arc additive manufacturing to become a new economical way of repairing damaged Ni-Cu parts was also proved.

The effect of travel speed and wire feed rate on the beads geometry and the dilution has been investigated for the Ni-Cu alloys deposited on a substrate plate with matching chemical composition. The knowledge obtained in this work allowed to fabricate defect-free simple shape components (multi-layered walls and single layer multi-bead plates) from two Ni-Cu alloys with various concentrations of Al, Ti, Mn and C. Post-deposition heat treatment designed in this work provided microstructure homogenisation, stress relieve and optimal partitioning of microalloying elements between solid solution and particles leading to improvement of mechanical properties.

The findings of the present research have contributed to in-depth understanding of the technology-microstructure-properties relationship in Ni-Cu alloys fabricated using wire arc additive manufacturing. The effect of alloy composition on microstructure (in particular, particle precipitation), hardness, tensile strength and wear resistance of as-deposited and heat treated alloys has been thoroughly investigated. A higher C content in alloy composition facilitated precipitation of TiC particles in all size ranges in as-deposited condition. In addition, a higher Al content could lead to a vast precipitation of nano-sized $Ni_3(Al,Ti)$ particles after heat treatment. As a result, the Ni-Cu alloy with higher Al and C contents exhibited higher hardness, yield stress, tensile strength, toughness and wear resistance in all studied conditions. The strain hardening behaviour of the studied alloys varied with heat treatment condition, and was affected by the dislocation density, size and number density of precipitates, and solid solute concentrations. Both alloys exhibited ductile fracture behaviour in all studied conditions

and decreasing average void size, corresponding to decreasing elongation, with age hardening heat treatment.

The results obtained for Ni-Cu alloys fabricated by WAAM were compared to these for hot-rolled Ni-Cu plate. It was proved that, although WAAM components have lower strength, due to cast microstructure, they possess similar or higher elongation and toughness than these of a hot-rolled plate in all heat treatment conditions. In addition, wire arc additively manufactured Ni-Cu components were found to retain good corrosion resistance in 3.5%NaCl environment, which is typical operating environment for traditionally manufactured Ni-Cu alloys.

1.4 Thesis organisation

Introduction, the current chapter, presents the research background, the thesis aim and objectives and contributions of this work. Rest of the thesis is organized as follows.

Chapter 2 Literature review presents a summary of the current knowledge related to this research work. It is divided into three subheadings. *2.1 Chemical composition and manufacturing technologies of Ni alloys* gives a brief overview of existing Ni-base alloys, summarises the role of alloying elements in Ni-Cu alloys and describes fabrication process of Ni-Cu alloys, mainly hot and cold working, heat treatment, machining and surface finishing. *2.2 Microstructure-property relationships of Ni-Cu alloys* is a characterisation of microstructure (in particular, matrix, intermetallic precipitates, carbides and carbonitrides, dislocations and annealing twins) and strengthening mechanisms (grain size strengthening, solution and precipitation strengthening and dislocations strengthening) in Ni-Cu alloys. It also provides information about mechanical properties (tensile strength, hardness, impact and fatigue strength) and corrosion resistance of Ni-Cu alloys in various media. *2.3 Repair techniques of Ni-base alloys* addresses existing repair methods such as thermal spraying and considers additive manufacturing (namely, laser metal deposition and wire arc additive manufacturing) as possible repair technique for the given alloys.

The materials and experimental techniques used in this study are described in **Chapter 3 Materials and experimental techniques**. It provides information about a chemical composition of the studied alloys and substrate; describes samples fabrication

and post processing heat treatment. It also describes equipment used for microstructural analysis, mechanical and corrosion testing.

The results obtained in this thesis are presented in **Chapter 4 Results and discussion**, which is divided into 6 subheadings as follows.

4.1 Analysis of the as-received materials presents an analysis of microstructure and mechanical properties (hardness) of the substrate Ni-Cu plate and two Ni-Cu wires chosen for WAAM deposition. *4.2 Development of the WAAM technology for Ni-Cu alloys* states the feasibility study of using WAAM for fabrication of Ni-Cu components and gives an analysis of the effect of deposition parameters (wire feed rate, travel speed, resulting heat input) on the geometry, microstructure and mechanical properties of the fabricated components. It also demonstrates the effect of post-processing heat treatment on the microstructure and mechanical properties of the depositions.

4.3 Microstructure and mechanical properties of as-welded Ni-Cu alloys represents an in-depth study of microstructure and mechanical properties of as-deposited beads, walls and plates fabricated using two Ni-Cu alloys at three travel speeds.

4.4 Microstructure and mechanical properties of heat treated Ni-Cu alloys is a further investigation which primarily focuses on the effect of heat treatment on microstructure (in particular, nano-size intermetallic precipitates) and mechanical properties of the two Ni-Cu alloys depositions (strength, hardness, wear resistance). In addition, considering the application environment of Ni-Cu alloys, the corrosion resistance of the depositions in all heat treatment conditions was investigated in this chapter. The results are compared with hot-rolled Ni-Cu plate.

4.5 Work hardening behaviour and fracture in as-welded and heat treated Ni-Cu alloys is a more detailed characterisation of nano-sized precipitates and their significant effect on work hardening and fracture behaviour in Ni-Cu alloys produced by WAAM is discussed.

4.6 Repair of a functional component by wire arc additive manufacturing shows the results obtained during simulation of repair of damaged Ni-Cu cylindrical shaft.

Chapter 5 Thesis Conclusions is a summary chapter, which concludes the major findings of this thesis. **Chapter 6 Future work** states the main challenges that could be addressed in future investigations of microstructure and mechanical properties of Ni-Cu alloys produced using WAAM.

2. LITERATURE REVIEW

2.1 Chemical composition and manufacturing technologies of Ni-base alloys

2.1.1 Ni-base alloys

Nickel 200 and 201 is a commercially pure nickel with up to 1 % additions of other elements (Table 2.1). It has good mechanical properties and excellent resistance to various corrosive environments. Ni retains an austenitic face-centered-cubic (FCC) crystal structure from its melting point down to sub-zero temperatures, providing freedom from ductile-to-brittle transitions and minimizing the fabrication problems that can be encountered with other metals [1]. When added to other alloys, Ni provides metallurgical stability, improved thermal stability and weldability, improved resistance to reducing acids and caustics, and increased resistance to stress corrosion cracking particularly in chlorides and caustics [2]. Ni is the “base” for various Ni-base alloys families which are one of the most important classes of engineering materials [3].

Table 2.1 Chemical composition of Nickel 200 and 201, wt. %

Alloy		**Ni**	**C**	**Mn**	**Fe**	**Co**	**S**	**Si**
Nickel 200	Max	-	0.15	0.35	0.40	0.25	0.01	0.35
	Min	99.0	-	-	-	-	-	-
Nickel 201	Max	-	0.02	0.35	0.40	0.25	0.01	0.35
	Min	99.0	-	-	-	-	-	-

Ni - base alloys retain austenitic matrix from solidification to absolute zero that is why they can be used both at cryogenic temperatures and temperatures approaching 1200 °C. They sustain high strength, ductility and toughness in this whole temperature range [4]. Ni is not a chemically active element and does not readily evolve hydrogen from acid solutions. The presence of an oxidizing agent is usually required for significant corrosion to occur. Generally, reducing conditions retard corrosion, whereas oxidizing conditions accelerate corrosion of Ni in chemical solutions. However, Ni may also form a protective corrosion-resistant, or passive, oxide film on exposure to some

oxidizing conditions [5]. These properties result in excellent aqueous and high temperature corrosion resistance of Ni-base alloys.

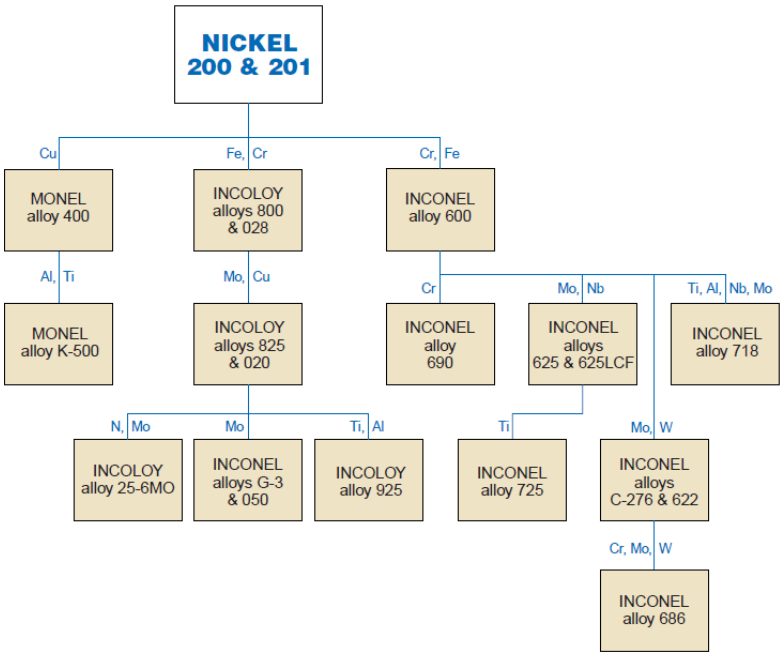

Figure 2.1. Ni-base alloys [2].

With appropriate alloying additions, these alloys provide useful properties and have applications in a wide range of industries, including marine engineering, power generation, petrochemical, chemical processing, aerospace, and pollution control [4]. Ni-base alloys have a higher tolerance for alloying elements in solid solution than stainless steels and other iron-based alloys but maintain good metallurgical stability. These factors have resulted in development of Ni-base alloys with multiple alloying additions to provide wide variety of properties (Figure 2.1) [2].

2.1.1.1 Monel alloy family

Major additions of copper (28-34 %) provide improvement in the resistance of Ni to nonoxidizing acids [5], [2]. In addition, Cu provides solid solution strengthening [6]. Ni and Cu exhibit very similar atomic characteristics. They are each face-centered-cubic, have less than three percent difference in atomic radii, and exhibit similar electronegativity and valence state. The Ni - Cu system has complete solid solubility, which allows production of single phase alloys over the entire composition range (Figure 2.2) [7]. Although the Ni - Cu system exhibits complete solid solubility [8], the

large differences in melting points between Ni (1455 °C) and Cu (1085 °C), coupled with the low diffusivity of Cu in Ni, can result in microsegregation of Cu. This may lead to inhomogeneity of microstructure and mechanical properties in fusion welds of Ni - Cu alloys, and therefore should be carefully controlled [9].

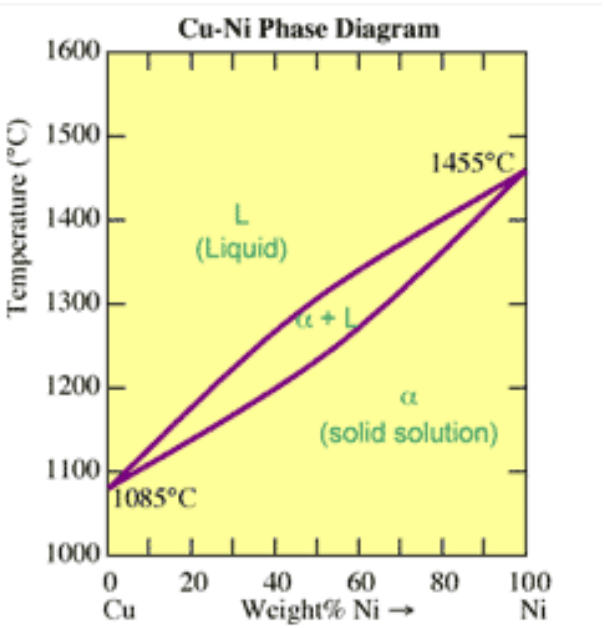

Figure 2.2. Ni-Cu binary phase diagram [7].

The Ni - Cu system forms the basis for the Monel alloy family. Monel was discovered by Robert Crooks Stanley who worked for the International Nickel Company (INCO) in 1901. The new alloy was named in honour of the president of the company, Ambrose Monell. The name is now a trademark of Special Metals Corporation [10].

Table 2.2. Chemical compositions of Monel alloys, wt. %

Monel Alloys		**Ni**	**Cu**	**C**	**Mn**	**Fe**	**Co**	**S**	**Si**	**Al**	**Ti**
Monel 400	Max	-	34.0	0.3	2.0	2.5	-	0.024	0.5	-	-
	Min	63.0	28.0	-	-	-	-	-	-	-	-
Monel 401	Max	45.0	Balance	0.1	2.25	0.75	0.25	0.015	0.25	-	-
	Min	40.0	-	-	-	-	-	-	-	-	-
Monel 404	Max	57.0	Balance	0.15	0.1	0.5	-	0.024	0.1	0.05	-
	Min	52.0	-	-	-	-	-	-	-	-	-
Monel R405	Max	-	34.0	0.3	2.0	2.5	-	0.060	0.5	-	-
	Min	63.0	28.0	-	-	-	-	0.025	-	-	-
Monel K500	Max	-	33.0	0.18	1.5	2.0	0.25	0.006	0.5	3.15	0.85
	Min	63.0	27.0	-	-	-	-	-	-	2.3	0.35

Minor alloy additions are made to Monel to provide unique properties of the Monel alloy family (Table 2.2), which composes of Monel 400, Monel 401, Monel 404, Monel R405 and Monel K500. The standard product forms are round, hexagon, flats, forging stock, pipe, tube, plate, sheet, strip, and wire [11].

Monel alloys are stronger than pure Ni and are resistant to corrosion by many agents, including rapidly flowing seawater. They can be fabricated readily by hot- and cold-working and machining. These alloys are usually quite weldable, but may be susceptible to porosity if proper shielding or well deoxidized consumables are not used [12]. The strength of Monel alloys can be increased by work hardening, solid solution strengthening (non-heat treatable) and precipitation strengthening (heat-treatable). The addition of Al and Ti to Ni - Cu alloys help to produce a much stronger version of the 70Ni - 30Cu alloy that would form a second phase when properly heat-treated [13]. The second phase is known as gamma prime (γ'). The ability to significantly increase the strength of Ni-base alloys by precipitation hardening became one of the most transformational technical discoveries of the Ni alloy industry in the 20^{th} century [14].

Monel alloys are expensive, with their cost ranging from 5 to 10 times the cost of Cu and Ni, hence their use is limited to those applications where they cannot be replaced with cheaper alternative. Compared to carbon steel, piping in Monel is about 30-120 times more expensive [15].

Monel 400 - is characterized by good general corrosion resistance, good weldability and moderate to high strength. The alloy has been used in a variety of applications. It has excellent resistance to rapidly flowing brackish water or seawater. It is particularly resistant to hydrochloric and hydrofluoric acids when they are de-aerated. The alloy is slightly magnetic at room temperature. It is widely used in the chemical, oil and marine industries for manufacturing of chemical plant equipment, pumps, valves, marine fixtures and piping systems [16], [17].

Monel 401 - has higher Cu content than Monel 400 for better electrical properties and good brazing characteristics. It is readily autogenously welded in the thin sections in which it is most often used. The alloy is designed for use in specialized electrical and electronic applications such as wire wound resistors, bimetal contacts, etc. [18].

Monel 404 - is used primarily in specialised electrical and electronic applications. The composition of Monel 404 is carefully adjusted to provide a very low Curie temperature, low permeability, and good brazing characteristics. Monel 404 can be

welded using common welding techniques and hot worked by forging. Cold working may be done using standard tooling and soft die materials for better finish. The alloy is used for manufacturing of capsules for transistors and ceramic-to-metal sealing [19].

Monel R405 - is the free machining version of Monel 400. It has a controlled amount of sulphur added to provide sulphide inclusions that act as chip breakers during machining and thus improve machinability. This alloy is resistant to sea water, steam at high temperatures, salt and caustic solutions, it also exhibits high strength [20]. The alloy is used for screw machine stock, fasteners and similar high production run items [21].

Monel K500 - combines the excellent corrosion resistance of Monel alloy 400 with the added advantages of greater strength and hardness. Depending on processing (cold worked, age-hardened), it may have approximately three times the yield stress and double the tensile strength when compared with Monel 400 [22]. The increased properties of the alloy are obtained by adding Al and Ti to the Ni-Cu, and by heating under controlled conditions (commonly called age hardening or aging) so that submicroscopic particles of Ni_3(Ti, Al) precipitate throughout the matrix [23]. Monel K500 can further be strengthened by cold working. It should be annealed before welding, and the weldment requires stress relief or annealing before aging. The alloy is non-magnetic [24].

The corrosion resistance of Monel K500 is substantially equivalent to that of Monel 400 except that, when in the age-hardened condition, Monel K500 is more susceptible to stress-corrosion cracking in some environments. Monel K500 has been found to be resistant to a sour-gas environment. The combination of very low corrosion rates in high-velocity seawater and high strength make Monel K500 particularly suitable for shafts of centrifugal pumps, propeller shafts, impellers, valve components in marine service (Figure 2.3). In stagnant or slow-moving seawater, fouling may occur followed by pitting, but this pitting slows down after a fairly rapid initial attack [25]. Monel K500 became a popular propeller shaft alloy for sea-going vessels and was chosen by naval architects for its good torsional stiffness, toughness, and corrosion resistance in marine environments. Later, it was widely used for non-magnetic drill collars [14].

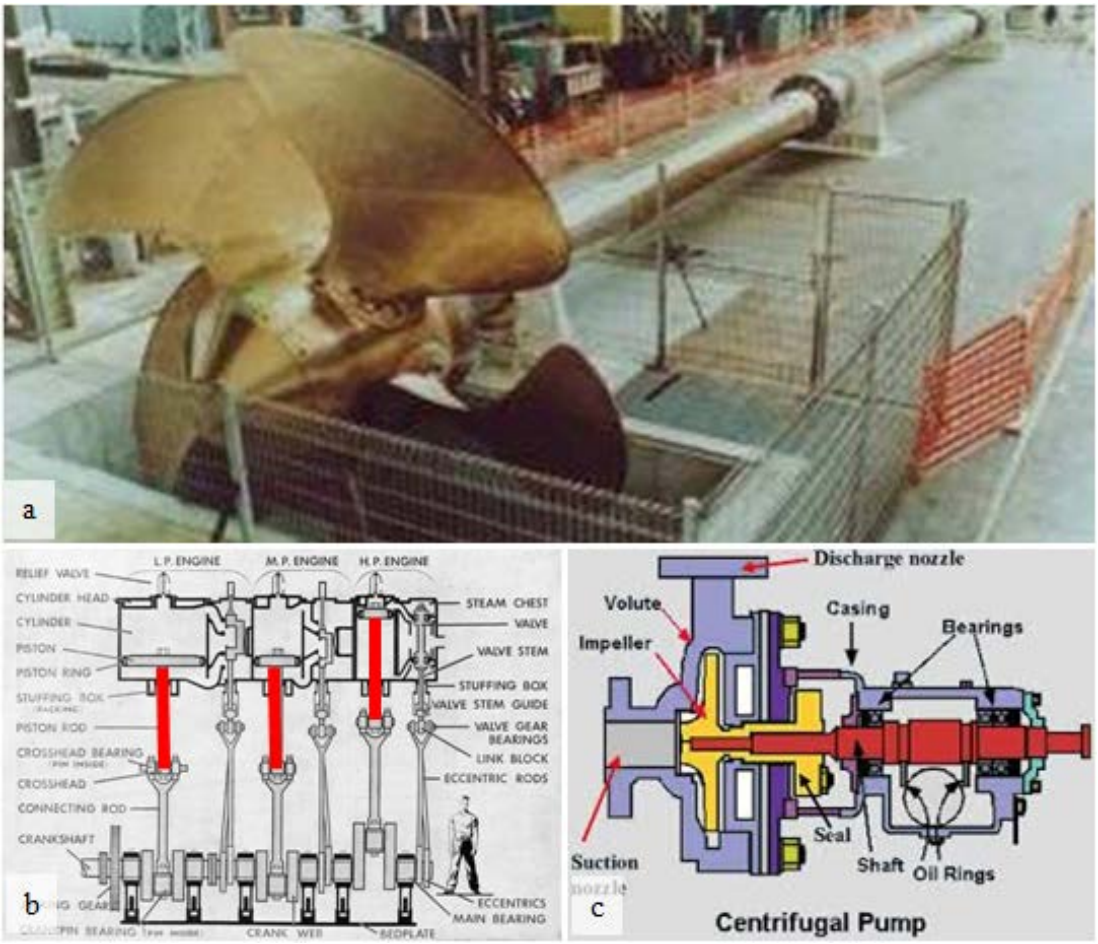

Figure 2.3. Maritime components made of Monel K500: (a) submarine propeller shaft [26], (b) diesel engine piston rod [27] and (c) centrifugal pump shaft [28].

2.1.1.2 Role of alloying elements in Ni-Cu alloys

The number of alloying elements can be combined with Ni to provide alloys with high mechanical properties and good corrosion resistance in a wide variety of environments (Table 2.3) [29]. Ni is capable of dissolving high concentrations of alloying elements compared to other metals [30].

Copper (33 % max) – provides solid solution strengthening [5]. Additions of copper also provide improvement in the resistance of Ni to nonoxidizing acids. In particular, alloys containing 30 to 40 % Cu offer useful resistance to nonaerated sulphuric acid and offer excellent resistance to all concentrations of nonaerated hydrofluoric acid [2].

Carbon (0.25 % max) **–** allows formation of carbides, which improve creep resistance [31]. Because C is relatively mobile in the Ni matrix above 315 °C, C

additions beyond the solubility limit (~0.02 wt. %) will result in precipitation of graphite particles that render the material brittle and weak [7].

Manganese (1.5 % max) – highly soluble in Ni, improves corrosion resistance and weldability. Promotes formation of $M_{23}C_6$ type carbides [8, 32].

Iron (2.0 % max) – provides solid solution strengthening, reduces costs of the Ni-base alloys, but does not promote corrosion resistance [2]. It also increases the solubility of C in Ni; this improves resistance to high-temperature carburizing environments [5].

Cobalt (0.25 % max) – provides increased high-temperature strength, solid solution strengthening, and resistance to carburization and sulphidation [2]. Additions of Co also raise solvus temperature of γ′ [5].

Sulphur (0.006 % max) - enhances machinability of Ni-base alloys [20].

Silicon (0.5 % max) - is typically present only in minor amounts in most Ni-base alloys as a residual element from deoxidation practice or as an intentional addition to promote high-temperature oxidation resistance [5].

Table 2.3. The effects of various alloying elements on phase stability in Ni-base alloys

Effect	Element
Solid solution strengthener	Cu, Co, Fe, Ti, Al
Gamma prime (γ′) - $Ni_3(Al,Ti)$ former	Al, Ti
Carbide formers: MC $M_{23}C_6$	 Ti Mn
Surface oxide (Al_2O) former	Al

Aluminium (2.3-3.15 %) - provides excellent corrosion resistance resulting from the formation of a protective Al_2O_3 surface oxide layer. This permits use of Ni-base alloys in a wide variety of applications that require protection due to various forms of degradation, such as aqueous corrosion, oxidation, and sulfidation [7].

Titanium (0.35-0.85 %) – promotes formation of MC-type carbides [33].

Although Ti and Al can be effective solid solution strengtheners, they typically improve strength by precipitation of the γ′ - $Ni_3(Ti,Al)$ phase in Ni-base superalloys used for applications that require a combination of high temperature strength and corrosion resistance [5]. Together they are often used in minor amounts in corrosion resistant alloys for the purpose of deoxidation or to tie up carbon and/or nitrogen respectively [2]. Both Ti and Al combine with oxygen to form oxides, thereby controlling porosity in the weld deposits [7].

2.1.2 Fabrication process of Ni-Cu alloys

2.1.2.1. Hot working and cold working

The hot working of Ni alloys is performed by the following methods: forging (Figure 2.4 a), hot rolling (Figure 2.4b) and extrusion [11]. Ni alloys are often closed-die forged into turbine blades, turbine discs, exhaust valves, chain hooks, heat-exchanger headers, valve bodies and pump bodies. Shafts and seamless rings are made by open-die forging. Seamless rings are also made by ring rolling [34].

Proper temperature during deformation is the most important factor in achievement of hot malleability. The maximum recommended heating temperature for hot working of Monel alloy K500 is 1150 °C. Metal should be charged into a hot furnace and withdrawn when uniformly heated. Prolonged soaking at this temperature is harmful. If a delay occurs, such that the material should be subjected to prolonged soaking, the temperature should be reduced to or held at 1038°C until shortly before ready to work, then brought to 1150 °C. When the piece is uniformly heated, it should be withdrawn. In the event of long delay, the work should be removed from the furnace and water-quenched [36].

The hot working temperature range is from 870 to 1150 °C. Heavy work is best done between 1040 and 1150 °C; deformation below 870 °C is not recommended. To produce finer grain structure in forgings, the final reheat temperature should be 1090 °C and at least 30% reduction of area should be applied in the last forging operation [38]. The rate of cooling after forging is critical for Monel K500 [34].When hot working has been completed, or when it is necessary to cool the alloy before further hot working, it should not be allowed to cool in air but should be quenched from a temperature of 790 °C or higher. If the piece is allowed to cool slowly it will self-heat-treat (age-harden) to some extent, and stress will be set up that may lead to thermal splitting or tearing during subsequent reheating. In addition, quenched material has better response to age-hardening, since more of the age-hardening constituent is retained in solution [36].

The cold working of Ni alloys is performed by rolling (Figure 1.6), drawing and pilgering (Figure 2.5) [11]. Nickel alloys are known for their excellent ductility and malleability in the annealed condition which makes them adaptable to virtually all methods of cold fabrication [40]. Resistance to deformation is a primary consideration

in cold forming of Ni and Ni-Cu alloys. However, when properly annealed, even the high-strength alloys have a substantial range between the yield and ultimate tensile strength. This range is the plastic region of the material and all cold forming is accomplished within the limits of this region. Hence, the high-strength alloys require only stronger tooling and more powerful equipment for successful cold forming [41].

Figure 2.4. (a) Forging process [35]; (b) billet in hot rolling process [37]; (c) cold-rolling process [42].

A universal characteristic of the Ni-base alloys is that they have face-centered cubic crystal structures, and, consequently, are subject to rapid strain hardening [43]. This characteristic is used to advantage in increasing the room-temperature tensile properties and hardness of alloys which otherwise would have low mechanical strength, or in adding strength to those alloys which are hardened by precipitation. Because of this increased strength, large reductions or extensive draws can be made without rupture of the material. However, the number of reductions in a forming sequence will be limited before annealing is required, and the percentage reduction in each successive operation must be reduced rapidly [40].

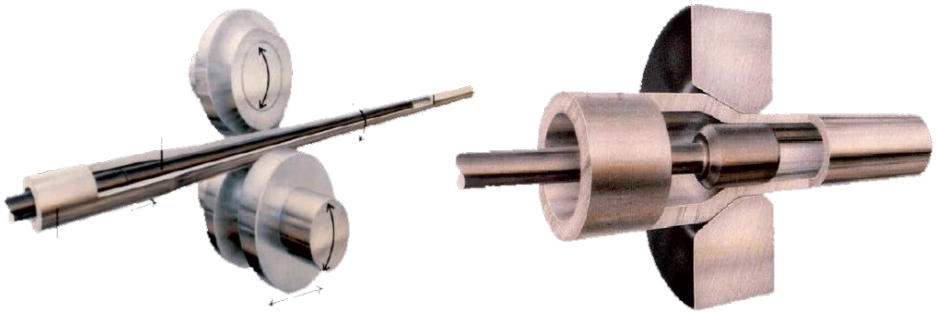

Figure 2.5. Pilgering (left) and drawing process (right) [44].

Since strain hardening is related to the solid-solution strengthening of alloying elements, the strain-hardening rate generally increases with the complexity of the alloy. Similarly, the age-hardenable alloys have higher strain-hardening rates than their solid-solution equivalents [45].

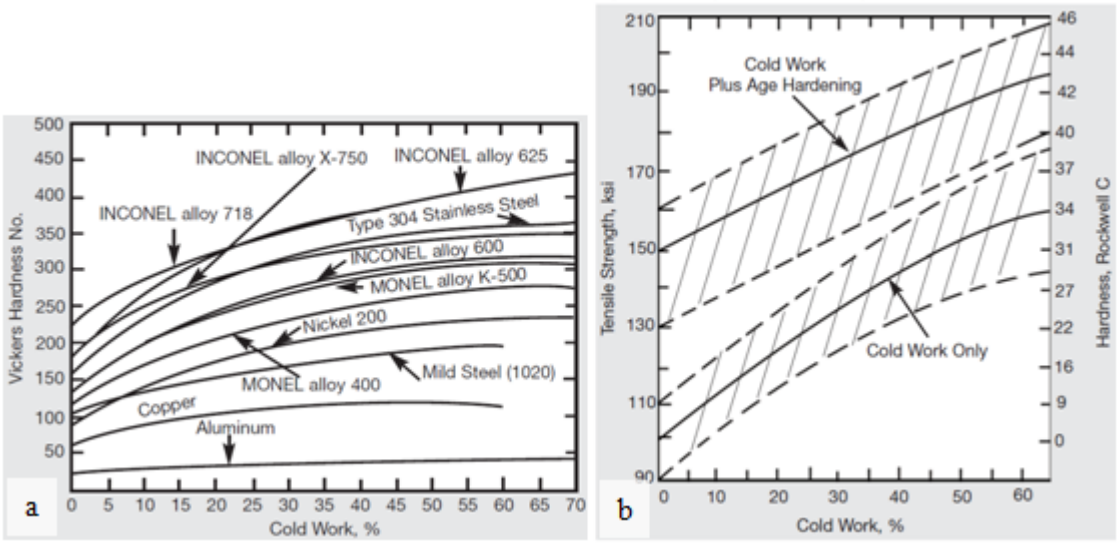

Figure 2.6. (a) Effect of cold work on hardness [23], (b) Effect of cold work and age hardening on properties of Monel K500 [23].

In the annealed condition, Monel K500 can be cold-worked by standard procedures. Although the alloy requires considerable power to form, it has excellent ductility. Its increase in hardness with increasing cold work, in comparison with other materials, is shown in Figure 2.6a. Figure 2.6b shows the effect of cold work and cold work plus age-hardening on tensile strength and hardness.

2.1.2.2 Heat treatment

The metallic alloys become work-hardened when they are plastically deformed at temperatures lower than their recrystallization points. This increases hardness and strength, decreases ductility, alters the grain structure and develops residual stresses in the material. It is usually necessary to reduce or eliminate the stresses resulting from cold working and soften the alloy by controlled heating before it can be further processed or placed in service [39]. There are two main heating methods used for Ni-base alloys: open heating and closed heating. The third method, salt-bath heating is used for special work with small parts.

In *open heating* the material is charged directly into the furnace and heated at the selected temperature for the desired time. This method is widey used in heating for mechanical properties and is the usual method in heating for hot working. Continuous furnaces are used for annealing; oil- or gas-burning directly fired furnaces are usually used in heating for hot working; bath furnaces are normally used for age hardening because of long time required to complete the operation.

In *closed or box heating* the work is placed in a container which is then sealed and charged into the furnace. Although both annealing and hardening can be accomplished by this method, closed heating is more appropriate for hardening. Box annealing is usually carried out at lower temperatures than open annealing and longer times are required.

Heating in salt bath is accomplished by placing the material in the molten salts, where it absorbs heat rapidly. After heating the work is washed in water to remove particles of the salt mixture [41]. Accurate temperature control is one of the most important factors in achieving good results in heating. The effect of heating temperature on the room temperature mechanical properties of precipitation hardened Monel K500 is shown on Figure 2.7.

After being heated for any purpose except age hardening, Monel alloy K500 should be water quenched not only to avoid excessive hardening and cracking that could occur if it was cooled slowly through the age hardening range, but also to maintain good response to subsequent aging [32]. All of the Ni-base alloys form an adherent oxide film if allowed to cool in air after heating. The film is difficult to remove and should be prevented if a bright surface is to be produced by subsequent pickling. When a cooling

rate equal to air cooling is desired, the material should be cooled in a protective atmosphere. If rapid cooling is required, it should be done by high-speed convection under a protective atmosphere or by a reducing quench bath [30].

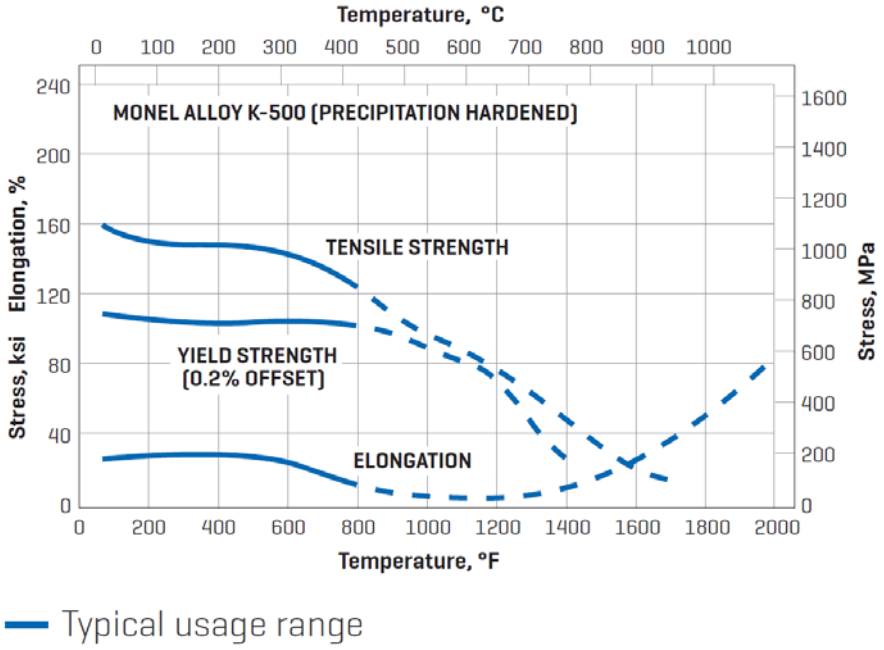

Figure 2.7. Mechanical properties of precipitation hardened Monel K500 [11].

There are five principal heat treatments used to produce desired mechanical properties in the Monel K500. These methods include *stress equalizing, precipitation hardening, process annealing, solution annealing and full annealing* [46]. The optimum temperature and time-at-temperature for any heat treatment depend on the composition, section size, shape and prior processing of the alloy [36]. Time and temperature are usually experimentally determined for each application.

Stress equalizing - is a low-temperature heat treatment, usually requiring temperatures in the range of 260 to 370 °C for work-hardened Ni alloys. Stress equalizing is a partial recovery of cold-worked coil springs, wire forms, and flat spring stampings. It is used to balance stresses in the material without an appreciable decrease in the mechanical strength produced by cold working [27]. This recovery precedes any detectable microscopic structural changes and consists of a considerable increase in the yield stress, a slight increase in hardness and tensile strength, and no significant change in elongation and reduction of area. In addition, stresses in the metal are balanced, and electrical conductivity returns toward the characteristic value of the material in the

annealed condition. This treatment enables springs to withstand higher stresses and usually lengthens fatigue life. If coil springs are to be given a cold set or cold pressing after coiling, stress equalizing should be done before the setting operation. Cold setting involves stressing the material beyond the elastic limit, and the cold-working stresses set up in the spring are in such a direction that they are beneficial rather than harmful. Stress equalizing after cold pressing removes this beneficial result of cold working [39].

Precipitation hardening (age hardening) – is a time-temperature-dependent process, the optimum schedule for heat treatment varies with the alloy composition and the end use for the material. Table 2.4 shows various age hardening methods found in the literature.

Table 2.4. Age hardening procedures

Step 1	Step 2	Step 3
[36]		
At 590 °C, hold for 16 hours;	furnace cool to 540 °C, hold 6 hours; furnace cool to 480 °C, hold 8 hours;	air-cool
At 590-610 °C hold for 8-16 hrs;	furnace cool to 480 °C, at 10-15 °C/hr	air-cool
[41]		
At 590-610 °C hold for 16 hrs[(a)]	furnace cool to 480°C at 10-15 °C/hr	Furnace/air cool or quench from 480 °C to RT without regard for cooling rate
At 590-610 °C hold for 8 hrs or longer[(b)]	furnace cool to 480°C at 10-15 °C/hr	Furnace/air cool or quench from 480 °C to RT without regard for cooling rate
At 530-540 °C hold for 6 hrs or longer[(c)]	furnace cool to 480°C at 10-15 °C/hr	Furnace/air cool or quench from 480 °C to RT without regard for cooling rate

Remarks:

(a) The procedure is recommended for soft materials (140-180 Brinell, 75-90 Rockwell B): as-forged and quenched or annealed forgings, annealed or hot-rolled rods, large cold-drawn rods, soft-temper wire and strip.

(b) The procedure is recommended for moderately cold-worked materials (175-250 Brinell, 8-25 Rockwell C): cold-drawn rods, half-hard strip, cold-upset pieces and intermediate-temper wire.

(c) The procedure is recommended for fully cold-worked material (260-325 Brinell, 25-35 Rockwell C): spring-temper strip, spring wire or heavily cold-worked pieces such as small, cold-formed balls.

Three types of annealing procedures are performed on Monel K500: *solution annealing, process annealing and full annealing.* The treatments are different in both their purpose and procedure [46].

Process Annealing - during mechanical processing in production and subsequent forming of Monel K500 products, intermediate process annealing may be required to soften the product. Such anneals recrystallize the structure and are typically conducted at temperatures between 760 – 870 °C. While higher temperatures will anneal the product, intermediate process annealing temperatures are limited to avoid excessive grain growth. Time at temperature must be limited to avoid the formation of secondary phases which can compromise the hardness of the aged Monel K500 product. Holding for one hour after the part has reached the set temperature and equalized is normally sufficient to soften the alloy product during processing. The exposure at temperature for times greater than 1.5 hours is not recommended. Excessive exposure can result in the formation of titanium carbide (TiC) [33]. This compound is stable at the aging temperatures used to harden Monel K500 such that Ti cannot participate in the hardening reaction (the formation of $Ni_3(Ti,Al)$). Thus, the strength and hardness can be compromised.

It is best to avoid the formation of the TiC phase. If, however, the phase is formed as a result of improper processing, solution annealing at 1120 °C for 30 minutes is required to dissolve the particles. It should be noted that this heat treatment will result in a large grain size which can somewhat compromise formability. However, the high-temperature solution treatment is necessary if the component is to develop full hardness and strength during the aging treatment [25].

Solution annealing (solution treating) - prior to the aging treatment, Monel K500 should be solution-annealed to dissolve any phases that may have formed in the alloy during previous processing. Solution annealing is normally performed by heating hot-finished products to 980 °C and cold-worked products to 1040 °C. To avoid excessive grain growth, time at temperature should be kept to a minimum (normally, less than 30 minutes). Heating and cooling times must be kept to a minimum to avoid precipitation of detrimental phases. Cooling after solution annealing is normally accomplished by water quenching [36].

Full Annealing – is used for complete softening of work-hardened material. The treatment requires exposure to a sufficient temperature for a time long enough to cause

full recrystallization of the work- hardened grain structure (Figure 2.8). That removes all of the stresses, softens the material, and decreases mechanical strength. Temperatures in the range of 705 to 1260 °C are used to anneal the Ni-base alloys [39].

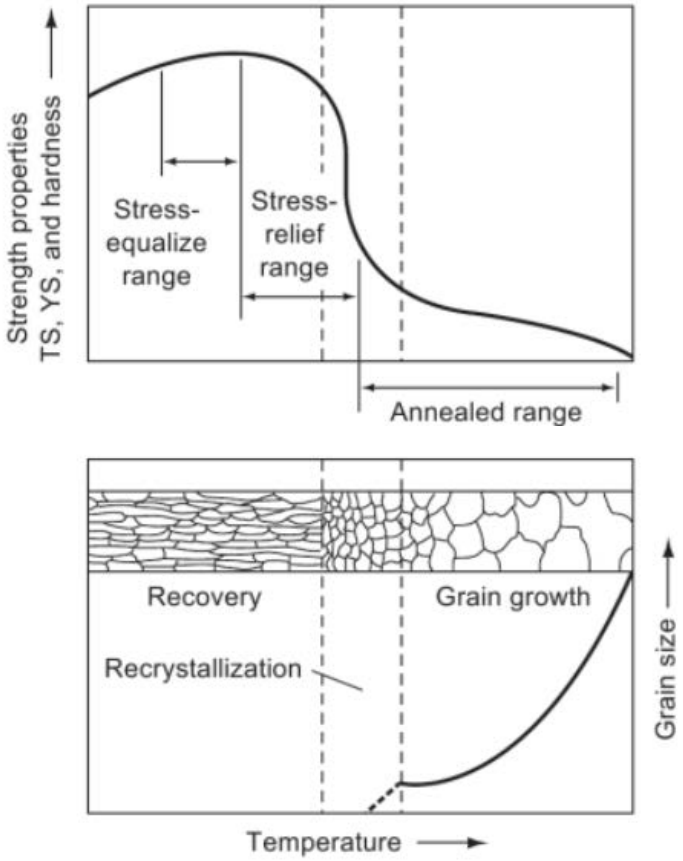

Figure 2.8. Schematic representation of the effect of annealing temperature on the properties and grain structure/size of Ni alloys [46].

Material which has been heated for any appreciable length of time in the temperature range 590 to 760 °C will be overaged to an extent dependent on time and temperature of exposure. Overaged material will have lower mechanical properties than properly aged metal, and the properties cannot be raised by subsequent aging treatments. In order to strengthen overaged material, it must be solution-annealed (980 - 1040 °C) to redissolve the age-hardening constituents, and then re-aged. All benefits of cold work are lost in annealing. The highest strength obtainable is that corresponding to the annealed and age-hardened conditions [46].

Material that has been age-hardened to produce maximum hardness will not show an appreciable change in properties if again heated to or held at any temperature up to that at which the original heat treatment was carried out. There may be a small increase

in properties if the rate of cooling in the original heat treatment was too rapid between 570 and 430 °C. If the hardened material is subsequently heated above 590 °C and then cooled, there will be a decrease in properties [40].

2.1.2.3 Machining, surface finishing

Ni-base corrosion-, temperature- and wear-resistant alloys, such as Monel K500, are classified as moderate to difficult when machining [45]. During machining these alloys work harden rapidly, generate high heat during cutting, weld to the cutting tool surface and offer high resistance to metal removal because of their high shear strengths [47].

The Ni alloys have an austenitic matrix and, like the austenitic stainless steels, work harden rapidly (Figure 2.9). The high pressures developed between the tool and workpiece during cutting or grinding produce a stressed layer of deformed material on the surface of the work. The deformation causes a hardening effect that retards further machining. The stresses in this deformed layer not only affect the mechanical properties of the workpiece but also can cause distortion of parts that have small cross sections [48, 49].

Grain size has little direct effect on machinability; indirectly it may have some effect since grain size does reflect thermal processing and change in constitution of structure. Some difference in surface finish may be noted but this can be minimized by correct cutting procedure. In general, *microstructure affects machinability in two ways*: i) The presence of graphite or sulphide phases will greatly enhance machinability; ii) Hard phases such as carbides, nitrides, carbonitrides, oxides, silicates and the gamma prime Ni_3(Al, Ti) particles are abrasive and tend to cause rapid tool wear.

The hardest and most abrasive of all the phases is titanium carbide (TiC), which is present in age-hardenable Monel K500 alloy. This and other phases are usually present in as-rolled or mill-annealed products. Solution annealing at high temperatures, 1095°C and above, is required to dissolve them. Age hardening facilitates precipitation of greater amounts of titanium carbides and the gamma prime particles. The refractory nature of these phases, together with their strengthening effect, makes age-hardened material less machinable although chip action is improved [23].

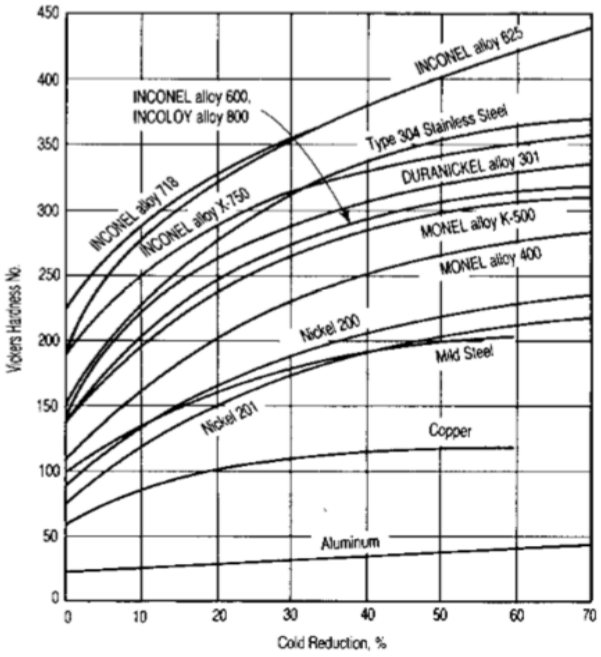

Figure 2.9. Degree of work hardening of some metals and alloys as indicated by the effect of cold reduction on hardness [48].

In *unaged condition* Monel alloy K500 can be hardened only by cold work and is machined most readily in the *cold-drawn* or *cold-drawn stress-relieved* condition. In *aged condition* Monel K500 is characterized by high strength and hardness. Material which has been solution annealed and quenched or rapidly air cooled is in the softest condition and does machine easily. Because of softness, the unaged condition is necessary for ease in drilling, tapping and all threading operations [48].

Heavy machining of the age-hardenable alloys is best accomplished when they are in one of the following conditions: s*olution annealed* or *hot worked and quenched or rapidly air cooled.* Although fully age-hardened material is usually too hard for tools with weak cutting edges, such as small drills and taps, and also for rough machining, material in this condition can be finish-machined to fine finishes and close tolerances. The best way to machine Monel K500, therefore, is to machine slightly oversize in the un-aged condition, age-harden, then finish to size. Because the age-hardening treatment will relieve machining stresses, allowance must be made for possible warpage. A slight permanent contraction (up to about 0.07%) takes place during aging [48]. Aged material has good dimensional stability.

2.2 Microstructure-property relationships of Ni-Cu alloys

2.2.1 Microstructure

2.2.1.1 Matrix

Monel K500 has Ni-Cu face-centered-cubic matrix (γ) with lattice parameter of 3.534 Å (Figure 2.10) [23]. The average grain size of the solution-treated specimens was measured being about 5 μm [50]. Due to full mutual solubility of Ni and Cu, the second phase does not form, although small particles of various chemistries can precipitate. Therefore, in this alloy strengthening occurs via four mechanisms: grain refinement, solid solution and precipitation strengthening, and work hardening (dislocation strengthening). To achieve a required level of precipitation strengthening the age hardening heat treatment can be applied. Work hardening usually occurs as a result of cold working [51].

2.2.1.2 Intermetallic precipitates

After an appropriate heat treatment, the alloy may contain the following intermetallic precipitates: $Ni_3(Al,X)$, Ni_3Ti and $Ni,Fe_3(Al,Fe)$ [52], [33]. $Ni_3(Al,X)$ particles, where X can be Cu, Mn, Ti or Si, are known as gamma prime precipitates (γ'). Gamma prime (γ') particles have an ordered fcc crystal structure (Figure 2.11a) that has very good crystallographic matching with the Ni fcc matrix (1% or less mismatch) [53]. The Al atoms reside in the cube corners while the Ni ones reside on the face centres. In commercial alloys, elements such as Co and Fe can substitute Ni [54], while Cu, Mn and Si have a tendency to substitute Al.

Gamma prime particles nucleate homogeneously, remain spherical in shape and coherent with the matrix even after prolonged aging (Figure 2.12) [55]. There is no tendency for precipitate alignment or for preferred nucleation at dislocations at small undercoolings. The good crystallographic matching between the γ matrix and γ′ precipitates in superalloys leads to a very low surface energy that, in turn, leads to very low coarsening rates of the precipitates [56]. The average γ' particle radius remains proportional to the cube root of time during coarsening, implying that the process is

controlled by the bulk diffusion of the γ'-forming solutes. The activation energy of the coarsening process is close to that of diffusion of Al in Ni. The precipitates can form 6-7% of volume fraction upon aging at 700°C or less, and remain spherical and coherent during coarsening [33].

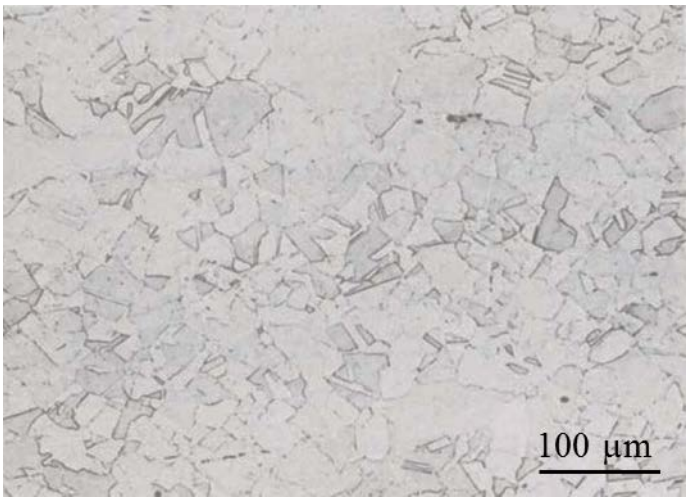

Figure 2.10. Typical microstructure of hot-rolled Monel K500 (etchant: Carapella's and glyceregia, magnification x100) [23].

The γ′ solvus temperature for the solution treated and quenched samples is between 700 and 750 °C [33]. This upper temperature limit for the γ + γ' phase field is rather low compared with those for most of the commercial γ'-hardened Ni-base superalloys in which the total amount of precipitate-forming elements such as Al, Ti, Nb and Ta is generally quite larger than the total Al and Ti content in Monel K500 [57]. The solution annealing temperature (950 °C and above) is well above the gamma-prime solvus; and the decomposition of the supersaturated austenite (γ), even on a very fine scale, did not occur during quenching [33]. This differs from other Ni-Al and Ni-Ti alloys, where γ' forms readily on quenching [58], [59]. The substitution of some neighbouring elements in the periodic table for Ni is known to decrease γ' solubility and, for this reason, Cr, Fe and Co can all be added to increase the γ' volume fraction at a given Al-plus-Ti level [60].

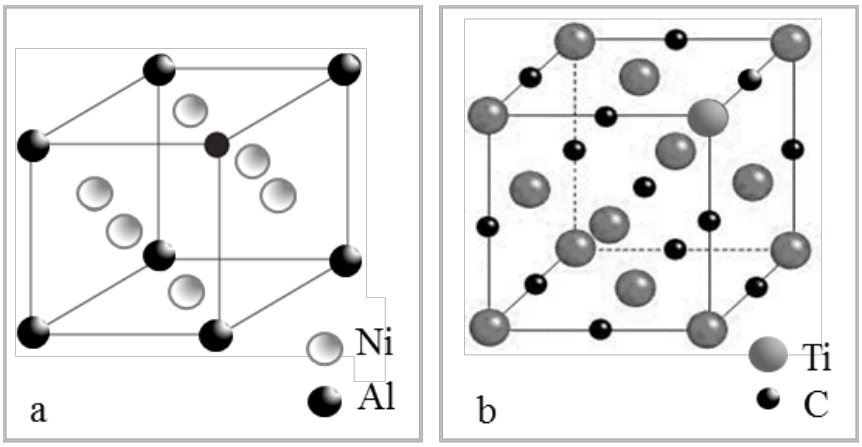

Figure 2.11. (a) Ordered fcc crystal structure of the γ′-Ni_3(Ti,Al) particle and (b) TiC particle.

The fact that γ' precipitation occurred in Monel K500 at 750 °C while the solubility of Al in Ni at this temperature is about 5wt.% in binary Ni-A1 alloys suggested that Cu also has a similar effect on γ' solubility [61]. The γ′ phase shows the remarkable effect of increasing yield strength with increasing temperature up to ~800 °C [62]. This effect is thought to occur due to ordering effects and the relatively low mobility of super lattice dislocations that occurs with increasing temperature.

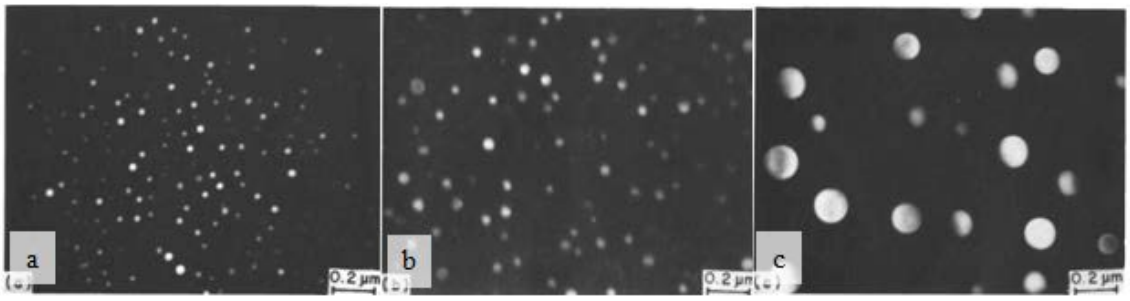

Figure 2.12. Micrographs illustrating the homogeneous distribution and the spherical shape of the γ′ precipitates retained even after prolonged aging: aged at 700 °C for a) 64 h, b) 128 h and c) 1000 h [33].

The Ni-Al and Ni-Ti systems (Figure 2.13) form the basis for precipitation hardened microstructures of Ni - base superalloys [63]. Ni can dissolve a maximum of approximately 11 wt.% of both Al and Ti. The solubility decreases appreciably with temperature, thus providing the driving force for precipitation strengthening reactions. Most superalloys have a combined Al + Ti content below 10 wt.%, and even small

additions of Al or Ti will result in precipitation of the Ni_3Al or Ni_3Ti phases. The stable form of Ni_3Ti phase, often designated as eta (η), exhibits a hexagonal closed packed crystal structure and forms at the specific stoichiometric composition of 75Ni - 25Ti (at. %). The Ni_3Ti phase can form the ordered metastable fcc structure at lower temperatures. Ti additions promote formation of the η - Ni_3Ti phase, while Al additions promote formation of the γ′ - Ni_3Al phase. The hexagonal η - Ni_3Ti phase typically appears as coarse platelets and does not provide significant strengthening. Thus, the γ′ - Ni_3Al phase is preferred in this system [62].

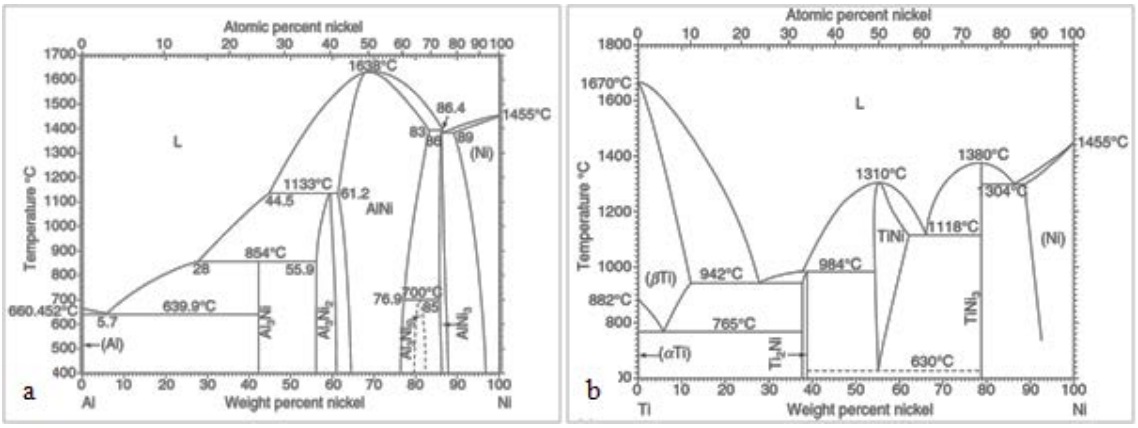

Figure 2.13. a) Binary Ni-Al phase diagram, b) binary Ni-Ti phase diagram [64].

2.2.1.3 Carbides and carbonitrides

In many Ni-base alloys with appreciable C levels, 0.18 wt. % in Monel K500, various types of carbides can form. Composition of the carbides and their amount depend on the alloy composition, processing route and service history [7]. The MC-type carbide is the principal carbide phase in Monel K500. It is identified as a titanium-rich MC-type phase (Figure 2.11b), coarse particles of which are distributed in a non-uniform manner within the grains or along the grain boundaries (Figure 2.14) [33]. MC-type carbides exhibit the fcc crystal structure and typically form at the end of solidification of the alloy by eutectic-type reactions with γ matrix [64].

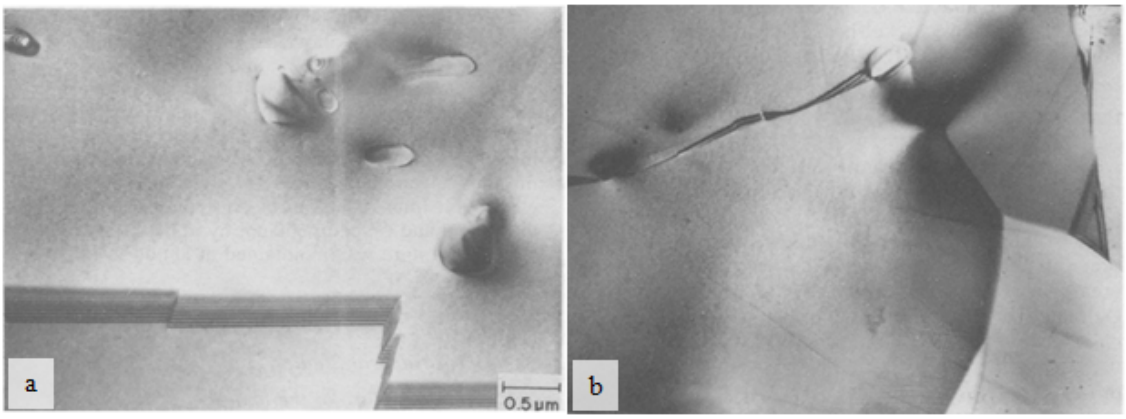

Figure 2.14. Formation of TiC particles: (a) within the grains and (b) at the grain boundaries [33].

The morphology and the heterogeneous distribution of these precipitates remain essentially unaltered during heat treatments at temperatures lower than 980 °C. However, these particles may slightly grow during these treatments [33]. Primary carbides are not easily dissolved during subsequent processing of the alloy and thus are present as stringers along the rolling direction. The MC carbides can often be replaced by $M_{23}C_6$ carbides during thermal processing and/or high temperature service [13]. The $M_{23}C_6$ carbides in Monel K500 are generally Mn rich and form in the 760-980 °C temperature range. These carbides tend to form on grain boundaries and, when present as discrete particles, can improve creep strength by restricting grain boundary sliding (Figure 2.15a).

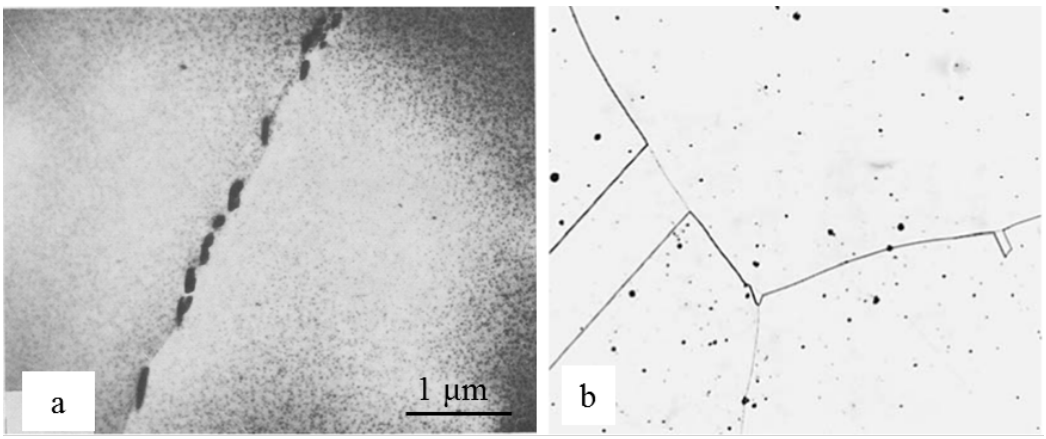

Figure 2.15. (a) Precipitates in Monel K500: (a) $M_{23}C_6$ – type carbides at the grain boundaries [50] and (b) Nitrides observed after the following heat treatment: holding during 1 h at 1205 °C, aging for 4 h at 595 °C, water quenching (magnification x100) [39].

In corrosion resistant alloys, many types of carbides are considered harmful because they can precipitate at grain boundaries during heat treatment or weld fabrication and subsequently promote intergranular corrosion or cracking in service. This results from the depletion of matrix in elements essential to corrosion resistance during the carbide precipitation process. In high-temperature alloys, the presence of carbides is generally desired to control grain size and to enhance elevated-temperature strength and ductility. However, careful attention must be paid to the carbide types and morphologies after solution heat treatment or post fabrication heat treatment in order to avoid cracking during component manufacture or loss of strength or ductility in service [39].

The M(CN) carbonitrides are similar to MC carbides, except that substantial levels of C are replaced by N (Figure 2.15b). These eutectic-type reactions and the concomitant carbides and carbonitrides are promoted by the strong tendency of C, N and some metallic elements (most notably Ti) to segregate to the liquid during solidification. As a result, carbonitrides are typically distributed along the interdendritic and solidification grain boundary regions. The following types of carbides and nitrides were observed in Monel K500: TiC; $M_{23}C_6$ (where M is Mn, Fe or Ni) form on isolated grain boundaries during prolonged aging [65]; TiN [39].

2.2.1.4 Dislocations

A moderate density of dislocations have been observed in Monel K500 thin (0.2 mm) sheets that were solution annealed, aged and water quenched [33]. It was proposed that the dislocations were formed as a result of the quenching stresses. These dislocations did not show any marked tendency either for distribution along planar arrays or for pairing suggesting that the stacking fault energy of the alloy was quite high, and that short-range order was absent in the solution-annealed and quenched material. The arrangement of dislocations in the solution-treated and deformed (3 pct deformation) specimens was found to be nonplanar in several regions of the grains (Figure 2.16) [50].

Although Ni is endowed with a high stacking fault energy [66], alloying may decrease the value of this parameter as has been noted, for instance, for many Ni-Cr-base alloys [67]. However, it appears that Cu additions to Ni are not very effective in reducing the stacking fault energy of the latter [68], [69]. The other alloying elements in Monel K500 are present only in small quantities and are unlikely to cause a large reduction in the stacking fault energy of the Ni-Cu matrix [33].

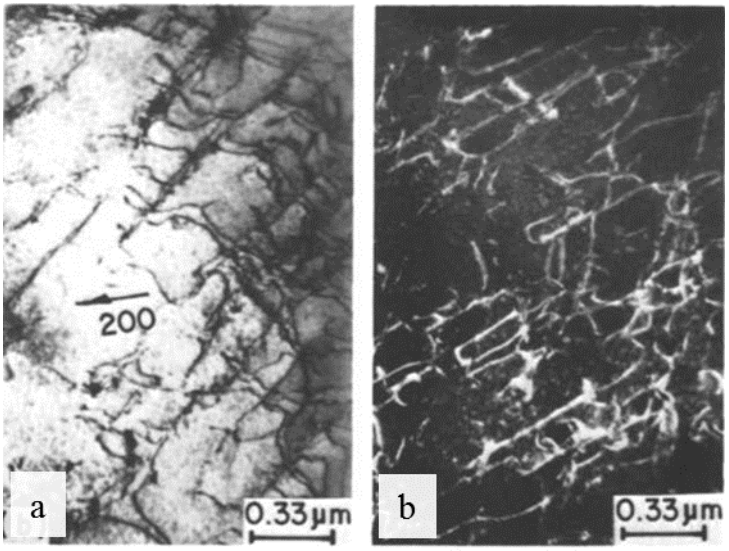

Figure 2.16. Non-planar dislocation arrangement in a slightly deformed sample: (a) a bright field micrograph and (b) a weak beam dark field micrograph [33].

2.2.1.5 Annealing twins

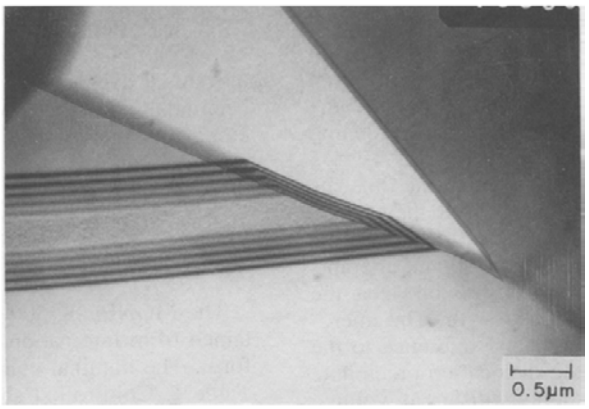

Figure 2.17. Annealing twins in the fully annealed specimen [50].

Annealing twins form a prominent feature of the microstructure of those recrystallized fcc metals and alloys in which the interfacial energies associated with the coherent twin boundaries are very much smaller than those associated with grain boundaries. Murr et al. [65] have reported that the coherent twin boundary energy in nickel is only about 3% of the grain boundary energy and that the situation is qualitatively similar in Nickel-2%ThO_2 alloy (TD Nickel) as well as in Inconel 600. Annealing twins in Monel K500 are prevalent in solution annealed, water quenched, air-cooled or aged material [33], [65]. The solutionized alloy was found to contain a moderate density of annealing twins, which usually appeared as parallel-sided bands bounded by coherent (111) planes (Figure 2.17).

2.2.2 Strengthening mechanisms

As Monel K500 is a single phase alloy, four strengthening mechanisms operate in it: grain size strengthening, solid solution strengthening, precipitation strengthening and work hardening. Depending on the microalloying element content (in particular, Ti, Al, Co, Fe) and processing schedule (age hardening heat treatment) either the solid solution strengthening or precipitation strengthening dominates.

2.2.2.1 Grain size strengthening

The strength of polycrystalline metals and alloys increases with a decrease in grain size (increase in grain boundary length), following the Hall-Petch relationship. This phenomenon has been attributed to the grain boundaries acting as barriers to the dislocation motion [70]. Grain boundaries are efficient in strengthening metals and alloys for two main reasons. First, the internal elastic stresses resisting plastic flow are greater in the vicinity of boundaries and second, the defect structures are more complex at lower overall strains near grain boundaries than in the grain interior [71]. These defect structures (secondary dislocations, microbands, tangles, etc.) increase the local flow stress necessary to penetrate this boundary layer, and, potentially, suppress the operation of dislocation sources at the boundary during subsequent plastic straining. Figure 2.18 shows an example of grain boundary strengthening in Monel 400. As can be seen, the grain size increase from 9.5 to 202 μm reduces the quasi-static yield stress from 290 to 130 MPa, while having a minimal effect on the work-hardening behaviour, i.e. the stress-strain curves for all the grain sizes are essentially parallel (Figure 2.18a). With strain rate increasing from the quasi-static to dynamic the stress-strain curves move up along the stress axis; however, the effect of strain rate on grain size dependence is weak (Figure 2.18b). The work-hardening rate at high strain rates remained invariant as a function of grain size [72].

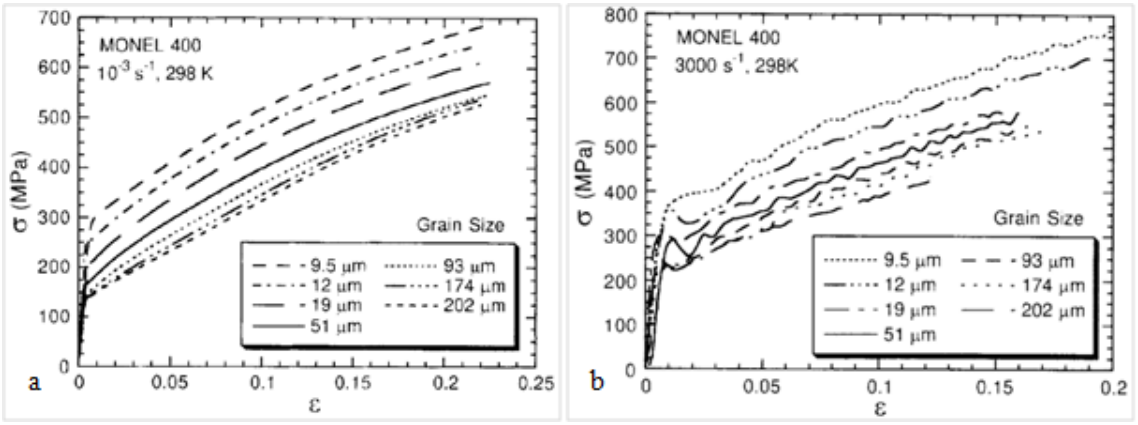

Figure 2.18. The stress-strain curves of Monel 400 for various grain sizes at (a) low and (b) high strain rate [72].

2.2.2.2 Solid solution strengthening

The ability of a dissolved element to increase an alloy strength by solid solution hardening is determined by its atomic size difference compared to that of the primary element. Addition of the substitutional alloying elements results in expansion of the fcc lattice of austenitic matrix, resulting in a net strengthening (hardening) of the austenite [73], [6]. Table 2.5 summarizes approximate atomic diameter variation between Ni and some other elements and solubility data for these elements in Ni at 1000 °C (1830 °F). As can be seen, Al, Ti, Mn, Ta, Mo and W provide the best combination of atomic radii mismatch and appreciable solubility needed for solid solution strengthening. Therefore, Mo, Mn, and W are frequently used in many single phase commercial alloys for solid solution strengthening. Cr, Fe, Cu, Co also can be used for solid solution strengthening due to their high solubility in Ni [22, 75]. The solid solution strengthening from additions of these elements will be effective only if the element concentrations do not exceed their solubility limits in Ni-based austenite (Table 2.5). Although Ti and Al can be effective solid solution strengtheners, they typically improve strength by precipitation of the γ'-Ni_3(Ti,Al) precipitates [7]. Nb may provide some solid solution strengthening, however it is primarily added to form carbides or Ni_3Nb intermetallic particles.

Table 2.5. Approximate atomic size variations and solubility limits of some elements in Ni.

Solute	Approximate atomic size difference compared to Ni, %	Approximate solubility in Ni at 1000°C, wt% [76]
C	82	0.2
Al	31	7
Si	38	8
Ti	-27	10
V	-22	20
Cr	-17	40
Mn	-12	20
Fe	-9	100
Co	-3	100
Cu	4	100
Nb	-49	6
Mo	-41	34
Ta	-51	14
W	-44	38

2.2.2.3 Precipitation strengthening

In Monel K500 significant hardening is associated with the precipitation of gamma prime (γ') particles. The γ' precipitates have the ordered fcc crystal structure; therefore, the dislocation interaction mechanisms with ordered precipitates dictate the level of strengthening. In most cases of precipitation hardening, in the initial stages of particle coarsening, the interparticle spacing is small and particle shearing is favoured. With the progress of coarsening, as the interparticle spacing increases, looping of the precipitates becomes possible. When precipitate shearing occurs, the strengthening of an alloy can arise from (a) lattice mismatch between particles and the matrix, (b) order hardening, and (c) modulus mismatch. In Monel K500, the order hardening prevails over other shearing mechanisms. The lattice mismatch is likely to make a very small contribution to the overall precipitation hardening effect, because the coherency strain value is extremely small (less than 0.003) [50]. The precipitation strengthening mechanism may change with aging, due to the precipitate size variation with aging. In the *underaged and peak-aged condition*, precipitation strengthening is governed solely by the shearing of particles. This is due to the fact that the shear stress required for particle shearing is lower than the Orowan stress associated with the looping of dislocations around precipitates [77]. In the *overaged condition*, two processes may take place, concurrently or in succession: (i) particle cutting

in slightly overaged conditions and (ii) looping in substantially overaged conditions. In a moving dislocation pair, when the first dislocation is impeded by a dislocation loop around a precipitate, the approach of the second dislocation increases the shear stress between the leading dislocation and the loop, and consequently, the particle may be sheared and the loop annihilated. Thus, planar slip may be observed in an alloy containing slightly overaged γ' particles. The reduction in stress due to the coarsening of precipitates is compensated by the transition of dislocation pairs to single dislocations, and thus, there is a net increase in strength in the initial stages of overaging.

Order hardening is brought about by the interaction of dislocations with ordered precipitates. As shown schematically in Figure 2.19, the initial cutting of an ordered precipitate by a single dislocation creates an antiphase boundary (APB) across the slip plane that represents an atomic layer of incorrect bonding (Figure 2.19b). Subsequent movement of a second dislocation through the ordered phase restores the order (Figure 2.19c, d). Thus, dislocations are forced to travel in pairs (often referred to as superlattice dislocations) to maintain the ordered structure after precipitate cutting.

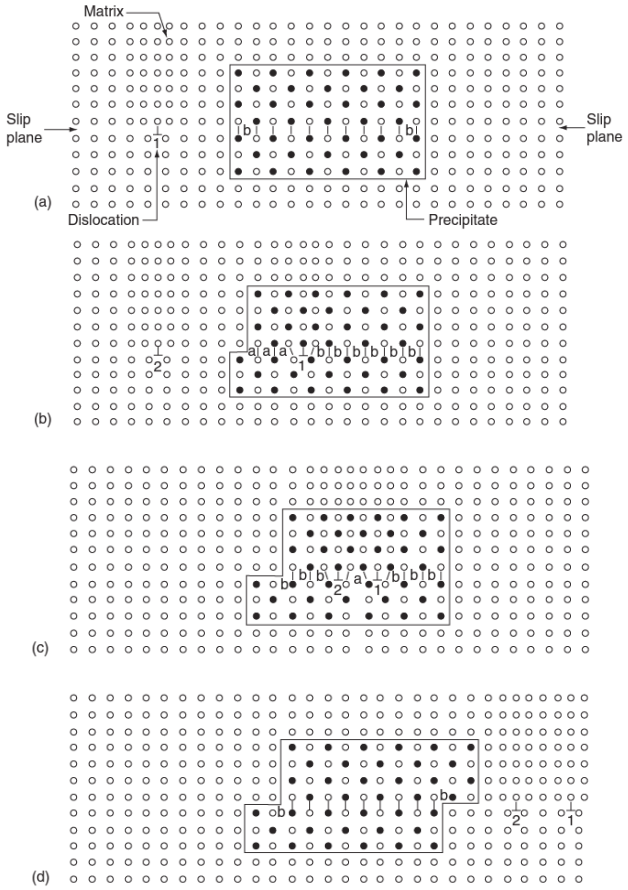

Figure 2.19. Schematic illustration of dislocations interacting with an ordered Ni_3Al precipitate [75].

Figure 2.20 shows examples of such paired super lattice dislocations and particle cutting in a Ni-base superalloy. This deformation involves cross-slip of segments of the superlattice dislocations from the {111} slip plane to {001} cross-slip plane. These cross-slipped segments cannot move without forming an APB and thus resist deformation. Strengthening from cross-slip becomes more important with increasing temperature because the cross-slip is thermally activated.

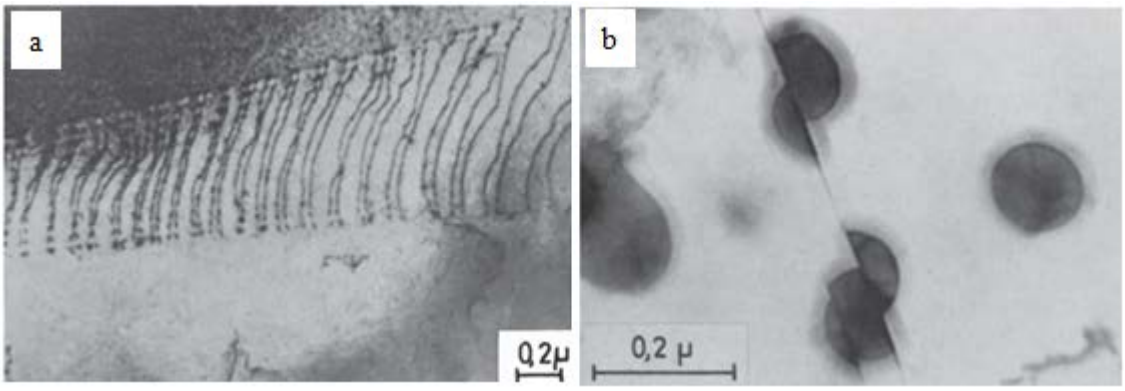

Figure 2.20. TEM photomicrographs showing a) paired super lattice dislocations and b) γ′ precipitate cutting by the moving dislocations in a Ni superalloys [75].

The initial cutting of an ordered precipitate by a single dislocation requires an increase in force that is associated with formation of the antiphase boundary. Thus, as the antiphase boundary energy increases more force is required to cut the precipitate, resulting in an increase in strength. The antiphase boundary energy is a significant contribution to the overall strength, but measurements to determine the effect of individual alloying elements are difficult. The data available all suggest that Ti, Co, Mo, and Fe are effective at increasing antiphase boundary energy [74].

For small precipitates (<20 nm) the pair of dislocations may not lie within an individual precipitate (Figure 2.21a). This case is referred to as weak pair coupling. When the precipitates are larger, the trailing dislocation enters a precipitate before the leading dislocation exits (Figure 2.21b). This situation is referred to as strong pair coupling. In both situations, the strengthening increment is due to the formation of an APB within the precipitate. Figure 2.21c schematically compares the stress required to push a pair of dislocations though a precipitate for each mechanism as a function of precipitate size. The active mechanism changes from weak pair coupling to strong pair coupling as the γ' size increases.

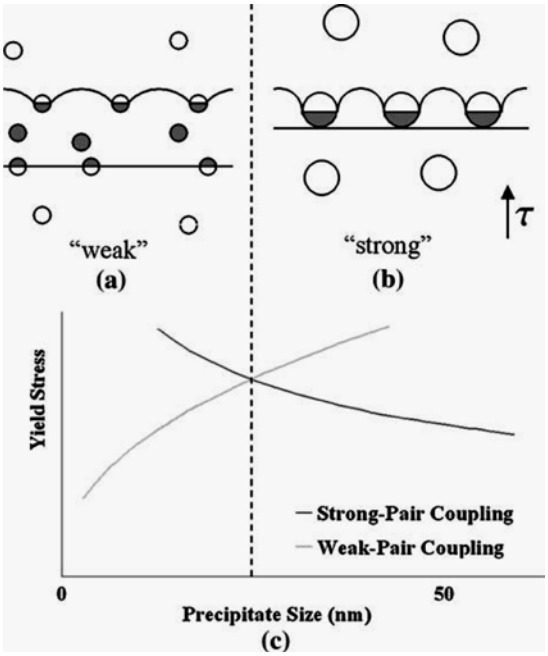

Figure 2.21. Schematic illustration of (a) weak dislocation coupling, (b) strong dislocation coupling and (c) strengthening effect variation with particle size [70].

Alloy strength shows a dependence with maximum on particle size (Figure 2.21), which is a function of the aging temperature and time [78]. At first, precipitation of the γ' from the supersaturated matrix leads to an increase in strength with increasing temperature and time; however, with further increase in temperature / time, an over-aging may lead to the particle coarsening and a decrease in particle volume fraction (Figure 2.22).

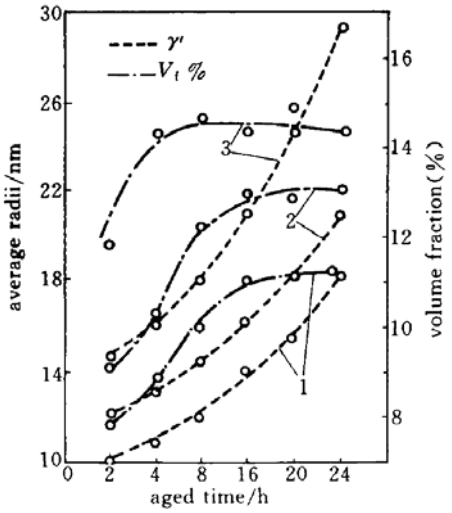

Figure 2.22. Effect of aging time on the γ′ size and volume fraction for various aging temperatures: 1 – 600 °C, 2 – 650 °C, 3 – 700 °C [22].

A decrease in particle volume fraction should be avoided as it results in a decrease in potential number of dislocation-particle interaction sites and strengthening capacity. Therefore, a careful design of heat treatment schedule is required to simultaneously maximise the particle size and particle volume fraction.

Figure 2.23 shows an example of the change in precipitate morphology as a function of γ/γ′ *lattice mismatch* in a Ni-base alloy [79]. The degree of lattice mismatch is noted in each figure. The shape of the precipitate will evolve in a manner that minimizes strain and surface energies. At small degrees of lattice mismatch, the strain energy is low and the most favourable shape that minimizes the surface energy is a sphere. At higher degrees of lattice mismatch, the strain energy becomes important and is orientation dependent. In this case, the orientation relationship between the γ and γ′ promotes a cuboidal morphology, where the γ ′ precipitates typically align themselves along the < 100 > directions of the matrix which have the lowest elastic stiffness. The precipitate morphology will also change as the precipitates coarsen. In this case, the starting morphology is typically spherical, but often gradually changes to cubes, arrays of cubes, and dendritic as coarsening proceeds. The lattice mismatch has important effects on long-term mechanical properties.

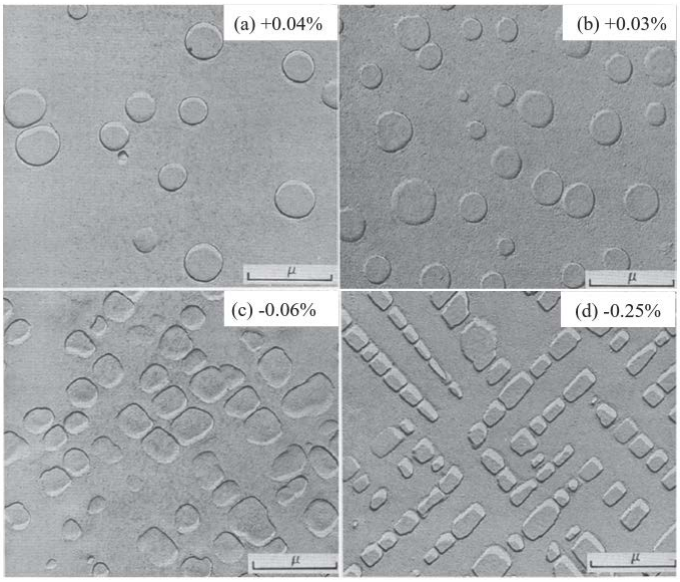

Figure 2.23. Optical images of γ′ particles in a Ni-Al-Mo alloy at different lattice mismatches [79].

Although it is not often recognized, the γ′ precipitate can also be hardened by solid solution strengthening (Figure 2.24). Mo, Si and Ti are the most effective elements for particle strengthening. Cu and Co exhibit appreciable solubility, although do not impart much the strength to γ′.

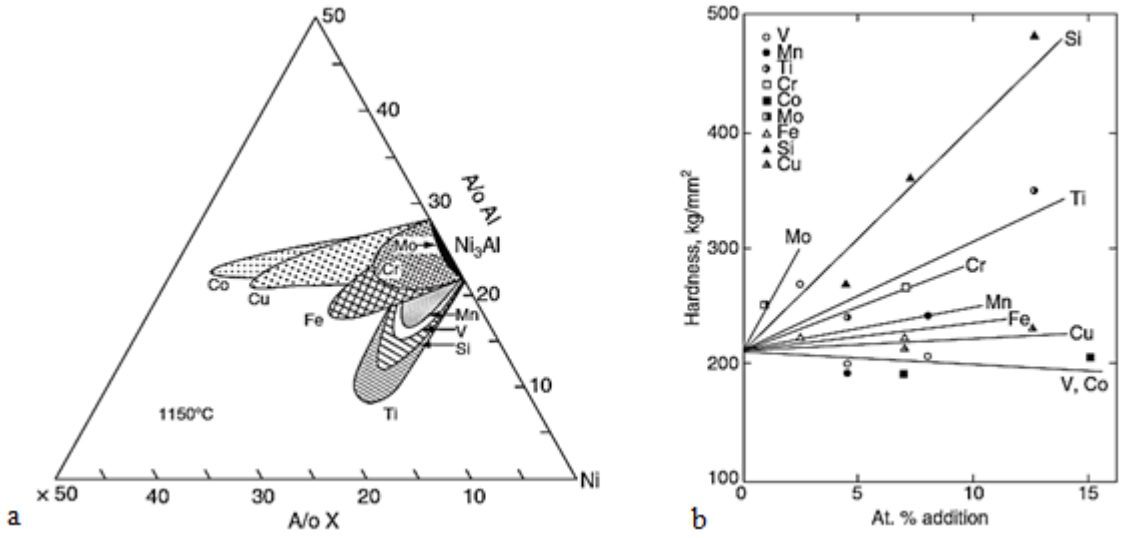

Figure 2.24. (a) Solubility of various elements in γ′ particles at 1150 °C in Ni-Al-X alloy system, (b) effect of various elements on the hardness of γ′ particles at 25 °C [80].

The lattice parameter of both the γ and γ′ phases will depend on the amount and type of alloying elements in solution. As elemental additions are made to an alloy, each element may partition differently to each phase and change the lattice parameter of each phase in a different way. The extent of γ/γ′ lattice mismatch thus depends on the relative partitioning and lattice parameter changes induced by each alloying element (Figure 2.25).

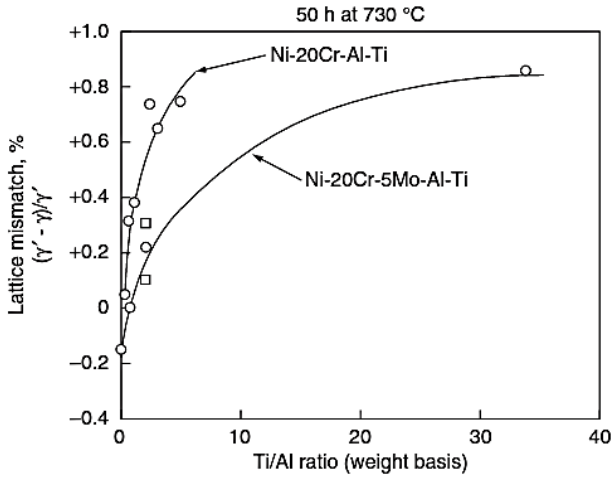

Figure 2.25. Effect of Ti/Al ratio on the γ/γ′ mismatch for Ni-20Cr-Al-Ti and Ni-20Cr-5Mo-Al-Ti alloys with a constant (Al+Ti) content of 3.5 wt.% [81].

2.2.2.4 Work hardening (dislocation strengthening)

The rate of work hardening in the presence of precipitates was found to be higher than that obtained in the case of the precipitate-free (solution-treated) matrix and increased with increasing precipitate size. In specimens where cutting of particles was noticed, the increase in work hardening rate was small. The enhancement in work hardening rate with increasing particle size, even in specimens where particle shearing occurred, was presumably owing to the fact that the passage of dislocations through a particle reduced that particle's diameter, making the passage of the next pair easier. The relative reduction in diameter for a small particle is known to be larger than that for a large particle. In specimens where looping occurred, work hardening was found to be very strong. A straightforward explanation for this is the gradual reduction in the effective interparticle spacing with the formation of loops around precipitates, making passage of dislocations progressively difficult [82].

The strength increases and ductility decreases with an increase in cold deformation (Figure 2.26a). The optimum deformation strain for Monel K500 was found to be about 20 % [22]: at this strain an increment to the yield stress is quite substantial (about 300 MPa) and the remaining ductility is still significant (about 30 % of elongation to failure).

Cold deformation has been shown to affect the strength variation during aging (Figure 2.26b). With an increase in aging temperature up to 600 °C the strength increased for 0 and 10 % cold worked samples. However, the samples cold worked to 20 % and 25 % showed strength peaks in the range of 560-600 °C followed by the strength decrease. Obviously with increase in cold deformation the strain induced precipitation occurs faster; this leads to faster particle growth, decrease in particle number density and strength decrease.

Irrespective of the aging temperature the strength was the lowest for 10 % of prior cold worked material (Figure 2.27). This could be explained if small amounts of deformation facilitated the dislocation breaking from their pinning points, increasing the dislocation mobility and decreasing the yield stress.

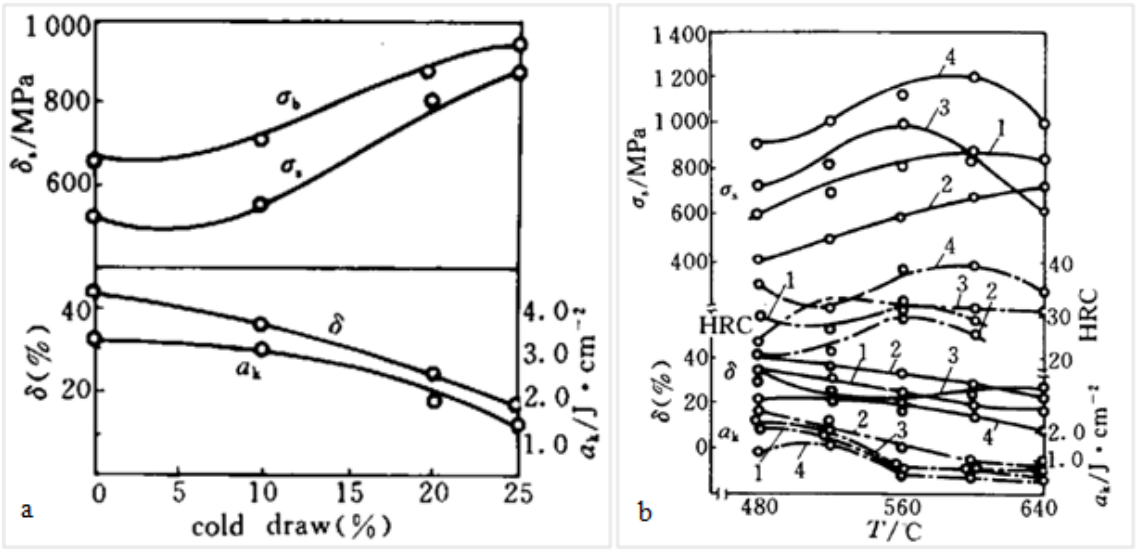

Figure 2.26. (a) Effects of cold work on properties of Monel K500 [22] and (b) Effect of age hardening temperatures on properties of Monel K500 at room temperature for various cold deformation strains: 1 – 0, 2 – 0.10, 3 – 0.20 and 4 – 0.25 [22].

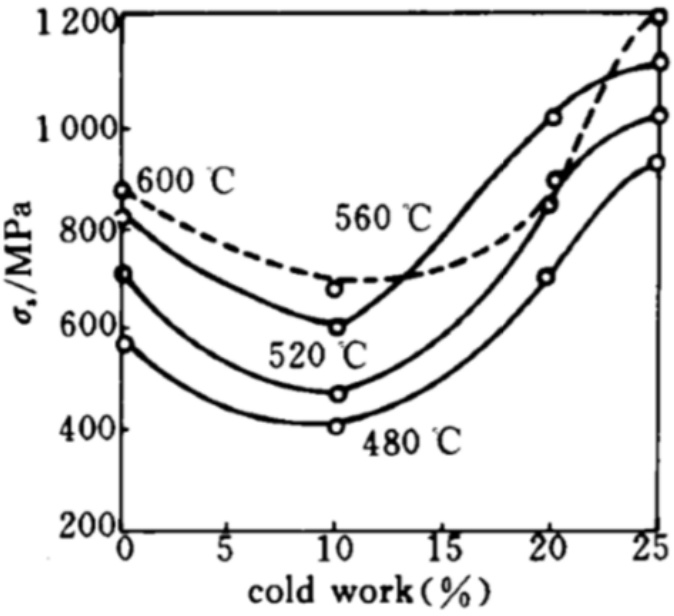

Figure 2.27. Effect of cold deformation on the yield stress of Monel K500 for various aging temperatures [22].

2.2.3 Mechanical properties

2.2.3.1 Tensile properties and hardness

Monel K500 has outstanding mechanical properties in a wide temperature range. The nominal range of room temperature mechanical properties of Monel K500 is shown in Table 2.6 [2]. Cold forming results in slightly higher yield stress values, compared to the hot forming, however the tensile strength varies insignificantly for both production methods. For the hot finished products, annealing may lead to strength decrease by about 30 %; on the other hand, age-hardening may result in 1.3-2.5 times increase in strength, although 1.5 times decrease in elongation. For the cold finish products, annealing may decrease strength by about 40-50 %; and the age-hardening may increase strength by up to 1.3 times and decrease elongation by about 15 %. As seen, the age-hardening heat treatment is more effective in increasing strength of the hot finished products, compared to the cold finished.

The relationships between tensile properties and hardness for various Monel K500 products are shown in Figure 2.28. Short time high temperature tensile properties of Monel K500 rod in various conditions are shown in Figures 2.29. For hot rolled product, with an increase in temperature the yield stress does not vary significantly until 650 °C (1200 °F), and the tensile strength starts decreasing at about 150 °C (300 °F). The hot rolled age-hardened material maintains its strength until about 300 °C (600 °F) and then decreases rapidly with increasing temperature. In contrast, the annealed age-hardened Monel K500 exhibits more stable properties: until about 370 °C (700 °F) no significant variation in YS, TS and elongation were observed (Figure 2.29c).

With a decrease in temperature, the tensile strength and yield stress both increase while ductility and toughness remain virtually unimpaired (Figure 2.30). No ductile-to-brittle transition occurs even at temperatures as low as that of liquid hydrogen. Thus, this alloy is suitable for many cryogenic applications.

Table 2.6. Nominal mechanical property ranges[(a)] of Monel K500 [2].

Form and Condition	Tensile Strength, MPa	Yield Strength, MPa	Elongation, %	Hardness, Brinell (3000-kg)
Rod and Bar				
Hot-Finished	621-1069	276-758	45-20	140-315
Hot-Finished, Aged[(b)]	965-1310	690-1034	30-20	265-346
Hot-Finished, Annealed	621-758	276-414	45-25	140-185
Hot-Finished, Annealed and Aged[(b)]	896-1138	586-827	35-20	250-315
Cold-Drawn, As-Drawn	690-965	483-862	35-13	175-260
Cold-Drawn, Aged[(b)]	931-1276	655-1103	30-15	255-370
Cold-Drawn, Annealed	621-758	276-414	50-25	140-185
Cold-Drawn, Annealed and Aged[(b)]	896-1310	586-827	30-20	250-315
Sheet, Cold-Rolled, Annealed	621-724	276-448	45-25	-
Strip, Cold-Rolled				-
Annealed	621-724	276-448	45-25	-
Annealed and Aged[(b)]	896-1172	621-827	25-15	-
Spring Temper	1000-1138	896-1103	8-3	-
Spring Temper, Aged[(b)]	1172-1517	896-1345	10-5	-
Tube and Pipe, Seamless				
Cold-Drawn, Annealed	621-758	276-448	45-25	-
Cold-Drawn, Annealed and Aged[(b)]	896-1241	586-827	30-15	-
Cold-Drawn, As-Drawn	758-1103	586-965	15-2	-
Cold-Drawn, As-Drawn, Aged[(b)]	965-1517	690-1379	25-3	-
Plate				
Hot-Finished	621-931	276-758	45-20	140-260
Hot-Finished, Aged[(b)]	965-1241	690-981	30-20	265-337
Wire, Cold Drawn[(c)]				
Annealed	552-758	241-448	40-20	-
Annealed and Aged[(b)]	827-1034	621-758	30-15	-
Spring Temper	1000-1310	896-1241	5-2	-
Spring Temper, Aged[(b)]	1103-1379	965-1310	8-3	-

Remarks:

(a) The ranges shown are composites for various product sizes and therefore are not suitable for specification purposes.

(b) Nominal properties for material age-hardened to produce maximum properties.

(c) Properties shown are for sizes 0.0625 - 0.250-in. diameter. Properties for other sizes may vary from these.

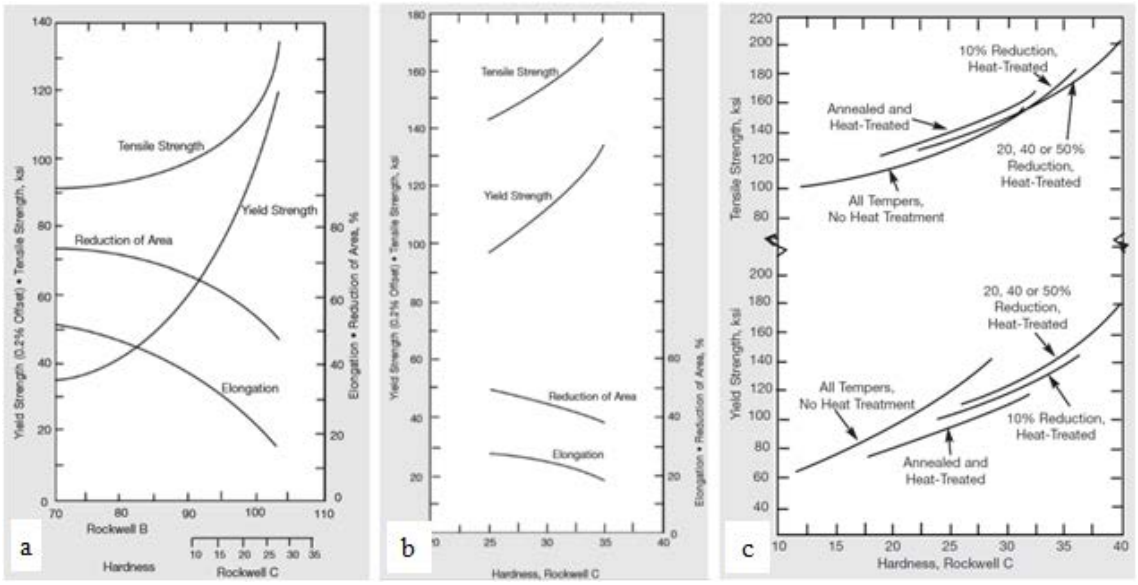

Figure 2.28. Relationships between tensile properties and hardness of Monel K500 for (a) hot-finished rods and forgings, (b) age-hardened rods and forgings and (c) strip and sheet [23].

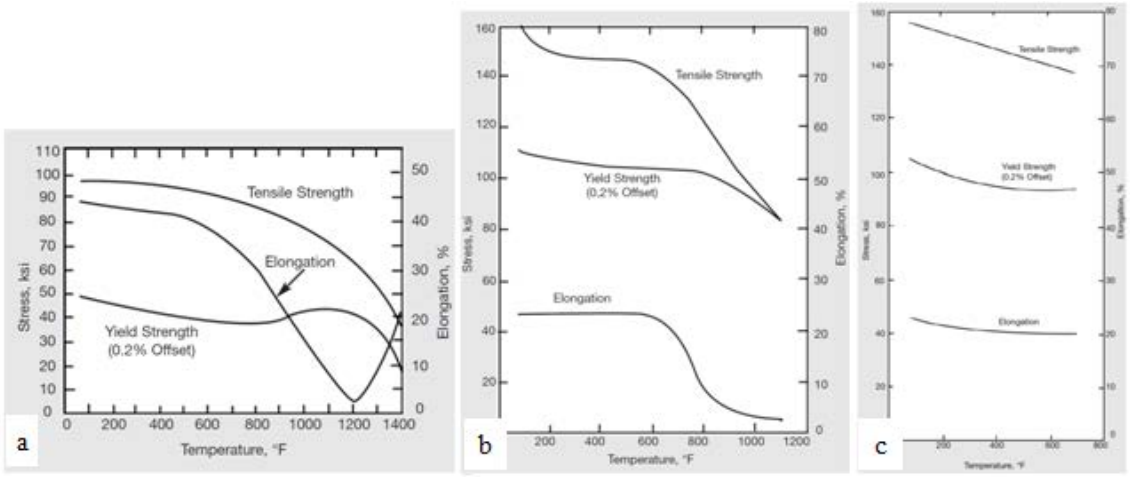

Figure 2.29. High-temperature tensile properties of Monel K500 (a) hot-rolled rod (b) hot-finished age-hardened and (c) annealed and age-hardened [23].

2.2.3.2 Compressive properties

The results of compressive tests on Monel K500, made on triplicate samples from the same melt, are given in Table 2.7 [23]. As seen, there is no significant difference between compression and tensile yield stress values.

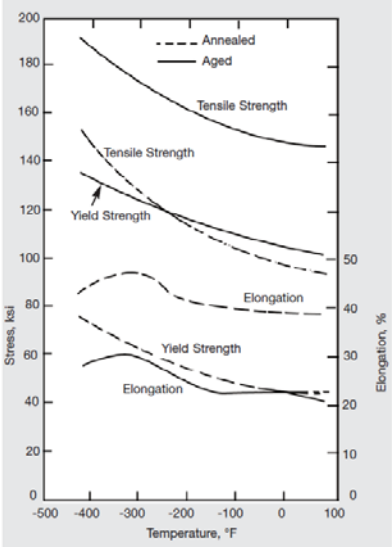

Figure 2.30. Low temperature tensile properties of Monel K500 (1.6 mm sheet) [23].

Table 2.7. Compressive strength of Monel K500 rod.

Property	Hot-rolled		Cold-drawn	
	As-rolled	Aged	As-drawn	Aged
Hardness				
Brinell (3000 kg)	165	300	205	330
Rockwell C	5	33	23	35
Vickers (30 kg – diamond pyramid)	167	316	210	336
Tension				
Yield strength (0.2% offset), ksi	47.0	111.0	85.0	120.0
Elongation, %	42.5	30.0	26.5	22.0
Compression				
Yield strength (0.2% offset), ksi	40.0	121.0	76.0	121.0
Yield strength (0.1% offset), ksi	34.0	96.0	55.0	102.0

2.2.3.3 Impact and fatigue strength

Charpy V-notch impact energy of hot-rolled and cold-drawn rod after annealing and ageing is shown in Tables 2.8 and 2.9, respectively [23]. As seen, there is no significant variation in impact properties with deformation temperature.

Fatigue strength (determined at room temperature for 10^8 loading cycles) for various Monel K500 products is given in Table 2.10 [83]. The fatigue strength slightly increases from the annealed condition to hot/cold rolled and to aged, which corresponds to the variation in tensile strength with processing history.

With an increase in test temperature to 540 °C the fatigue strength of aged Monel K500 decreases by about 6 % (Table 2.11). Such a minor variation in fatigue strength with increasing temperature is a significant advantage of this alloy. With a decrease in temperature

the fatigue strength increases (Table 2.12), which corresponds to the increasing tensile properties and almost unaffected ductility with a decrease in temperature (Figure 2.31).

The surface finish was found to alter the fatigue properties (Table 2.13): the surface oxidation may reduce the fatigue fracture stress by 20 % for hot-rolled and by 30 % for cold-rolled material. These tests indicate the preference of polished surfaces for parts subjected to cyclical stresses in service. The fatigue curve for Monel K500 shows a modest decrease (0.5 % with 10^4 times increase in the number of cycles) in the stress amplitude with an increase in number of cycles (Figure 2.31).

Table 2.8. Properties of hot-rolled Monel K500 rod after annealing at 980 °C for 30 min, ageing at 590 °C for 16 hr, furnace cooling to 540 °C during 6 hr, cooling to 480°C during 6 hr, air cooling to room temperature.

Rod diameter, [(a)] in.	Yield strength (0.2% offset), ksi	Charpy V-notch impact strength, ft-lb
1.250	97.3	54
1.250	92.5	72
0.875	109.3	45
1.00	111.0	38

Remarks: (a) each diameter from different heat.

Table 2.9. Properties of cold-drawn Monel K500 rod after annealing at 980 °C for 30 min, ageing at 590 °C for 16 hr, furnace cooling to 540 °C during 6 hr, cooling to 480°C during 6 hr, air cooling to room temperature.

Rod diameter, in	Yield strength (0.2% offset), ksi	Charpy V-notch impact strength, ft-lb
1.250	92.5	76.25
0.812	103.0	43.75
0.687	110.6	39.5

Table 2.10. Room-temperature fatigue strength of Monel K500.

Condition	Fatigue strength (10^8 cycles), ksi	Tensile strength, ksi	Ratio, fatigue strength / tensile strength
Form: Rod			
Annealed	38	88	0.43
Hot-rolled	43	99	0.43
Hot-rolled, aged	51	155	0.33
Cold-drawn	45	120	0.37
Cold-drawn, aged	47	170	0.28
Form: Strip			
Annealed	27	88	0.31
Hot-rolled, aged	37	153	0.24

Table 2.11. Fatigue strength of Monel K500 (cold-rolled and aged sheet) at elevated temperatures.

Condition	Temperature, °C	Fatigue strength (10^8 cycles), ksi
Hot-rolled, aged	27	46.0
	540	43.0
Cold-drawn, aged	27	52.0
	540	48.0

Table 2.12. Fatigue strength of Monel K500 at low temperatures.

Temperature, °C	Stress, ksi, for a fatigue life of		
	10^5 cycles	10^6 cycles	10^7 cycles
20	90	55	37
-80	99	67	-
-195	105	69	-
-250	143	101	-

Table 2.13. Effect of surface finish on fatigue strength of Monel K500 (R.R. Moore rotating-beam specimens).

Condition	Surface finish	Tensile strength, ksi	Fatigue strength (10^8 cycles), ksi	Ratio, fatigue strength/tensile strength
Hot-rolled, aged	Polished	171.0	50.0	0.29
	Oxidized	172.5	39.5	0.23
Cold-drawn, aged	Polished	174.5	57.0	0.33
	Oxidized	167.5	39.5	0.24

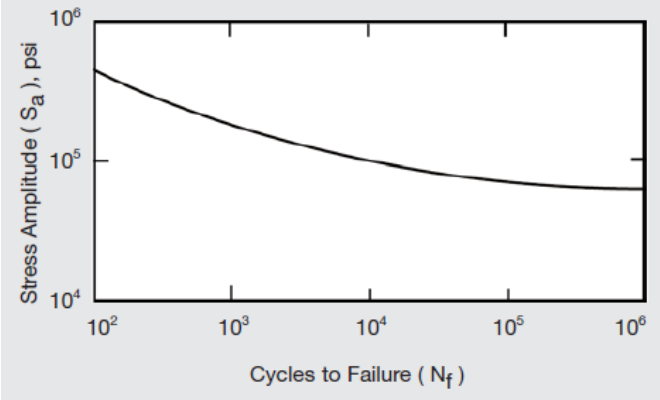

Figure 2.31. Typical stress-cycle fatigue curve of age-hardened Monel K500 [23].

2.2.4 Corrosion resistance

Corrosion is the electrochemical deterioration of metallic materials by reaction with environment. Chemical change of a metallic alloy leading to corrosion either causes or is caused by the flow of direct electrical current. A complete electrical circuit is required for a current to flow. In a corroding system, this circuit is made up of four components: anode, electrolyte, cathode and metallic path (Figure 2.32). The *anode* is the electrode of an electrolytic cell at which oxidation is the principal reaction. Electrons flow away from the anode to the external circuit. It is usually the electrode at which corrosion occurs and metal ions enter solution. The *electrolyte* is a conductive liquid through which the current is conveyed by positively charged ions to the cathode. Negatively charged ions are simultaneously attracted to the anode. The *cathode* is the electrode of an electrolytic cell at which reduction is the principal reaction. Electrons flow toward the cathode in the external circuit. A *metallic path* is an external circuit to complete the connection between anode and cathode.

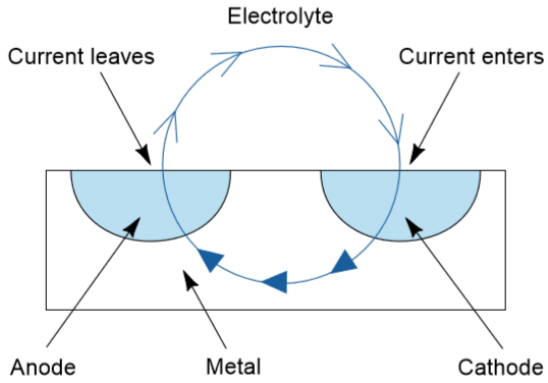

Figure 2.32. Schematic illustration of a corroding system [2].

In the absence of an externally applied current, a potential difference or voltage must exist between the anode and cathode or no current will flow. This voltage is the driving force of the corrosion reaction. The potential difference or driving force for corrosion is most evident in the case of bi-metallic junctions. It is somewhat more difficult to see why a single metal should display both anodic and cathodic areas. In practice, such differences are caused by many factors inherent in the metal such as inclusions, exposure of various crystallographic planes, variations in alloy content, or microscopic surface imperfections. Discrete anodes and cathodes can also be caused by

variations in the electrolyte, such as temperature differences or concentration gradients of the solution, of ions in the solution, or of dissolved gases such as oxygen. In any event, the anodic reaction converts the metal atom to its positive ion, releasing electrons through the metallic junction, which comprises the external circuit.

Metallic corrosion under aqueous conditions can take place by many mechanisms with quite various results. Corrosion may be general or localised. There are also several types of the environmentally assisted corrosion. *General corrosion* is a process of uniform surface deterioration and is the mostly observed type of corrosion. It is characterized by a chemical or electrochemical reaction which progresses uniformly over the whole surface area. In certain conditions the corrosion may occur in specific locations. Such attack is called *localized corrosion* and may appear in several forms: pitting, crevice and microbially influenced corrosion.

Pitting is a form of localized corrosion that results in formation of holes in the metal. While these holes are generally small at the beginning they can grow very quickly, which leads to the material perforation and failure. *Crevice corrosion* usually takes place in confined volumes, for example in narrow gaps between two surfaces. As with pitting, the micro-environment in the crevice can substantially differ from the general medium. Concentration cells can cause this type of corrosion to progress at a very rapid rate. *Microbially influenced corrosion* is a recently identified form of crevice attack. Certain types of bacteria form dome-shaped colonies on the metallic surface. The inside of the structure is sealed from the outside. The life cycle of the bacteria produces a corrosive environment within the colony which causes a crevice attack of the metal. While this type of corrosion usually takes place on components exposed to natural water, it has also been encountered in industrial waters.

Some types of corrosion take place as a result of chemical conditions within the environment and the mechanical condition of the metal itself. Both conditions must be present for this type of corrosion to take place. Corrosion fatigue, stress corrosion cracking, liquid metal cracking, and hydrogen embrittlement are all forms of *environmentally assisted cracking. Corrosion fatigue* takes place due to the reduction of fatigue resistance of a metal with the presence of a corrosive medium. Thus it is normally encountered not as a visible degradation of the metal but as a premature failure of a component under cyclic loading. The stress under which the material fails as a result of corrosion fatigue would not normally be considered sufficient to cause

failure. *Stress corrosion cracking* is caused by the simultaneous presence of tensile stress and a specific corrosive medium. During this type of cracking, the metal is unattacked over most of the surface while fine cracks progress faster due to the corrosive environment. Chloride stress cracking of stainless steels and ammonia stress cracking of nickel-copper alloys are examples of this type of attack. Figure 2.33 shows a dependence of the time to cracking on Ni content in an alloy: alloys containing more than 45% Ni, including Monel, are not susceptible to the stress corrosion cracking in chloride environment.

Hydrogen embrittlement takes place due to the penetration of the surface of vulnerable metals by elemental hydrogen. Formation of metallic hydride compounds and interatomic interaction of dissolved hydrogen may lead to formation and propagation of fine voids and cracks in the metallic structure.

Intergranular corrosion is a selective type of attack at the grain boundaries. Several conditions can lead to a material being susceptible to intergranular corrosion: (i) because of thermal or mechanical processing some metallic compounds may precipitate or migrate to the grain boundaries; if these are more reactive than the metallic matrix, they can be selectively attacked; (ii) areas adjacent to the grain boundaries may become depleted of some element, making these zones less resistant to corrosion.

Erosion corrosion is the acceleration in rate of surface degradation due to relative movement of a corrosive medium along the metal surface. Mechanical wear or abrasion, which is involved with the relative movement, helps to sweep away the corrosion products and, thus, helps deeper propagation of the corrosion attack.

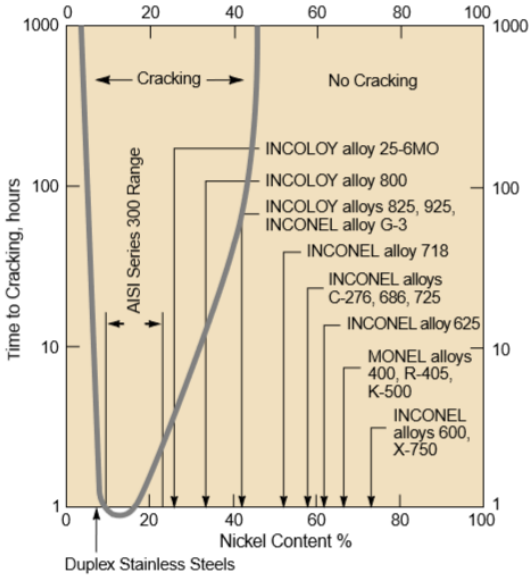

Figure 2.33. Susceptibility of Ni-base alloys to chloride-ion stress-corrosion cracking [23].

2.2.4.1 Corrosion resistance of Ni-Cu alloys in different media

The corrosion resistance of Monel K500 is similar to this of Monel 400, although Monel K500 is more susceptible to stress corrosion cracking in certain environments (sulphide brines) in the age-hardened condition [25]. Table 2.14 summarised the corrosion resistance of Ni and Ni-base alloys in various corrosive media.

Table 2.14. Corrosion resistance of Ni and Ni-base alloys [2].

Alloy Good to excellent Acceptable Not suitable	Sulphuric acid	Hydrochloric acid	Hydrofluoric acid	Phosphoric acid	Nitric acid	Organic acids	Alkalines and salts	Seawater
Nickel 200 and 201					-			
Monel 400					-			
Monel R405					-			
Monel K500					-			

Atmospheric Corrosion

Atmospheric corrosion depends on a number of factors, such as relative humidity, temperature, sulphur dioxide content, hydrogen sulphide content, chloride content, amount of rainfall, dust. In an atmosphere free of contaminants only negligible corrosion would be expected. In an industrial atmosphere many types of contaminants can be expected, but the presence of sulphur (in the form of sulphur dioxide, sulphur trioxide or hydrogen sulphide) is the most important. The formation of sulphurous and sulfuric acids in the presence of air and moisture accelerates corrosion. Marine atmospheres severely corrode many metals. The atmospheric test laboratory at Kure Beach in North Carolina shows that steels exposed 25 meters from the ocean corrode ten to fifteen times faster than steels exposed at a distance of 250 meters [2]. However, corrosion of Monel K500 is negligible in all types of atmospheres, including the marine (Table 2.15). Indoor exposure produces a very light tarnish, which is easily removed by wiping. Outdoor surfaces, that are exposed to rain, develop a thin gray-green patina. In sulfurous atmospheres a smooth, brown, adherent film forms.

Table 2.15. Corrosion resistance of Ni alloys to marine atmosphere at Kure Beach, North California [2].

Alloy	Test lot	Time, y	Ave. corrosion rate mpy (mm/a)	Pitting attack, mils (mm)
Nickel 200	80 ft (25 m)	20	<0.1 (<0.0025)	Nil
Nickel 200	800 ft (250 m)	36	<0.1 (<0.0025)	0
MONEL alloy 400	80 ft (25 m)	20	<0.1 (<0.0025)	<1 (<0.025)
MONEL alloy 400	800 ft (250 m)	36	<0.1 (<0.0025)	<4 (<0.1)
MONEL alloy K-500	800 ft (250 m)	36	0.008 (0.0002)	8 (0.2)

Corrosion in waters

Water can be divided into three main types: distilled and high purity water, fresh water, and seawater. Distilled and high purity waters are the least corrosive because of minimum contents of dissolved gases and solids in them. Fresh waters (potable or "tap" water) are intermediate, and seawater is the most severe. Monel alloys 400 and K500 have excellent resistance to distilled and both hard and soft fresh waters. Rates of corrosion are usually less than 1 mpy (0.03 mm/a) under the most severe conditions of temperature and aeration. In acid mine waters that contain oxidizing salts, attack is accelerated. In seawater Monel alloys 400 and K500 exhibit excellent corrosion resistance in moderate and high velocity interactions (corrosion is 0.01 mm/a). The position of Monel 400 in the galvanic series in seawater with a reference to other metals and alloys is shown on Figure 2.34.

The alloys have excellent resistance to cavitation and erosion corrosion, and the corrosion rates in flowing seawater are usually less than 0.03 mm/a. Monel K500 has very good corrosion fatigue strength of 179 MPa at 10^8 cycles. In stagnant or slow moving seawater, fouling may occur followed by pitting. Such pitting tends to slow down after a fairly rapid initial attack and rarely exceeds 1.3 mm in depth, even after exposure for several years [2]. Salts dissolved in water increase their conductivity and corrosion currents. Therefore, galvanic effects are more pronounced in salt solutions than in pure water. However, Nickel 200 and Monel 400 are not subject to stress corrosion cracking in any of the chloride salts and have excellent general resistance to all of the non-oxidizing halides.

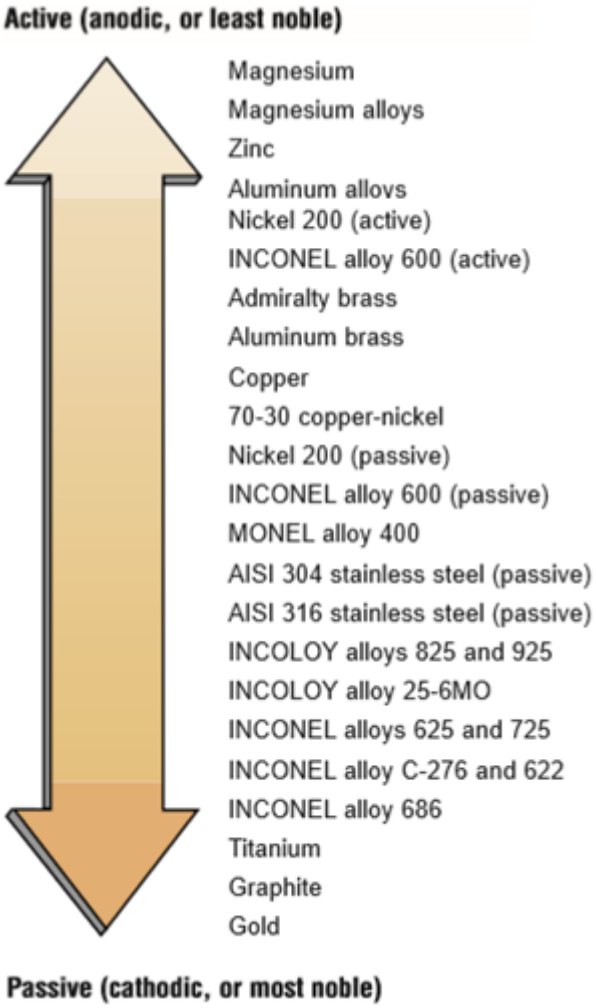

Figure 2.34. Galvanic series in seawater [2].

2.2.4.2 Effects of welding on corrosion resistance

The welding process and choice of welding product can greatly affect the corrosion resistance of the component being fabricated. In most corrosive media, the resistance of the weld metal to corrosion is similar to that of the base metal. If the component is designed to be used in aggressive environments, it is recommended to weld the material with over-matching composition (more highly alloyed, more corrosion-resistant) welding products. Aqueous corrosion takes place as a flow of electric current between an anode and a cathode, corrosion occurs at the anode. The relative sizes of the anode and the cathode can significantly affect the corrosion rate. If the cathode is significantly larger than the anode, the rate can be significantly increased. Thus, when designing a welded structure it is best that the weld metal be cathodic to the base metal. In other words, the weld should be more corrosion-resistant than the base

metal. Since the weld is generally much smaller in area than the base metal, were the weld to be anodic, disastrous consequences could result. For example, the weld could simply corrode away preferentially to the base metal [74].

Corrosion may be due to sensitization of the base metal in heat-affected zones, formation of secondary phases, segregation in the weld metal, or residual stress. The structure of a weldment is similar to that of a casting. Dendrite formation and growth occur first from the highest melting point constituents as the liquid pool solidifies. As dendrites grow, lower melting point materials segregate into the inter-dendrite spaces. Such a chemical inhomogeneity dendritic structure can cause the weld metal to become anodic to the base metal in corrosive environments. Thus, a relatively small anode (weld metal) and a large cathode (base metal) can lead to galvanic corrosion. Post-weld heat treatment is usually impossible and gives only a limited improvement in the corrosion resistance of Ni-base alloy welds. A proven method to prevent corrosion of the welded structures is to use a welding metal, which is more noble than the base metal. The use of more highly alloyed welding metal can compensate for the elemental segregation inherent in the welds [2]. Figure 2.35a shows a corner of GTAW weld from a shipboard desalination unit manufactured using Monel 400. The weld made using the ERNiCu7 welding material with a matching composition has suffered severe pitting (Figure 2.35b) and local corrosion at the fusion boundary (Figure 2.35c) with little attack in the base metal. To avoid this, the NiCrMo-3 consumable was suggested to make the weld cathodic to the base metal in seawater and brine (Tables 2.16 and 2.17) [74].

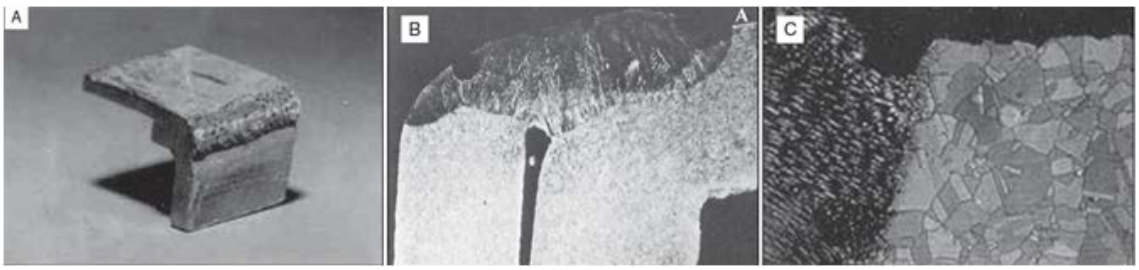

Figure 2.35. (a) A corner welded of Monel 400, (b) the corner cross section, (c) localised corrosion at the fusion boundary [74].

Table 2.16. Galvanic series for several Ni based alloys in synthetic seawater at 25 °C [84]

Voltage (a)	Material
Cathode (protected)	
+0.25	FM 625 (ERNiCrMo-3)
0	
−1.25	Cast 400 (b)
−1.50	Wrought 400
	WE 190 (ENiCu-7)
−1.60	FM 60 (ERNiCu-7)
Anode (Corroded)	

(a) Voltage vs. SCE (Saturated Calomel Electrode).
(b) Cast 400 was produced by induction melting a small piece of wrought Alloy 400.

Table 2.17. Galvanic series for several Ni based alloys in brine at 67 °C [84]

Voltage (a)	Material
Cathode (protected)	
−1.25	FM 625 (ERNiCrMo-3)
−1.40	Wrought 400
−1.50	ENiCrFe-2
−1.70	WE 190 (ENiCu-7)
−1.80	Cast 400 (b)
−3.25	FM 60 (ERNiCu-7)
Anode (Corroded)	

(a) Voltage vs. SCE (Saturated Calomel Electrode).
(b) Cast 400 was produced by induction melting a small piece of wrought Alloy 400.

2.3 Additive manufacturing as a repair technique for Ni-base alloys

Despite its good mechanical and corrosion resistance properties, Monel K500 components may fail in operation. As this alloy is often used for manufacturing of machine parts in which mating metal surfaces rub together, wear is one of the key failure origins. Not only this directly affects equipment life, especially when operated in corrosion environment, but also it may endanger an entire mechanical system if a critical part is damaged [85]. *Sliding wear* is the most common form of wear that results from two metal surfaces rubbing together under sufficient load (Figure 2.36a, b). This type of wear is dependent on physical and chemical factors such as material properties, presence of corrosive atmosphere or chemicals, as well as the dynamics such as the velocity and applied load. *Galling* is another form of wear caused by adhesion of one sliding surface to another. When a material galls, some part of it is pulled with the contacting surface, especially if there is a large amount of force compressing the surfaces. Galling is caused by a combination of friction and adhesion between the surfaces, followed by slipping and tearing of crystal structure beneath the surface. This will generally leave some material stuck or even friction welded to the adjacent surface, whereas the galled material may appear gouged with balled-up or torn lumps of material stuck to its surface. Galling is a major challenge for large components of equipment (Figure 2.36c) [85]. It is common in nickel alloys used for manufacturing high-pressure premium connections, such as valve reciprocating pistons [86]. Pitting corrosion, which is extremely localized corrosion leading to the creation of small holes on the surface, is another form of failure of Monel K500 components (Figure 2.36d). The driving power for pitting corrosion is the depassivation of a small area, which becomes anodic while an unknown but potentially vast area becomes cathodic, leading to very localized galvanic corrosion.

Since Ni-base alloys are expensive, repair is often a more economic choice than replacement. For example, turbine engine components such as frames, buckets, and blades may be repaired multiple times during their service lifetime. There are several principles of repair of such components, the main two of them, thermal spraying and additive manufacturing, are discussed and compared below.

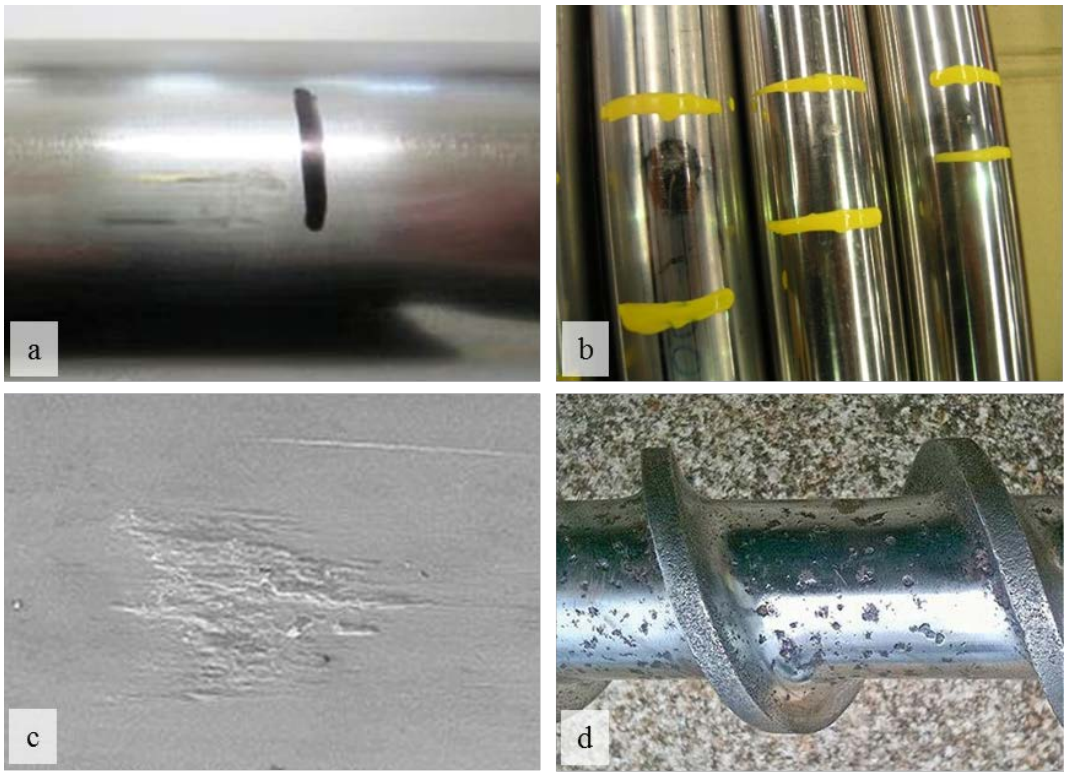

Figure 2.36. Examples of (a, b) sliding wear of Monel K500 piston rods (courtesy of MacTaggart Scott Australia), (c) galling [87], (d) pitting corrosion [88].

Additive manufacturing, or 3D printing, can be applied not only for production of new functional components, but also for repair of old components. This technology is considered one of the rapidly developing advanced manufacturing techniques in the world [89]. Different to the material removal method in conventional machining processes, additive manufacturing is based on a completely contrary principle, i.e. material incremental manufacturing. Additive manufacturing involves layer-by-layer depositing of feedstock (powder or wire) using a computer controlled laser or an electric arc as the energy resource [90].

The microstructural features (such as grain size or texture) and resultant mechanical properties (strength, hardness, residual stresses) are normally difficult to adjust for a specific material processed with additive manufacturing technology [91, 92]. The complex metallurgical phenomena during additive manufacturing processing are strongly material and process dependent and governed by both feedstock characteristics (chemical composition, particle shape, size and distribution, loose packing density, and flowability (for powders)) and processing parameters (heat source type, scan/deposition speed and spacing, feedstock layer thickness) [93]. That is why

significant attention is required for both design strategy of feedstock materials and control of heat source, in order to achieve the feasible metallurgical mechanism for powder consolidation in additive manufacturing processes and resultant favourable microstructural and mechanical properties.

2.3.1. Thermal spraying

Thermal spraying is often used for repair of the components which have shallow evenly distributed defects. In this process a coating material is heated in a hot gaseous medium, and simultaneously projected at a high velocity onto a prepared substrate surface where it builds up to produce the desired coating. It is possible to spray any material that melts (or becomes substantially molten) without significant degradation during a short residence in a heat source [94, 95]. A finishing process is often required for components repaired using this technique as tight control on depth and spread of deposited material is not possible in thermal spraying. The machining of such material can be a difficult task. Sprayed coatings are composed of well-defined particles and have poor thermal conductivity compared to the same material in wrought form. Heat transfer away from the cutting point is slow. The acceptable methods, practices and techniques used for machining materials in their wrought form do not apply to the same materials when sprayed. Materials which are abrasion resistant are especially difficult to machine. To prevent the repair ‘plug’ from coming away off the component, the adhesion of the repair material to the substrate has to be strong enough to resist the forces involved in cutting. Also, the bond between the sprayed particles is primarily mechanical, therefore individual particles can be pulled out if cutting pressures are excessive. For certain applications where surface finish is important, highly reflective finishes are difficult to achieve for sprayed materials with a relatively porous structure. Factors which influence the choice of finishing method include type of material to be finished, the shape of the part, finish and tolerance required, and economics [96].

The high velocity oxygen fuel (HVOF) thermal spraying process (Figure 2.37a) is based on a combination of thermal and kinetic energy transfer, i.e. the melting and accelerating of powder particles, to deposit desired coatings. Powder particles of the coating material are fed axially into a hot gas stream, then into a spray gun, are melted, and propelled to the surface of the workpiece to be coated. Carbon-hydrogen gases

(propane, propylene, acetylene) or pure hydrogen are used as fuel gases and the gas temperature depends on the choice of fuel gas [97].

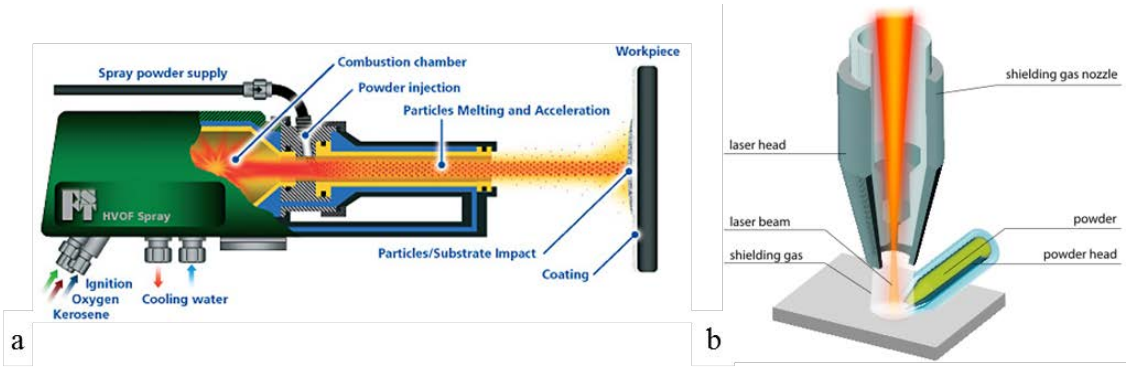

Figure 2.37. (a) Schematic illustrations of: (a) thermal spraying [98] and b) laser metal deposition [104] systems.

HVOF thermally sprayed components contain residual stresses that result from contraction during cooling and solidification. The magnitude of the stresses vary depending upon process parameters used in spraying the coating. The coated material will crack if the magnitude of its tensile residual stresses exceeds its adhesion strength to the substrate. Methods which are generally used to reduce residual stresses in the coatings include: expanding the substrate prior to spraying by pre-heating, selecting a coating material with matching properties to the substrate, and macro-roughening of the substrate surface [99]. Also a degree of inherent porosity can be found in thermal spray coatings ranging from 2 to 20% [100]. Porosity can have a detrimental effect on the performance of anti-corrosion coatings in service because the corrosive media eventually find a path to the substrate [101].

2.3.2 Laser metal deposition

Laser metal deposition allows to coat, build, and rebuild components having complex geometries with a sound material integrity and dimensional accuracy [102]. The laser metal deposits are metallurgically bonded to the substrate, not mechanically bonded like spray or chroming processes [103]. Its powder delivery system consists of a powder feeder that delivers powder into a gas delivery system via the nozzles. The high-energy laser beam is delivered along the z-axis in the centre of the nozzle array and focused by a lens in close proximity to the work piece (Figure 2.37b). Moving the lens and powder nozzles in the z-direction controls the height of the focuses of both laser

and powder. The work piece is moved in the x–y direction by a computer-controlled drive system under the beam/ powder interaction zone to form the desired cross-sectional geometry. Consecutive layers are additively deposited, producing a three-dimensional component.

The temperature during laser metal deposition is difficult to control. At the same time, processing problems (insufficient densification, heterogeneous microstructures and properties) tend to occur in laser sintering processed prealloyed powders. Therefore, post-processing treatment such as furnace post-sintering [105], hot isostatic pressing [106] or secondary infiltration with a low melting point material [107] is normally required to improve mechanical properties. The powder melting by a laser requires a higher energy level, good beam quality, high laser power and thin powder layer thickness, which results in long building time. Consequently, the laser melting suffers from the instability of molten pool. A large degree of shrinkage tends to occur during liquid–solid transformation, accumulating considerable stresses in the processed parts [107]. The residual stresses arising during cooling are regarded as key factors responsible for the distortion and even delamination of the final products. Also, the melt instabilities may result in spheroidisation of the liquid melt pool (known as balling effect) and attendant interior porosity [98].

Due to the layer by layer additive nature of laser metal deposition, the complex thermal histories are experienced repeatedly in different regions of the deposited material, e.g melting and numerous reheating cycles at a relatively lower temperature [108]. Such complicated thermal behaviour during laser metal deposition results in the complex phase transformations and microstructural developments [109]. There, consequently, exist significant difficulties in tailoring a required composition-microstructure-property relationship. Complicated residual stresses tend to be locked into the parts during the building process, due to the thermal transients encountered during solidification [110]. The presence of residual stresses causes deformation or, in the worst instance, cracks formation in laser metal deposition processed components. The uncontrollability of microstructure-property relationship and the formation of residual stresses are regarded as two major difficulties associated with laser metal deposition. During laser melting and laser metal deposition of Ni based superalloys, there is a high cracking susceptivity because of a high amount of alloying elements and gamma-prime forming elements. Cracks mainly nucleate and propagate in the overlap

zone between two adjacent deposited passes. Post-processing, such as hot isostatic processing, are required to realise a substantial improvement of mechanical properties [111].

2.3.3 Wire arc additive manufacturing

Wire arc additive manufacturing (WAAM) has been closely investigated since the 1990s [112] to nowadays [113]. This technique combines an electric arc as heat source and a wire as feedstock and employs either gas tungsten arc welding (GTAW) [114], gas metal arc welding (GMAW) [115], or plasma arc welding (PAW) [116] (Figure 2.38). A consumable electrode is deposited layer by layer to manufacture a new component or repair an old component reducing material wastage and production/repair time [117]. This technique is advantageous due to its high deposition rate, low cost and has virtually no limitations in deposition size. Another advantage of WAAM technology is the absence of a technically complex and expensive powder bed system. WAAM can be implemented using off-the-shelf welding equipment.

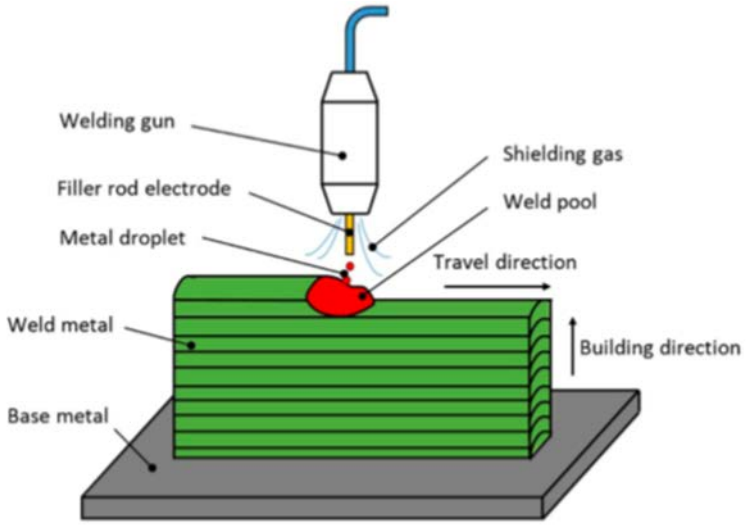

Figure 2.38. Schematic illustration of wire arc additive manufacturing technology.

The solid solution strengthened Ni-base alloys can be easily welded. The weld fabrication does not require preheat, but may require stress relief or annealing, and interpass temperature control during welding is normally not critical. The precipitation hardenable alloys, on the other hand, are less weldable and, because of the presence of the gamma prime

particles, tend to be susceptible to strain-age cracking [5]. Cracks can occur in the heat affected zone (HAZ) on aging or in service at temperatures above the aging temperature, as a result of residual welding stress and stress induced by precipitation. A solution annealing is usually recommended before welding these alloys, and after welding, the appropriate ageing heat treatment is performed. If possible, heat treatment should be done in a controlled-atmosphere furnace to limit oxidation and minimize subsequent surface cleaning. The alloys age-hardenable by Al and Ti precipitates must be solution treated after welding [14]. To avoid prolonged exposure of the welded structure to temperatures within the precipitation range, rapid heating in a preheated to the appropriate temperature furnace is recommended.

The stresses created by welding repair must be relieved in a similar fashion by rapid heating to the solution-treating temperature prior to re-aging. If satisfactory stress relief of the weldment is not feasible, particularly if the structure is complicated, then preweld overaging treatments may be helpful. Preheating, however, is not a satisfactory substitute for postweld heat treatment. Although age-hardenable alloys can be welded in the aged condition, if temperatures encountered in service are in temperature range for precipitation, then the weldment must be solution treated and re-aged [118].

Precipitation hardenable alloys are usually welded by the gas tungsten arc welding (GTAW) process (Figure 2.39a), but gas metal arc welding (GMAW) (Figure 2.39b) and Shield metal arc welding (SMAW) processes are also applicable [119]. Heat input during the weld operations should be held to a moderately low level in order to obtain the highest possible joint efficiency and minimize the extent of heat affected zone. For multiple-bead or multiple-layer welds, many narrow stringer beads should be used instead of a few large beads. Either precipitation hardenable or solid solution strengthened filler metal may be used for welding precipitation hardenable alloys. Maximum mechanical properties, particularly in thick metal, are obtained when precipitation hardenable filler metals are used, because most of the weld deposit is composed of filler metal. The solid solution filler metals produce welds with lower mechanical properties, but they can be used where maximum strength is not needed [14].

For *GTAW* helium, argon, or a mixture of the two are recommended for shielding. Additions of oxygen, carbon dioxide, or nitrogen to argon gas will usually cause porosity or erosion of the electrode and thus should be avoided. Pure-tungsten *electrodes* or tungsten alloyed with thorium or zirconia can be used. A 2% thoria electrode will give good results for most welding applications. Although the initial cost

of the alloyed electrodes is greater, their longer life, resulting from lower vaporization and cooler operation in conjunction with greater current-carrying capacity make them more economical in the long term. Regardless of the electrode used, it is important to avoid overheating them at excessive current levels. The shape of the electrode tip can have a significant effect on the depth of penetration and the width of the bead, especially with welding current over 100 A [118].

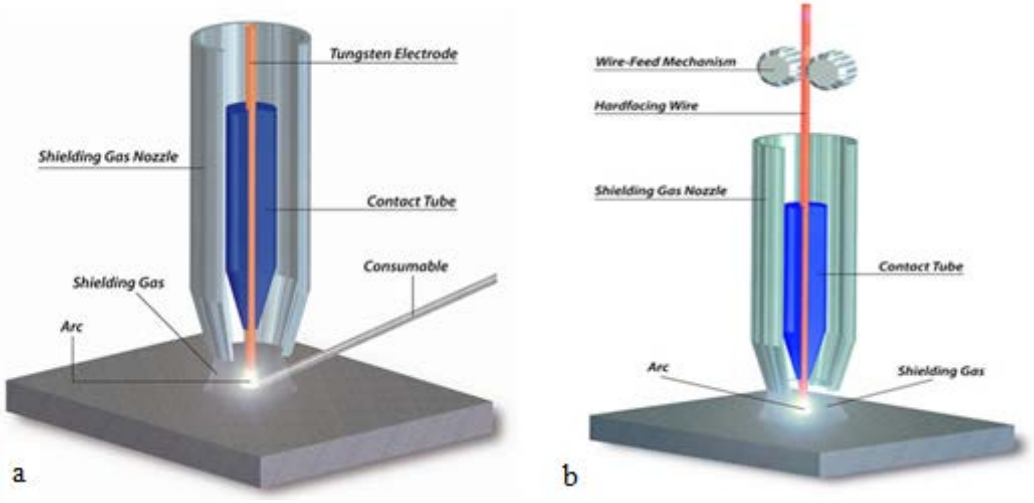

Figure 2.39. Schematic illustrations of (a) gas tungsten arc welding [120], and (b) gas metal arc welding [121] processes.

Compositions of the *filler metals* used with the GTAW process are, in general, similar to those of the base metals with which they are used. Because of high welding temperatures, filler metals are alloyed to resist porosity and hot cracking of the weld metal. Filler-metal additions and dilution ratios should be adjusted to ensure that the weld metal contains about 75% of filler metal [5].

GTAW process for welding Ni-base alloys provides the following *advantages*: minimal post-weld cleanup (no slag to remove); all position welding capability (particularly useful for pipe welding); no weld spatter; no alloy loss during welding; good as-welded surface, which helps to minimise the finishing procedure [122]. The guidelines for GTAW of Monel 400 are presented in Table 2.18.

In the *GMAW* process, an arc is established between a consumable, bare wire electrode, and the work piece. The protective atmosphere dependent upon the metals being joined and the welding procedure. The optimum *shielding gas* will vary with the type of metal transfer used. Argon or argon mixed with helium are used for most Ni alloy welding applications.

Welding torches that are rated for use with inert gases (argon and helium) should be selected for use with nickel alloy filler metals. They are shielded with inert gas with an air-cooled torch. Occasionally wire feed problems are reported. These problems are usually traced to torch overheating. This is because air-cooled torches are normally rated for use with CO_2 shielding gas. CO_2 provides significantly more cooling than inert gases. When inert gas shielding is used, the torch rating is reduced by approximately half of the standard duty cycle rating with CO_2. Optimum welding conditions vary with method of metal transfer. The arc should be maintained at a length that will not cause spatter. A too short arc will cause spatter, but an excessively long arc is difficult to control. The wire feed should be adjusted in combination with the current to give the proper arc length. Lack of fusion can occur with the short-circuiting method if proper manipulation is not used. The gun should be advanced at a rate that will keep the arc in contact with the base metal and not the puddle. In multiple pass welding, highly convex beads can increase the tendency toward cold lapping. With pulsing transfer, manipulation is similar to that used for shielded metal-arc welding. A slight pause at the limit of the weaves is required to avoid undercut. [118].

Table 2.18. Guidelines for manual gas tungsten arc welding of 1.6 mm thick Monel 400 [5].

Joint type	Beveled butt, 1.6 mm root opening
Electrode	2.4 mm diam., EWTh-2, tapered to 0.04 mm diam.
Filler metal	1.6 mm diam., ERNiCu-7
Number of passes	3
Welding current, A	70-90 (DCEN)
Voltage, V	10-12
Shielding gas: At torch, m^3/h Backing gas, m^3/h	 0.6 0.08-0.14
Preheat and postheat treatment	None
Interpass temperature, ºC	175 maximum

GMAW has the following *advantages* over GTAW: faster welding speeds; no slag, minimizing post-weld cleanup; ease of automation; good transfer of elements across the arc [5]. The guidelines for GMAW with filler metal FM60 are given in Tables 2.19 and 2.20.

Welds of Monel K500 can be produced with the strength of age-hardened base metal with no serious loss in ductility if age hardening is performed after welding annealed material. Welding of age-hardened material should be avoided because of greatly reduced ductility. Welding of the alloy K500 is best accomplished by the

GTAW process [14] using the filler metals FM64 and 60, the chemical compositions of which are shown in Table 2.21.

Table 2.19. Guidelines for spray arc transfer gas metal arc welding with FM60 (gas flow 35-60 ft3/h, direct current electrode positive polarity) [118].

Wire diameter (mm)	Wire feed (in/min)	Voltage (V)	Current (A)	Shielding gas
0.89	475-520	26-32	175-260	Argon
1.14	250-300	26-32	225-300	
1.57	150-200	27-33	250-330	

Table 2.20. Guidelines for pulsed-arc-transfer gas metal arc welding with FM60 [118].

Wire Diameter in (mm)	Wire Feed (in/min)	Gas (%)	Flow Rate (cFH)	Voltage (volts)	Average Current (amps)	Frequency (pps)	Peak Current (amps)	Start Current (amps)	Time @ Peak (ms)	Background Current (amps)
.035 (0.9)	300-500	75Ar/25 He or 65Ar/35 He	35-50	22-29	90-140	50-110	250-400	300	1.5-3.5	40-80
.045 (1.2)	250-450	75Ar/25 He or 65Ar/35 He	35-50	24-30	120-170	60-120	300-450	300	1.8-4.0	40-120

Table 2.21. Composition (wt.%) of typical filler metals used for Monel K500 [14].

Alloy	Classification	C	Fe	Mn	Ni	Ti	Al	Cu
FM64	UNS: N05500	0.25	2.00	1.50	63.0-70.0	0.35-0.85	2.3-3.15	Bal.
FM60	AWS: ERNiCu-7	0.15	2.5	4.0	62-69	1.5-3.0	1.25	Bal.

Typical mechanical property ranges of filler metals used for welding of Monel K500 are given in Table 2.22. The tensile properties of filler metals are approximately the same as of the base metals in the annealed condition. For maximum tensile strength, a post weld solution annealing is typically used followed by a custom-designed heat treatment that precipitates the pertinent strengthening phase. Slightly higher temperature and longer aging times generally provide for better impact properties.

Table 2.22. Mechanical properties of filler metals used for Monel K500 [14].

Alloy	Tensile strength, MPa	Yield strength, MPa	Elongation, %	Reduction in area, %	Hardness, HV
FM64	690-1035	550-760	30-15	45-28	290-350
FM60	483-517	276	30-40	50	160

Although nowadays thermal spraying is often used for repair of Ni-base alloys, it can be applied only in case where small evenly distributed defects are present. Additive manufacturing techniques, on the other hand, give wider opportunities for building of a new component as well as for repair of a damaged component. Powder-based processes, such as selective laser melting, selective laser sintering or electron-beam melting are capable of producing complex parts with high geometrical accuracy. However, powder-based process has significant downsides: porosity, low deposition rates (0.1-0.2 kg/h), limited size of the fabricated parts, high cost of powder and the inert gas required for the process.

In contrast, the wire-based additive manufacturing is a relatively simple and cheap process. Compared to powder, metal wires are lower in cost and readily available. The wire-feed processes are more environmentally friendly and have a higher material usage efficiency with up to 100% of melted wire material deposited to build a component. Compared to the powder-based methods, the deposition rates of wire-based methods are much higher (up to 12 kg/h), which allows to economically produce larger size components, although the complexity and accuracy of the fabricated part may be sacrificed.

WAAM combines all the advantages of wire-based additive manufacturing methods, such as:

- Use of readily available feedstock - metal wire that can be produced of a very complicated chemical composition, for example it may contain particle forming elements, which helps to equalise mechanical properties of the repair and base metal in such a precipitation hardenable alloy as Monel K500;

- A stronger adhesion of the repair plug to the base metal, due to full melting of the deposited material and a layer of the base metal. Reliability of a repair technology is of primary importance for such components as maritime;

- A more accurate control over welding parameters results in a more homogeneous grain structure, less porosity and cracking, better mechanical properties, wear resistance and corrosion resistance;

- High deposition rates (high wire feed rate and welding speed), which can result in minimal repair time and faster return of a component to service;
- High energy efficiency.

In addition, WAAM can be applied using off the shelf welding machinery: welding power sources, torches and wire feeding systems. Moreover, it has potentially unlimited build volume, which allows to fabricate large machinery parts.

Recent publications reported successful application of WAAM for making Ti-base [123, 124], Fe-base [125,126], Al-base [127], Cu-base [128] and Ni-Cr-base [129, 130] alloy components. However, a detailed investigation of the effect of WAAM processing parameters on microstructure and mechanical properties of the components has not been conducted. WAAM of Ni-Cu alloys has not been previously reported. In this work a first ever study of the effect of heat treatment on microstructure, mechanical properties, wear resistance and corrosion resistance of Ni-Cu alloys fabricated using WAAM technology is presented.

3. MATERIALS AND EXPERIMENTAL TECHNIQUES

3.1 Materials

Two welding consumables, commercially produced Monel K500 wire with diameter 1.0 mm and ERNiCu-7 (FM60) wire with diameter 1.2 mm were used in this study for comparison. Monel K500 plate with dimensions 600x260x8 mm was used as the substrate and a reference for the mechanical properties. The chemical compositions of Monel K500 (plate, wire and component) and FM60, measured in this work using Optical emission spectroscopy, are listed in Table 3.1.

Table 3.1. The chemical compositions of Monel K500 (plate and wire) and FM60 used in the study (wt. %)

Element / Alloy	Ni	Mn	Fe	Si	Al	Ti	C	S	P	Cu
Monel K500 (plate)	68.1	1.01	1.25	0.09	3.18	0.68	0.009	0.004	0.004	bal.
Monel K500 (wire)	68.3	0.8	1.29	0.17	3.0	0.5	0.088	0.003	0.003	bal.
FM60 (wire)	67.2	3.2	0.08	0.07	0.2	1.5	0.004	0.014	0.003	bal.

3.2 Experimental techniques

3.2.1 Samples fabrication

The samples for the study were produced using a robotic welding system at the University of Wollongong (Figure 3.1). A computer interface (a) was used to program the experimental processes, the robot controller (b) aided in coordinating both the welding power source (c) and the robot motions (d). CMT welding torch (e) was used to deliver the wire arc. The process parameters were monitored from control panel (f). The experiment set up is shown in Figure 3.1g.

The wire deposition was carried out by cold metal transfer (CMT) technology using an ABB 1400 robot with a Fronius CMT welder in flat position. CMT technology is a modified gas metal arc welding process with controlled droplet detachment in short circuit transfer mode. When a short circuit occurs, the welding current drops and the filler wire starts to retract. At this moment one droplet of metal is detached into the

molten weld pool, then the filler wire moves forwards and the cycle is repeated. This technology facilitates a controlled droplet detachment and gives a clean, spatter-free material transfer. No base metal preheating was conducted prior to commencing the deposition process; therefore, the cooling rate of the first deposited layer was maximum. The deposition of two alloys was carried out using a wide range of welding parameters: welding torch travel speed varied from 200 to 500 mm/min, wire feed from 5.4 to 10.5 m/min; heat input from 200 to 700 J/mm. Welding grade argon (99.995% purity) was used for shielding with 10 L/ min gas flow rate.

Figure 3.1. Schematic diagrams of the WAAM system: (a) computer, (b) robot controller, (c) welder, (d) ABB 1400 robot, (e) CMT welding torch, (f) control panel, (g) set up of the robotic CMT process.

Both wires were deposited in simple forms of beads, plates and walls. The resulting heat input was higher for Monel K500, even though the deposition of FM60 was carried out using the same pre-set welding parameters (travel speed and wire feed rate). This can be related to the variation in the wires diameter and alloys composition (thermal conductivity). Thus, the average calculated heat input in Monel K500 was 530, 430 and 330 J/mm, and in FM60 - 410, 300 and 240 J/mm, for travel speeds of 300, 400 and 500 mm/min, respectively.

The horizontal plates (55 mm wide by 180 mm long) were fabricated by depositing one pass of material next to the other until the required width was reached

(Figure 3.2a,c,d). Fewer layers were required for a slower travel speed and more layers for a faster travel speed. Namely, 10, 11 and 15 beads were required for Monel K500 depositions at 300, 400, 500 mm/min travel speed, respectively; and 11, 14 and 16 beads were required for FM60 depositions at 300, 400, 500 mm/min travel speed, respectively.

Figure 3.2 Wire arc additive manufacturing process: (a) deposition of multi-bead single-layer plates; (b) deposition of single-bead multi-layer walls; plates and walls produced at travel speeds of 300, 400, 500 mm/min with (c) Monel K500 and (d) FM60.

The vertical walls (40 mm high by 180 mm long) were built by depositing one layer of material on top of another until the required height was reached (Figure 3.2b-d). The number of layers varied with a welding travel speed: bigger bead was produced

with slower travel speed, so that fewer layers were required to build the wall with 300 mm/min travel speed, than with 500 mm/min travel speed. Namely, 15, 18 and 20 layers were deposited with Monel K500 and 18, 21 and 24 layers were deposited with FM60 at travel speeds of 300, 400, 500 mm/min, respectively.

The deposited walls and plates were cut using an EDM wire cutting machine, Struers Axitom and Struers Accutom cutting machines according to the required geometry (Figure 3.3).

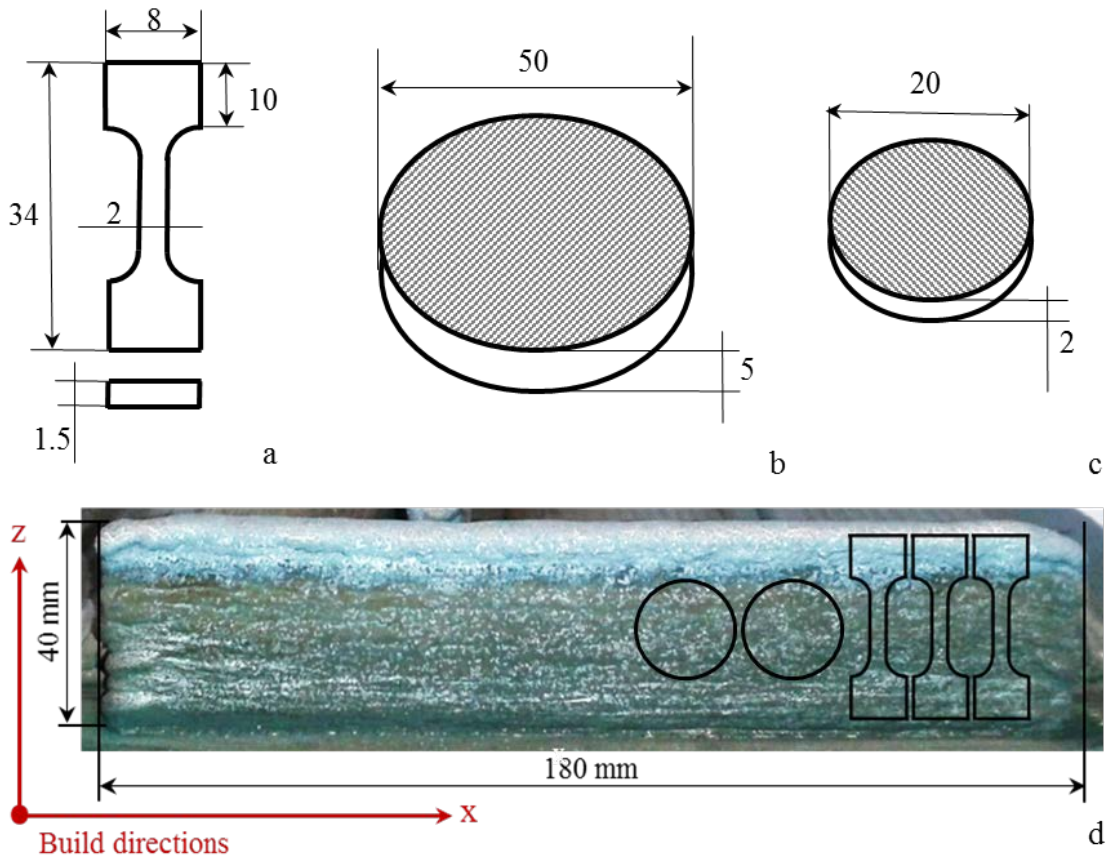

Figure 3.3 Geometry of samples for mechanical testing: (a) tensile test sample; (b) wear test sample; (c) corrosion test sample; (d) schematic diagram showing the direction of vertical wall deposition and samples extraction locations.

A summary of all experiments conducted in this work is given in Table 3.2.

Table 3.2. Summary of experiments conducted in this work

Experiment / Stage	WAAM	Heat treatment	Macro- and microstructure characterisation	Mechanical properties testing
Development of WAAM: Monel K500 wire on Monel K500 plate	12 single-bead lines, 5-layered wall, travel speed 300-500 mm/min	3 schedules	Microscopy: Optical, Scanning electron	hardness
Investigation of WAAM: Monel K500 and FM60 wires on Monel K500 plate	6 single-bead lines, 6 walls and 6 plates, travel speed 300-500 mm/min	3 schedules	Microscopy: Optical, Scanning electron, Transmission electron, Atomic resolution	hardness, tensile, wear, corrosion
Repair using WAAM: Monel K500 wire on Monel K500 rod	single-bead lines along the cylindrical surface of the rod, travel speed 200 mm/min	3 schedules	Microscopy: Optical, Scanning electron	hardness

3.2.2 Heat treatment

The heat treatment procedures have been designed in order to improve the properties of the depositions following the guidance given in the current Defence standard 02-771. These schedules included heating up to the annealing temperature of 1100°C with a rate of 10°C per minute, holding for 15 minutes and either: i) air cooling to room temperature, or ii) furnace cooling to 610°C followed by holding for 8 hours at this temperature and air cooling to room temperature, or (iii) furnace cooling to 610°C, holding for 8 hours, furnace cooling to 480°C, holding for 8 hours, followed by air cooling to room temperature.

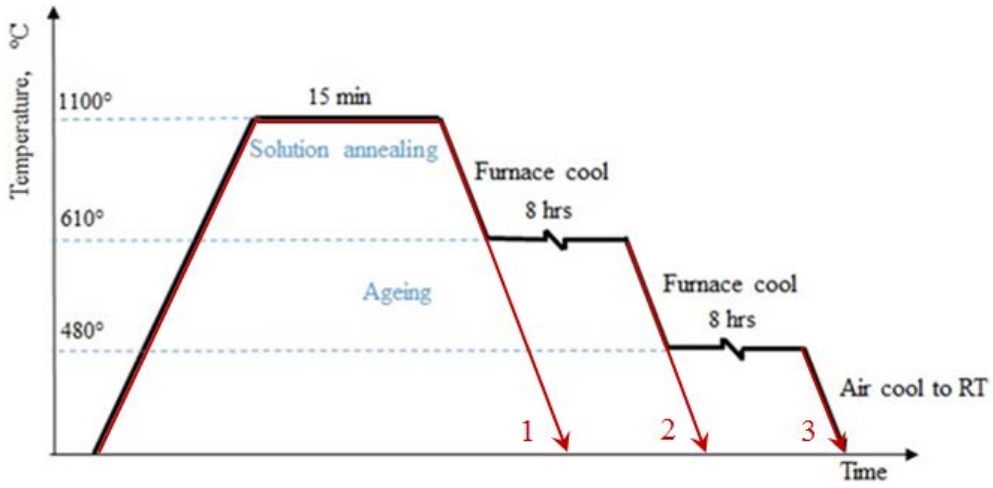

Figure 3.4. The heat treatment procedures.

The three heat treatment schedules are shown in Figure 3.4. Heat treatment was performed using an “Across International” KTL1400 Tube Furnace. The samples were treated in vacuum.

3.2.3 Microstructural analysis

The chemical compositions of Monel K500 plate, Monel K500 wire and FM60 wire were measured using the Optical emission spectroscopy by Oxford Instruments UVTouch probe (Figure 3.5). This method uses arc and spark excitation (Arc Spark OES) in order to determine the chemical composition of metallic samples. At least seven test probes were taken in order to calculate accurate average values, first three have not been taken in consideration as they were used for the gun warm up and recalibration.

Figure 3.5. (a) Oxford Instruments UVTouch probe; (b) testing of sample;
(c) monitor displaying test results.

Sample preparation for optical and scanning electron microscopy included mounting in Polyfast resin, polishing on Struers Tegramin-25 automatic polisher to 1 μm finish and etching with ferric chloride solution. Samples for transmission electron microscopy and atomic resolution microscopy, 3mm in diameter discs, were manually polished to approximately 80 μm in thickness, dimpled ground to 35-40 μm thick in the centre of the dimple, polished with alumina, and ion milled on Gatan precision ion polishing system (PIPS) model 691. The foil thickness was measured by converging beam diffraction technique to be about 80 nm.

Optical microscopy was carried out by using Leica M205A stereo microscope and Leica DM 6000M microscope equipped with Leica Application Suite (LAS) 4.0.0 image processing software. Scanning electron microscopy was conducted using JEOL7001F FEG scanning electron microscope (SEM) operating at 15 kV. The energy dispersive X-ray spectroscopy (EDS) of precipitates and the element distribution mapping were carried out using an AZtec 2.0 Oxford SEM EDS system. For the determination of >20 nm particles size and number density values, up to 350 particles have been measured for each studied condition. Particle compositions were analysed on up to 60 particles for each condition. The element distribution mapping was carried out 2-3 times from various locations for each studied condition. The line scans for evaluation of Cu segregation were carried out 3-4 times per each studied welding condition. The data was taken from at least 35 points per image with a step of 0.4 μm between points.

Transmission electron microscopy was conducted using JEOL JEM-2011 operating at 200 kV. For the determination of <20 nm particles size and number density values, up to 1600 particles have been measured for each studied condition. Particle types were analysed using selected area diffraction technique. The dislocation density was evaluated on area of 980059.6 nm^2 for each studied condition. The dislocation imaging was conducted near the [101] grain zone axis. Atomic resolution microscopy was carried out using JEOL JEM-ARM200F, a probe corrected scanning transmission electron microscope, operating at 200kV. Atomic resolution EDS mapping was conducted using a JEOL Centurio SDD detector.

3.2.4 Tensile testing

Tensile tests were performed on MTS Landmark servohydraulic testing machine, model 370.02 (Figure 3.6a). Flat dog-bone type samples of 10-mm gage length, 2-mm width, and 1.5-mm thickness (Figure 3.6b) were cut perpendicular to the direction of material deposition. For each condition, 3-4 samples were tested at an ambient temperature at a strain rate of 1×10^{-3} s^{-1}.

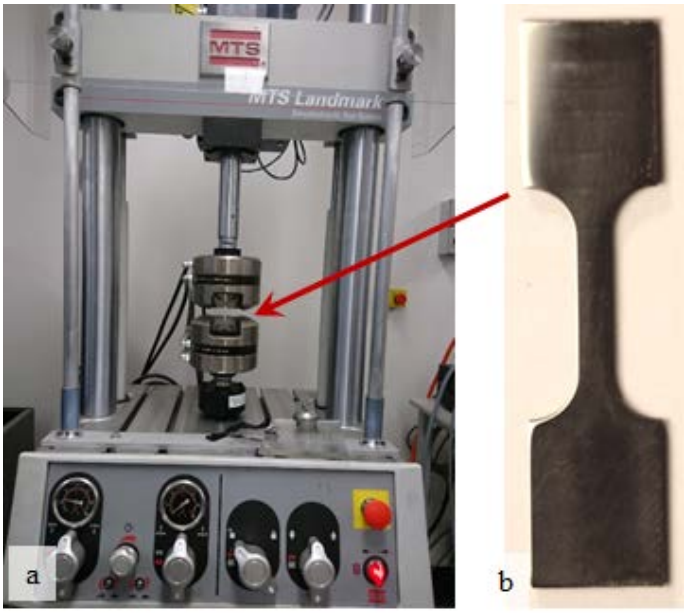

Figure 3.6. Tensile testing: (a) MTS Landmark servohydraulic test system; (b) tensile test sample.

3.2.5 Wear testing

Wear resistance of material depositions and base plate was investigated using the pin-on-disk type of test utilised in a CETR tribometer (Figure 3.7a). The wear testing was performed according to the standard ASTM G 99-95a. For this test two specimens are required: a pin with a radiused tip, which is positioned perpendicular to the flat circular disk. The test machine causes the disk specimen to revolve about the disk centre, the sliding path is a circle on the disk surface. The rigidly held pin specimen is pressed against the disk at a specified load. Wear results are reported as mass loss in grams for the disk.

Discs for the wear testing (Figure 3.7b), were grinded to flat surface and polished on Struers Tegramin automatic polisher with silicon carbide polishing foil 2000 (10

micron). 6 samples (Monel K500 wire and FM 60 deposited with three welding speeds) were tested for each heat treatment condition (in as-weld, annealed and aged at 610°C, and annealed and aged at 610°C and 480°C condition). The wear resistant steel with martensitic microstructure (hardness 500HV) was used as a pin. Each sample underwent 3 successive testing cycles, 750 sec of total sample-disk interaction time, track diameter 30 mm, velocity 0.758 m/c (500 rpm), total path length 600 m. One test cycle included vertical loading of the pin to 15 N load (in compression against the sample disk) and rotation of the disk for 250 sec. The wear resistance was assessed via the sample mass loss measured after each cycle (i.e. after 250, 500 and 750 sec of testing time). The sample mass was measured on fine analytical scales Nuweight AS 310.R2 with accuracy of 0.0001 gram.

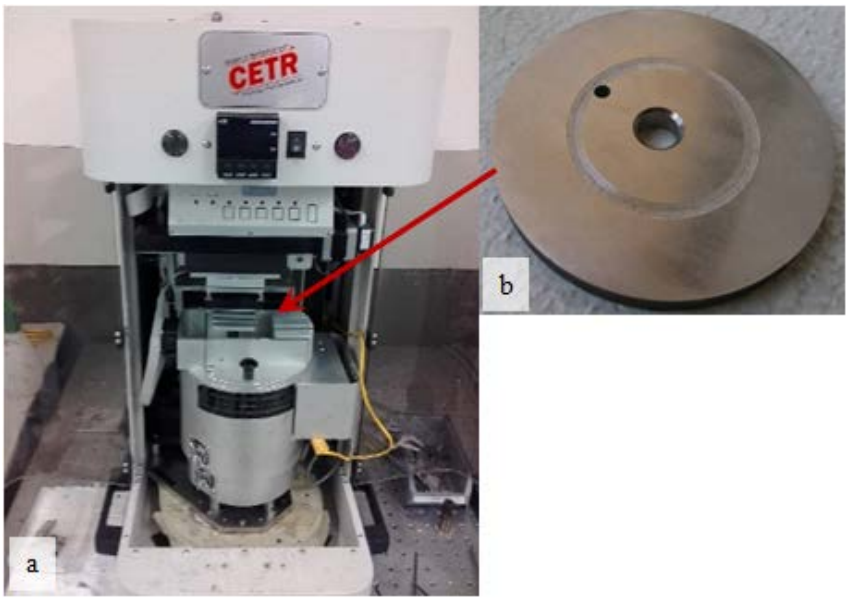

Figure 3.7. Wear testing (a) CETR tribometer; (b) wear test sample.

3.2.6 Surface roughness testing

The roughness of the samples' surface after the wear testing was assessed with a help of the ContourGT-K 3D Optical Microscope equipped with the Vision 64 software (Figure 3.8). The measurements were performed in the VSI mode, green light was used to illuminate the sample.

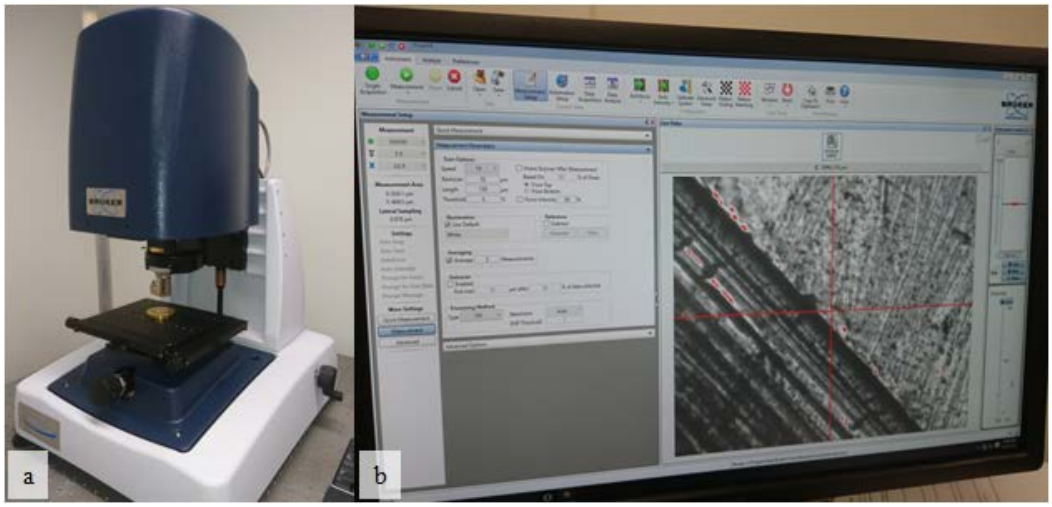

Figure 3.8. (a) ContourGT-K 3D Optical Microscope; (b) Vision 64 software interface.

3.2.7 Hardness testing

Micro hardness testing was performed on Struers DuraScan Vickers hardness tester with 0.5 kg load. The data was acquired from the base metal, heat affected zone (HAZ), remelted zone (RZ) and fusion zone (FZ) for evaluation study, as-weld condition of single-bead weld lines of deposited Monel K500 and FM 60 and component repair. The microhardness of all other samples was measured in the FZ only. Up to ten indentations were performed in each section, with a distance of approximately five times the length of the indent diagonals to ensure that the results were not contaminated by work hardening from previous indentations. The indentation dwell time was 14 s according to the standard ASTM E384.

3.2.8 Corrosion testing

The electrochemical corrosion behaviour of all samples was studied with a help of a standard three-electrode polarisation cell. The polarisation cell consisted of an electrolyte solution - 3.5 wt. % NaCl, a counter electrode (CE) - Pt wire, a reference electrode (RE) - saturated calomel electrode Hg/Hg_2Cl_2 and a working electrode (WE) – the sample of interest (Figure 3.9). The electrical circuit of polarisation cell is shown in Figure 3.10. The 3.5 wt. % NaCl electrolyte solution was chosen as similar to seawater environment, in which the tested alloys would potentially be operated.

The electrodes were connected to the potentiostat Gill AC - ACM Instruments. The samples were polished with 1200 µm polishing foil, degreased with ethanol, rinsed

with water and placed in the electrochemical cell. The samples' surface area exposed to the electrolyte was 0.95 cm^2.The data was analysed with the Sequencer software. The open circuit potential (E_{ocp}) was recorded after the values were stabilized (approximately after 5 min). The cyclic polarisation test was performed with the sweep rate 120 mV/min. The polarisation start potential and reverse potential were -250 mV and +700 mV from $E_{ocp,}$ respectively. One complete cycle of polarisation was performed. The corrosion current (I_{corr}) was measured with a classic Tafel analysis of polarisation curves. At least 3 tests have been performed for each sample condition to improve the accuracy.

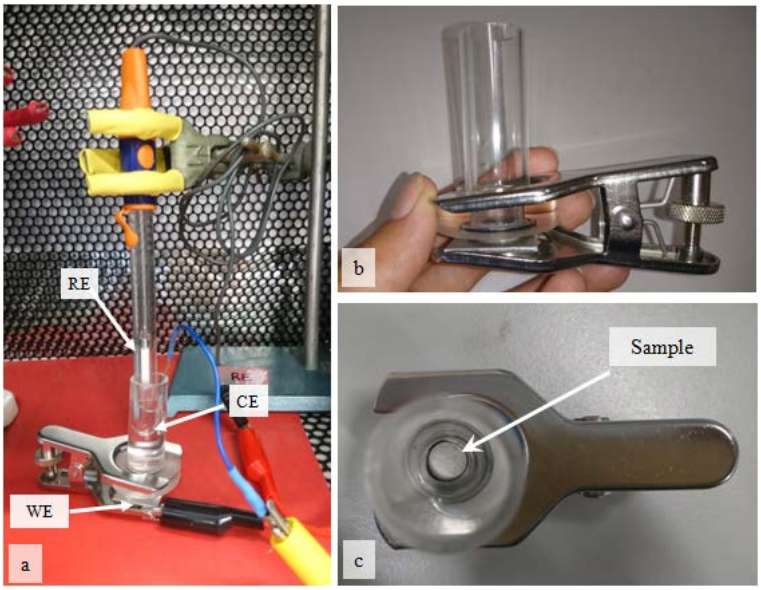

Figure 3.9. Electrochemical test set-up.

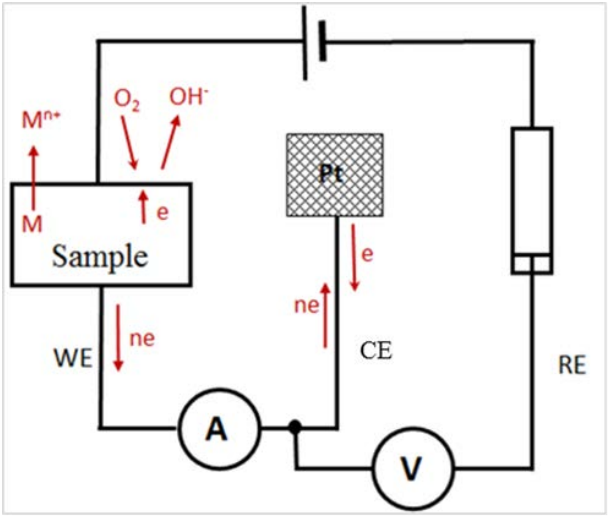

Figure 3.10. Electrical circuit of polarisation cell.

4. RESULTS AND DISCUSSION

4.1 Analysis of as-received materials

4.1.1 Monel K500 plate

Three pieces have been cut out of the received Monel K500 plate for determination of the rolling direction (Figure 4.1.1), microstructural analysis and mechanical testing.

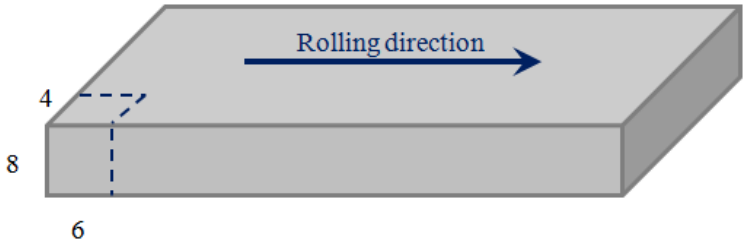

Figure 4.1.1. Diagram showing cutting lines of the sample.

Optical microscopy of as-received Monel K500 plate has shown the hot rolled microstructure. The microstructure consisted of single phase fcc grains with average size of 25 μm and 200-600 nm particles evenly distributed through the volume (Figure 4.1.2). The SEM-EDS elemental mapping has shown the particles to be of TiCN type (Figure 4.1.3). Some particles contained sulphur (Figure 4.1.4). The mean hardness value of 180 HV, which is quite low for Monel K500, suggested that the plate did not undergo the age hardening heat treatment after rolling.

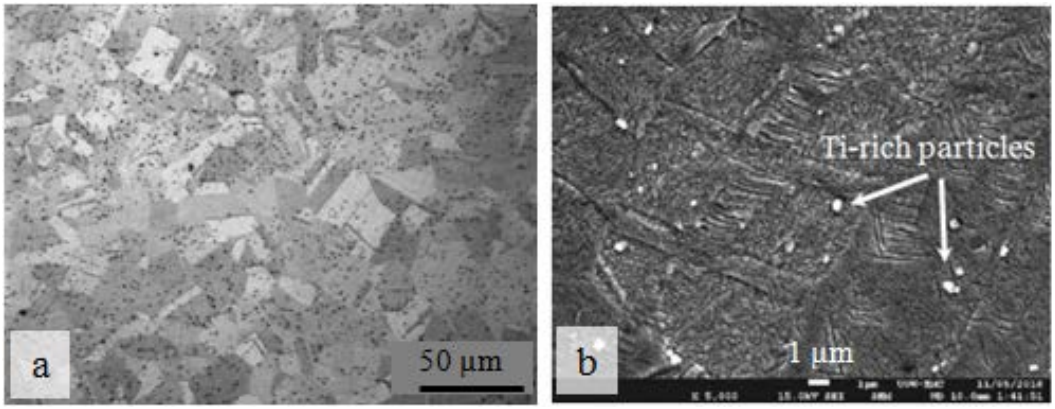

Figure 4.1.2. (a) Optical and (b) SEM images showing Ti-rich particles in as-received Monel K500 plate.

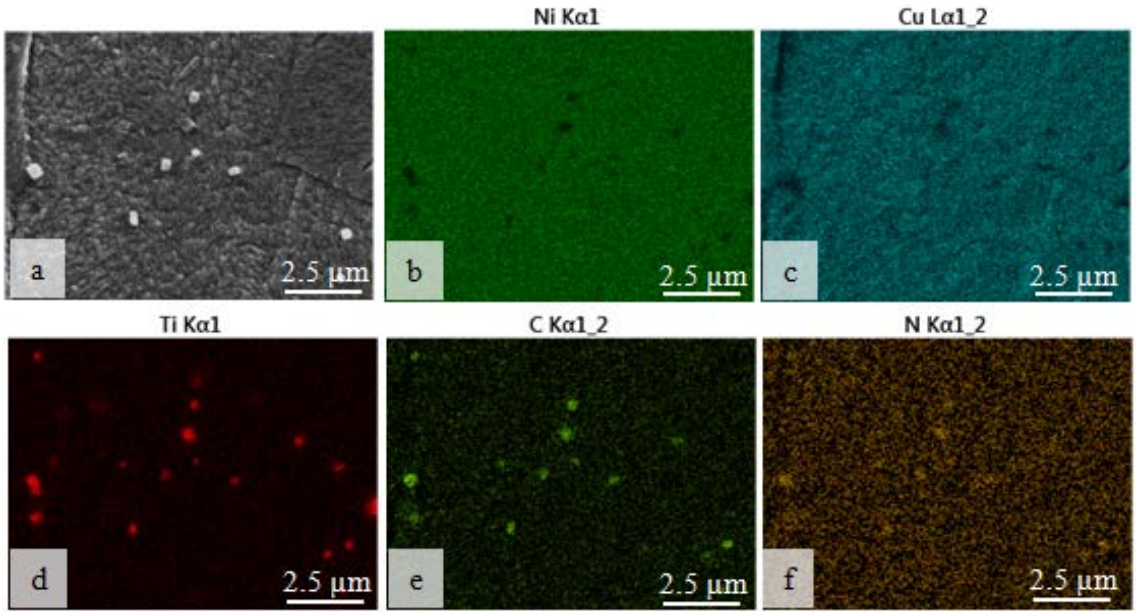

Figure 4.1.3. (a) Representative SEM image of as-received Monel K500 plate microstructure and (b-f) EDS maps showing TiCN particles.

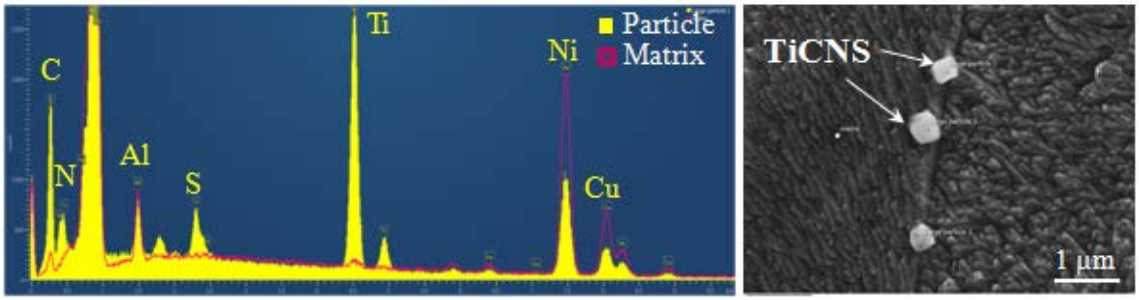

Figure 4.1.4. EDS spectra showing chemical composition of TiCNS particles; the matrix spectrum is shown in purple, the particle spectrum is shown in yellow.

4.1.2 Monel K500 and FM60 wires

The microstructure of Monel K500 and FM60 wires consisted of single phase fcc grains. The average grain size in Monel K500 was 8 µm and 300-850 nm spherical and rectangular particles were evenly distributed through the volume (Figure 4.1.5 a-c). More than 60 particles have been analysed on the SEM-EDS, the point and ID analysis has shown them to be Ti-rich (TiC and TiCN) (Figure 4.1.6). The mean hardness value was measured to be 334 HV. Larger average grain size of 20 µm was observed for FM60 (Figure 4.1.5 d-f). Bulky spherical and rectangular particles of 500-1500 nm have shown to be Mg-rich. Some of the particles contained Ce (Figure 4.1.6c), which sometimes is added to the welding consumables to form (CeTi)-based oxide in order to

increase the trapping efficiency for hydrogen [131]. The number density of particles in as-received Monel K500 wire was 25 times higher than in FM60 (Table 4.1.1). A finer grain size and a higher particle number density explain a higher hardness of Monel K500 wire (334 HV) compared to this of FM60 (296 HV).

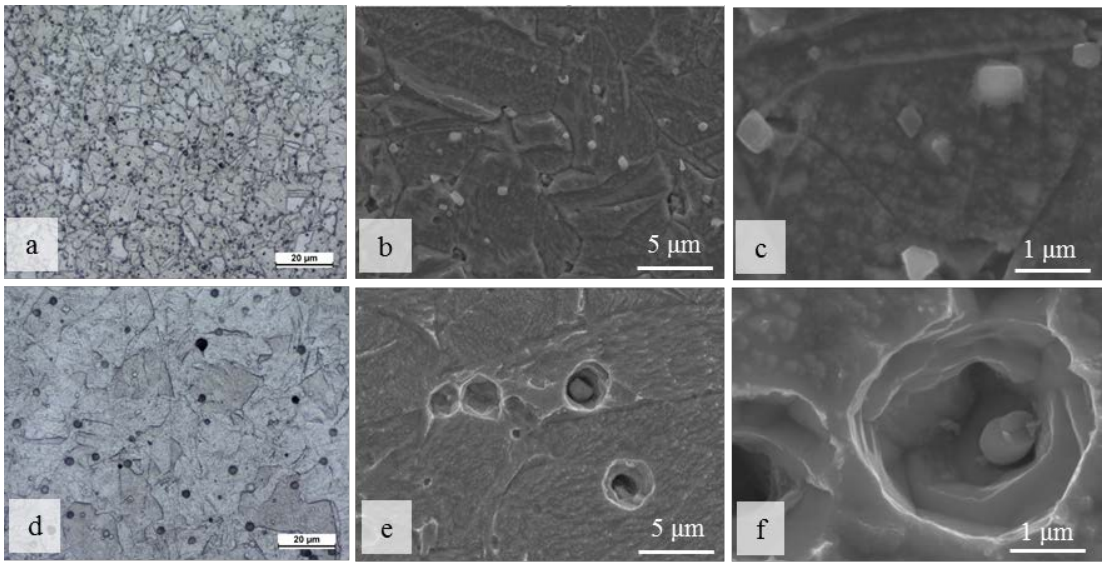

Figure 4.1.5. Optical and SEM images of as-received wires: (a-c) Monel K500 and (d-f) FM60.

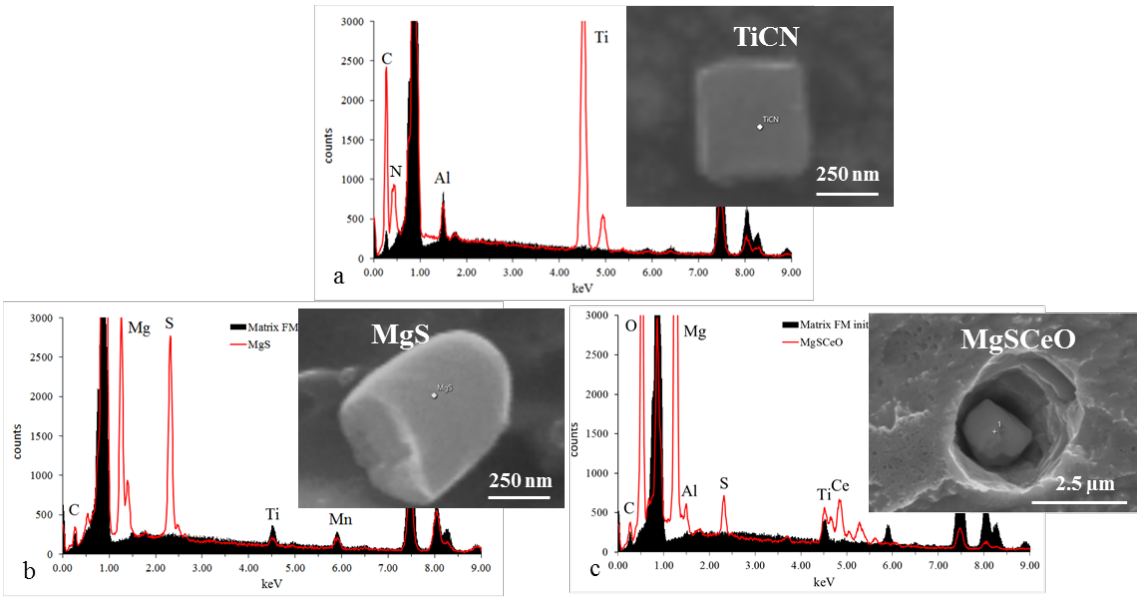

Figure 4.1.6. EDS spectra showing chemical composition of (a) TiCN particles in Monel K500; and (b) MgS and MgSCeO particles in FM60 in as-received condition; the matrix spectrum shown in black, the particle spectrum shown in red.

The comparison of Monel K500 and FM60 matrixes is shown on Figure 4.1.7. It can be seen that Al concentration is higher in Monel K500, whereas FM60 has higher concentrations of Ti and Mn. The SEM spectra qualitatively correspond to the elements concentrations in alloy compositions measured with Optical emission spectroscopy (Table 4.1.1).

Table 4.1.1. Microstructural parameters of as-received Monel K500 and FM60 wire.

Sample	Average grain size, μm	particles			HV0.5
		chemistry	number density, $x10^{-3}$ μm^{-2}	average size, nm	
Monel K500	8	Ti-rich	55.21	480	334
FM60	20	Mg-rich	2.27	800	296

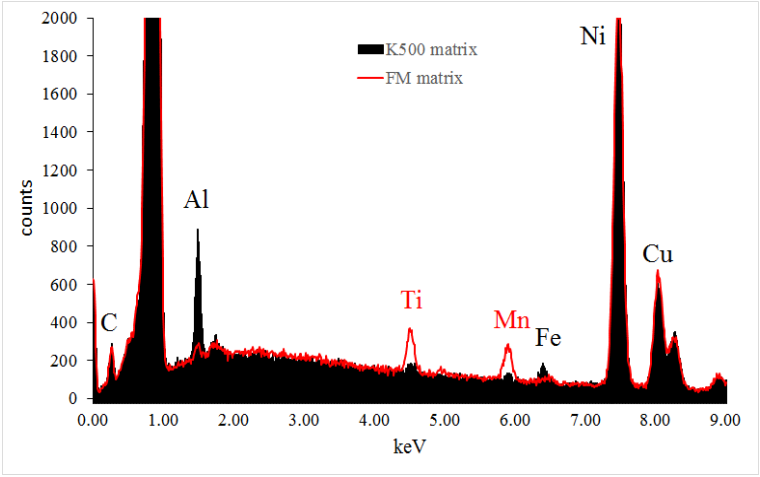

Figure 4.1.7. Comparison of Monel K500 (black) and FM60 (red) matrices.

4.2 Development of the WAAM technology for Monel alloys

In order to adjust welding parameters and understand the material behaviour, the WAAM technology for Ni-Cu alloys has been developed for the first time. 12 single-bead weld lines of Monel K500 wire have been deposited on a Monel K500 plate (Figure 4.2.1). A wide range of welding parameters has been tested in order to determine the optimum combination of welding speed and wire feed. One single bead was deposited for each of 12 procedures; a single-bead 5-layer wall was built using the most successful welding speed/wire feed combination obtained from deposition of 12 weld lines (Table 4.2.1).

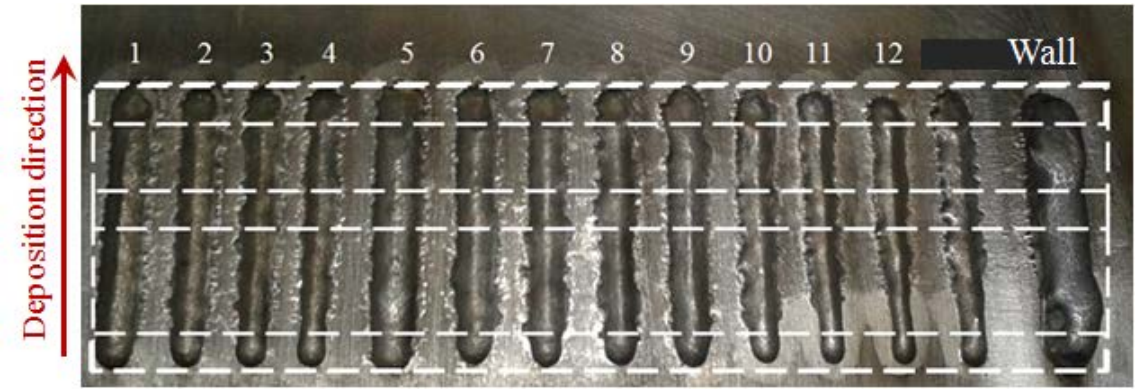

Figure 4.2.1. Deposited single-bead lines and a single-bead 5-layered wall (on the right) with cut lines.

The substrate plate with depositions was cut into three strips representing the beginning, middle and end sections of the weld bead (see white horizontal lines in Figure 4.2.1). Then the strips were cut vertically, separating each test sample. Three conditions for each bead underwent optical and scanning microscopy investigations, micro-hardness was measured for the three welding zones: heat affected zone (HAZ), remelted zone (RZ) and fusion zone (FZ).

Table 4.2.1. Welding parameters for deposition of Monel K500 single-beads and a single-bead 5-layered wall.

Test number	Single beads					Wall				
	Travel speed, mm/min	Current, A	Voltage, V	Heat input, J/mm	Wire feed, m/min	Travel speed, mm/min	Current, A	Voltage, V	Heat input, J/mm	Wire feed, m/min
1	400	161	17.2	420	8.6	400	157	16.7	390	8.0
2	400	133	16.0	320	7.2	400	162	17.1	420	8.2
3	400	124	15.8	290	6.4	400	158	18.6	440	8.5
4	400	112	15.4	260	5.8	400	158	18.3	430	8.8
5	300	154	17.1	530	8.0	400	156	19.6	460	9.2
6	300	127	15.7	400	6.6					
7	300	123	15.9	390	6.3					
8	300	113	15.1	340	5.8					
9	500	162	19.2	370	8.6					
10	500	134	16.0	260	7.0					
11	500	120	14.9	210	6.2					
12	500	115	15.2	210	6.1					

4.2.1 Macrostructure of single beads cross section

An example of the variation in the shape of the single bead line along the deposition path is illustrated in Figure 4.2.2. The high dome-shape cross section was observed at the beginning of the deposition, it usually got lower in the middle where the welding process was stabilized, and got more flat at the end due to heat accumulation.

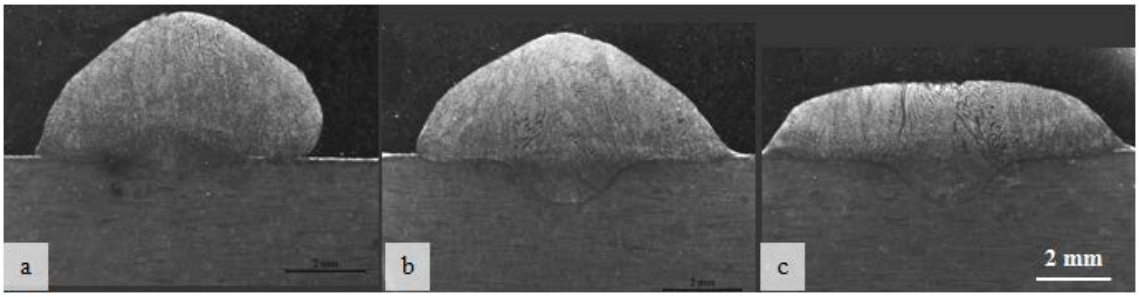

Figure 4.2.2. Optical image illustrating the variation in shape of a welding bead, deposited with a heat input 420 J/mm and cut from different sections: (a) beginning; (b) middle; (c) end of a bead.

The optical images of 12 single beads cross sections are sorted according to the welding heat input in descending order (Figure 4.2.3 and 4.2.4 at higher magnification). With a decrease in heat input from 530 J/mm to 210 J/mm the bead height and width decreased by 58% and 37 %, respectively. The dilution of beads (the cross section area of the melted base metal divided by the total area of the weld metal) showed dependence on the heat input: beads deposited at a higher heat input had higher dilution values (Figure 4.2.5). In high strength steels, the high dilution values may result in decreased strength of welds [132]. The effect of dilution in Ni-Cu alloys depositions requires further investigation.

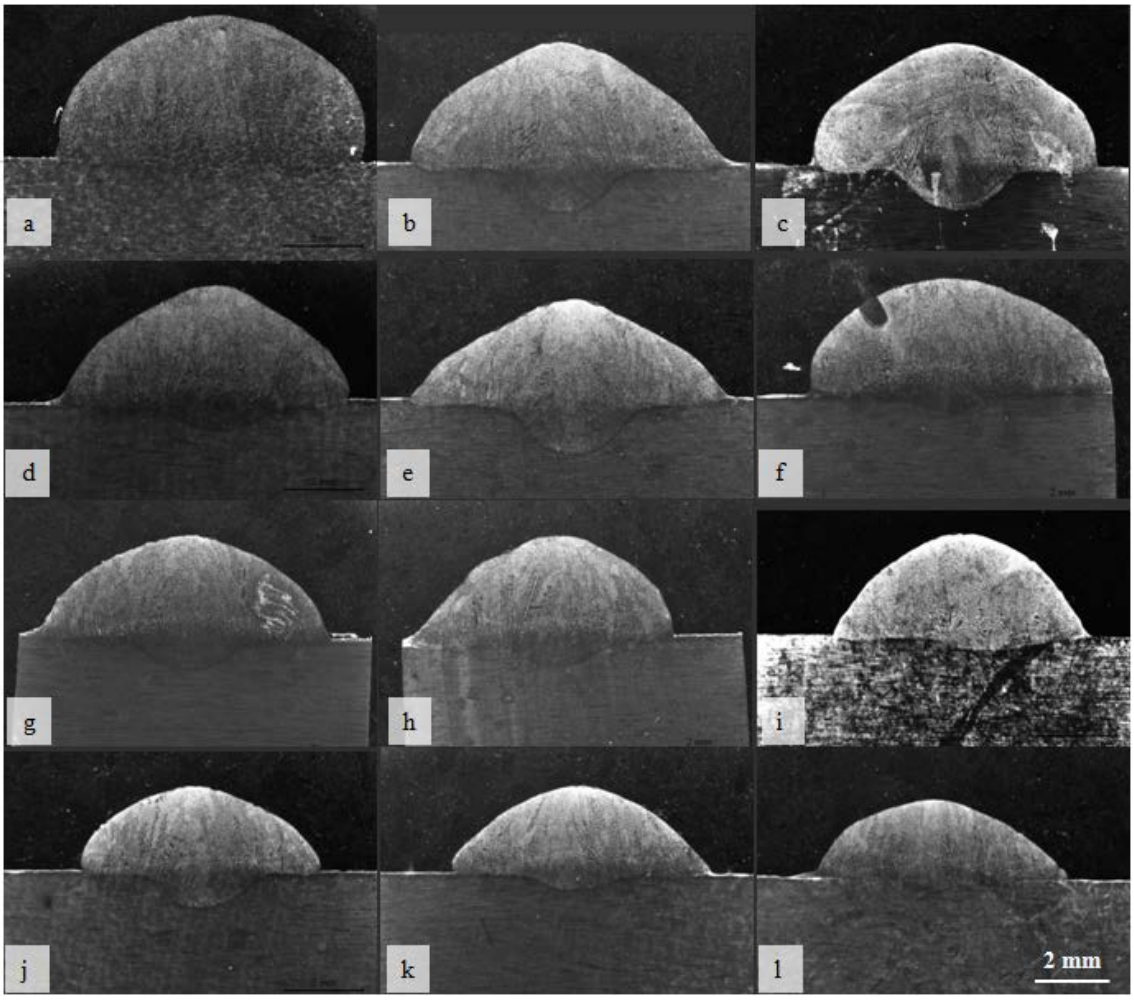

Figure 4.2.3. Optical images at lower (x14) magnification taken from the middle cross section of 12 weld beads, heat input is decreasing from a to l: (a) 530; (b) 420; (c) 400; (d) 390; (e) 370; (f) 340; (g) 320; (h) 290; (i-j) 260; (k-l) 210 J/mm.

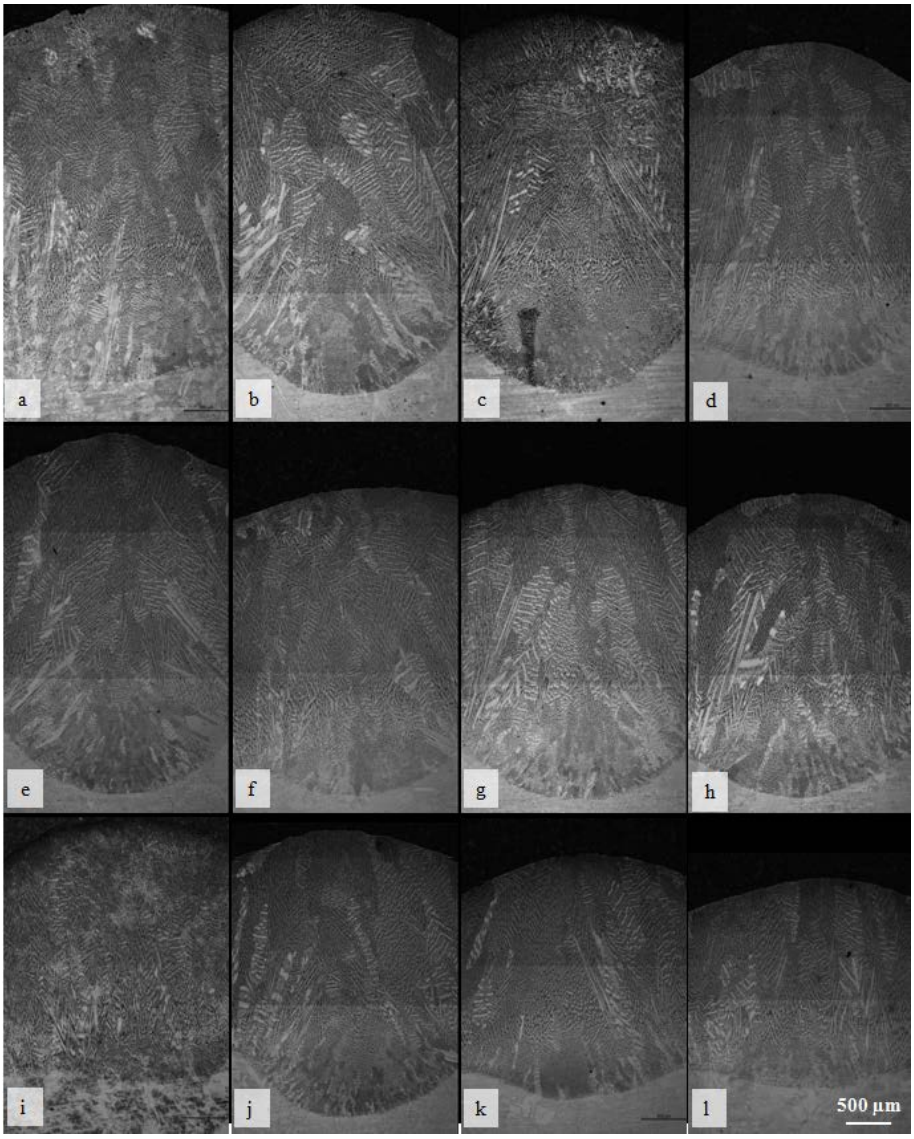

Figure 4.2.4. Optical images at higher (x50) magnification taken from the middle cross section of 12 weld beads, heat input is decreasing from a to l: (a) 530; (b) 420; (c) 400; (d) 390; (e) 370; (f) 340; (g) 320; (h) 290; (i-j) 260; (k-l) 210 J/mm.

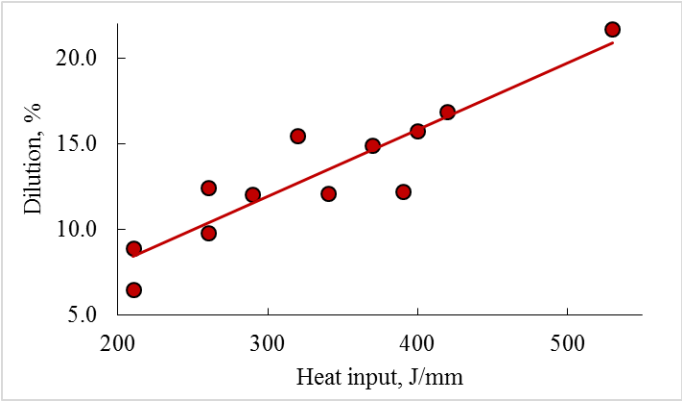

Figure 4.2.5. Dilution variation with heat input.

Table 4.2.2. Characterisation of single weld beads

Heat input, J/mm	Welding speed, mm/min	Bead width, mm	Bead height, mm	Width/ height ratio	Dilution, %	Mean HV		
						HAZ	RZ	FZ
530	300	10.0	3.8	2.6	21.7	170	166	147
420	400	9.3	3.5	2.7	16.9	170	152	143
400	300	8.2	3.5	2.3	15.8	170	160	146
390	300	8.3	3.2	2.6	15.5	170	160	155
370	500	9.2	2.8	3.3	14.9	170	157	149
340	300	8.7	3.3	2.6	12.4	170	161	152
320	400	8.3	2.9	2.5	12.2	170	163	144
290	400	8.2	2.8	2.9	12.1	170	161	141
260	400	7.5	2.8	2.7	12.0	170	156	149
260	500	7.0	2.5	2.8	9.8	170	159	153
210	500	7.5	2.6	2.9	8.9	170	157	150
210	500	7.3	2.4	3.0	6.5	170	159	145

The selected optical images of the three welding zones: HAZ, RZ and FZ are shown in Figure 4.2.6. A typical dendritic microstructure was observed in the FZ (Figure 4.2.6b). Columnar grain growth and heterogeneous epitaxial grain growth (Figure 4.2.6c and d, respectively) were registered in the whole range of heat inputs (from 530 to 210 J/mm). The grain growth occurred along the heat flow direction (from the base metal towards the fusion zone). The middle cross section of a 5-layered single bead wall is shown in Figure 4.2.7. The columnar grains grow through each deposited layer in the direction of heat flow.

The microhardness in different zones of the weld cross section did not vary significantly with the heat input (Table 4.2.2). The average microhardness decreased from 180 HV for the base metal to 170 HV for HAZ, to 160 HV for the RZ and to 150 HV for the FZ. The decreased hardness in HAZ, compared to the base metal, can be related to stress relief and dislocations annihilation following heating in this area. RZ and FZ exhibited typical cast microstructure the hardness of which is obviously lower than that of based metal with deformed microstructure.

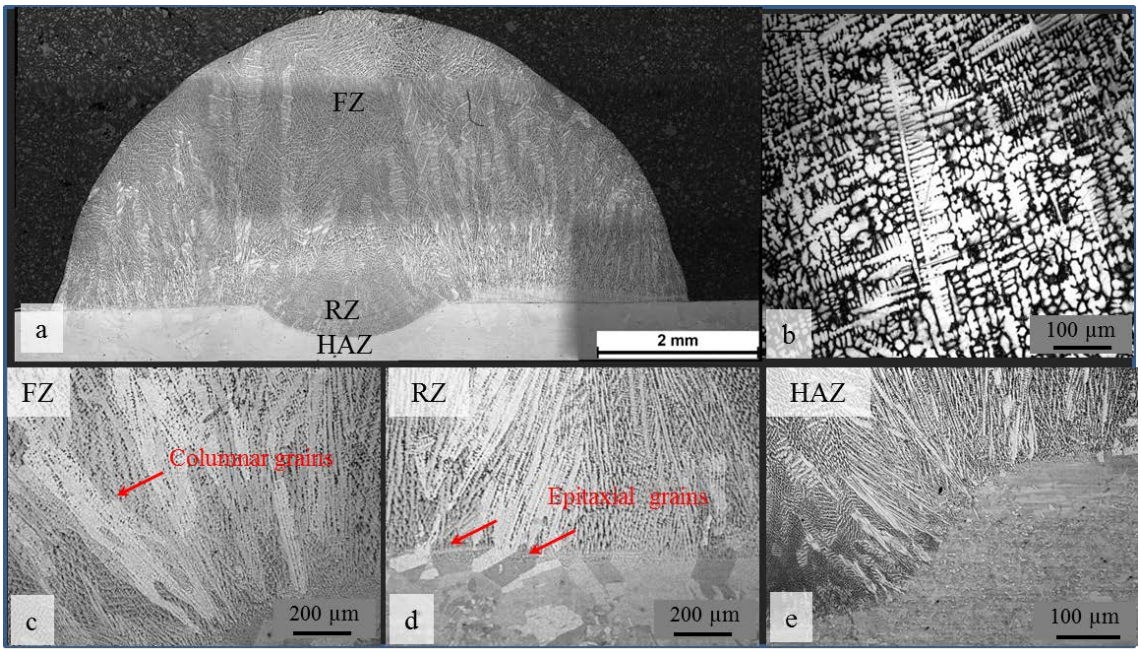

Figure 4.2.6. Optical micrographs of (a) as-welded single bead cross section showing three welding zones; (b) dendritic microstructure in the fusion zone; (c) columnar grains in the fusion zone; (d) epitaxial grains in remelted zone; (e) no significant grain growth observed in the heat affected zone of the base metal.

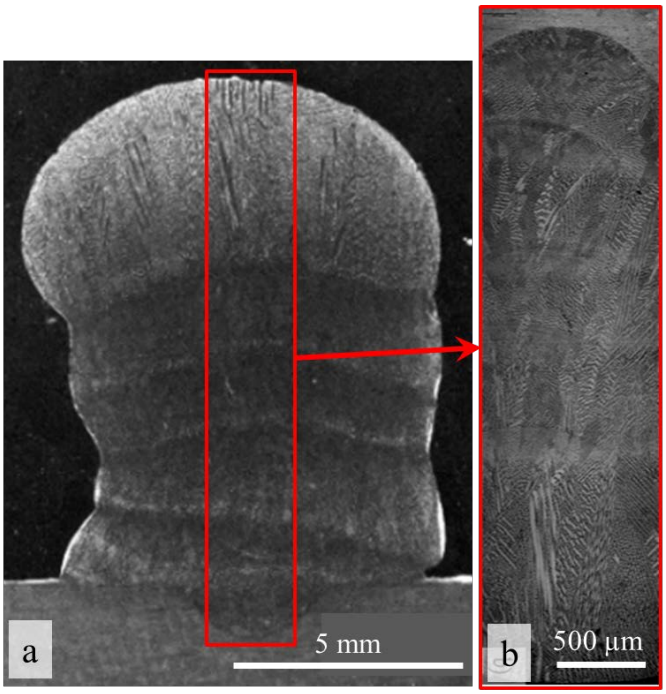

Figure 4.2.7. Optical micrographs of the middle cross section of 5-layered wall at (a) a lower (x10) and b) higher (x50) magnification.

4.2.2 Microstructure of single beads in as-welded condition

A detailed SEM-EDS analysis of three weld samples with maximum, medium and minimum heat inputs (530, 370 and 210 J/mm respectively) was carried out. The analysis revealed segregation of Cu in the fusion zone of all samples (Figure 4.2.8 a-i), which was caused primarily by the large differences in melting points of Ni (1455 °C) and Cu (1085 °C) and by the low diffusivity of Cu in Ni [9]. The segregation was characterised by the thickness of Cu-rich bands determined by EDS maps (Figure 4.2.8) and relative Cu concentrations in the Cu-rich bands determined by EDS line scans across the bands (Figure 4.2.9a). With a decrease in heat input the segregation decreased: the Cu-rich bands thickness decreased from about 6±0.2 μm for 530 J/mm to 5±0.2 μm for 370 J/mm and to 4±0.2 μm for 210 J/mm; and the Cu concentration in the bands decreased by about 15% with a decrease in heat input from 530 J/mm to 210 J/mm (Figure 4.2.9b). No segregation was found in the base metal (Figure 4.2.8 j-l).

TiSCN particles with average size of 400 nm were observed in the fusion zone for the whole studied range of heat inputs (Figure 4.2.10 a-l). There was no significant variation in particle parameters with heat input. These particles number density was measured to be 3 times higher in the base metal (Figure 4.2.10 m-p) compared to the welds. This can be explained by short solidification time after fusion to allow for the particles precipitation and growth to the sizes visible in SEM.

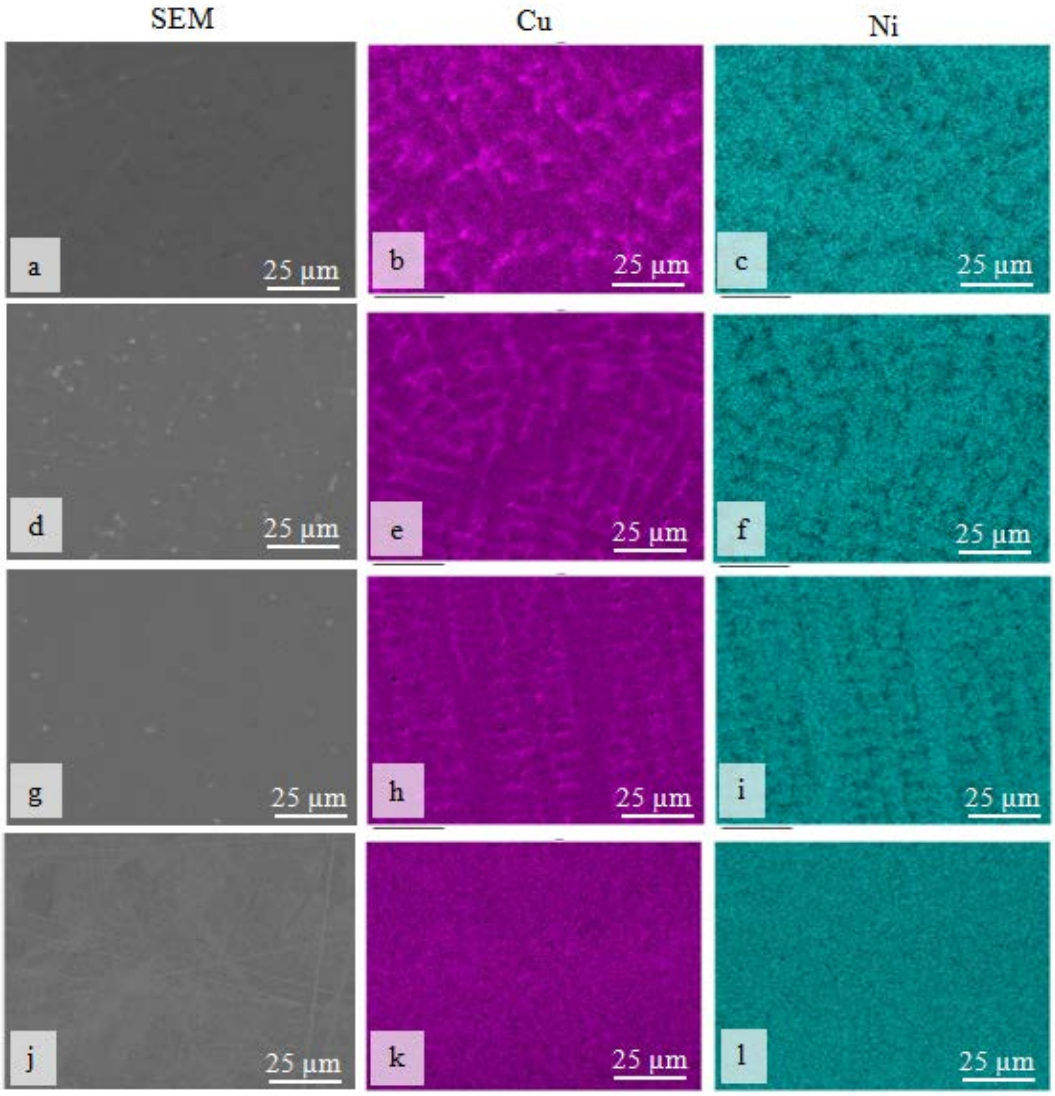

Figure 4.2.8. Variation of Cu segregation in fusion zone with heat input: (a-c) 530 J/mm, (d-f) 370 J/mm, (g-i) 210 J/mm and (j-l) base metal.

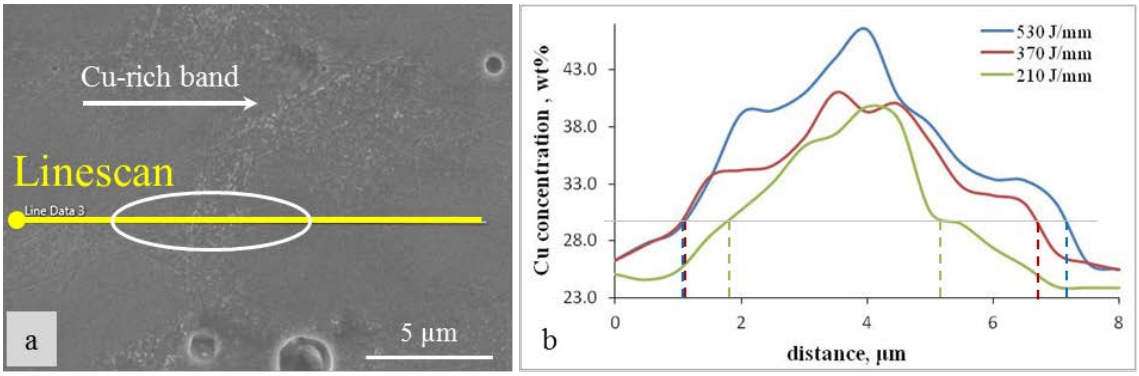

Figure 4.2.9. (a) EDS line scan across Cu-rich bands; (b) diagram showing variation in Cu concentrations along the line of scan for depositions at 530 J/mm, 370 J/mm and 210 J/mm before annealing.

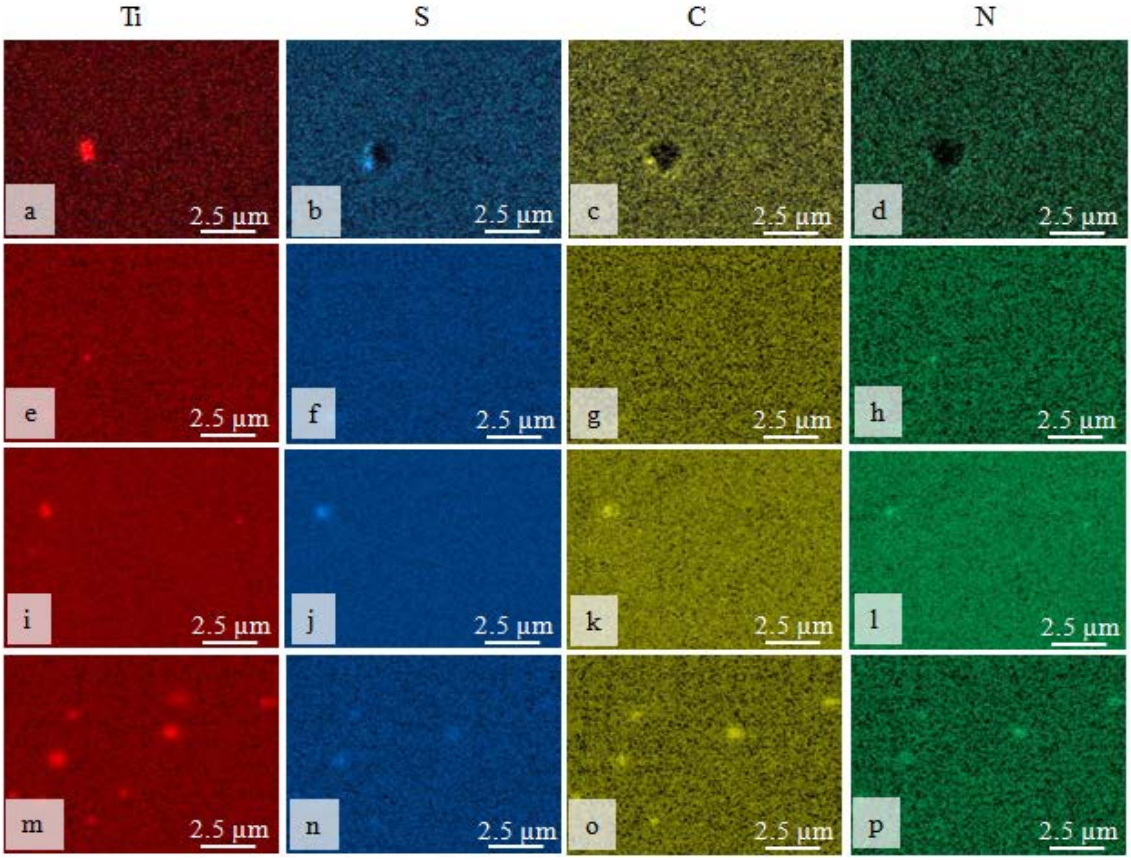

Figure 4.2.10. EDS elemental maps of TiSCN particles in fusion zone of samples with heat inputs of (a-d) 530 J/mm, (e-h) 370 J/mm, (i-l) 210 J/mm in as-weld condition and in the (m-p) base metal.

4.2.3 Microstructure of single beads after heat treatment

The microsegregation of Cu in fusion zone is a very undesirable phenomenon as it may lead to inhomogeneity of microstructure and mechanical properties of the welds. That is why the first stage of post weld heat treatment was chosen to be annealing. The annealing temperature of 1100 °C was applied in compliance with the melting temperatures of Ni and Cu and the annealing time (15 minutes) was kept at minimum to avoid excessive grain growth. After annealing, the segregation was removed in all studied samples (Figure 4.2.11). The difference in Cu concentration measured by the EDS line scan did not exceed 10% for all welding conditions (Figure 4.2.12).

During annealing the bulky TiSCN particles partially dissolved in the depositions for all studied heat inputs (Figure 4.2.13 e-h). The new TiC particles precipitated during ageing (Figure 4.2.13 i-l and n-q). A few Al-rich particles were observed after ageing

(Figure 4.2.13 m and r). This may indicate precipitation of <20 nm γ′ Al-rich precipitates known to give additional strengthening. A detailed characterisation of fine precipitates using transmission electron microscopy (TEM) was carried out later.

In contrast to the depositions, no significant variation in the TiSCN particles distribution with heat treatment has been observed in the base metal (Figure 4.2.13).

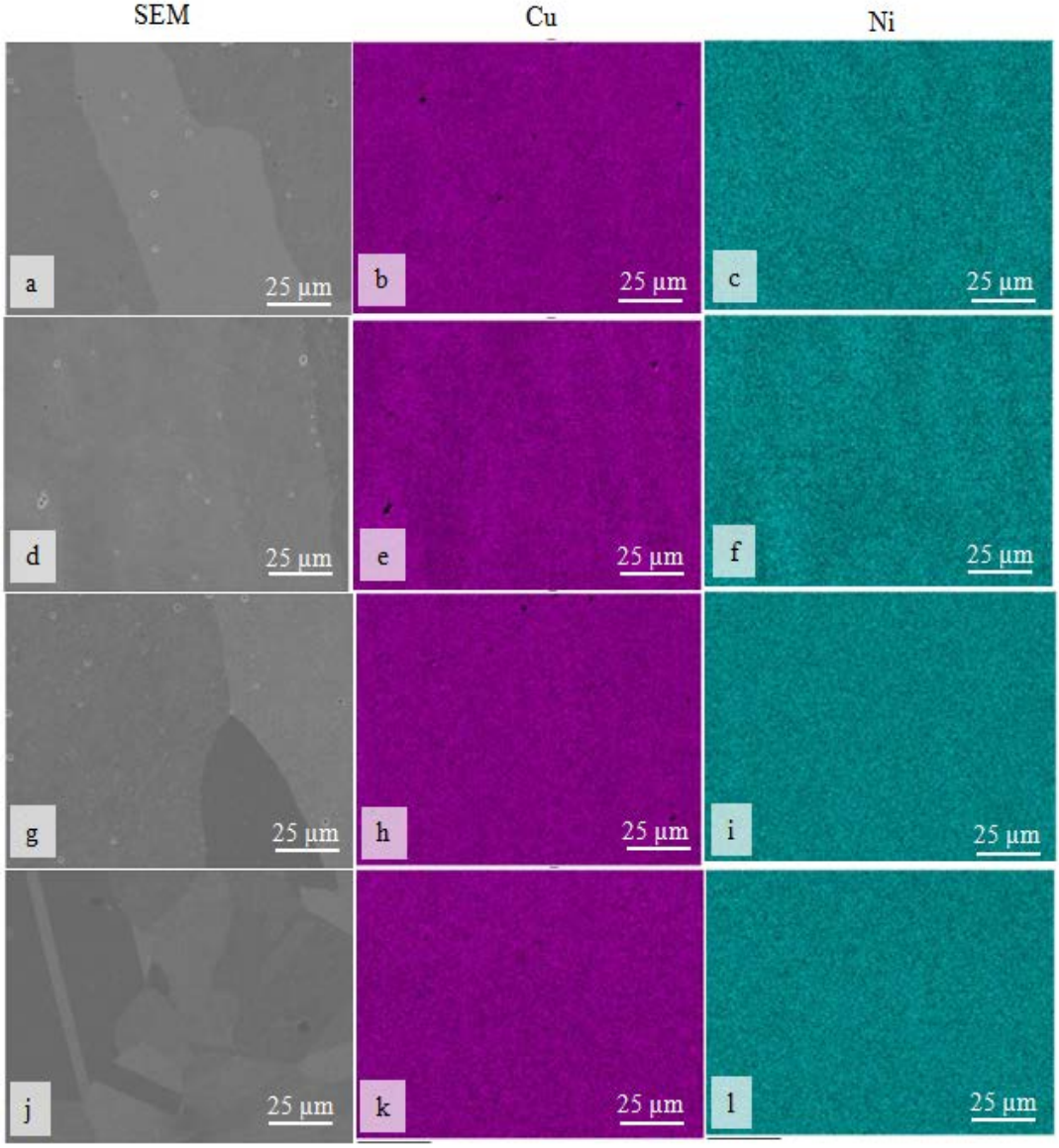

Figure 4.2.11. EDS elemental maps showing Cu and Ni distribution after annealing at 1100 °C for 15 min in welds with heat inputs of (a-c) 530 J/mm, (d-f) 370 J/mm, (g-i) 210 J/mm and in the (j-l) base metal.

The different dissolution behaviour of the TiSCN particles was mainly due to the different initial processing conditions of the base metal (hot-rolled) and depositions (cast). In the base metal particles had longer time to precipitate and grow during multi-

pass rolling process, which resulted in larger particle sizes and number density in the rolled product, compared to the cast (Figure 4.2.14). Consequently, during 15 minutes annealing at 1100 °C large particles in the rolled base did not fully dissolve. Whereas in depositions (Figure 4.2.13) particles formed during welding, followed by fast air cooling, were of smaller sizes and a lower number densities, compared to the base metal, and thus they dissolved faster during annealing.

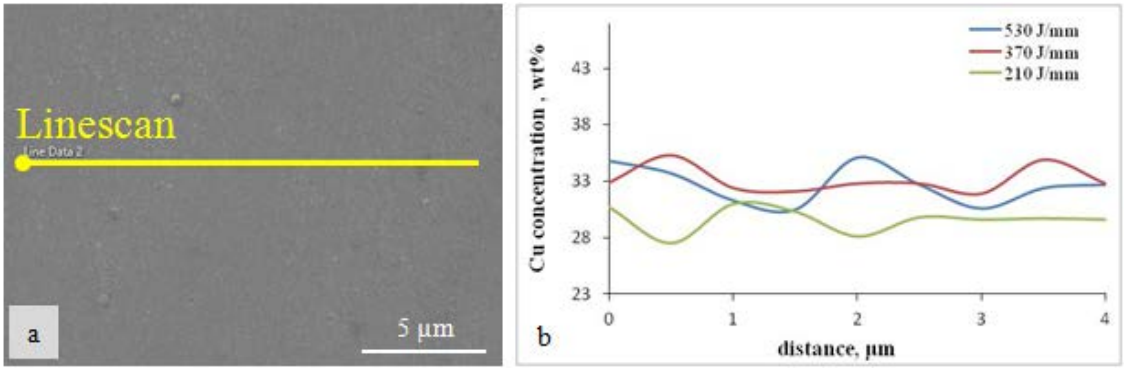

Figure 4.2.12. (a) EDS line scan across the former Cu-rich band; (b) diagram showing minor variation in Cu concentrations in welds with heat inputs of 530 J/mm, 370 J/mm and 210 J/mm after annealing.

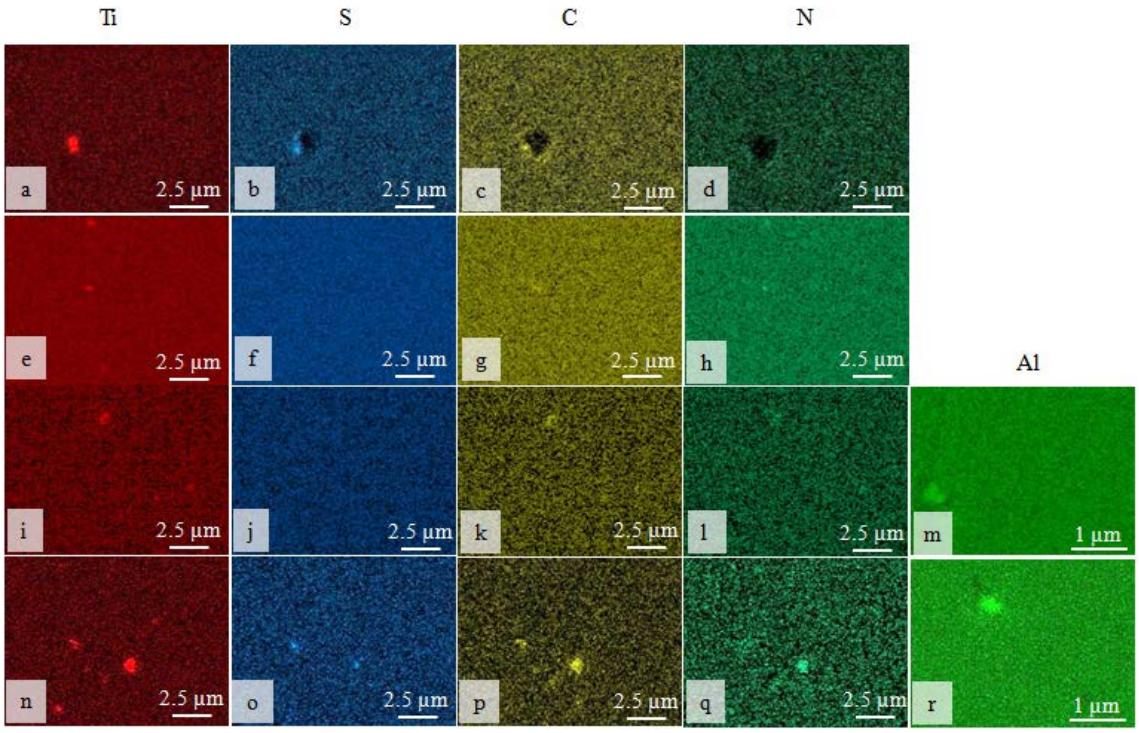

Figure 4.2.13. Particle variation in the fusion zone of the bead (heat input 530 J/mm) for various heat treatment conditions: (a-d) as-welded; (e-h) annealed; (i-m) annealed + aged at 610 °C; (n-r) annealed + aged at 610 °C + aged at 480 °C.

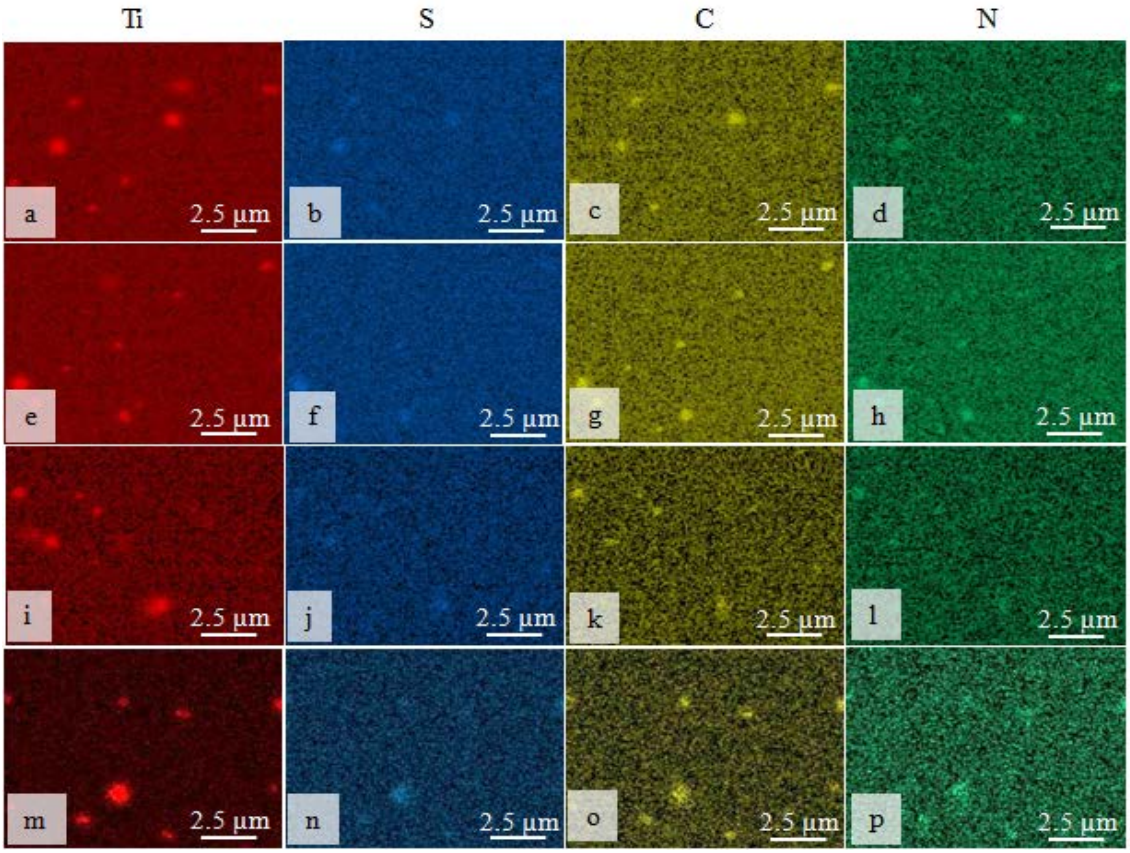

Figure 4.2.14. Particle variation in the base metal for various heat treatment conditions: (a-d) as-welded; (e-h) annealed; (i-l) annealed + aged at 610 °C; (m-p) annealed + aged at 610 °C+ aged at 480 °C.

4.2.4 Hardness of single beads in as-welded condition and after heat treatment

Hardness variation with processing condition is shown in Table 4.2.3 and Figure 4.2.15. As expected, hardness in both depositions and base metal increased after ageing, following annealing, due to precipitation of new Ti-rich particles. However, the hardness profile varied with heat input (Figure 4.2.15d): lower heat input applied during welding led to a higher strengthening effect during ageing. This can be related to a variation in the particle precipitation kinetics with heat input, leading to a variation in the <20 nm particles distribution after ageing. A more detailed investigation of this effect was carried out in the following chapters. The second ageing stage did not show a significant hardness increase compared to the condition after the first ageing stage. However, this stage may affect ductility and wear resistance of the welds.

Table 4.2.3. Hardness variation with heat treatment in selected depositions and base metal

Heat treatment condition	530 J/mm		370 J/mm		210 J/mm		Base metal
	RZ	FZ	RZ	FZ	RZ	FZ	
As-welded	158	141	151	146	154	140	180
Aged at 610°C	243	241	249	247	263	256	247
Aged at 610°C + 480°C	251	243	266	255	273	263	259

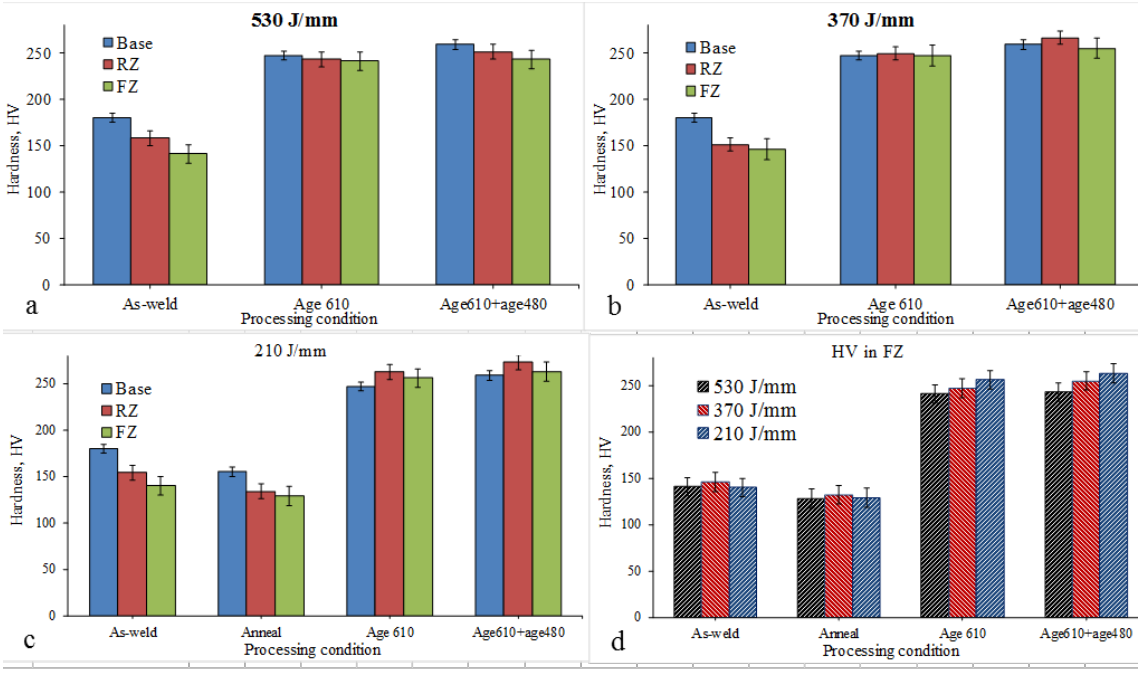

Figure 4.2.15. Hardness variation with processing conditions for selected heat inputs: (a) 530 J/mm; (b) 370 J/mm and (c) 210 J/mm; (d) hardness variation with processing condition in the fusion zone for selected heat inputs.

4.2.5 Conclusions to Chapter 4.2

Welding trials conducted at the University of Wollongong have proved a possibility of using welding as a repair and manufacturing method for Monel K500 components. The first experiments, deposition of a Monel K500 wire on as-rolled Monel K500 plate, were successfully carried out with various welding parameters. The following major results were obtained:

1. The strength of depositions is slightly lower than that of base metal due to the variation in microstructure (in particular, larger grain size and lower particle number density). However, the variation in strength can be minimised with post-processing heat treatment.

2. Microstructure inhomogeneity of weldments (microsegregation of Cu) increases with an increase in heat input, which should be taken into account while designing the wire arc additive manufacturing technology.

3. Annealing at 1100°C for 15 min was shown to effectively minimise the Cu mirosegregation.

4. The first ageing at 610 °C for 8 hours results in 70% hardness increase in both base metal and depositions and a decrease in hardness variation between them. This is considered to be related to precipitation of <20nm Al-rich particles, which should be further confirmed by transmission electron microscopy.

5. The second ageing, namely holding at 480 °C for 8 hours, did not result in significant hardness variation. Thus, the effect of this stage on microstructure and mechanical properties requires further investigation.

4.3 Microstructure and mechanical properties of as-welded Ni-Cu alloys

4.3.1 Grain structure and segregation

Based on the results obtained in previous chapter, new deposition trials have been carried out. This time two Ni-Cu alloys, Monel K500 and FM60 wires have been deposited in shapes of single beads, multi-bead single-layer plates and of single-bead multi-layer walls at three welding conditions: 300, 400 and 500 mm/min of welding torch travel speed and 8.3 m/min of the wire feed rate. Monel K500 hot-rolled plate was used as the substrate.

Optical microscopy of 6 single weld beads was applied to analyse the shape and size variation of a single bead cross sections with different welding parameters (Figure 4.3.1). The higher heat input resulted in deposition of bigger welding bead. The Monel K500 bead deposited at travel speed 300 mm/min was 9.1 mm width and 4.4 mm high. In FM60 the bead was smaller: 8.1 mm wide and 3.7 mm high for the same travel speed. The width to height ratio was 2.1 for both alloys irrespective of welding condition.

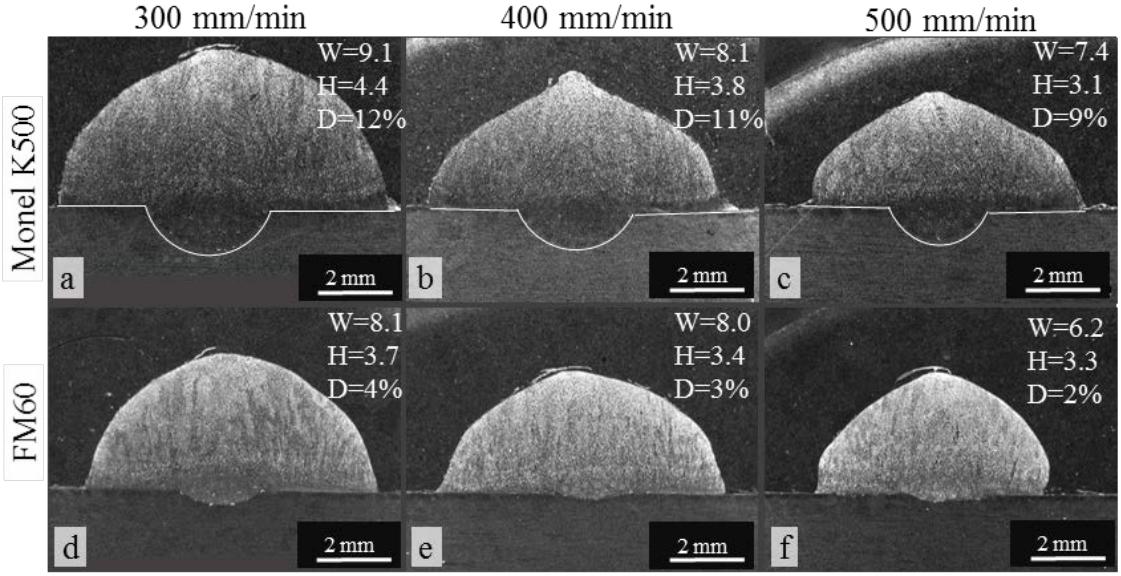

Figure 4.3.1. Optical images at lower (x14) magnification taken from the cross section of single bead depositions of (a-c) Monel K500 and (d-f) FM60; deposition speed is increasing from left to right. W and H are width and height of a bead, respectively, in mm, D is dilution.

As shown in Figure 4.3.1, with an increase in deposition speed (decrease in heat input) the dilution of welds reduced for both deposited materials. Namely, the dilution in Monel K500 was calculated to be of 12%, 11% and 9% for travel speed of 300, 400 and 500 mm/min, respectively. In FM60, the dilution was much smaller due to lower heat input: 4%, 3% and 2% for travel speed of 300, 400 and 500 mm/min, respectively. Dilution was calculated as remelted zone area divided by the total bead area multiplied by 100%.

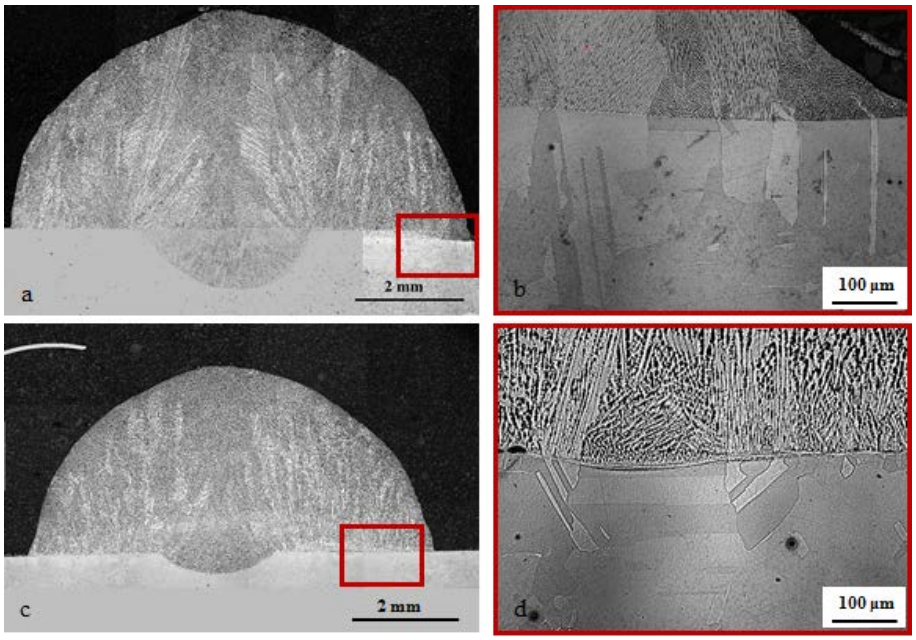

Figure 4.3.2. Optical images of a-b Monel K500 and c-d FM60 beads showing columnar grains (a and c) and epitaxial grains (b and d) in the fusion zone.

Columnar grain growth in the fusion zone (Figure 4.3.2a,c) and heterogeneous epitaxial grain growth in the heat affected zone of base metal (Figure 4.3.2b,d) were observed for both materials at all deposition speeds. The grain growth occurred from the base metal towards the fusion zone. The grain size in the fusion zone was characterised as a space between the secondary dendrite arms (Figure 4.3.3c). Due to the large grain size in cast microstructure of depositions, the number of primary dendrite arms was insufficient to obtain good statistics to characterise the grain structure. In addition, the secondary dendrite arm spacing is a more representative because moving dislocations would earlier interact with the secondary arm boundaries than with the primary arm boundaries. This was measured to be smaller in Monel K500, 4-9 µm, compared to FM60, 6-12 µm (Table 4.3.1). Probably, strong TiCN particles, present in Monel K500, effectively pinned the grain boundaries retarding the grain growth in this alloy.

Capability of TiCN particles to control the grain size was previously observed in Ti-microalloyed steels [133, 134].

In Monel K500 the average grain size slightly decreased with an increase in deposition speed (decrease in heat input), which could be a result of faster cooling time, lower average temperature and less pronounced grain growth during deposition at a higher speed. Although in FM60, the grain size did not vary significantly with deposition speed. Grain coarsening behaviour requires further investigation in the studied alloys.

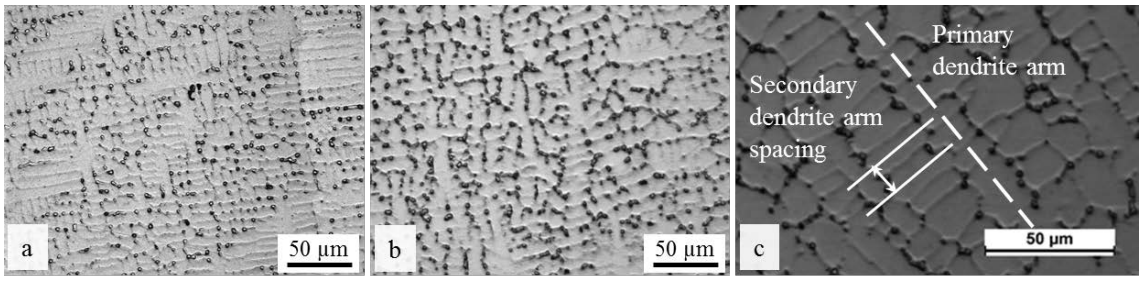

Figure 4.3.3. Optical images of as-welded dendritic microstructure in the fusion zone of (a) Monel K500; and (b) FM60; (c) characterisation of the grain growth.

The microstructure of fabricated walls and plates was similar to one observed for single beads (Figure 4.3.4).

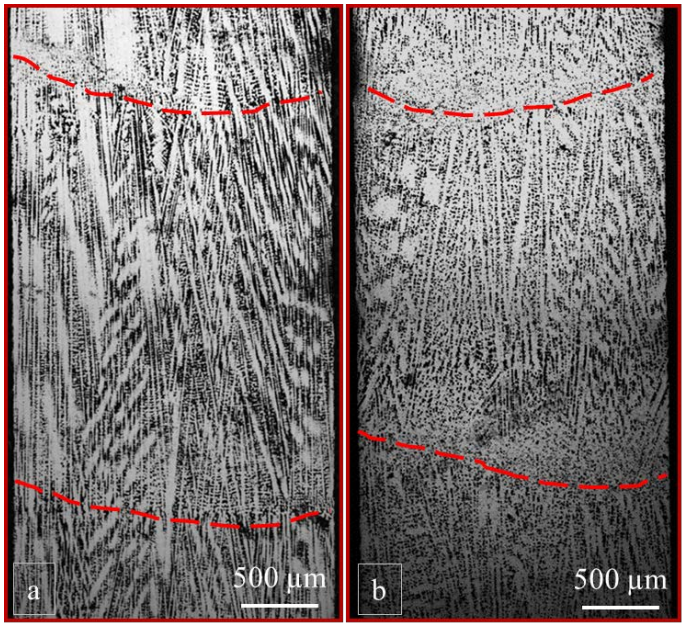

Figure 4.3.4. Optical images of as-welded walls: (a) Monel K500 and (b) FM60. The interface between deposited layers is shown in red broken lines. Z build direction increases vertically upward.

Energy dispersive X-ray spectroscopy (EDS) of two alloys revealed moderate segregation of Cu in the fusion zone in all welding conditions (Figure 4.3.5b,e). This was caused primarily by the large difference in melting points of Ni and Cu [9l]. With a decrease in heat input, the segregation decreased. No segregation was found for other alloying elements (Figure 4.3.5c,f).

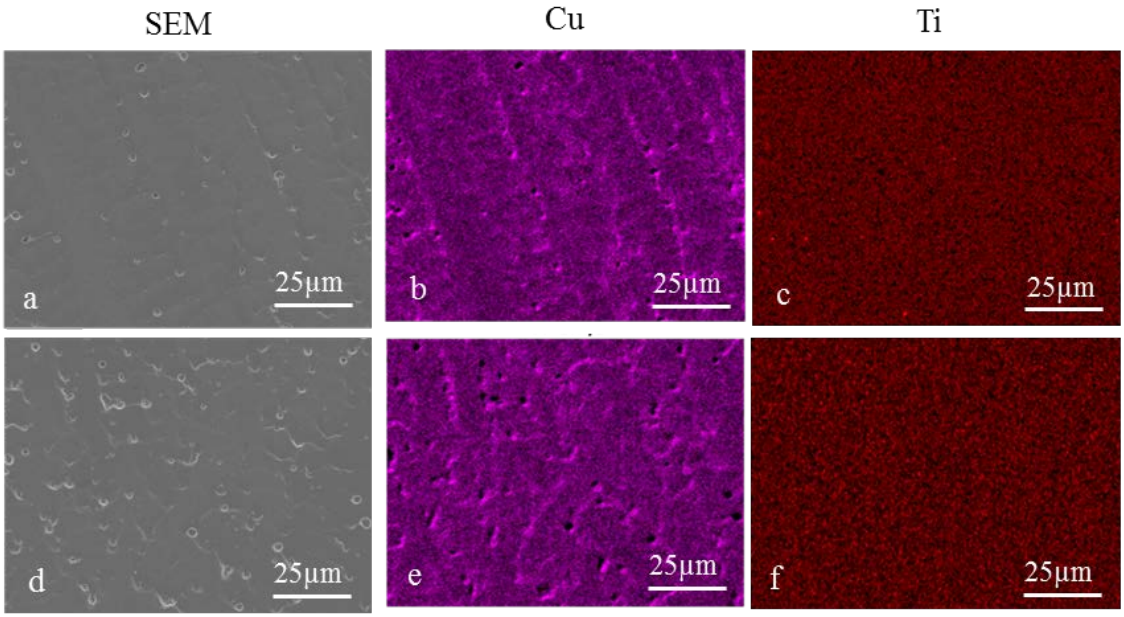

Figure 4.3.5. Representative SEM images of microstructure in (a) Monel K500 and (d) FM60, and EDS maps showing Cu segregation in (b) Monel K500 and (e) FM60 and absence of Ti segregation in (c) Monel K500 and (f) FM60.

4.3.2 Particle precipitation

In Monel K500 the Ti-rich particles of TiCN and TiCAlMgS type dominated, 64-72% to the total amount analysed, other particles including Mn-rich ones of MnS, MnSMgO, MnMgSTiC, and MnMgSAlO type, 14-18%, and Al-rich particles of AlOMgS type, 11-18%, were also observed (Figure 6.3.6 a-c, Table 6.3.1). The particle sizes were in the range of 300-700 nm for 300 and 400 mm/min deposition speeds and in the range of 250-550 nm for the 500 mm/min deposition speed. The average particle size decreased with an increase in deposition speed, which can be explained by faster cooling and less time available for the particle growth. The particle number density decreased from 3.64 to 2.62 $x10^{-3}$ μm^{-2} with an increase in deposition speed from 300 to 500 mm/min, which is consistent with a decrease in average particle size.

In FM60 the majority of particles were Mn-rich of MnSMgO and MnSAlMgOCa type, 66 to 80% of all the analysed particles, Ti-rich ones of TiAlMgO and TiSAlMgO type, 18-30%, and Al-rich particles of AlMgO type, 2-7%, were also present (Figure 4.3.6 d-f, Table 4.3.1). It is worth to note a much lower fraction of Ti-rich particles in FM60, compared to Monel K500, although the Ti content in FM60 composition is higher. This could result from lower carbon and nitrogen contents in FM60, and a possible increase in solubility of Ti in FM60 due to increased Mn content. In Ti-microalloyed steels the rate of Ti particle precipitation has been shown to decrease with an increase in Mn content [135, 136].

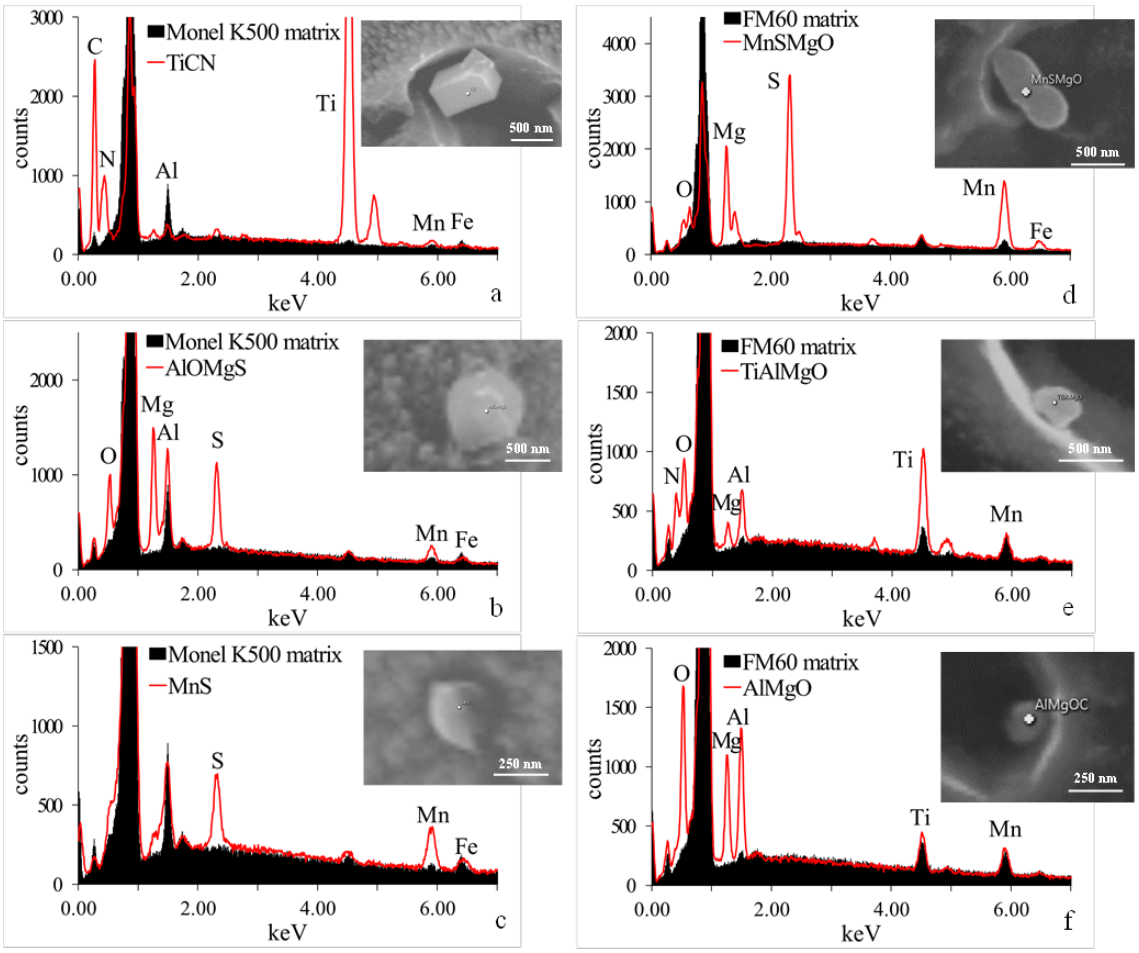

Figure 4.3.6. EDS spectra showing chemical composition of particles in as-deposited (a-c) Monel K500 and (d-f) FM60; the matrix spectrum shown in black, the particle spectrum shown in red.

The particle sizes were in the range of 200-800 nm for all deposition speeds. The average particle size showed a maximum at the speed of 400 mm/min, although the particle size variation with deposition speed was within the measurement error. The particle number density in FM60 decreased from 11.4 to 4.7 $x10^{-3}$ μm^{-2} with an increase in deposition speed from 300 to 500 mm/min, which is consistent with similar trend in Monel K500. The average particle size was slightly larger in Monel K500 than in FM 60 because the temperature of TiCN precipitation is usually much higher (1000-1500 °C [137]) than that of MnS precipitation (800-1000 °C [138]). Thus, TiCN particles have more time for growth.

Table 4.3.1. Microstructural parameters and mechanical properties of the studied materials in as-welded condition

Parameter		Monel K500			FM60		
		300	400	500	300	400	500
Grain size, μm		6-9	5-9	4-8	6-10	6-12	6-10
Particles	size, nm	437±150	448±140	331±160	311±170	392±150	388±160
	ND* $x10^{-3}$ μm^{-2}	3.64	3.06	2.62	11.39	7.24	4.71
	Chemistry,%	72Ti-rich 17Mn-rich 11Al-rich	69Ti-rich 14Mn-rich 17Al-rich	64Ti-rich 18Mn-rich 18Al-rich	67Mn-rich 26Ti-rich 7Al-rich	66Mn-rich 30Ti-rich 4Al-rich	80Mn-rich 18Ti-rich 2Al-rich
Hardness in FZ/RZ/HAZ of bead		131/136/ 156	135/142/ 159	140/150/ 163	125/131/ 141	122/129/ 139	130/132/ 142
Hardness in FZ of wall		144	141	148	131	132	134
Hardness in FZ of plate		178	165	171	200	192	187
YS, MPa		170±5	165±10	160±5	146±14	160±12	150±5
UTS, MPa		430±15	410±10	408±15	356±10	363±20	360±5
Elongation, %		47±2	51±3	50	48±3	47±1	48±2
MPa·%		14100	14662	14200	12048	12290	12240
Wear mass loss, g		0.0560	0.0420	0.0460	0.0622	0.0574	0.0628
Wear track width, mm		2.101	2.124	2.160	2.234	2.240	2.379
Wear track depth, μm		106	100	75	132	124	95

ND* - number density of particles

4.3.3. Hardness, strength, toughness and wear resistance

The microhardness (HV), yield stress (YS) and ultimate tensile strength (UTS) in Monel K500 plates obtained in this work using WAAM were in the range of 141-163 HV, 160-170 MPa and 408-430 MPa, respectively. This is about 1.7, 2.4 and 1.6 times lower than the values expected for a cast microstructure, 277 HV, 415 MPa and 690 MPa, respectively [139]. In accordance with lower strength, the elongation to failure (El) 47-51 % was 5 times higher than this for a cast microstructure, 10 %. On the contrary, hardness 133-142 HV, YS = 146-160 MPa and UTS = 356-363 MPa in FM60 were only 5.5, 6 and 24 % lower than the corresponding values in cast Monel 400 with composition similar to FM60, 150 HV, 170 MPa and 450 MPa, respectively. And the elongation to failure, 48 % in FM60, was about 2 times higher compared to the cast Monel 400, 25 % [139].

The significant variation in properties of Monel K500 could be explained by the variation in cooling rates between WAAM and casting: very fast cooling rates (short cooling time) inherent for WAAM prevent particle precipitation required for enhanced strength of Monel K500. However, for FM60 the same variation in cooling rates is not so critical for the mechanical properties variation, because the FM60 and Monel 400 are not designed for age-hardening (the precipitation strengthening mechanism is weak).

Analysis of the stress-strain curves (Figure 4.3.7 a-c) has shown that Monel K500 exhibits slightly higher YS, UTS and elongation to failure than FM60, which was expected due to the variation in alloy composition, in particular a higher C content (Table 4.3.1). Although the particle number density measured using SEM imaging was higher in FM60, a higher C content in Monel K500 could result in more pronounced particle precipitation in the <15 nm size range. This would explain higher strength and ductility in Monel K500. To support this a more detailed characterisation of particles with transmission electron microscopy is required. For the tested deposition speed range, no significant variation in tensile properties with speed was observed. Toughness, evaluated as a product of 0.5(YS+UTS) and El [140], was higher in Monel K500 than in FM60. This corresponds to the higher strength and ductility of Monel K500. For both alloys, the maximum average toughness was observed for the medium deposition speed of 400 mm/min.

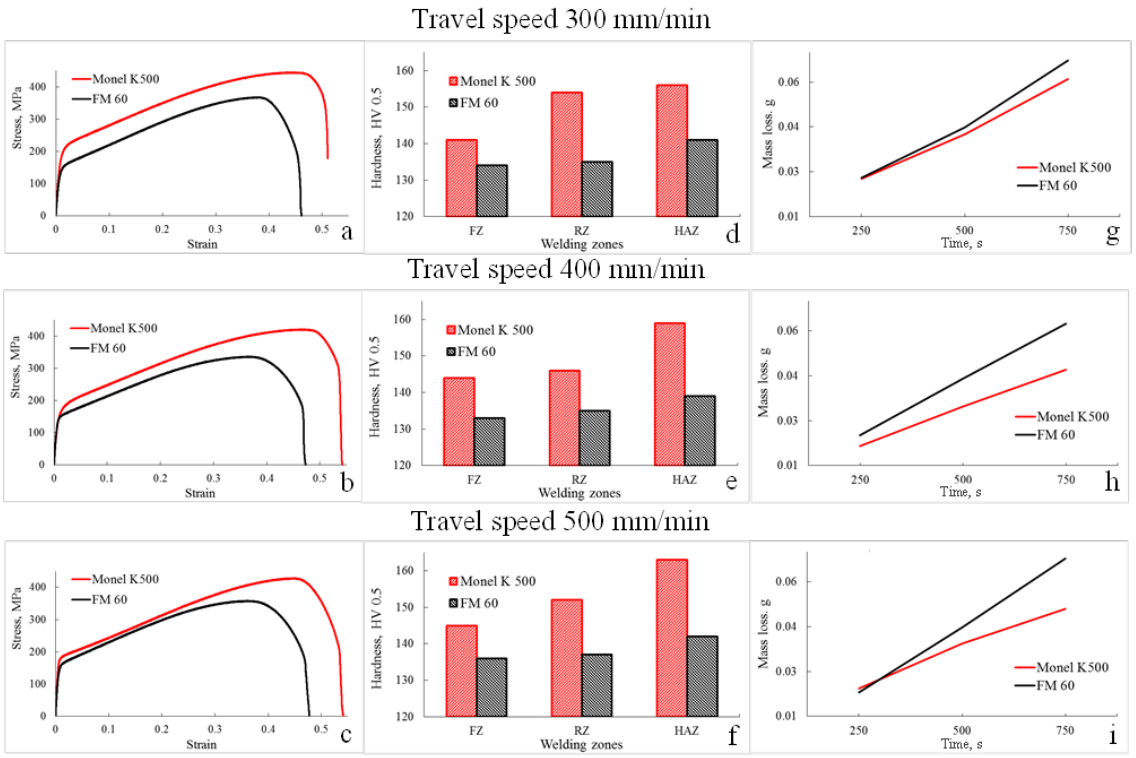

Figure 4.3.7. Mechanical properties of wire deposited Monel K500 (red) and FM 60 (black): (a-c) tensile stress-strain curves; (d-f) hardness variations in different welding zones; (g-i) wear resistance (mass loss).

The average microhardness of Monel K500 depositions decreased from 170 HV for the base metal to 160 HV for HAZ, to 150 HV for the remelted zone and to 145 HV for the fusion zone (Figure 4.3.7 d-f). The average microhardness of FM60 depositions decreased from 170 HV for the base metal to 140 HV for HAZ, to 135 HV for the remelted and fusion zones. The decreased microhardness in HAZ, compared to the base metal, can be related to stress relief and dislocation annihilation following heating in this area. Remelted and fusion zones exhibited typical cast microstructure the hardness of which is obviously lower than that of base metal with deformed microstructure. The microhardness in different zones of the weld cross section did not vary significantly with the deposition speed for both alloys (Table 4.3.1). However, the hardness of Monel K500 was definitely higher than that of FM60 for all deposition speeds, which corresponds to the smaller SDAS and precipitation of hard TiCN particles in Monel K500.

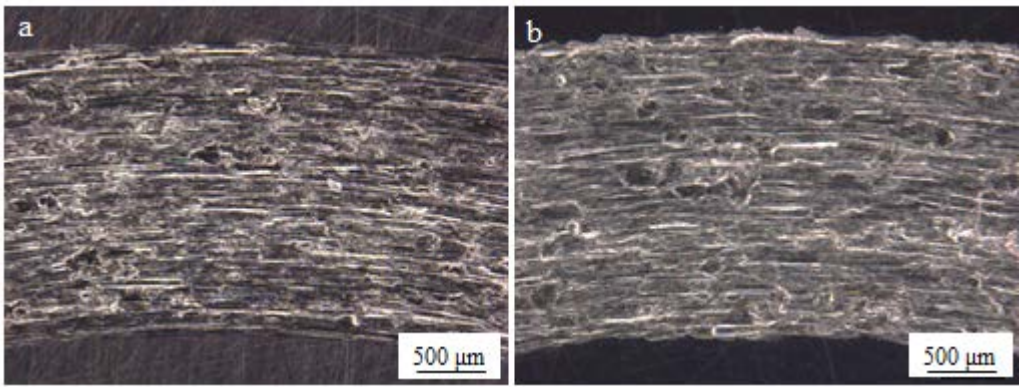

Figure 4.3.8. Optical images of the wear track on (a) Monel K500 and (b) FM60 disks after full cycle of the pin-on-disk test.

The wear resistance of Monel K500 depositions was higher (mass loss lower) than that of FM60 depositions for all three speeds (Figure 4.3.7 g-i). This corresponds to the higher hardness and toughness of Monel K500, related to its smaller SDAS and precipitation of hard TiCN particles. For both alloys the highest toughness at 400 mm/min deposition speed corresponded to the highest wear resistance (lowest mass loss during the wear testing) for this speed. Optical images of the wear tracks (Figure 4.3.8) illustrate rough wear surfaces for both alloys with numerous debris and deep wear track grooves, indicating pronounced plastic deformation, fatigue and ductile fracture during the wear process. The wear track width was 7% narrower for Monel K500 than for FM60, which corresponds to a lower mass loss of Monel K500 and supports its higher wear resistance. An increase in wear resistance with an increase in hardness was previously observed in medium carbon steels [141, 142]. In particular, wear resistance increased with precipitation of hard Nb- and Cr-rich carbides [143, 144]. On another hand, increased toughness, or rather a proper balance between hardness and toughness, was suggested to be the major reason for increased wear resistance [145, 146].

On the next stage of this research age-hardening heat treatment will be used to modify the precipitate distributions and further improve the mechanical properties of WAAM-deposited Ni-Cu alloys. In addition to the Ti-rich particles, Ni-rich gamma prime particles may be expected to affect the microstructure-properties relationship in the studied alloys. However, due to their small size, <15 nm, they cannot be observed in SEM. Therefore, an in-depth study of precipitates will be conducted using transmission electron microscopy.

4.3.4 Conclusions to Chapter 4.3

Investigation of the microstructure and mechanical properties of WAAM-produced Ni-Cu alloys resulted in the following conclusions:

1. In Monel K500 the secondary dendrite arm spacing was smaller than in FM60, which corresponded to a higher number density of TiCN precipitates in Monel K500. Moderate Cu segregation in depositions was observed in both alloys. This could result from a variation in the Ni and Cu solidification temperatures irrespective of other elements concentrations.

2. The majority of precipitates were Ti-rich particles in Monel K500 and Mn-rich ones in FM60, although the Ti content is higher in FM60. This could result from the lower carbon and nitrogen contents in FM60 and a possible increase in Ti solubility in FM60 due to an increased Mn content in it. With an increase in deposition speed, the particles number densities decreased in both alloys, which can be explained by a faster cooling rate (less time available for precipitation) for a faster deposition speed.

3. Hardness, strength, ductility, toughness and wear resistance were higher in Monel K500, compared to FM60. This mainly resulted from the precipitation of Ti-rich particles in Monel K500. For both alloys, the highest wear resistance corresponded to the highest toughness observed at the medium deposition speed of 400 mm/min.

4.4 Microstructure and mechanical properties of heat treated Ni-Cu alloys

4.4.1 Grain structure and segregation

In order to remove the segregation of Cu, observed in all as-welded samples (Figure 4.4.1 a-f), an annealing heat treatment at 1100 °C for 15 minutes was carried out (Figure 4.4.1 g-l).

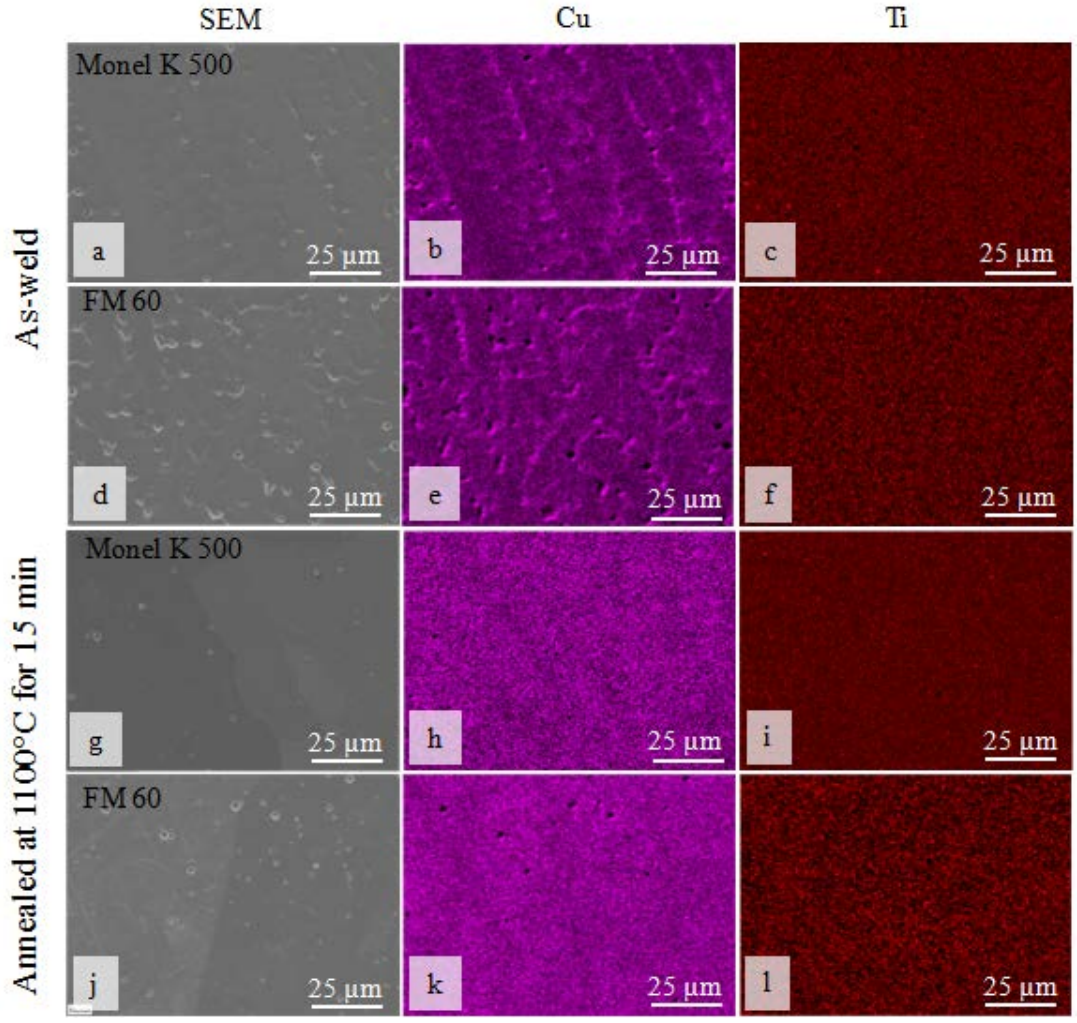

Figure 4.4.1. Representative SEM images of microstructure in (a,g) Monel K500 and (d,j) FM60, and EDS maps showing Cu segregation in as-welded (b) Monel K500 and (e) FM60, absence of Cu segregation in annealed (h) Monel K500 and (k) FM 60, absence of Ti segregation in as-welded (c) Monel K500 and (f) FM60, and absence of Ti segregation in annealed (i) Monel K500 and (l) FM60.

The secondary dendrite arm spacing (SDAS) was measured to be 4-12 μm in both alloys in as-welded condition. In Monel K500 SDAS decreased with an increase in deposition speed, from 6-12 μm for 300 mm/min to 5-10 μm for 400 mm/min to 4-8 μm for 500 mm/min. Higher travel speed leads to higher cooling rate, which means that less time is available for grain growth. In addition, higher travel speed (higher cooling rate) probably results in precipitation of higher number density of nano-sized TiAl-rich precipitates, which means a more pronounced grain boundary pinning effect.

However, in FM60 no dependence of SDAS on deposition speed was observed. Although the same trend – smaller grain growth with higher travel speed (faster cooling rate) would be expected for this alloy, the absence of nano-sized TiAl-rich precipitates in FM60, which play an important role in grain boundary pinning effect, makes variation of SDAS with travel speed less pronounced.

During annealing and subsequent ageing, the SDAS was growing in both alloys, however the growth was larger in FM60 (up to 10-18 μm after the second ageing) compared to Monel K500 (up to 6-14 μm after the second ageing).

4.4.2 Particle precipitation

In the as-welded condition, the majority of particles were Ti-rich (64-72 %) in Monel K500 and Mn-rich (66-80 %) in FM60. The particle number density was on average 2 times higher in FM60. The particle number density decreased with an increase in deposition speed from 3.6×10^{-3} μm^{-2} for 300 mm/min to 3.1×10^{-3} μm^{-2} for 400 mm/min to 2.6×10^{-3} μm^{-2} for 500 mm/min in Monel K500 and from 11.4×10^{-3} μm^{-2} for 300 mm/min to 7.2×10^{-3} μm^{-2} for 400 mm/min to 4.7×10^{-3} μm^{-2} for 500 mm/min in FM60.

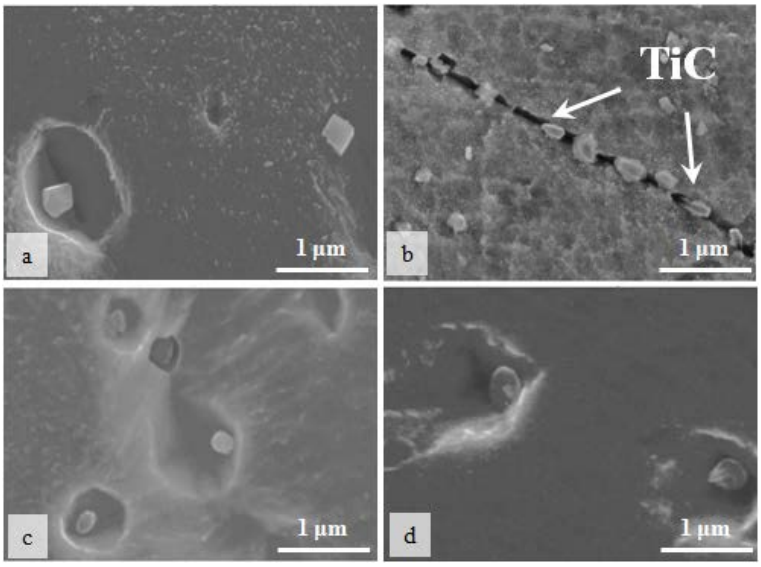

Figure 4.4.2. SEM images of precipitates in (a, b) Monel K500 and (c, d) FM60 in (a,c) as-welded and (b,d) aged at 610°C conditions.

After annealing and ageing at 610 °C the particle number density increased by 240 - 290 times in Monel K500 and only up to 70% in FM60. This coincided with 4 - 6 times decrease in the average particle size in Monel K500 and only 10-60 % decrease in FM60. After annealing and ageing almost all the particles in Monel were Ti-rich (Figure 4.4.3 a,b). Although in the as-welded condition, around 70 % of particles were Ti-rich. In contrast, in FM60 the particle chemistry did not vary significantly in aged condition compared to the as-welded (Figure 4.4.3 c,d). In Monel K500 the dependence of particle parameters on deposition speed, observed in the as-welded conditions, disappeared after annealing and ageing. Although in FM60 the dependence on deposition speed (a decrease in the particle number density with an increase in speed) remained after annealing and ageing. All these indicate a stronger effect of annealing and ageing on particle precipitation in Monel K500, compared to FM60: Ti-rich particles broadly precipitated in Monel K500 during ageing, although in FM60 this process was much slower.

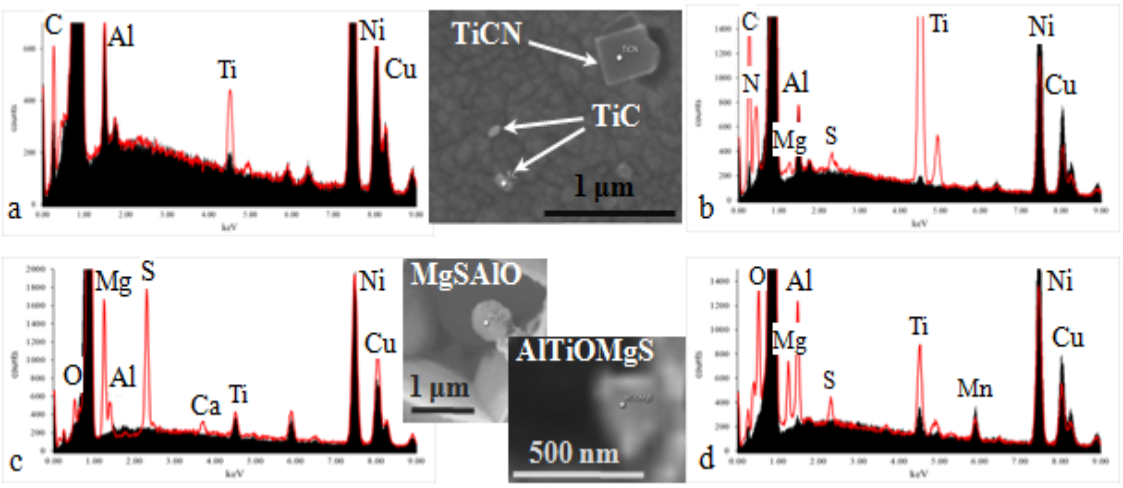

Figure 4.4.3. EDS spectra showing chemical composition of (a) TiC and (b) TiCN particles in Monel K500 aged at 610°C, and (c) MgSAlO and (d) AlTiOMgS in FM60 aged at 610°C; the matrix spectrum is shown in black, the particle spectrum is shown in red.

During the second ageing at 480 °C, following annealing and ageing at 610 °C, the particle coarsening accompanied by a decrease in the particle number density took place in both alloys. However, this was more pronounced in Monel K500 (up to 1.7 times increase in the average particle size and up to 2 times decrease in the particle number density with respect to the condition after first ageing) compared to FM60 (up to 10 % increase in the average particle size, which could be within the experimental error, and up to 40 % decrease in the particle number density). In Monel K500 no significant variation in the particle chemistry was observed with the second ageing, all the particles were Ti-rich. In FM60 the relative amount of Mn-rich particles increased after the second ageing.

Table 4.4.1. Microstructural parameters and mechanical properties variation with heat treatment in Monel K500.

Heat treatment	Travel speed, mm/min	Particles (SEM size range)			Mechanical properties							
		ND* $x10^{-3}$ μm^{-2}	size, nm	Chemistry, %	HV	YS, MPa	UTS, MPa	El, %	MPa·%	Wear mass loss, g	Wear track	
											width, mm	max. depth, μm
As-welded	300	3.6	437 ±150	72Ti-rich 28 Mn-rich	144	170±5	430±15	47±2	14100	0.0896	2.101	106
	400	3.1	448 ±140	69Ti-rich 31Mn-rich	141	165±10	410±10	51±3	14662	0.0662	2.124	100
	500	2.6	331 ±160	64Ti-rich 36 Mn-rich	148	160±5	408±15	50±1	14200	0.0685	2.160	75
Aged at 610 °C	300	865	90 ±50	100 Ti-rich	256	250±4	522±25	39±1	15054	0.0758	1.923	106
	400	898	75 ±45	100 Ti-rich	255	300±3	615±20	37±1	16928	0.0601	2.057	90
	500	692	85 ±47	100 Ti-rich	262	290±4	609±15	32±1	14384	0.0556	2.190	47
Aged at 610°C +480 °C	300	448	160 ±74	100 Ti-rich	259	320±3	536±5	12±1	5136	0.0748	2.020	82
	400	667	90 ±50	100 Ti-rich	236	250±5	563±5	34±4	13821	0.0625	2.105	48
	500	641	95 ±45	100 Ti-rich	265	280±3	622±20	31±1	13981	0.0589	2.270	43

ND* - number density of particles.

Table 4.4.2. Microstructural parameters and mechanical properties variation with heat treatment in FM60

Heat treatment	Travel speed, mm/min	Particles (SEM size range)			Mechanical properties							
		ND $x10^{-3}$ μm^{-2}	size, nm	Chemistry, %	HV	YS, MPa	UTS, MPa	El, %	MPa·%	Wear mass loss, g	Wear track	
											width, mm	max. depth, μm
As-welded	300	11.4	311 ±170	67Mn-rich 33TiAl-rich	131	146±3	356±10	48±3	12048	0.0902	2.234	132
	400	7.2	392 ±150	66Mn-rich 34TiAl-rich	132	149±5	361±20	47±1	11985	0.0722	2.240	124
	500	4.7	388 ±160	80Mn-rich 20TiAl-rich	134	160±4	375±5	48±2	12840	0.0744	2.379	95
Aged at 610 °C	300	12.7	278 ±90	52Mn-rich 48TiAl-rich	163	160±3	397±5	41±1	10804	0.0689	1.730	107
	400	8.5	274 ±110	50Mn-rich 50TiAl-rich	164	155±5	410±10	43±1	11718	0.0639	2.085	85
	500	8.1	236 ±95	55Mn-rich 45TiAl-rich	162	205±3	428±20	36±3	11034	0.0587	2.105	65
Aged at 610°C +480°C	300	9.2	285 ±100	61Mn-rich 39TiAl-rich	139	115±4	358±10	48±2	11160	0.0734	2.200	94
	400	8.9	288 ±97	70Mn-rich 30TiAl-rich	192	170±3	490±20	39±1	12870	0.0680	2.208	86
	500	7.7	261 ±95	62Mn-rich 38TiAl-rich	173	190±5	428±20	40±2	11760	0.0602	2.220	79

4.4.3 Hardness, strength, toughness and wear resistance

Hardness in Monel K500 was higher than in FM60 for all studied conditions (Table 4.4.1 and 4.4.2). However, the difference was minor (9-14 HV) in the as-welded condition and increased significantly (90-100 HV) after annealing and ageing at 610 °C. This coincides with a larger hardness response of Monel K500 to ageing: as a result of annealing and ageing at 610 °C, hardness in Monel K500 increased by 112-114 HV, although in FM60 it increased by only 28-32 HV. The second ageing at 480 °C did not improve hardness of Monel K500. However, in FM60 hardness could increase by up to 28 HV as a result of second ageing. A decrease in hardness following the second ageing was also observed (for 400 mm/min deposition speed in Monel K500 and for 300 mm/min speed in FM60).

The yield stress (YS) and ultimate tensile strength (UTS) were higher in Monel K500 than in FM60 for all studied conditions, although this discrepancy varied with heat treatment (Figure 4.4.4, Tables 4.4.1 and 4.4.2). In the as-welded condition YS and UTS were 16-24 MPa (depending on deposition speed) and 33-74 MPa, respectively, higher in Monel K500. And after annealing and ageing at 610 °C the YS and UTS were 90-145 MPa and 125-205 MPa, respectively, higher in Monel K500. These indicate a higher strength growth with ageing at 610 °C in Monel K500, compared to FM60: in Monel K500 the YS and UTS increased by 80-130 MPa and 92-205 MPa, respectively; however, in FM60 the YS and UTS increased by only 6-45 MPa and 42-53 MPa, respectively. With the second ageing at 480 °C, following annealing and ageing at 610 °C, the YS and UTS could decrease in both alloys by up to 45 MPa. In the as-welded condition the elongation to failure was slightly higher in Monel K500 (50-51 %) compared to FM60 (47-48 %). However, after ageing the elongation in Monel K500 decreased faster than in FM60 and became lower than in FM60.

Toughness was assessed via calculation of the area under stress-strain curves. The shape under stress-strain curves was approximated by a trapezoid with the area calculated as 0.5(YS+UTS)·elongation. For such a calculation method, the toughness units were MPa·%. Toughness in Monel K500 was higher than in FM60 for all studied conditions (except for 300 mm/min deposition speed aged at 480 °C, which showed abnormally low elongation in Monel K500). In Monel K500 toughness increased after annealing and ageing at 610 °C by up to 15 %, which corresponds to a significant

increase in strength, and decreased after the second ageing at 480 °C by up to 8 %, due to a decrease in elongation. In FM60 the opposite trend was observed: toughness decreased after annealing and ageing at 610 °C by up to 15 % and increased after the second ageing at 480 °C by up to 10 %.

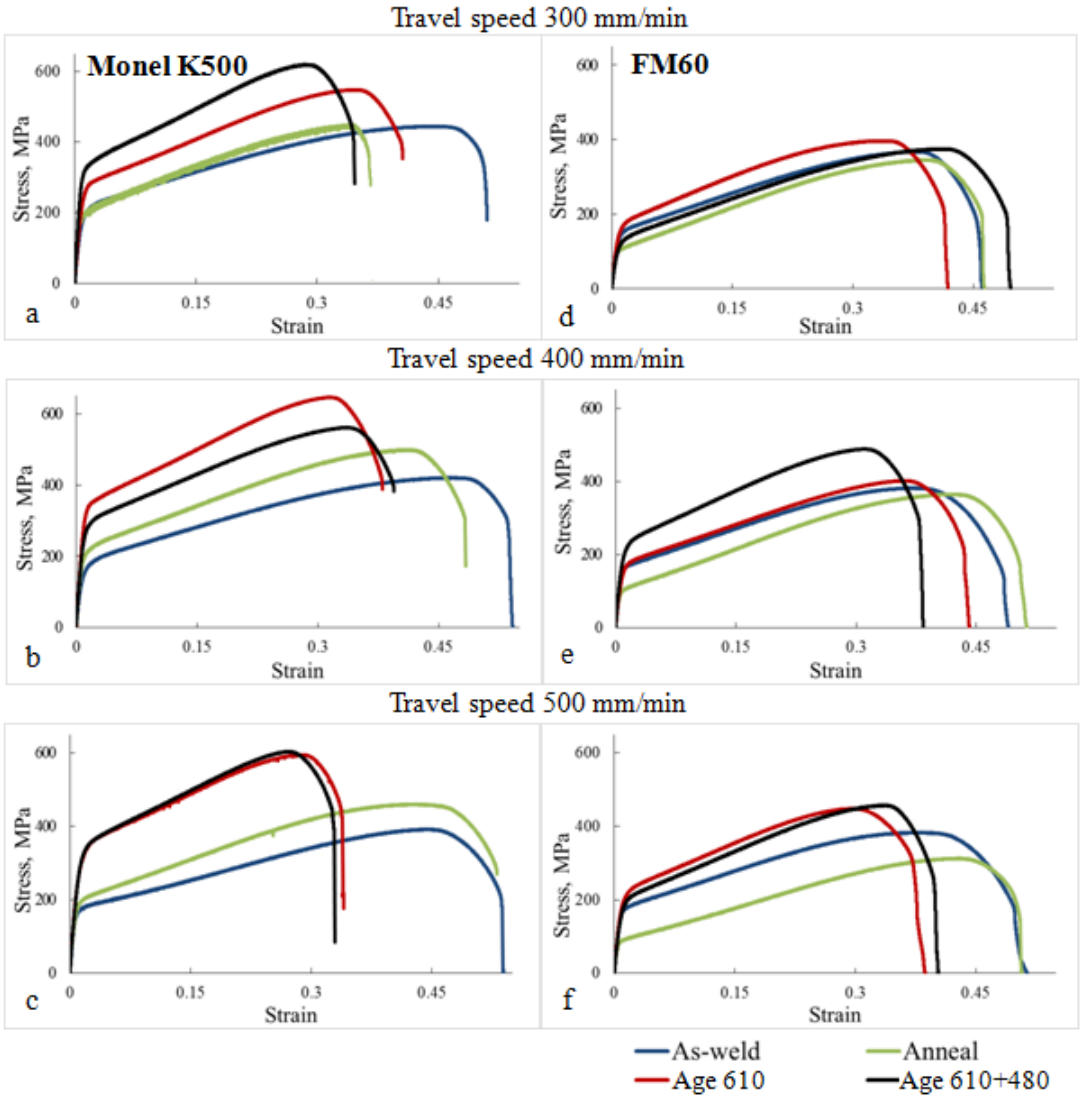

Figure 4.4.4. Stress-strain curves of (a-c) Monel K500 and (d-f) FM60 for various travel speeds and heat treatment conditions.

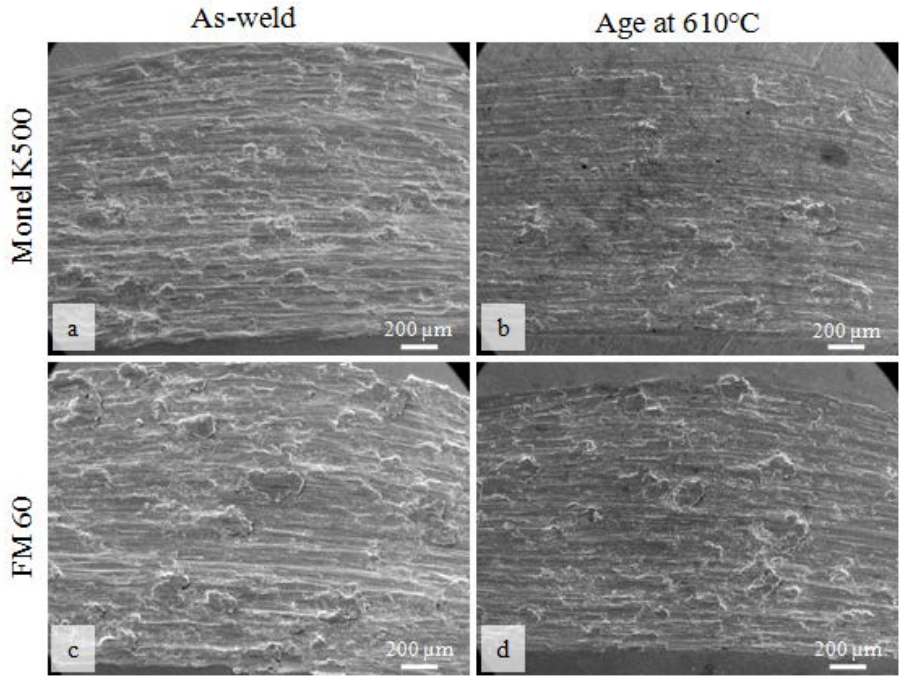

Figure 4.4.5. SEM images of wear tracks for Monel K500 (a) as-welded and (b) annealed and aged at 610°C conditions, and for FM60 (c) as-welded and (d) annealed and aged at 610°C conditions.

The wear resistance was higher (sample mass loss lower) in Monel K500 for almost all studied conditions. After annealing and ageing at 610 °C, the wear resistance increased by up to 16 % in Monel K500 and up to 24 % in FM60. These correspond to an increase in hardness in both alloys and some increase in toughness in Monel K500. After the second ageing at 480 °C the wear resistance slightly (by up to 6 %) decreased in both alloys. In Monel K500 this coincided with a decrease in toughness. Although in FM60 no direct correlation with hardness and toughness was observed. Imaging of the wear surfaces (Figure 4.4.5) and measurements of the wear track roughness (Figures 4.4.6 – 4.4.8) supported the mass loss data. In the as-welded condition, both alloys exhibited quite rough wear surfaces with numerous debris and deep wear track grooves (Figure 4.4.9), indicating pronounced plastic deformation, fatigue and ductile fracture during the wear process (Figures 4.4.5 a,c and 4.4.6 – 4.4.8 a,d). This indicates existence of a mixed abrasive-adhesive wear mechanism in the studied alloys. Although, the wear track width was 6-10 % narrower and the depth was 25 % shallower for Monel K500 than for FM60, meaning more difficult penetration of the pin into the Monel K500 disk surface. This corresponds to a lower mass loss measured for Monel

K500 and contributes to the overall conclusion that the wear resistance of as-welded Monel K500 was higher.

After annealing followed by ageing at 610 °C the wear track roughness decreased for both alloys (Figures 4.4.5 b,d, 4.4.6- 4.4.8 b,e and 4.4.9). In particular, the track depth decrease reached 65 % in both alloys, which corresponds to a decrease in mass loss for both alloys. This can be correlated to an increase in hardness for both alloys with the ageing, and indicates transition towards a more sliding abrasion type of wear from more fatigue type for the as-welded condition. After the second ageing at 480 °C the wear track width could increase for both alloys, although the track depth mainly decreased. This corresponds to an increase in mass loss and supports a decrease in wear resistance with the second ageing.

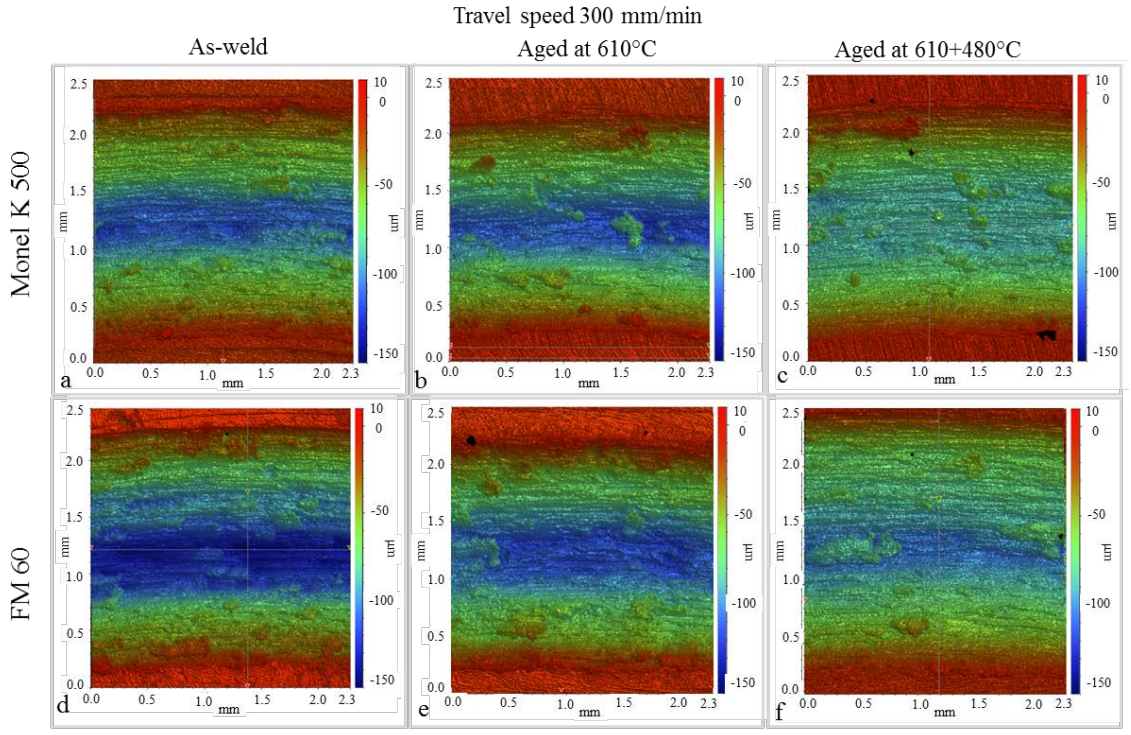

Figure 4.4.6. Wear track surface roughness for (a-c) Monel K500 and (d-f) FM60 deposited with travel speed 300 mm/min.

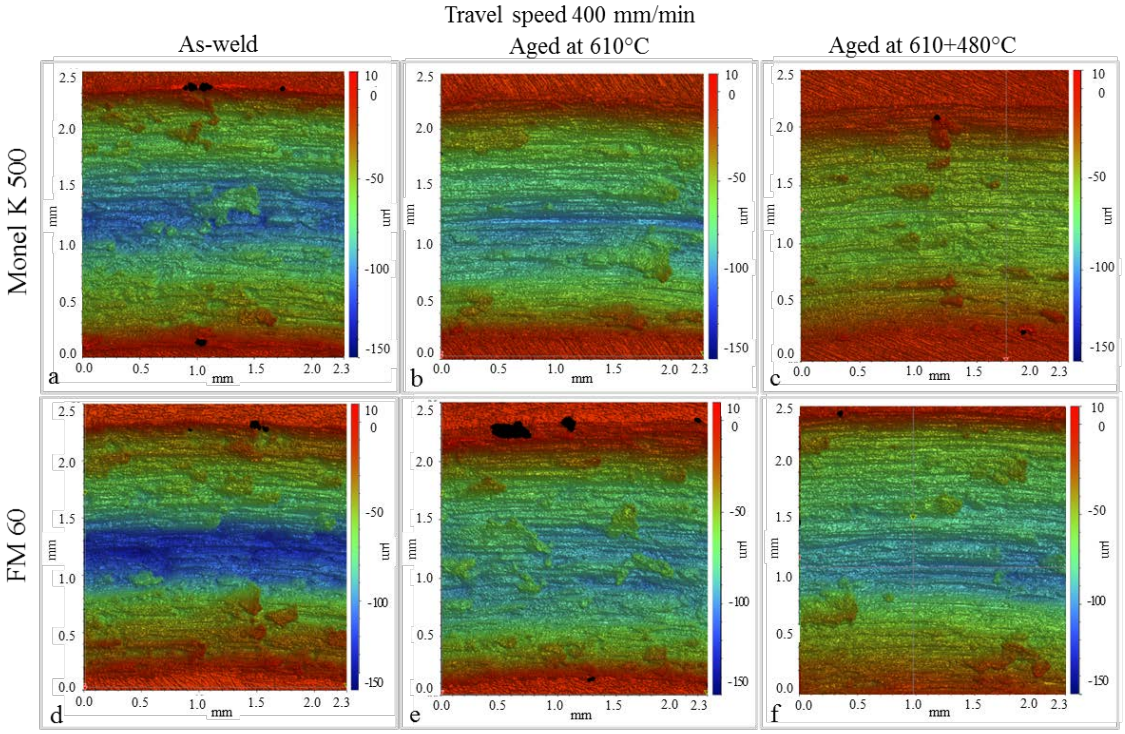

Figure 4.4.7. Wear track surface roughness for (a-c) Monel K500 and (d-f) FM60 deposited with travel speed 400 mm/min.

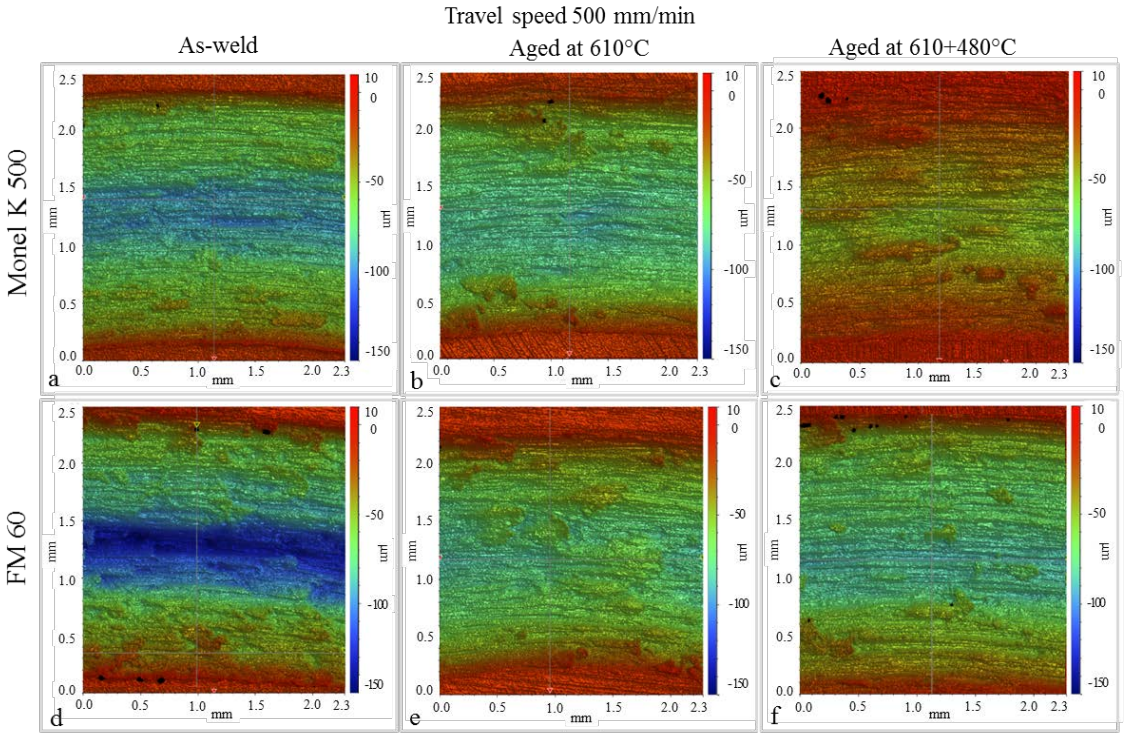

Figure 4.4.8. Wear track surface roughness for (a-c) Monel K500 and (d-f) FM60 deposited with travel speed 500 mm/min.

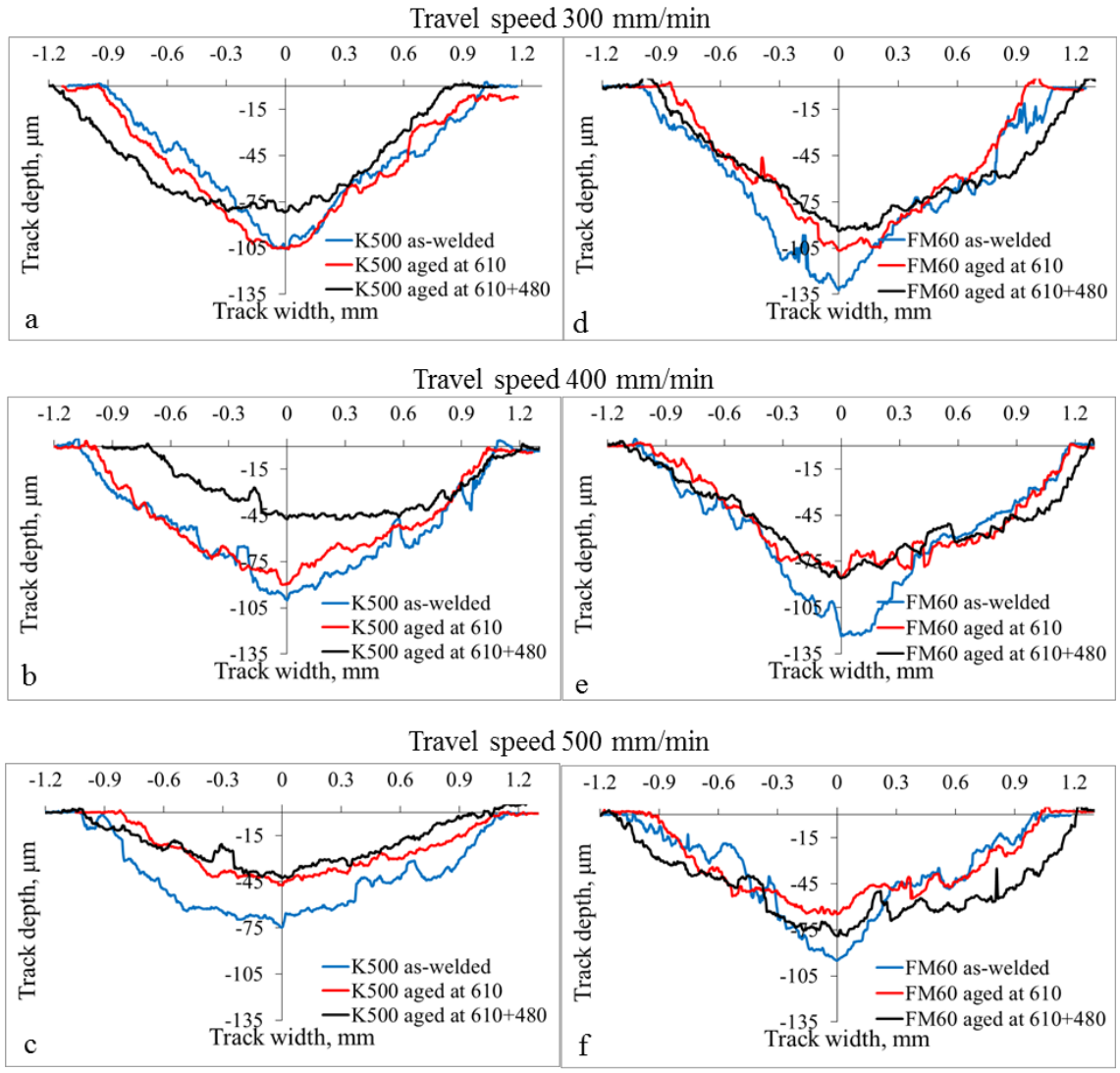

Figure 4.4.9. Variation in wear track surface roughness with deposition travel speed in (a-c) Monel K500 and (d-f) FM60.

4.4.4 Effect of alloy composition and processing on grain structure and particle parameters

Compared to FM60, Monel K500 wire contained several times lower Mn and Ti contents, although higher Al and C contents. The higher C content has led to precipitation of TiC/TiCN particles in Monel K500. However, in FM60 a higher Ti content did not lead to precipitation of TiCN but rather to precipitation of Ti-rich oxides. Ti-rich oxides were frequently observed in Ni-based alloys [149, 150], in particular, in the core of TiN particles [151]. The latest indicates a possibility of Ti

oxide precipitation at temperatures higher than TiCN. In our alloy FM60 this would mean a decrease in free Ti in solid solution available for carbonitride precipitation after the Ti-rich oxides have precipitated.

In the as-welded condition, the number density of particles in both alloys decreased with an increase in deposition speed. This resulted from an increased cooling rate and decreased time available for precipitation with an increase in deposition speed. The number density of precipitates was 2-3 times (depending on deposition speed) higher in FM60 than in Monel K500. This mainly originated from 4-7 times higher number density of Mn-rich particles in FM60, what corresponded to the 4 times higher Mn content in the FM60 composition. With an increase in deposition speed the relative amount of Ti-rich particles decreased in both alloys (although to a greater extent in FM60). Faster cooling rates, due to higher deposition speeds, largely affected the precipitation of Ti-rich particles than the Mn-rich ones, as the precipitation temperatures of Ti oxides (>1600 °C [150]), nitrides (>1200 °C [151]) and carbide (>1000 °C [137, 133]) are higher than those observed for Mn-rich particles (down to 800 °C [138, 152]).

After annealing and ageing at 610 °C almost all the particles in Monel K500 were TiC/TiCN, and the particles number density dramatically (by 240 - 290 times) increased compared to the as-welded condition. It remains unclear whether the precipitation of Ti occurred during annealing or during subsequent ageing. For the Ti and C contents in Monel K500 (0.5 and 0.088 wt. %, respectively) and the solubility equation $\log [Ti]\cdot[C] = 2.75 - 7000/T$ presented in [133], the temperature of full TiC dissolution could be about 1430 °C in our Monel K500. This means that during annealing at 1100 °C not dissolution but precipitation of TiC could take place. In FM60 the calculated dissolution temperature of TiC was lower (1135 °C) than in Monel K500, although still a bit higher than the annealing temperature. However, precipitation of TiC in FM60 had to be slower not only because of lower C content, but also because of higher Mn content. Mn was reported to increase solubility of Ti in fcc lattice [135, 136]. A decrease in relative amount of Mn-rich particles and increase in TiAl-rich ones in FM60 after annealing and ageing at 610 °C could be due to the dissolution of some Mn-rich particles and growth of fine TiAl-rich ones to the sizes large enough for observation in SEM. The variation in particle number density with deposition speed (namely, a decrease in number density

with the speed increase) disappeared after annealing and ageing in Monel K500 and remained in FM60. Obviously, a significant variation in the particle chemistry, associated with precipitation of TiC/TiCN in Monel K500 for all deposition speeds, altered this dependence.

During the second ageing at 480 °C, particle coarsening (Oswald ripening), accompanied by a decrease in number density, took place in both alloys. This phenomenon was observed previously in aged Ni alloys [153, 154]. In addition, in FM60 either precipitation and growth of new Mn-rich particles or growth of the Mn-rich shell on top of the Ti-rich core took place. This has led to the increase in relative amount of Mn-rich particles in FM60 after the second ageing.

In the as-welded condition, secondary dendrite arm spacing (SDAS) was in the same range of 4-12 μm in both alloys. This can be related to similar solidification and cooling conditions irrespective of the alloy composition. However, in Monel K500 SDAS decreased with an increase in deposition speed, and in FM60 no dependence of SDAS on deposition speed was observed. SEM visible Ti-rich particles, which could affect the grain growth rate during solidification, were of similar number density in both alloys; and therefore, probably, did not play a significant role in formation of SDAS value. Particles smaller than 20 nm could be of varying density and might have influenced SDAS. However, these were not studied here and require further investigation using transmission electron microscopy (TEM). During annealing and subsequent ageing SDAS was growing in both alloys. However, the growth was larger in FM60 (up to 10-18 μm after the second ageing) compared to Monel K500 (up to 6-14 μm after the second ageing). Slower SDAS growth in Monel K500 can be explained by a much higher number density of TiC/TiCN particles pinning the dendrite boundaries and preventing their migration.

4.4.5 Effect of alloy composition and processing on mechanical and wear properties

Due to precipitation of TiC/TiCN particles and smaller SDAS, Monel K500 exhibited higher hardness, YS and UTS than FM60 for all the studied conditions (Tables 4.4.1 and 4.4.2). In spite of FM60 elongation being larger in annealed and

aged conditions, toughness of Monel K500 was higher due to higher strength. In accordance with higher hardness and toughness, the wear resistance of Monel K500 was higher in almost all conditions (Figure 4.4.10).

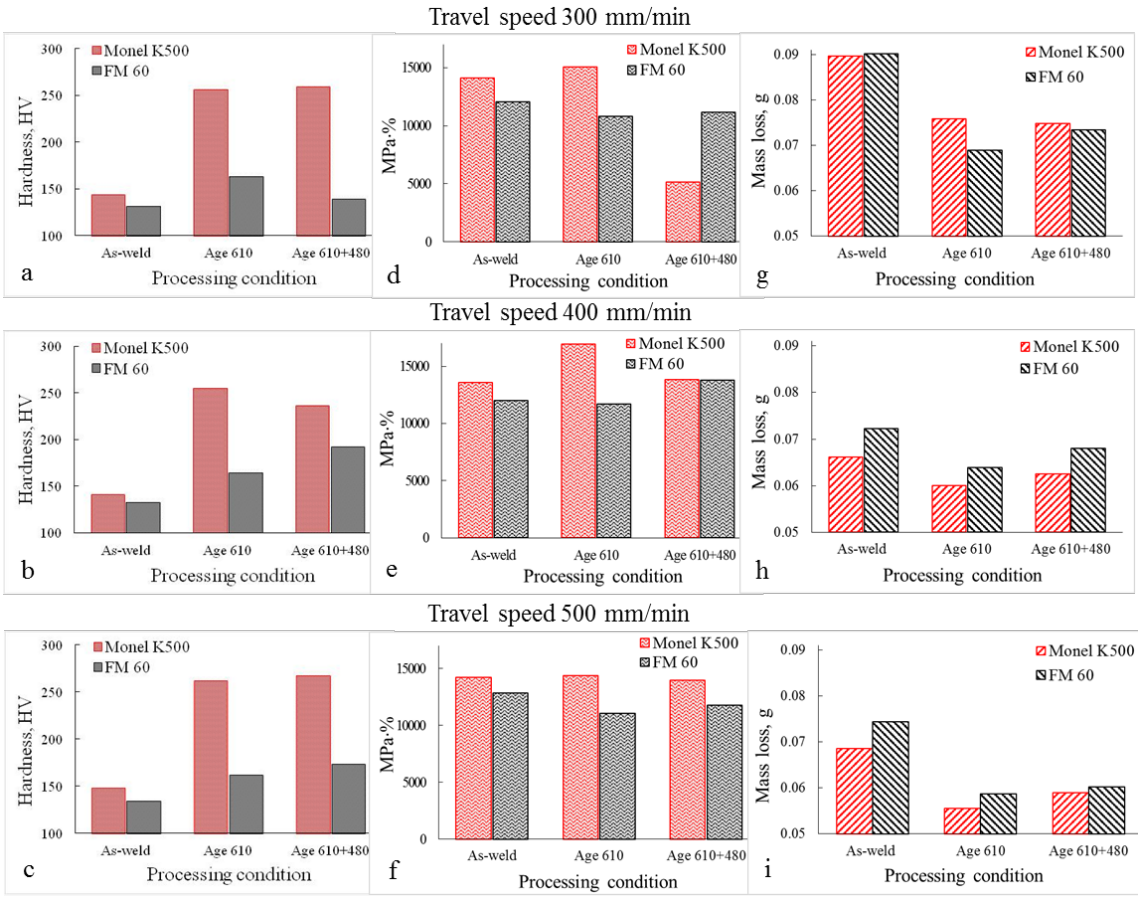

Figure 4.4.10. Variation in mechanical properties of Monel K500 (red) and FM60 (black) with heat treatment for three travel speeds: (a) hardness, (b) toughness (c) wear resistance (mass loss).

Annealing followed by ageing at 610 °C led to the hardness, strength and wear resistance increase in both alloys and toughness increase in Monel K500. These were due to precipitation of Ti-rich particles in both alloys: TiC/TiCN in Monel K500 and Ti-rich oxides in FM60. However, 240 - 290 times increase in the particle number density in Monel K500 seems being disproportional to only 16 % increase in wear resistance, as only 2 times increase in the particle number density in FM60 resulted in 24 % increase in wear resistance. Obviously, fine (< 20 nm) particles not visible in SEM play a significant role in determining mechanical properties in the

studied alloys. These particles require a detailed investigation using TEM. Second ageing at 480 °C, following ageing at 610 °C, resulted in the particle growth accompanied by a decrease in the particle number density in both alloys. This could lead to either minor variations in hardness and strength or noticeable decrease in those parameters in both alloys, and a decrease in toughness in Monel K500. In spite of some increase in toughness in FM60, the wear resistance decreased in both alloys after the second ageing.

In the as-welded condition, the lowest hardness, strength and wear resistance in both alloys were observed for the slowest deposition speed of 300 mm/min. These coincided with the highest particle number density in both alloys. At slow deposition speed the cooling time is longer and particles have more time for precipitation in growth. While the large (SEM visible) particles are growing, the fine (TEM visible) particles may lose their number density, which would soften the matrix and reduce strength and wear resistance. In the annealed and aged conditions, the highest wear resistance (supported by either the highest hardness or strength) in both alloys was obtained at the highest deposition speed of 500 mm/min. These coincided with the low particle number density in the SEM visible particle size range (>20 nm). The role of <20 nm particles requires further investigation.

On the basis of this discussion, for future practical applications of wire deposited Ni-Cu alloys we would recommend to avoid the second ageing heat treatment and apply reasonably high speeds during wire-arc deposition.

4.4.6 Mechanical properties of hot rolled Monel K500 plate

Mechanical properties of Monel K500 hot rolled plate are presented in Figure 4.4.10 and Table 4.4.3. As can be seen, the age hardening heat treatment at 610 °C has led to the increased strength, hardness and wear resistance compared to the annealed condition. Although the elongation to failure decreased after ageing by 60%. The second stage of ageing at 480 °C did not affect the mechanical properties significantly. The same trend was observed for both Monel K500 and FM60 depositions, however, the absolute values of strength and wear resistance varied.

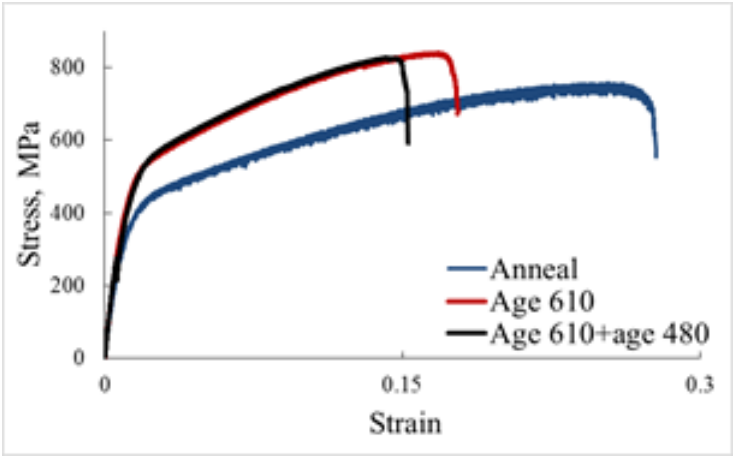

Figure 4.4.11. Tensile stress-strain curves of Monel K500 plate.

The comparison of as-welded depositions to the annealed hot-rolled plate and the corresponding age-hardening treatments has shown the hardness values of wire-arc deposited Monel K500 to be very close to the corresponding hardness values of Monel K500 plate. However, the strength of plate was higher than this of depositions for all studied heat treatment conditions. Thus, YS and UTS in annealed Monel K500 plate were 198-208 MPa and 294-316 MPa, respectively, higher than in deposited Monel K500. After annealing and ageing at 610 °C the YS and UTS were 215-265 MPa and 218-311 MPa, respectively, higher in the plate. Despite that, for all studied conditions, the wear resistance of the plate was on average 2 times lower (mass loss higher) than that of the depositions. This coincided with a 2-2.5 times lower elongation and up to 1.7 times lower toughness in Monel K500 plate. In addition, the fracture of Monel K500 plate was quasi-cleavage in contrast to fully ductile fracture in Monel K500 and FM60 depositions (Figure 4.4.12).

Table 4.4.3. Mechanical properties of Monel K500 plate

Heat treatment condition	HV	YS, MPa	UTS, MPa	El, %	MPa·%	Mass loss, g
Anneal	155	368	724±20	25±1	13 650	0.1821
Age at 610 °C	250	515	833±5	15±1	10 110	0.1392
Age at 610°C +480°C	270	518	815±10	12±1	7 998	0.1380

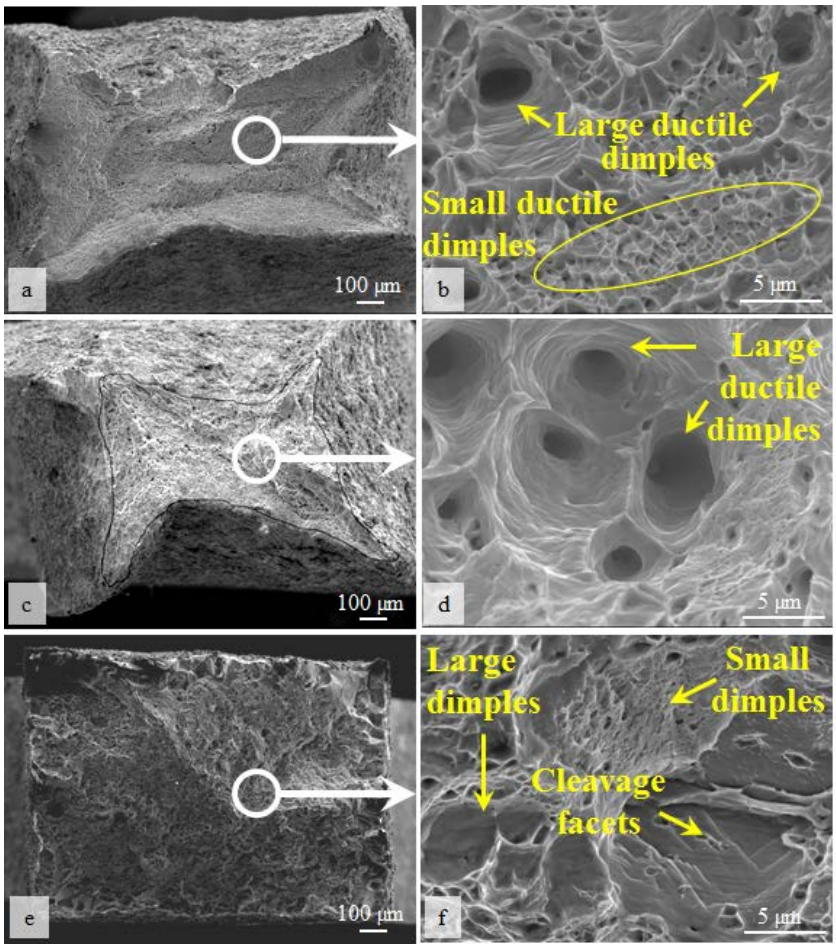

Figure 4.4.12. SEM images of fracture surface in annealed and aged at 610 °C condition: (a,b) Monel K500, (c,d) FM60 and (e,f) Monel K500 plate.

4.4.7 Corrosion resistance of Monel K500 and FM60 and Monel K500 plate

All corrosion is an electrochemical process of oxidation and reduction reactions. As corrosion occurs, electrons are released by the metal (oxidation) and gained by elements (reduction) in the corroding solution. Because there is a flow of electrons (current) in the corrosion reaction, it can be measured and controlled electronically. Therefore, controlled electrochemical experimental methods can be used to characterize the corrosion properties of metals and metal components in combination with various electrolyte solutions [147]. Electrochemical corrosion experiments measure and/or control the potential and current of the oxidation/reduction reactions.

The corrosion behaviour of Monel K500 and FM60 depositions in as-welded, annealed, aged at 610°C and aged at 610°C+480°C in three welding conditions have been studied in this work. The corrosion of Monel K500 hot-rolled plate in as-received and aged according to similar heat treatment conditions as depositions has been used for comparison.

Open-circuit potential (E_{ocp}), a potential at which the rate of anodic dissolution of the electrode equals the rate of cathodic reactions and there is no net current flowing in or out of the electrode, was measured between the sample (working electrode, WE) and reference electrode (RE). The material with higher negative value of E_{ocp} will be sacrificed first when used in galvanic couple.

A potentiodynamic experiment, the cyclic polarisation test, has been performed in a standard three-electrode cell to determine the corrosion current density (I_{corr}), which characterises the corrosion rate. In this test, the potential was applied to the working electrode and the resulting current was constantly measured. Polarisation begun -250 mV from Eocp and increased until the potential was +700 mV from OCP. Anodic polarisation was reversed at 700 mV and the scan proceeded back to OCP.

The oxidation and reduction reactions are given below:

Oxidation (anodic) reaction:

$$Ni \rightarrow Ni^{2+} + 2e^-$$

$$Ni^{2+} + 2OH \rightarrow Ni(OH)_2$$

Reduction (cathodic) reaction:

$$\tfrac{1}{2} O_2 + H_2O + 2e^- \rightarrow 2OH^-$$

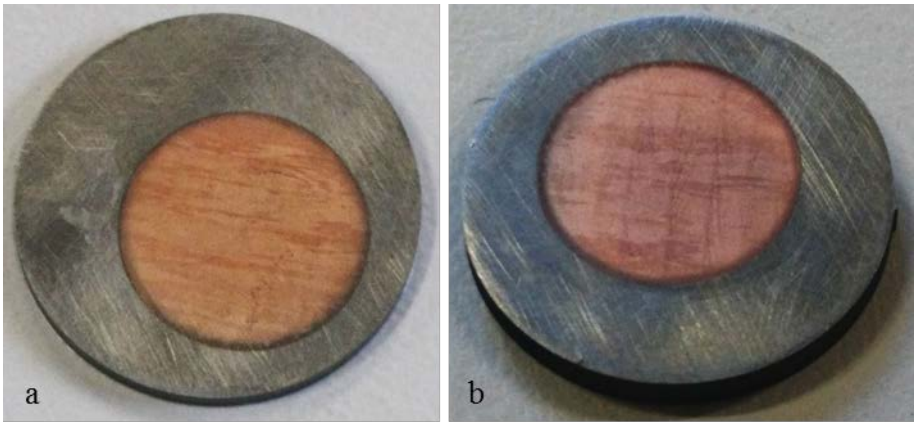

Figure 4.4.13. Samples after cyclic polarisation test: (a) Monel K500 and (b) FM60.

After the test all samples looked like ones shown in Figure 4.4.13. The area, which was exposed to the electrolyte solution 3.5%NaCl, changed its original colour

from Ni-white to Cu-yellow. This happened because Ni, as less noble metal, compared to Cu, acted as a sacrifice metal, protecting the sample.

The corrosion current density, which indicates how fast the corrosion proceeds, was calculated using Tafel Slope Analysis. It was determined as the current at the intersection of the linear extrapolation of the cathodic Tafel slope with the rest potential. An example of cyclic polarisation curves and I_{corr} measurements are shown in Figure 4.4.14 for as-welded Monel K500 and FM60.

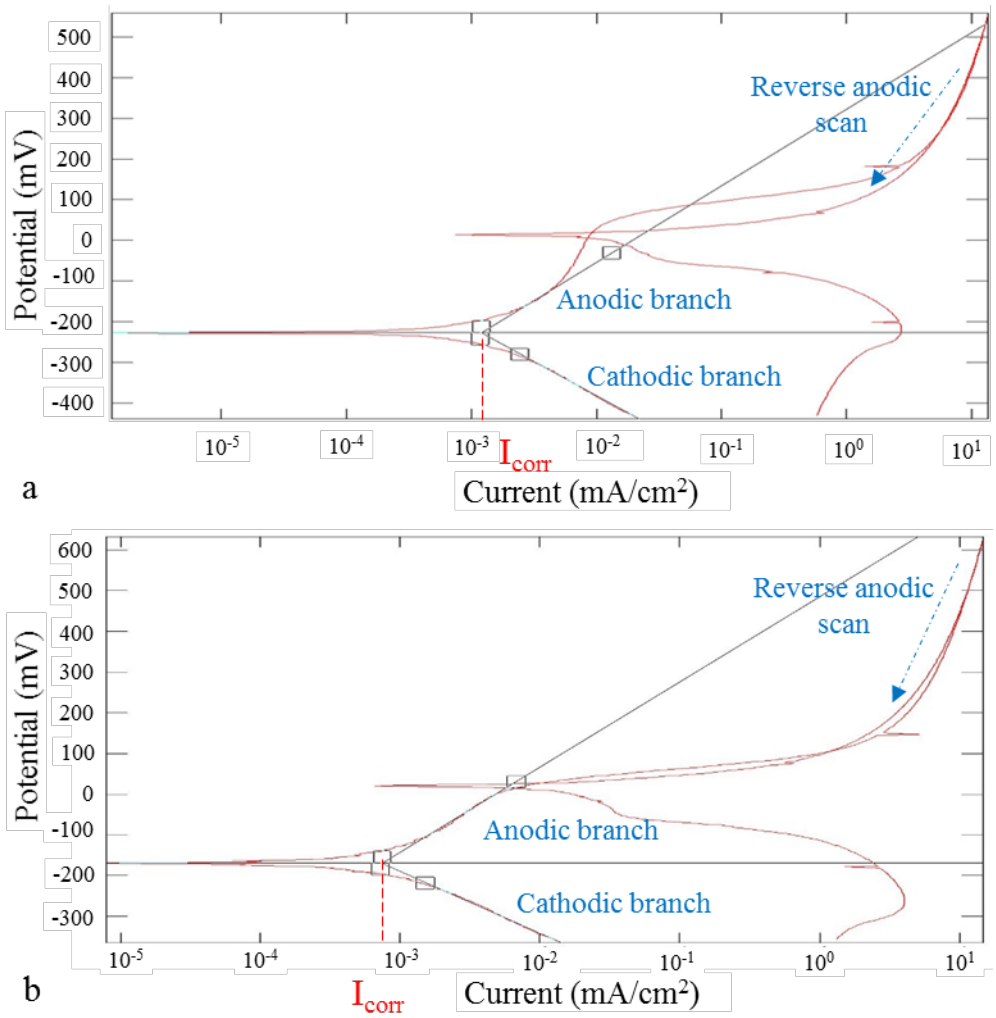

Figure 4.4.14. Cyclic polarisation curves for as-welded depositions: (a) MonelK500 and (b) FM60.

The cyclic polarization curves for Monel K500 and FM60 depositions in all heat treatment conditions exhibited a passive behaviour of both alloys. The summary of cyclic polarization parameters for Monel K500 and FM60 depositions in various heat

treatment conditions are given in Table 4.4.4. A very low values of corrosion current density (0.5-4.0 nA/cm^2) suggest that these alloys would have a good corrosion resistance in 3.5%NaCl environment. To compare, Ni-Cr alloys 600, 601 and C22, tested under similar conditions in 3.5%NaCl environment, demonstrated I_{corr} values 100 times higher [148] than values obtained in this study for Ni-Cu alloys.

The order of I_{corr} measured for Monel K500 plate was the same as for both depositions, which suggests a similar corrosion resistance in the tested media, regardless of the manufacturing method (Table 4.4.5).

For most studied conditions the value of I_{corr} increased in both depositions and plate after first ageing and futher increased after second ageing. It was observed before that this allloys are more susceptible to corrosion in age-hardened state [25]. The variation in Icorr with heat treatment for two depositions at welding speed of 300 mm/min and a base plate is shown in Figure 4.4.15.

Table 4.4.4. Summary of cyclic polarization parameters for Monel K500 and FM60 depositions in various heat treatment conditions

Heat treatment	Travel speed, mm/min	E_{ocp} vs E_{RE}, mV*	I_{corr}, nA/cm$^{2\,\#}$	E_{ocp} vs E_{RE}, mV	I_{corr}, nA/cm^2
		Monel K500		FM60	
As-welded	300	-163	1.11	-99	0.72
	400	-115	0.86	-102	0.69
	500	-105	1.74	-50	1.40
Aged at 610°C	300	-174	1.18	-69	2.53
	400	-172	1.78	-92	2.20
	500	-146	2.77	-141	3.01
Aged at 610°C + 480°C	300	-165	2.16	-118	2.55
	400	-175	2.78	-96	4.02
	500	-57	2.97	-45	3.78

*standard deviation for E_{ocp} is ±25mV; #standard deviation for I_{corr} is ±0.2 nA/ cm^2

Table 4.4.5. Summary of cyclic polarization parameters for Monel K500 plate tested in various heat treatment conditions

Heat treatment condition	E_{ocp} vs E_{RE}, mV	I_{corr}, nA/cm^2
As-received	-125	1.44
Aged at 610 °C	-144	2.62
Aged at 610°C + 480°C	-72	5.69

Figure 4.4.15. The variation in I_{corr} with heat treatment for Monel K500 and FM60 deposited at welding speed of 300 mm/min (red and black) and Monel K500 plate (blue).

4.4.8 Conclusions to chapter 4.4

First ever investigation of the effect of heat treatment on microstructure, mechanical properties and wear resistance of Ni-Cu alloys processed using the wire arc additive manufacturing technology has resulted in the following conclusions:

1. In the as-welded condition, precipitation of TiC and TiCN particles was observed in Monel K500, the alloy with a higher C content, rather than in FM60, containing a higher Ti content. In FM60 the precipitation of Ti-rich oxides and MnS-core particles took place, what coincided with a higher Mn content in FM60.

2. Annealing at 1100 °C followed by ageing at 610 °C resulted in extensive precipitation of TiC particles in Monel K500 (240-290 times increase in the TiC number density compared to the as-welded condition). However, in FM60 the particle precipitation was relatively sluggish (up to 70% increase in the number density). The second ageing at 480 °C has led to the particle coarsening, accompanied by a decrease in the particle number density, in both alloys.

3. Due to precipitation of TiC/TiCN particles and smaller secondary dendrite arm spacing, Monel K500 exhibited higher hardness, yield stress and tensile strength than FM60 for all the studied conditions. In spite of FM60 elongation being larger in annealed and aged conditions, toughness of Monel K500 was higher due to higher strength. In accordance with higher hardness and toughness, the wear resistance of Monel K500 was higher in almost all conditions.

4. In the as-welded condition, the lowest hardness, strength and wear resistance in both alloys were observed for the slowest deposition speed of 300 mm/min. These coincided with the highest particle number density in both alloys. In the annealed and aged conditions, the highest wear resistance (supported by either the highest hardness or strength) in both alloys was obtained at the highest deposition speed of 500 mm/min. These coincided with the low particle number density. In spite of 240 - 290 times increase in the particle number density in Monel K500, after annealing and ageing at 610 °C the wear resistance increase by only 16 %; and only 70% increase in the particle number density in FM60 resulted in 24 % increase in the wear resistance. Obviously, fine (<20 nm) particles, not visible in SEM and not studied here, played their role in properties development. This requires further investigation.

5. In all heat treatment conditions both Monel K500 and FM60 depositions and Monel K500 plate exhibited passive behaviour with low corrosion rates in 3.5 wt. % NaCl. The value of I_{corr} increased after ageing, which suggested that these alloys are more susceptible to corrosion in age hardened state.

6. The corrosion behaviour of hot-rolled Monel K500 plate was similar to that observed for both Monel K500 and FM60 depositions in all heat treatment conditions. This indicates that WAAM samples retain good corrosion resistance typical for Monel K500.

4.5 Work hardening behaviour and fracture in as-welded and heat treated Ni-Cu alloys

4.5.1 SEM characterisation of >20 nm precipitates

SEM studies of as-welded depositions have shown 200-700 nm particles in both alloys, with average sizes of 448 nm and 400 nm in Monel K500 and FM60, respectively (Figure 4.5.1a,e). The number density of these particles was 2.4 times higher in FM60 than in Monel K500. The particles chemical compositions were identified as Ti-, Mg- and Al-rich, namely, MgMnS, TiC and TiCAlMgO in Monel K500 (Figure 4.5.2 a, b) and MgMnS, AlTiO and AlTiMgO in FM60 (Figure 4.5.3c, d).

The pronounced difference in precipitation between the two alloys occurred following annealing. In Monel K500 annealing resulted in almost complete dissolution of Mn-, Mg- and Al-rich particles and led to precipitation of new densely dispersed primary carbides TiC. SEM studies have shown down to 30 nm particles in Monel K500 with their number density increasing by 170 times and average size decreasing by 2.9 times compared to the as-welded condition (Table 4.5.1). Whereas, in FM60 the chemical composition, size and number density of particles in SEM visible size range remained virtually the same as in as-welded condition (Table 4.5.2).

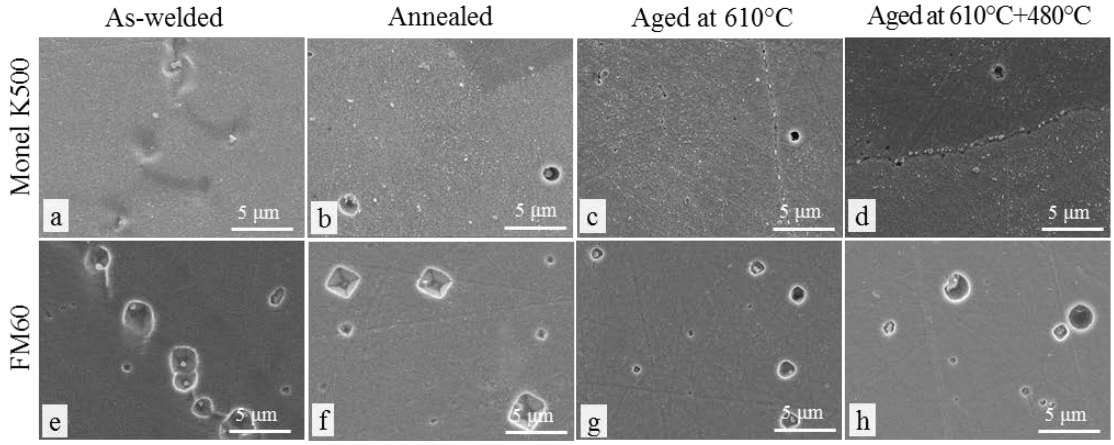

Figure 4.5.1. Representative SEM images summarising evolution of the particles with heat treatment: (a-d) in Monel K500 and (e-h) in FM60.

The first stage of age hardening at 610 °C for 8 hours led to the increase in particles number density and decrease in particles average size in both alloys, although this was more pronounced in Monel K500. In Monel K500 the >30 nm particles number density increased by 1.7 times and the average particle size decreased by 2 times compared to the annealed condition. In FM60, these particles number density increased by 23% and the particles average size decrease by 1.5 times compared to the annealed condition. The particle chemical compositions after the first age hardening were mainly TiC, TiCS in Monel K500 and TiAlOMgS, MgAlO in FM60 (Figure 4.5.3).

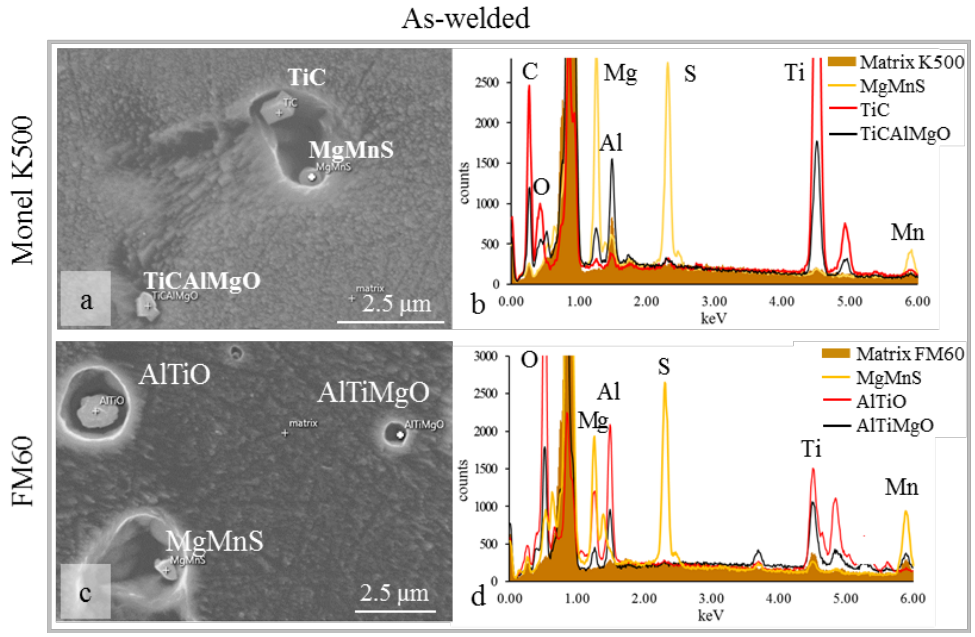

Figure 4.5.2. SEM images and EDS spectra showing chemical composition of particles in as-welded depositions: (a, b) MgMnS, TiC and TiCAlMgO in Monel K500 and (c, d) MgMnS, AlTiO and AlTiMgO in FM60. The matrix spectrum in shown in orange.

During the second age hardening at 480 °C for 8 hours, following age hardening at 610 °C, a 20% increase in the average size and a 35% decrease in the number density were observed for >30 nm particles in Monel K500 (Table 4.5.1). In FM60 no significant variation in the >30 nm particle parameters with the second ageing was observed. The particle compositions did not change with the second ageing: TiC, TiCS were observed in Monel K500 and TiAlOMgS, MgAlO in FM60.

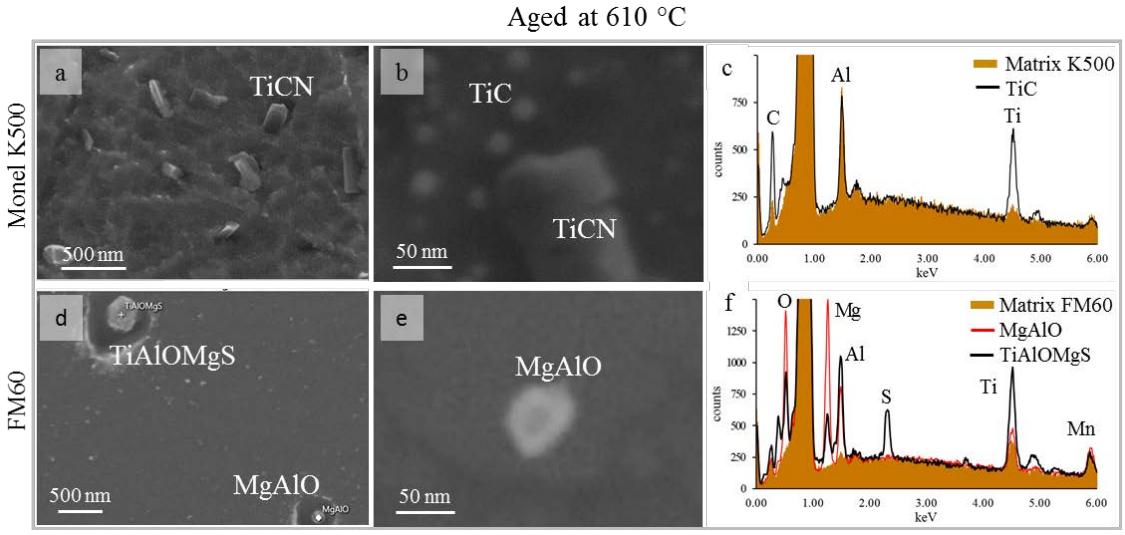

Figure 4.5.3. SEM images and EDS spectra showing chemical composition of particles in annealed and aged at 610°C depositions: (a-c) TiC/TiCN in Monel K500 and (d-f) MgAlO and TiAlOMgS in FM60. The matrix spectrum in shown in orange.

The evolution of particle size distributions with heat treatment in both alloys is shown in Figure 4.5.4. The difference in particle sizes in as-welded, annealed and aged conditions is clearly seen for Monel K500: with annealing and ageing the fraction of smaller particles increased (notice a shift of the peak of particle size distribution to the left, Figure 4.5.4a). Although in FM60 the distributions look similar irrespective of the heat treatment condition (Figure 4.5.4b).

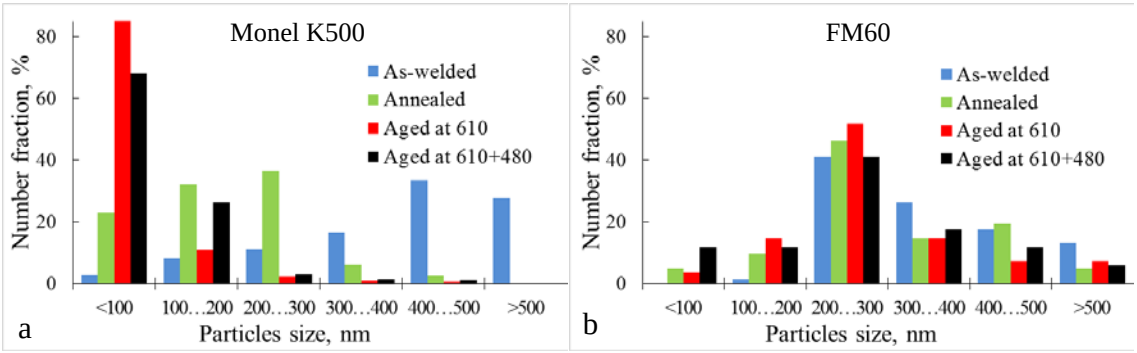

Figure 4.5.4. Size distributions of >30 nm particles observed with SEM in: (a) Monel K500 and (b) FM60.

4.5.2 TEM and TEM-ARM characterisation of <20 nm precipitates

Transmission electron microscopy has shown spherical evenly distributed precipitates with <10 nm sizes in all samples (Figure 4.5.5). The as-welded Monel K500 contained precipitates 2 times larger in size and 1.4 times lower in number density than as-welded FM60 (Figure 4.5.5a,e, Tables 4.5.1 and 4.5.2). The analysis of TEM diffraction patters confirmed the precipitates to be TiC in both alloys. A diffraction pattern showing the [112] matrix || [011] TiC orientation relationship on Figure 6.5.7 a,c originated from the cubic crystal lattice, characteristic for TiC particles; and the measured $d_{\bar{2}00}$ spacing of 0.217 nm was in good agreement with 0.216 nm calculated based on the TiC lattice parameter a = 0.432 nm [155, 156]. The ARM-EDS mapping did not show any local increase in element concentrations (Figure 4.5.7 a-c and g-i), which might be expected due to atom clustering or precipitation. Most likely, this was caused by very small sizes of particles.

Annealing led to an increase in the <10 nm average precipitates size by 15% and 30% in Monel K500 and FM60, respectively. Compared to as-welded condition, the precipitate number density increased by 9% in Monel K500 (Table 4.5.1), although in FM60 no variation in the <10 nm particle number density was observed (Table 4.5.2). Particle growth during annealing increased the particle volume fraction by 1.4 times in Monel K500 and by 3 times in FM60. Similar to as-welded condition, the chemical composition of nano-sized precipitates in both alloys after annealing was identified as TiC.

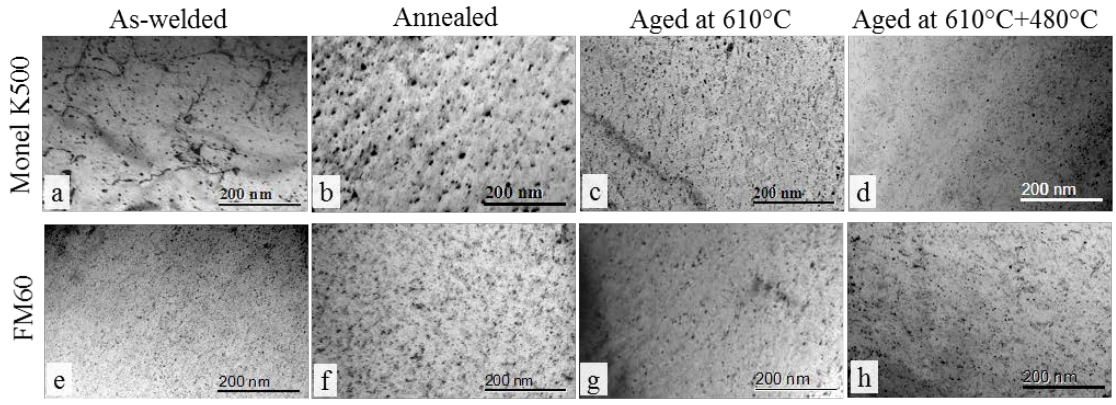

Figure 4.5.5. Representative TEM images showing distribution of particles for different heat treatment conditions: (a, e) as-welded; (b, f) annealed; (c, g) aged at 610 °C; (d, h) aged at 610 °C + aged at 480 °C in (a-d) Monel K500 and (e-h) FM60.

The first stage of age hardening resulted in 2.8 times increase in the precipitate number density and 1.8 decrease in the average precipitate size in Monel K500 (Table 4.5.1). TEM diffraction patterns have shown the presence of two types of precipitates – TiC and supposedly $Ni_3(Al,Ti)$ phase (Figure 4.5.6b). Due to the good crystallographic matching with the matrix, $Ni_3(Al,Ti)$ was hard to identify, although the forbidden reflection of its diffraction pattern can be clearly seen on Figure 4.5.6b (red circles). ARM-EDS maps have shown Ni-, Al- and Ti-rich areas (Figure 4.5.7 d-f), which confirm presence of γ′ - $Ni_3(Al,Ti)$ phase. The second age hardening led to 24% decrease in the precipitate number density and slight (8%) increase in the average precipitate size. The chemical composition of precipitates did not vary during the second stage of ageing. Particle growth during the first and second stages of age hardening decreased the <10 nm particle volume fraction.

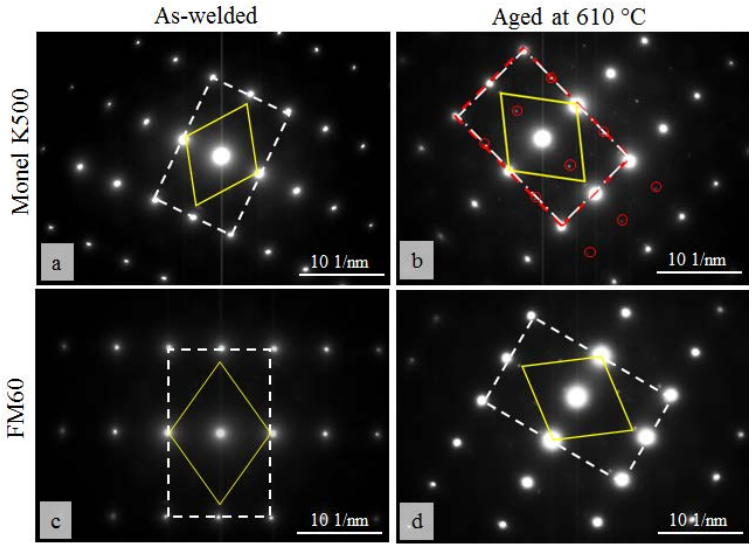

Figure 4.5.6. TEM diffraction patterns of: (a) as-welded Monel K500 showing [112] matrix || [011] TiC orientation relationship, (b) aged at 610 °C Monel K500 with [112] matrix || [112] $Ni_3(Al, Ti)$ || [011] TiC, (c) as-welded FM60 [112] with matrix || [011] TiC, (d) aged at 610 °C FM60 with [112] matrix || [011] TiC. Matrix is shown in white broken line, TiC in yellow line and $Ni_3(Al, Ti)$ in red broken line and red circles for its forbidden reflection.

In contrast to Monel K500, the age hardening heat treatment has shown little effect on FM60. During the first and second age hardening the precipitate number

density and average size increased by only 1% and the volume fraction increased by up to 10 % (Table 6.5.2). The chemical composition did not change during ageing (observe similar diffraction patterns in Figure 6.5.6c,d). Analysis of ARM-EDS maps of FM60 aged at 610 °C provided additional confirmation of the precipitates chemical composition: Ti-rich areas can be seen in Figure 6.5.7l. These results support the general perception that FM60 is a non-heat treatable alloy, i.e. can be strengthened only by solid solution strengthening.

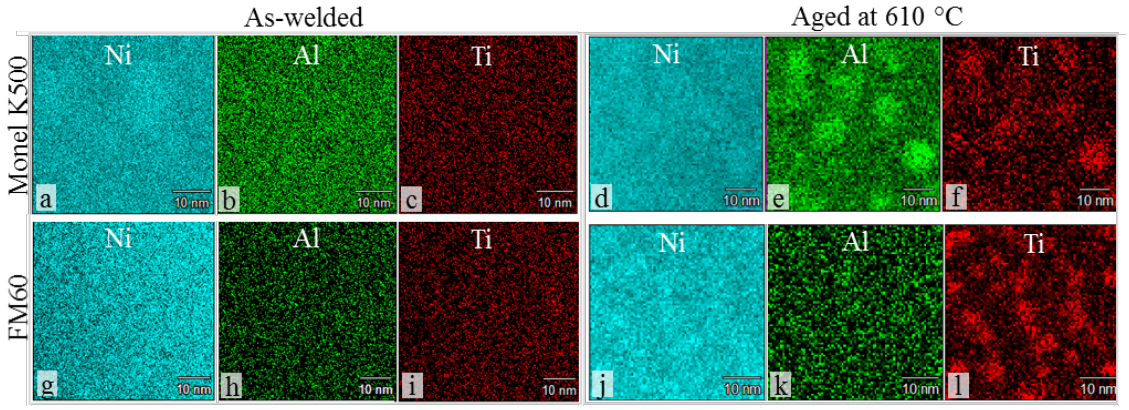

Figure 4.5.7. ARM-EDS elemental maps showing absence of AlTi-rich particles in as-welded (a-c) Monel K500 and (g-i) FM60; and presence of (d-f) AlTi-rich particles in aged at 610 °C Monel K500 and (j-l) Ti-rich particles in aged at 610 °C FM60.

The variation in <10 nm precipitate number density distributions with heat treatment is shown in Figure 4.5.8. It is clearly seen that in Monel K500 age hardening led to pronounced precipitation of new particles (observe the increase in <4 nm particle number density after age hardening). However, in FM60 new particle probably did not precipitate, although some growth of existing particles could take place.

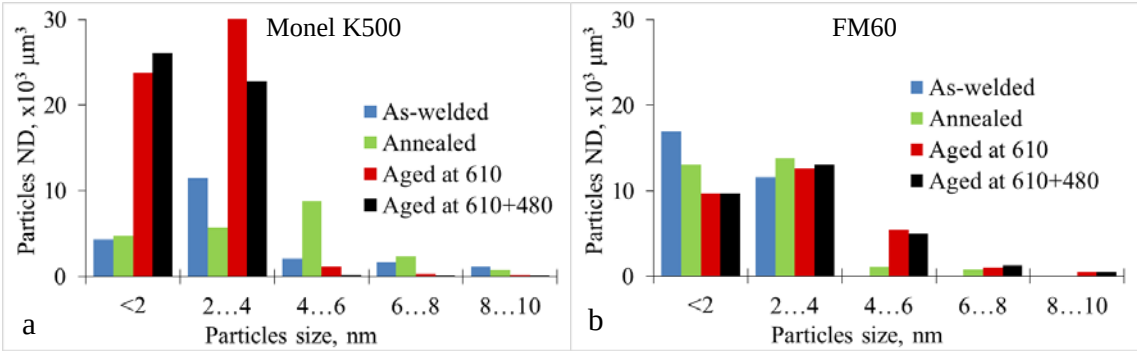

Figure 4.5.8. TEM size particle distributions in (a) Monel K500 and (b) FM60.

The variation in particle precipitation in the studied alloys followed their discrepancies in chemical composition. The C content was 22 times higher in Monel K500, although the Ti content was 3 times higher in FM60. In the as-welded condition, this facilitated precipitation of TiC/TiCN particles in Monel K500 in all size ranges. However, in FM60 only minor precipitation of TiC in <10 nm size range took place. The majority of coarse particles in both alloys were TiMnMgAl-rich sulphides and oxides. Although, the number density of these coarse particles was 2.4 times higher in FM60, due to a 3 times higher Ti and 4 times higher Mn content in FM60. The volume fraction of <10 nm TiC was 7 times higher in Monel K500 due to a higher C content.

In Monel K500 the majority of MnMgAl-rich particles dissolved during annealing, and new Ti-rich carbides, carbonitrides and sulphides precipitated. This increased the number density of coarse particles by 170 times and the volume fraction of <10nm TiC by 45%. For the given Ti and C contents in Monel K500 (0.5 and 0.088 wt. %, respectively) and the solubility equation log [Ti]·[C] = 2.75 - 7000/T presented in [133], the temperature of full TiC dissolution could be about 1430 °C. This supports the suggestion that during annealing at 1100 °C not dissolution but precipitation of TiC took place. In FM60 no Mn-rich particles have been observed after annealing, most particles were MgTiAl-rich oxides and sulphides. The amount of sulphides increased after annealing by 25%, compared to the as-welded condition. This may indicate that a slight growth of particles during annealing could occur via precipitation of S atoms on top of the existing particles. Although the volume fraction of <10 nm TiC precipitates in FM60 increased by 3 times, compared to the as-welded condition, it was still 3.4 times lower than in annealed Monel K500. Precipitation of TiC in FM60 had to be slower not only because of lower C content, but also because of higher Mn content, which can increase solubility of Ti in fcc lattice [135, 136].

After the first stage of ageing, in Monel K500 the particle number density increased and the average size decreased in all size ranges. In TEM-size range this resulted from precipitation of new $Ni_3(Al,Ti)$ particles, in addition to TiC. The relative fraction of TiC and γ′ in the <10 nm size range was not calculated. Although, judging from the increased number density and decreased average particle size in SEM-size range, we can assume that more TiC particles have grown to sizes larger than 20 nm (SEM visible size threshold). The size of γ′ appeared rather small, ranging from 3 to 8

nm, with an average size of 2.5. This resulted from a relatively short ageing times used in this study. Coarser γ′ precipitates have been previously observed in Monel K500 after prolonged ageing at higher temperatures (for example, 8 h at 700°C was required to obtain 7 nm precipitates and 1000 h at 700°C – to get up to 100 nm precipitates [33]). In FM60, first ageing led to a slight increase in number density and decrease in size of coarse particles (by 23% and 50%, respectively), due to dissolution of large complex MgTiAl-rich oxides and precipitation of Mg-rich oxides and sulphides. No significant changes in parameters of <10 nm particles were observed.

The second ageing led to particles coarsening (Oswald ripening), accompanied by a decrease in number density, in Monel K500. This phenomenon was observed previously in aged Ni alloys [153, 154]. The fraction of Ti-rich carbosulfides in the range of coarse particles has increased with ageing, which also could contribute to an increase in average particle size. In FM60 no significant changes have been observed with the second ageing. The lattice parameter decreased with heat treatment in both alloys, which corresponded to precipitation and growth of particles, leading to solution depletion.

4.5.3 Dislocation structure

The dislocation structure was characterised for as-welded and annealed conditions. Both as-welded alloys exhibited a quite developed dislocation structure with knots and tangles (Figure 4.5.9a,c), which might be associated with fast cooling and local stress gradients. During annealing the dislocation annihilation occurred leading to the breakdown of tangles and appearance of single isolated dislocations (Figure 4.5.9b,d). The dislocation densities in the as-welded condition were measured to be $3.7 \cdot 10^{14}$ m^{-2} and $3.6 \cdot 10^{14}$ m^{-2} in Monel K500 and FM60, respectively. These values correspond to those observed in hot deformed nickel alloys [157]. The dislocation densities in the annealed condition were $3.4 \cdot 10^{13}$ m^{-2} and $7.4 \cdot 10^{13}$ m^{-2} in Monel K500 and FM60, respectively. An order of magnitude decrease in dislocation density during annealing might be expected on the basis of previously published data [157], although the absolute values after annealing looked a bit high. Probably, the dislocation annihilation during annealing was retarded by the highly concentrated solute atoms and precipitates.

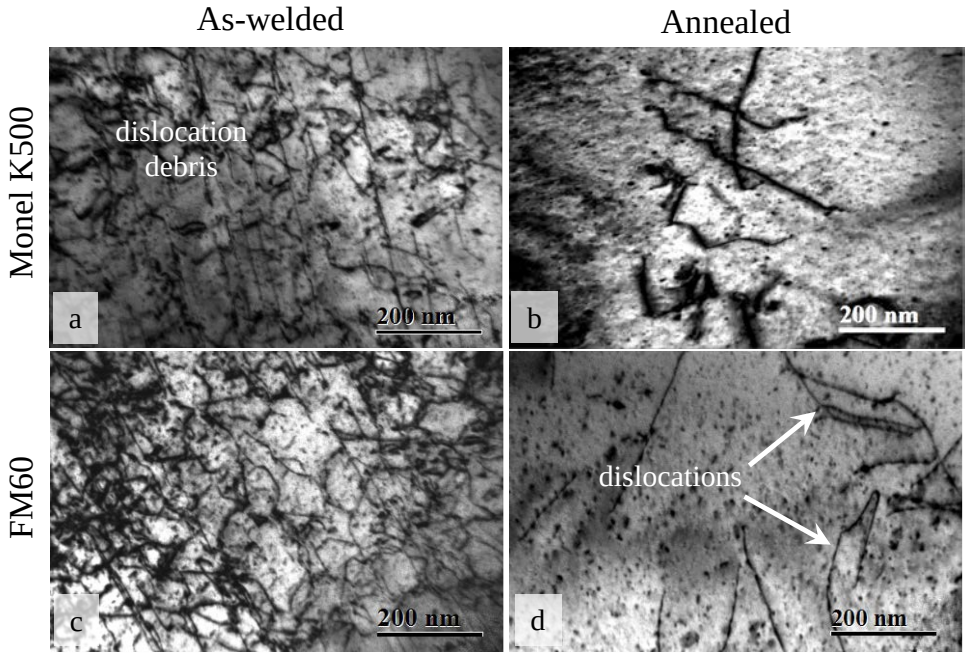

Figure 4.5.9. Typical dislocation structures in as-welded (a) Monel K500 and (c) FM60, and annealed (b) Monel K500 and (d) FM60.

To estimate the levels of solute atom concentrations in the matrix, the matrix lattice parameters have been measured using diffraction patterns for both alloys in all studied heat treatment conditions (Tables 4.5.1 and 4.5.2). A larger matrix expansion would indicate a higher concentration of solute atoms [158]. The absolute values of lattice parameter in the studied alloys were 5-8 % larger than the reported for other nickel alloy [33, 159], which may be due to an increased concentration of elements in the alloy compositions. No significant variation in the lattice parameter between Monel K500 and FM60 was observed. For both alloys, the lattice parameter decreased with heat treatment. This corresponds to precipitation and growth of particles, leading to solution depletion.

Table 4.5.1. Microstructure and mechanical properties of Monel K500

Heat treatment condition		As-welded	Annealed	Aged at 610 °C	Aged at 610 °C +480 °C
SEM particles	ND* x10^{-3} μm^{-2}	3.06	522	898	667
	Average size, nm	448±140	155±60	75± 45	90±50
	Chemistry	TiMnMgAl-rich	TiC	TiCS	TiCS
TEM particles	ND x10^{3} μm^{-3}	20.5	22.4	62.0	50.0
	Average size, nm	3.8±1.5	4.4±1.8	2.5±0.8	2.7±1.2
	Volume fraction	0.00114	0.00165	0.00094	0.00055
	Matrix lattice parameter, nm	0.3838	0.3790	0.3770	0.3742
	Chemistry	TiC	TiC	TiC +Ni_3(Al,Ti)	TiC +Ni_3(Al,Ti)
Mechanical properties	HV	141	186	255	236
	YS, MPa	165±10	195±5	300±3	250±5
	UTS, MPa	410±10	477±20	615±20	563±5
	El, %	51±3	43±3	37±1	34±4
	MPa·%	14663	14448	16928	13821
	Fracture area, %	33	39	49	54
	Average void size, μm	1.93	1.47	1.00	0.87

Table 4.5.2. Microstructure and mechanical properties of FM60

Heat treatment condition		As-welded	Annealed	Aged at 610 °C	Aged at 610 °C +480 °C
SEM particles	ND x10^{-3} μm^{-2}	7.2	6.9	8.5	8.9
	Average size, nm	392±150	412±90	274±110	288±97
	Chemistry	TiMnMgAl-rich	TiMgAl-rich	TiMgAl-rich	TiMgAl-rich
TEM particles	ND x10^{3} μm^{-3}	28.4	28.6	29.0	29.4
	Average size, nm	1.9±0.7	2.5±1.1	2.6±1.5	2.6±1.5
	Volume fraction	0.00016	0.00048	0.00051	0.00057
	Matrix lattice parameter, nm	0.3855	0.3780	0.3754	0.3752
	Chemistry	TiC	TiC	TiC	TiC
Mechanical properties	HV	132	123	164	174
	YS, MPa	149±5	99±3	155±5	170±3
	UTS, MPa	361±20	356±2	410±10	490±20
	El, %	47±1	49±1	43±1	39±1
	MPa·%	11985	11148	11718	12870
	Fracture area, %	30	23	32	40
	Average void size, μm	1.86	2.75	1.66	1.49

4.5.4 Work hardening behaviour

For all studied conditions, the yield stress (YS) and ultimate tensile strength (UTS) were higher in Monel K500 than in FM60 (Tables 4.5.1 and 4.5.2). In the as-welded condition YS, UTS and elongation to failure were 10, 13 and 9 %, respectively, higher in Monel K500. The YS and UTS of annealed Monel K500 were 2 times and 34%, respectively, higher than these of FM60, although the elongation of Monel K500 was 14% lower than of FM60. Ageing at 610 °C resulted in the increase of YS and UTS in both alloys, yet it was more noticeable in Monel K500. The YS and UTS of Monel K500 aged at 610 °C was by 94% and by 50%, respectively, higher than these in FM60. The elongation of Monel K500 after first stage of ageing was 16% lower than this in FM60. The second ageing resulted in a decrease in strength for Monel K500 and in an increase in strength for FM60. Thus, the YS and UTS of Monel K500 after second ageing were 47% and 15%, respectively, higher than these of FM60; and the elongation was 14% higher in FM60.

The two alloys have shown a different behaviour during heat treatment. The trend of mechanical properties variation with heat treatment is demonstrated in Figure 4.5.10. In Monel K500 annealing resulted in YS and UTS increase by 30 and 67 MPa, respectively, compared to as-welded condition. After the first stage of ageing, this alloy showed its maximum strength: YS and UTS further increased by 105 and 138 MPa. The second ageing led to both YS and UTS decrease by 50 MPa. The elongation to failure decreased by 50% compared to the as-welded condition.

In contrast, the annealing of FM60 led to a decrease in YS and UTS by 50 and 5 MPa, respectively, and to an increase in elongation by 2%, compared to the as-welded condition. The first ageing resulted in YS and UTS increase by 56 and 54 MPa, respectively, compared to annealed condition, and the second ageing led to further increase in YS and UTS by 55 and 97 MPa, respectively. The elongation decreased by only 20%, compared to the as-welded condition.

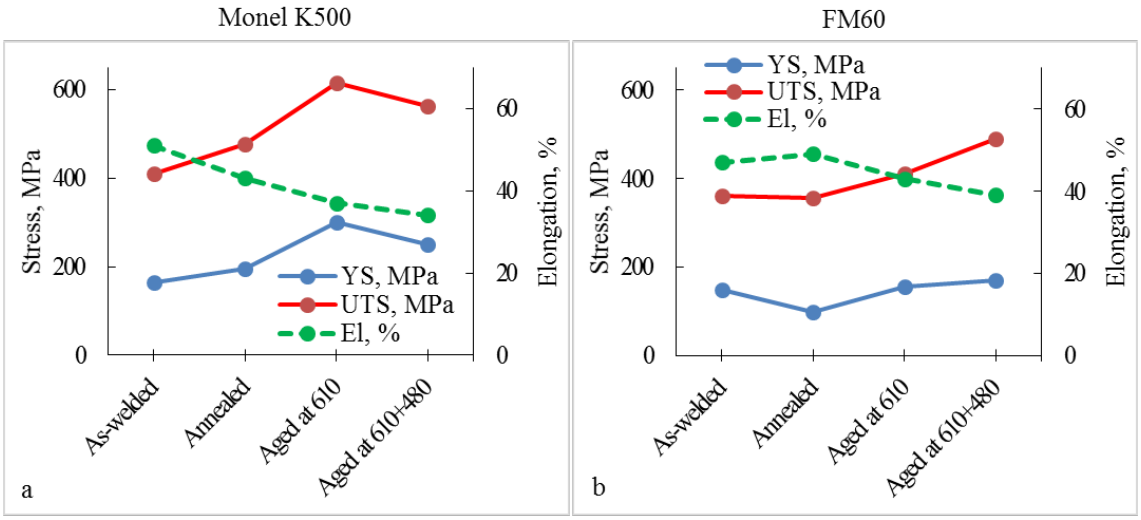

Figure 4.5.10. Mechanical properties variation with heat treatment for (a) Monel K500 and (b) FM60.

The stress-strain curves and corresponding strain hardening rates variations with strain for both alloys are shown in Figure 4.5.11. In Monel K500 the highest strength and strain hardening rate were observed after the first ageing (red curve in Figure 4.5.11a,b), and these went down along the stress axis after the second ageing. In FM60 the stress-strain curve was moving upwards with each stage of ageing, and the maximum strain hardening rate was reached after the second ageing (black curve in Figure 4.5.11c,d).

The work hardening behaviour of the samples comprised of three stages (see for example Figure 4.5.11d black curve). In regime I, a rapid decrease of strain hardening rate with increasing strain was observed. Regime II was identified by slight increase in strain hardening rate followed by a period of near-constant strain hardening rate, which corresponded to the linear section on the stress-strain curve (Figure 4.5.11c). In regime III the strain hardening rate gradually decreased. The data characterising strain hardening behaviour for all conditions is given in Table 4.5.3, where ε_1/ σ_1/ θ_1 stands for strain/stress/strain hardening rate at the end of regime I and ε_2/ σ_2/ θ_2 – for the strain/stress/strain hardening rate at the end of regime II. Stress and strain hardening rate values are given in MPa. Strain hardening rate was calculated as $\theta=(d\sigma/d\varepsilon)$.

In regime I a sharp decrease in strain hardening rate was observed in all conditions, although the values at the end of this stage varied with alloy composition and heat treatment. In Monel K500 the minimum strain hardening rate was observed for

the as-welded condition. With annealing and age hardening at 610 °C strain hardening rate increased by 8% and 57%, respectively, and decreased after the second age hardening at 480 °C by 10%. In contrast, in FM60 the minimum strain hardening rate was measured for the annealed condition. It increased after ageing at 610 °C and 480 °C by 17% and 57%, respectively.

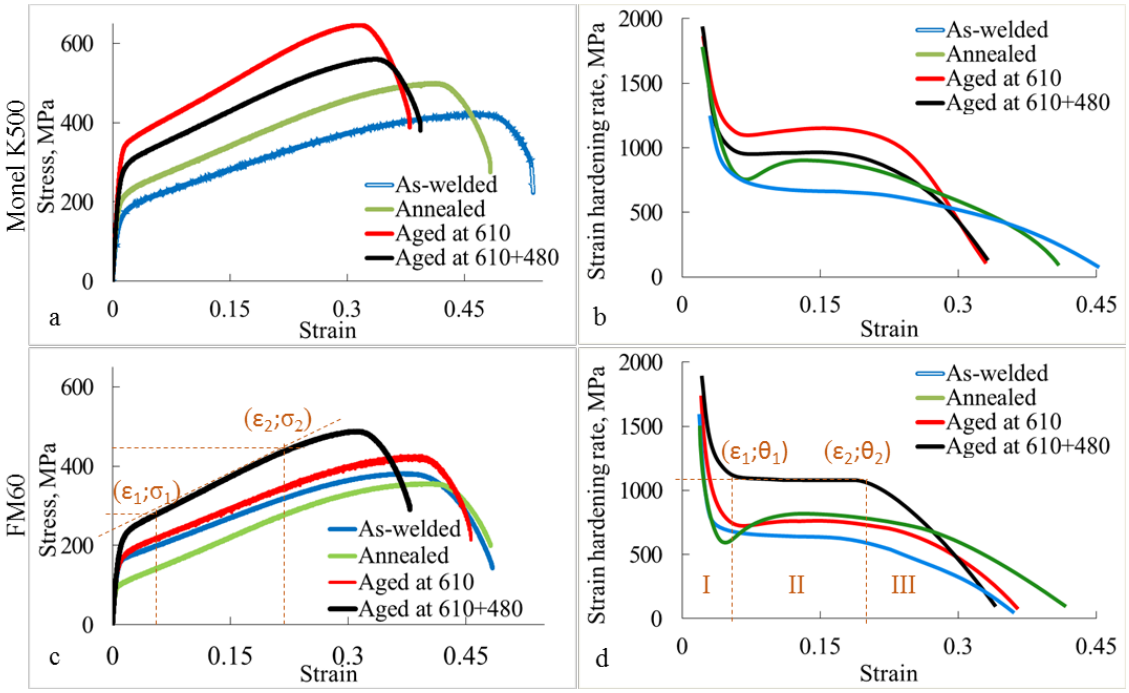

Figure 4.5.11. Effect of heat treatment on stress-strain behaviour (a,c) and strain hardening rate (b,d) in (a,b) Monel K500 and (c,d) FM60.

In regime II both alloys in as-welded condition demonstrated a near-constant strain hardening rate of the same values. In annealed condition, both alloys first exhibited an increase in strain hardening rate by 29% and 67% in Monel K500 and FM60, respectively, and then a section with a near-constant strain hardening rate. Compared to the as-welded condition, the average strain hardening rate in regime II increased with annealing by 27% and 22% in Monel K500 and FM60, respectively. After age hardening both alloys revealed a near-constant strain hardening rate, although the maximum values in Monel K500 were reached after one stage of ageing, and in FM60 – after two stages of ageing.

In regime III the strain hardening rate decreased in both alloys in all conditions, although a more rapid decrease was observed for Monel K500 after one and two stages of ageing and for FM60 after two stages of ageing.

Table 4.5.3. Strain hardening behaviour.

Heat treatment condition		As-welded	Annealed	Aged at 610°C	Aged at 610°C +480°C
Monel K500	$\varepsilon_1/ \sigma_1/ \theta_1$	0.05/220/650	0.06/267/700	0.04/389/1100	0.04/335/1000
	$\varepsilon_2/ \sigma_2/ \theta_2$	0.27/373/650	0.23/408/900	0.19/546/1200	0.20/486/1000
	θ average in regime II	653	829	1121	956
FM60	$\varepsilon_1/ \sigma_1/ \theta_1$	0.02/166/700	0.03/165/600	0.05/206/700	0.05/273/1100
	$\varepsilon_2/ \sigma_2/ \theta_2$	0.22/296/650	0.26/294/800	0.26/360/700	0.20/455/1000
	θ average in regime II	652	794	727	1072

For all studied heat treatment conditions, Monel K500 has shown higher hardness, than FM60 (Table 4.5.1 and 4.5.2), which corresponds to higher tensile properties. In Monel K500 the hardness increased by 1.8 times from as-welded to aged at 610°C condition, but then dropped by 8% after the second ageing (blue line in Figure 4.5.12a). In FM60 the hardness decreased by 7% after annealing, and then gradually increased with ageing: by 33% and by 17% after the first and second ageing, respectively (blue line in Figure 4.5.12b). Thus, the maximum hardness values of 255 HV were reached in Monel K500 after the first ageing and 192 HV in FM60 after the second ageing.

Toughness was estimated via calculation of the area under stress-strain curves. The shape under stress-strain curves was approximated by a trapezoid with the area calculated as 0.5(YS+UTS)·elongation. For this calculation method, the toughness units were MPa·%. Toughness in Monel K500 was by up to 40% higher than in FM60 for all heat treatment conditions (red broken line in Figure 4.5.12). Similarly to hardness and strength, the maximum toughness in Monel K500 was reached after the first age hardening (16928 MPa·%), and in FM60 after the second age hardening (12870 MPa·%). The minimum toughness in Monel K500 (13821 MPa·%) was observed after the second ageing, due to the lowest elongation at this condition, and in FM60 (11148 MPa·%) after the annealing, due to the lowest strength.

Due to precipitation of TiC/TiCNS and γ′ particles, Monel K500 exhibited higher hardness, YS and UTS than FM60 for all the studied conditions (Tables 4.5.1 and 4.5.2). In spite of FM60 elongation being larger in annealed and aged conditions, toughness of Monel K500 was higher due to higher strength. The first ageing led to the

hardness and strength increase in both alloys and toughness increase in Monel K500. These were due to precipitation of >30 nm TiCNS and <10 nm TiC and γ′ in Monel K500 and >100 nm MgTiAl-rich oxides and <10 nm TiC in FM60. Obviously age hardening improves the properties of FM60 to some extent, even if it is considered a solely solution strengthened alloy, but not as much as of Monel K500. The second ageing resulted in the particle growth accompanied by a decrease in the particle number density in Monel K500, which lead to decrease in hardness and strength. In FM60 the growth and precipitation of particles continued, even though slowly, which resulted in further slight increase in hardness and strength.

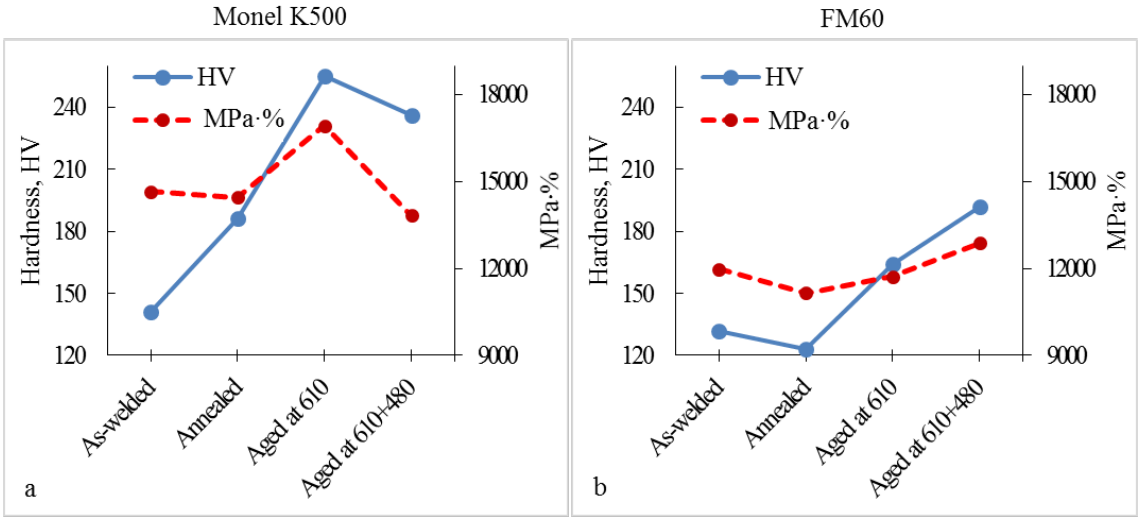

Figure 4.5.12. Hardness and toughness variations with heat treatment in (a) Monel K500 and (b) FM60.

The work hardening behaviour of polycrystal alloys is a complex phenomenon influenced by many factors, such as stacking fault energy, grain size, elements in solution, previous processing history [160, 161, 162, 163]. The strain hardening behaviour of precipitation hardenable polycrystal alloys is even more complex and, in addition to the mentioned above, is dictated by the nature, number density and size of precipitates, which in turn affect the mechanism of dislocation bypass (looping or shearing) [164, 165, 166]. The alloys studied here exhibit coarse grain size due to cast microstructure, high stacking fault energies (between 106 and 124 mJ/m^2, measured for Cu-Ni system containing 60% and 80% Ni, respectively [167]), elements in solution as well as precipitates which are different in composition and number density for each

alloy and heat treatment condition. In Monel K500 both SEM and TEM visible particles contribute to the work hardening, as the average size of particles visible in SEM for aged conditions is small (<100 nm). In FM60 only TEM visible particles play significant role in work hardening, as long as SEM visible particles remain bulk in size and low in number density even after ageing. We can assume that solution and clustering contributed to the work hardening of this alloy, although this has not been studied here and requires additional investigation.

The initial strain hardening rate at 1% strain in both alloys was highest for the age hardened conditions (4800 MPa in both alloys after two ageing) and lowest for the annealed condition (2800 MPa in Monel K500 and 800 MPa in FM60). Age hardened alloys have a higher number density of precipitates, which act as anchoring points slowing down the dislocation motion. This dependence was previously observed in precipitation hardenable Cu-base [168] and Ni-base alloys [164, 165].

The decreasing strain hardening rate in regime I is associated with a dynamic recovery caused by cross-slip and annihilation of screw components of dislocations [169, 170, 164, 165]. The decrease is less sharp in aged conditions of both alloys, which could be due to the higher number density of particles that could potentially pin dislocations and hamper the fall of strain hardening rate. Lower number density of particles in as-welded and annealed condition result in “easier” deformation with lower strain hardening rates. The lowest strain hardening rate at the end of regime I was observed in the annealed FM60. This condition may be regarded as the “weakest” among others: it has a minimal dislocation density (by an order of magnitude lower than in as-welded condition) combined with a lower number density of precipitates (compared to the aged conditions). In FM60, the volume fraction of Ti-rich precipitates in annealed condition increased by only 3 times compared to the as-welded condition, which could not compensate a considerable decrease in the dislocation density, and thus the minimal strain hardening rate at the end if regime I was by 17 % lower than in as-welded condition. In contrast, in Monel K500 the number density of Ti-rich particles of SEM size range increased by 170 times and the volume fraction of <10 nm Ti-rich precipitates increased by 45%, compared to the as-welded condition. Because of this, the minimal strain hardening rate at the end of regime I in annealed Monel K500 was not lower but 8% higher, than in as-welded condition (Table 4.5.3).

An increase or stabilisation of strain hardening rate indicates the beginning of regime II (Figure 4.5.12b and d). A near-constant strain hardening rate on this stage was seen in both alloys in as-welded and aged conditions. Although, in annealed condition, a section with a near-constant strain hardening rate was preceded by an increase in strain hardening rate by 29% in Monel K500 and by 67% in FM60. This resulted in the average strain hardening rate of annealed alloys in regime II being by 27% and 22% higher than in as-welded Monel K500 and FM60, respectively. A similar behaviour was previously observed in hot-rolled Cu-Ni alloys with various Ni content [160]. An increase in strain hardening rate may have resulted from the formation of planar-slip dislocation structures (planar slip bands) caused by well-developed short-range clustering. With increasing strain, the dominant dislocation structures become extended dislocation walls, which act similar to the grain refinement and thus lead to an increase in work hardening rate. On the near-constant section of strain hardening rate vs strain curve a pronounced planar slip was previously observed in solid solutions with well-developed short-range ordering and short-range clustering as well as in precipitation-hardened alloys where the precipitates have an ordered atomic structure [171]. As the deformation proceeds, the interaction of moving dislocations with other dislocations (forest hardening) leads to the formation of dislocation tangled network structure (i.e. cell like structure), which has a similar effect as reducing a grain size and thereby leads to nearly constant strain hardening rate [164]. In Monel K500 the highest strain hardening rate of 1200 MPa was demonstrated after the first ageing. In this condition the highest number density of <100nm particles and the highest number density and volume fraction of <10nm particles were observed. After the second ageing the strain hardening rate decreased by 20%, which coincided with particles coarsening and a decrease in their number density by 35% and 24% for <100 nm and <10 nm particles, respectively, compared to the first ageing. A similar strain hardening behaviour was previously observed for the precipitation hardenable Ni alloys Nimonic C-263 and Supercast 247A [164, 165]. Precipitation of γ' after ageing, in addition to TiC, played and important strengthening role and provided an additional barrier for dislocation movement, thus, increasing strain hardening rate. In contrast to Monel K500, in FM60 the strain hardening rate was increasing with each step of heat treatment, which goes in a good agreement with a gradual increase in the precipitates average size and volume fraction. Thus, by the second ageing the maximum strain hardening rate of 1100 MPa

was demonstrated in FM60, which was by 57% higher than in as-welded condition. The average size and volume fraction of precipitates after the second ageing increased by 37% and 3.6 times, respectively, compared to the as-welded condition.

The decreasing strain hardening rate in regime III may be related to dynamic recovery caused by cross-slip and annihilation of screw components of dislocations of opposite sign from adjacent cells or tangled dislocation networks [164, 165, 169]. Both alloys demonstrated a sharper decrease of strain hardening rate in regime III for the aged conditions, compared to the annealed and as-welded. Obviously, earlier occurring dislocation-particle interactions, due to a higher particle number densities, facilitated the operation of dislocation generation sources leading to the increase in dislocation density prior to pile-up and micro crack development.

Although the dislocation structure at various stages of deformation has not been studied here, an evidence of dislocation-particle interaction and planar slip were noticed in Monel K500 (Figure 4.5.13).

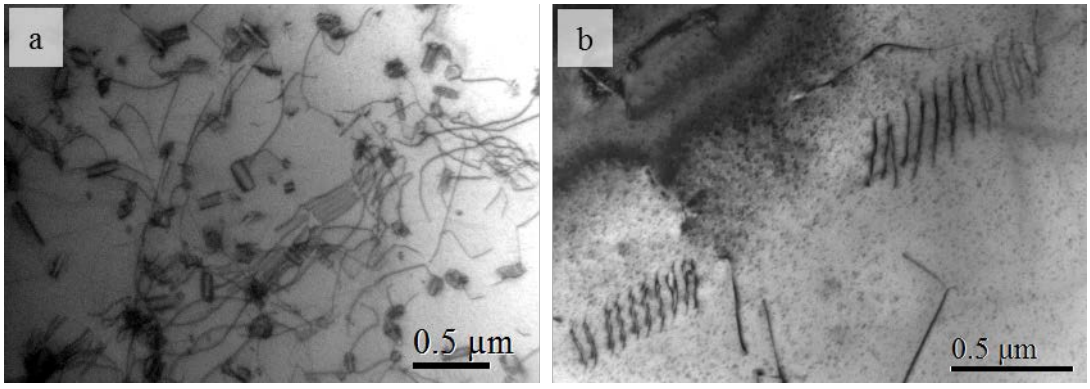

Figure 4.5.13. Selected TEM images of (a) dislocation-particle interactions and (b) planar slip in as-welded Monel K500.

4.5.5 Fracture

Figure 4.5.14 displays the surface deformation features of both alloys after tensile tests to fracture. It can be seen that the specimens experience a severe plastic deformation, and show an obvious necking near the fracture point. The fracture area was calculated as the remaining portion of the tensile specimen cross section (highlighted by black lines in Figure 4.5.14a,c,e,g) divided by the initial specimen cross section. As seen from Table 4.5.1, the fracture area was increasing

with heat treatment in Monel K500. This corresponds to the decreasing total elongation and indicates transition to more brittle mode of fracture in Monel K500 with heat treatment. Such fracture behaviour in Monel K500 can be explained by particle coarsening and its role in fracture stimulation. In FM60 the minimum fracture area (maximum total elongation) was observed for annealed condition, and the maximum fracture area (minimum total elongation) was in the condition after second ageing (Table 4.5.2). Obviously, in FM60 the dislocation annihilation during annealing, and softening related to it, plaid a more significant role than the particle precipitation, and possible hardening related to it.

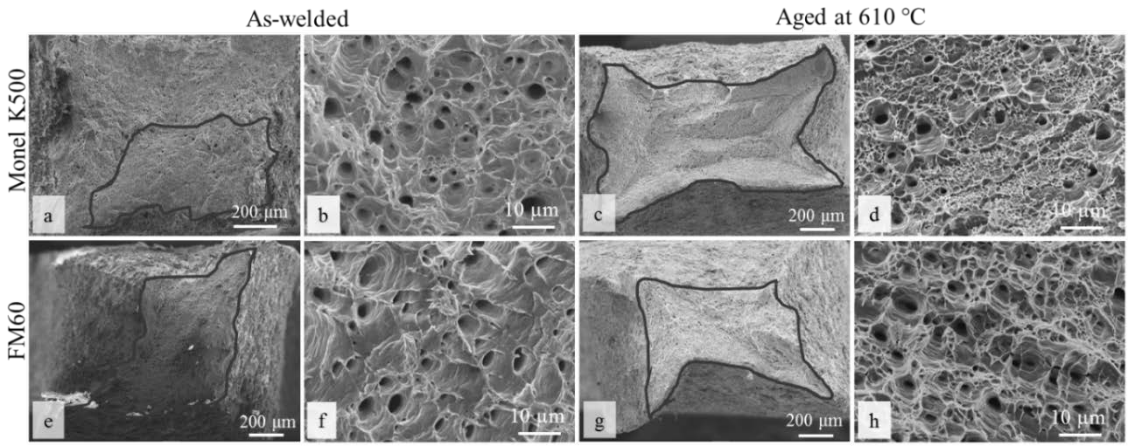

Figure 4.5.14. SEM images showing the fracture surfaces at (a,c,e,g) lower and (b,d,f,h) higher magnifications in (a-d) Monel K500 and (e-h) FM60 for as-welded and aged at 610 °C conditions.

The fracture surfaces studied at a higher magnification have shown a dimpled structure for both alloys in all processing conditions (Figure 4.5.14 b,d,f,h). It is known that the dimple formation comprises three stages, void nucleation, growth and coalescence [172], and indicates ductile fracture behaviour. The void nucleation often occurs in metals via loss of cohesion at the particle-matrix interface. In this work, SEM images of the fracture surfaces of Monel K500 and FM60 confirmed the void nucleation on particles (Figure 4.5.15). In spite of presence of large carbide/oxide particles, the fracture was ductile in both alloys, as the stress concentrations around spherical particles are relatively low to initiate brittle fracture, which is known to occur when cuboidal particles precipitate. Voids nucleation was preferred over particle fracture

because less stress was required to brake the softer Ni matrix away from particles than to break the hard carbide/oxide particles themselves.

The average void size in as-welded condition was 1.9 μm for both alloys (Tables 4.5.1 and 4.5.2). Although the fraction of <2 μm voids was higher in FM60 (observe the peak difference on the void size distributions, Figure 4.5.17), which may suggest a more brittle fracture behaviour in as-welded FM60. The average void size was decreasing in Monel K500 by 30%, 47% and 15% after annealing, first ageing and second ageing, respectively (observe an increase in fraction of <2 μm voids with heat treatment in Figure 4.5.16a). However, in FM60 the average void size increased after annealing by 48% compared to the as-welded condition and remained 66-87% larger than in Monel K500 for all heat treated conditions. This indicates more ductile fracture behaviour in FM60, than in Monel K500, and coincides with its higher elongation.

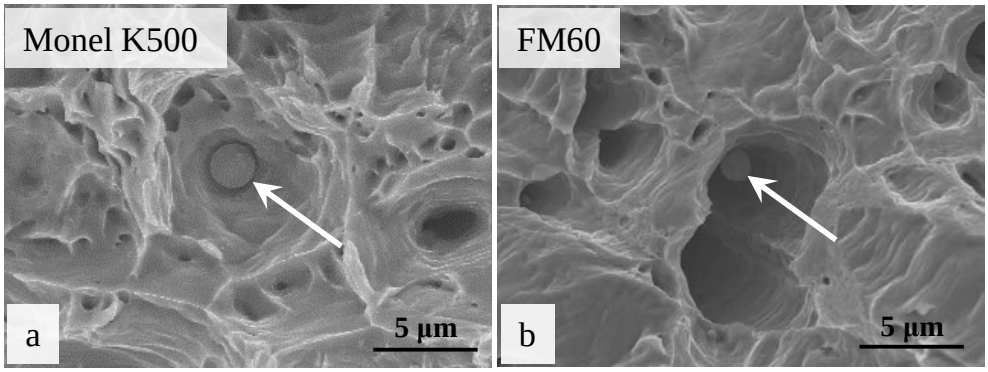

Figure 4.5.15. Void formation initiated by spherical TiC and TiMgAl-rich oxides (marked with arrows) in (a) Monel K500 and (b) FM60 aged at 610°C condition.

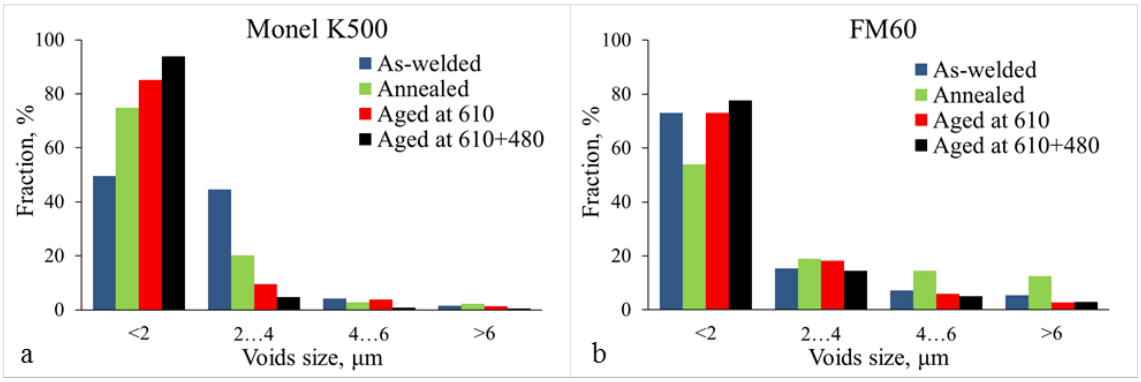

Figure 4.5.16. Distributions of fracture void sizes in (a) Monel K500 and (b) FM60.

4.5.6 Conclusions to Chapter 4.5

The investigation of work hardening behaviour and fracture of heat-treated Ni-Cu alloys fabricated using the wire arc additive manufacturing technology has resulted in the following conclusions:

1. Heat treatment (annealing followed by age hardening) resulted in a vast precipitation of TiC and Ni_3(Al,Ti) particles in Monel K500. Precipitation of Ni_3(Al,Ti) coincided with substantial (3.0 wt.%) Al content in Monel K500. In contrast, in FM60 age hardening led to only minor increase in the particles number density in all size ranges.

2. Due to precipitation of TiC and Ni_3(Al,Ti) particles, Monel K500 exhibited higher hardness, yield stress and tensile strength than FM60 in all the studied conditions. In spite of FM60 elongation being larger in annealed and aged conditions, toughness of Monel K500 was higher due to higher strength.

3. The strain hardening behaviour of the studied alloys varied with heat treatment condition, and was affected by the dislocation density, size and number density of precipitates, and solid solute concentrations. The lowest strain hardening rate at the end of regime I (following the yield point) was observed in both alloys in annealed condition. This corresponded to the lowest dislocation density after annealing. The highest strain hardening rate was observed after the first ageing in Monel K500, and after the second ageing in FM60. This can be related to the highest number density of <10 nm precipitates, and potentially the highest number of dislocation-particle interaction sites, in Monel K500 and FM60 after the first and second ageing, respectively.

4. Both alloys exhibited ductile fracture behaviour in all studied conditions and decreasing average void size, corresponding to decreasing elongation, with age hardening. This supports transition to a more brittle fracture mode with age hardening in both alloys. However, toughness did not follow the trend for elongation and void size, i.e. did not decrease with heat treatment, but rather followed the trend for strength.

4.6 Repair of a functional component by wire arc additive manufacturing

A used Monel K500 component, a cylinder 120 mm long and 40 mm in diameter, has been provided by MacTaggart Scott Australia for simulation of the weld repair technology. The component was covered by multiple defects 2-6 mm in diameter, 0.2-0.4 mm deep, caused by pitting corrosion. To prepare the part for repair, 2/3 of the component surface was machined to the depth of 0.6 mm in order to remove all defects, 1/3 of the length remained untouched for further comparison (Figure 4.6.1a). Monel K500 wire was deposited by cold metal transfer technology using an ABB 1400 robot with a Fronius welder on the machined surface (Figure 4.6.1b and 4.6.2a,b).

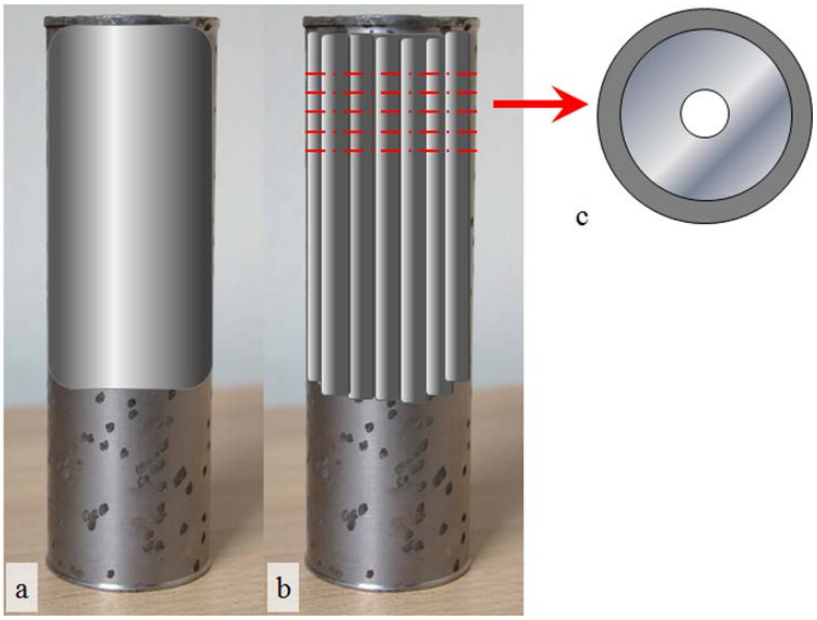

Figure 4.6.1. Schematic diagram of the component repair procedure: (a) machining of 2/3 surface, (b) depositing of the wire, (c) cutting-off cross section for microstructure and mechanical properties investigation.

Geometry of the component's surface resulted in faster cooling rates during wire deposition and the welding parameters tested previously for the plate substrate did not work for a cylindrical substrate (the heat input was too low for a proper wire deposition). Therefore, a higher travel speed was used. The welding parameters were as follows: welding travel speed of 200 mm/min, average current value of 153 A, average voltage of 14.8 V; the resulting average heat input was 679 J/mm. After deposition, 3

mm thick discs were cut perpendicular to the wire deposition to investigate the component-bead interface (Figure 4.6.1c and 4.6.2c).

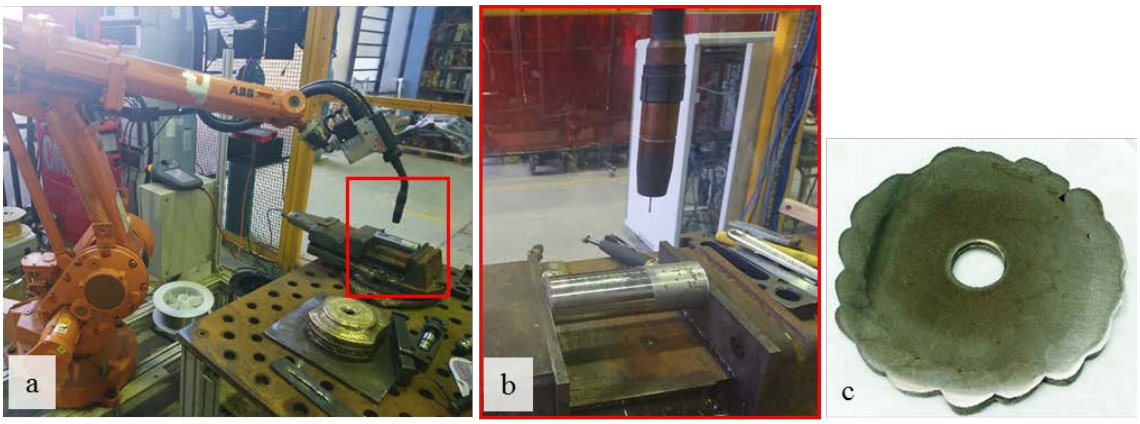

Figure 4.6.2. (a and b) wire-arc deposition of Monel K500 wire on the component surface (c) polished and etched cross section of a component with deposited layer without post-machining.

The following heat treatment conditions have been studied: (i) as-welded/as-received; (ii) annealed at 1100 ºC for 15 minutes, then age-hardened at 610 ºC for 8 hours, followed by air-cooling; (iii) age-hardened at 610 ºC for 8 hours, followed by air-cooling (Figure 4.6.3).

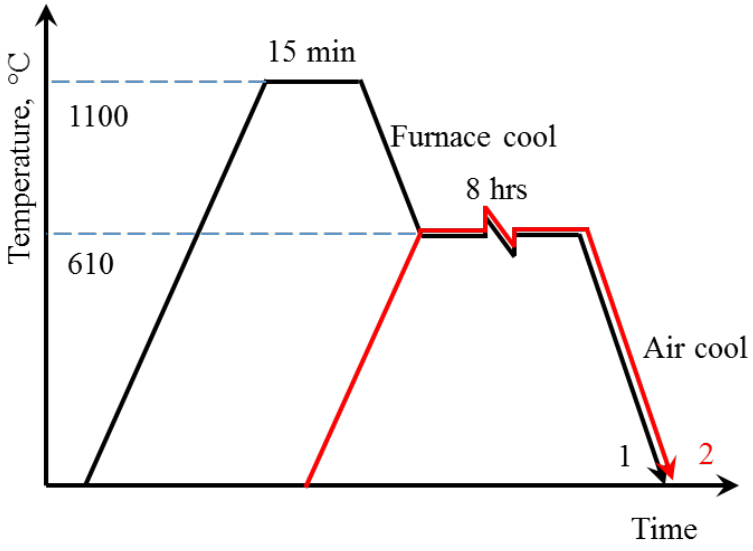

Figure 4.6.3. Heat treatment schedules for the component repair.

Optical microscopy of the repaired component cross section was used to analyse the microstructure of the deposition and base metal (Figure 4.6.4a). Columnar grains in the fusion zone (Figure 4.6.4b), heterogeneous epitaxial grains in the remelted zone (Figure 4.6.4c) and single phase fcc grains in base metal (Figure 4.6.4d) were observed. Small areas of lack of fusion can also be seen.

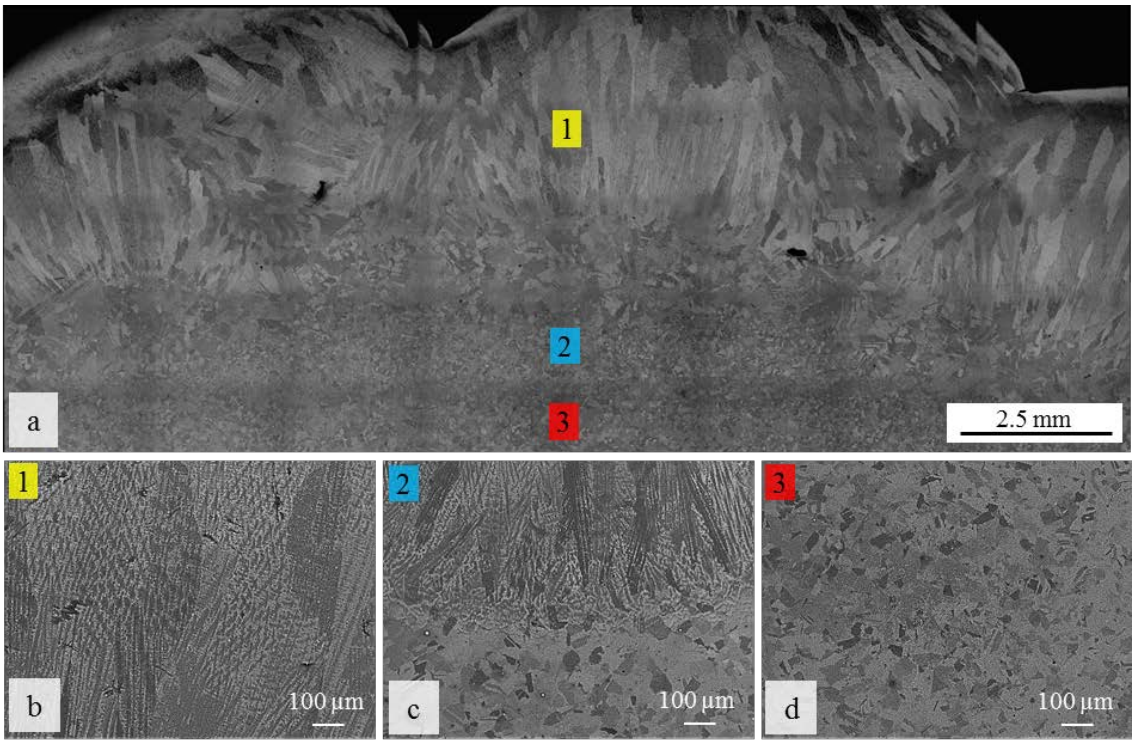

Figure 4.6.4. (a) Optical image of the component cross section with as-deposited layer; SEM images of the (b) fusion zone; (c) remelted and heat affected zone; and (d) component base metal.

4.6.1 Microstructure characterisation of the deposition

The grain size of the deposition, characterised as a space between the secondary dendrite arms, was measured to be 5-15 µm in as-welded and aged at 610 ºC conditions. In annealed + aged at 610 ºC condition it was by 30% larger (Figure 4.6.5 and Table 4.6.1), due to grain growth taking place during annealing.

Energy dispersive X-ray spectroscopy (EDS) of deposition revealed moderate segregation of Cu between the secondary dendrite arms in as-welded and aged at 610 ºC conditions (Figure 4.6.6 b and j). Annealing at 1100 ºC, followed by ageing at 610 ºC removed this segregation (Figure 4.6.6f). No segregation was found in other alloying elements (Figure 4.6.6 d, h and l). The areas around large particles, which were

observed in all previous experiments and looked like a dimple, were found to be caused by Cu segregation. During solidification the particle is pushed out to the last solidifying volume, which is reach in Cu (Ni solidifies first). During preparation, the samples were etched with ferric chloride, which washes out Cu leaving a dimple. This was confirmed by SEM-EDS maps shown in Figures 4.6.8 - 4.6.10: no Cu signal was coming from the area around particles, whereas the Ni signal did come.

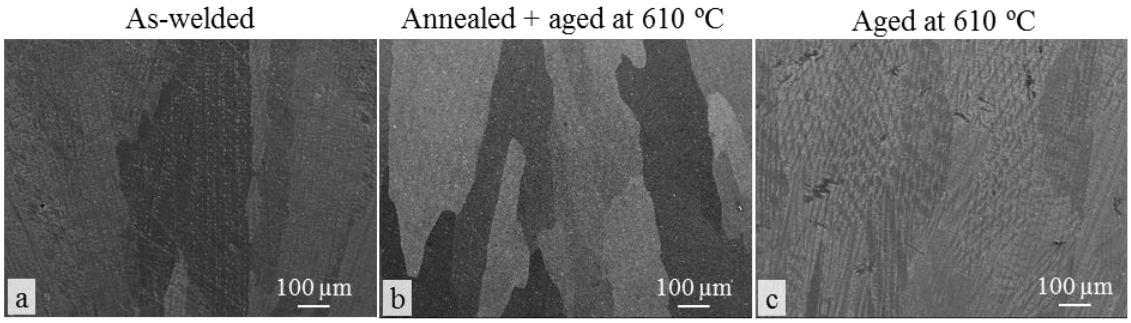

Figure 4.6.5. SEM images showing grain size in the depositions for various heat treatment conditions.

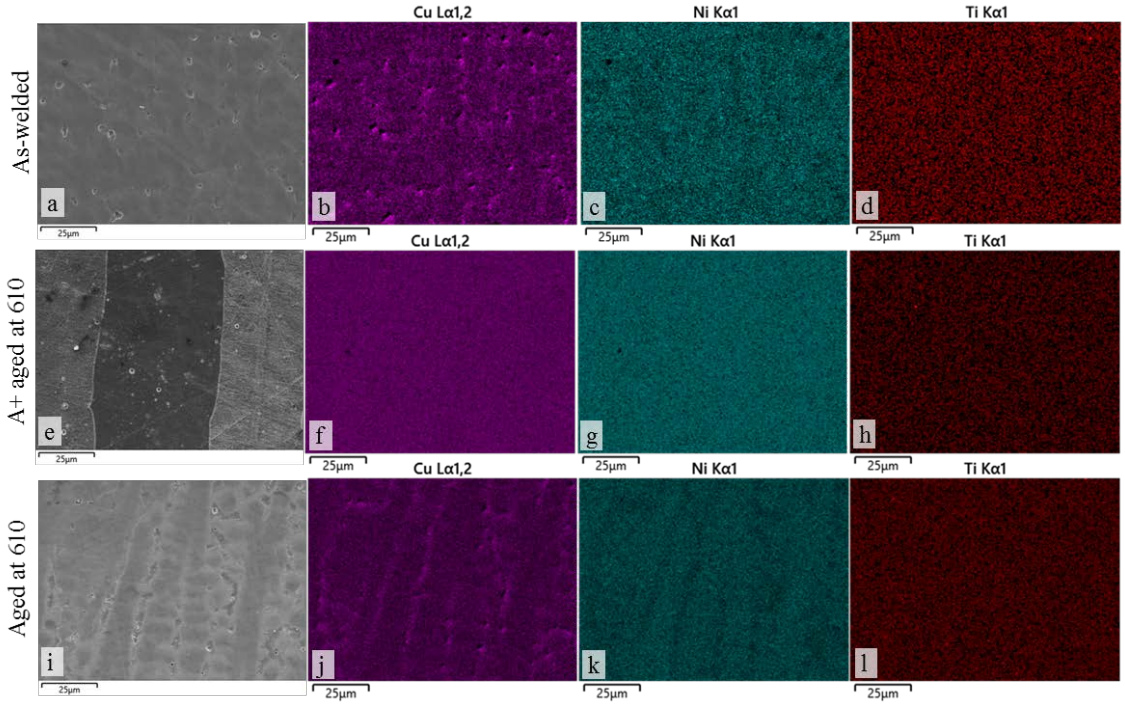

Figure 4.6.6. SEM-EDS elemental maps showing variation in Cu segregation (purple) for various heat treatment conditions in: (a-d) as-welded, (e-h) annealed and aged at 610 ºC, (i-l) aged at 610 ºC conditions.

Spherical and cubic particles were evenly distributed in depositions in all studied heat treatment conditions. In the as-welded condition, particles ranged from 350 to 950 nm in size (Table 4.6.1). In the annealed + aged condition the average particle size decreased by 60%, compared to the as-welded condition, whereas in the aged only condition it remained within the same range as in the as-welded condition. The number density of particles in as-welded and aged at 610 ºC conditions was similar around 4 $x10^{-3}$ μm^{-2}. In the annealed + aged at 610 ºC condition it was by 25% lower (Figure 4.6.7 and Table 4.6.1). In the as-welded condition, particles were of TiCNMgMnSAlO-rich type (Figures 4.6.8), although in the annealed + aged and aged only conditions they were TiCNMgSAlO-rich (Figures 4.6.9 and 4.6.10). All these data indicate that most Mn dissolved during annealing or ageing; this corresponds to the results obtained previously in this work. However, a significant difference in particle precipitation during annealing was observed for these depositions on a cylindrical shape component, compared to the previously studied deposition on plate. Thus, deposition on plate showed an increasing particle number density in SEM size range after annealing, in contrast to a decreasing particle number density observed for the deposition on component. This can be related to a variation in heat input and cooling rates during solidification. If during deposition on plate the cooling rate was slower, it would allow more time for the particle nucleation and growth to <5 nm size; during annealing these particles would grow to those visible in SEM (>20 nm), and an increase in the particle number density during annealing was observed for the deposition on plate. In contrast, in the depositions on a component the cooling rate was faster, particle nucleation did not occur, and during annealing only nucleation and slight growth to <15 nm particle sizes occurred. To prove this theory a more detailed investigation, in particular TEM imaging of particles in deposition on the component is required. This can be done in future.

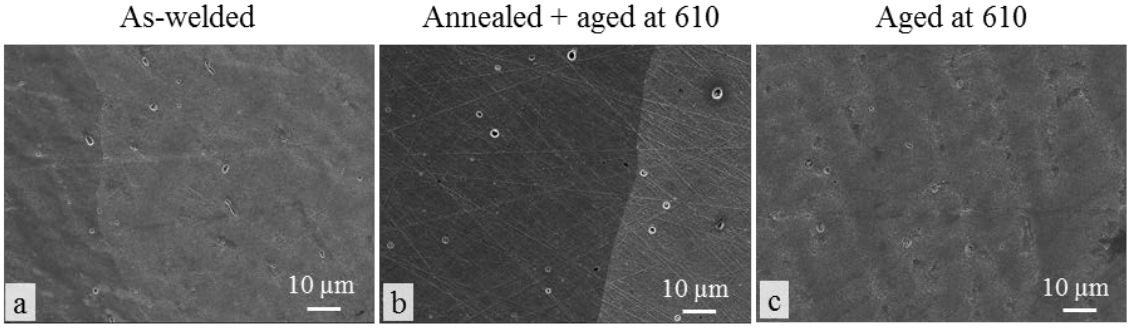

Figure 4.6.7. SEM images showing distribution of particles in the deposition for various heat treatment conditions.

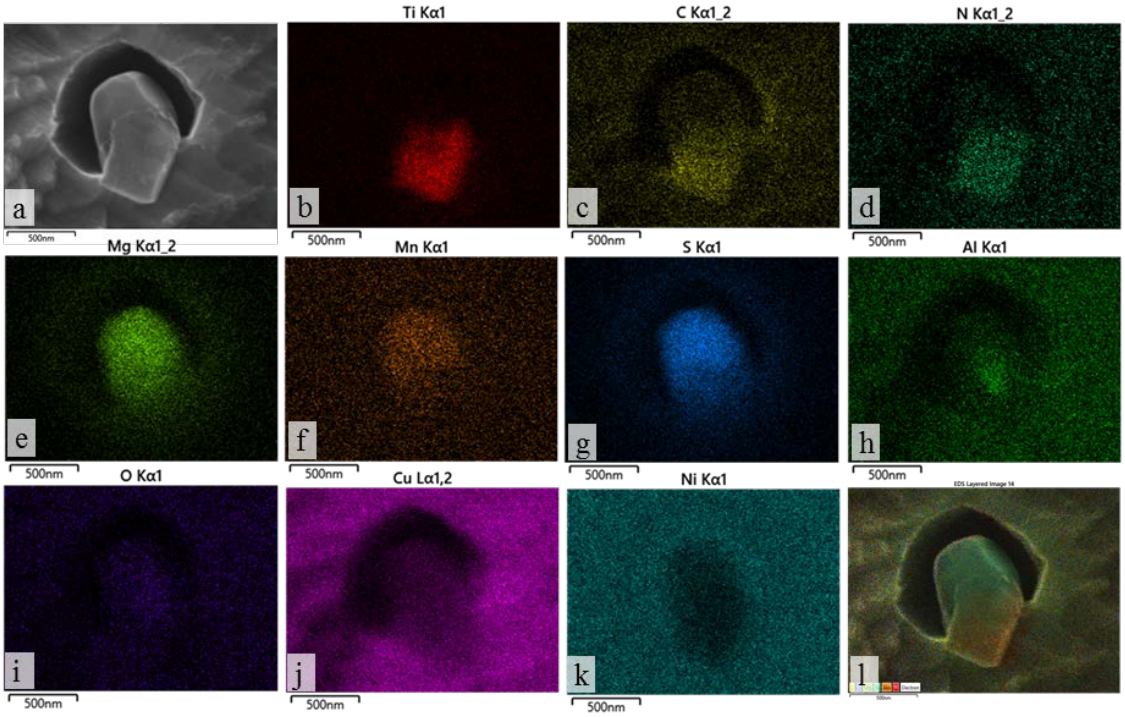

Figure 4.6.8. SEM-EDS elemental maps showing TiCNMgMnSAlO–rich particles in deposition in as-welded condition: (a) representative SEM image of a particle; (b-k) EDS maps of Ti, C, N, Mg, Mn, S, Al, O, Cu and Ni, respectively; (l) EDS elemental overlay.

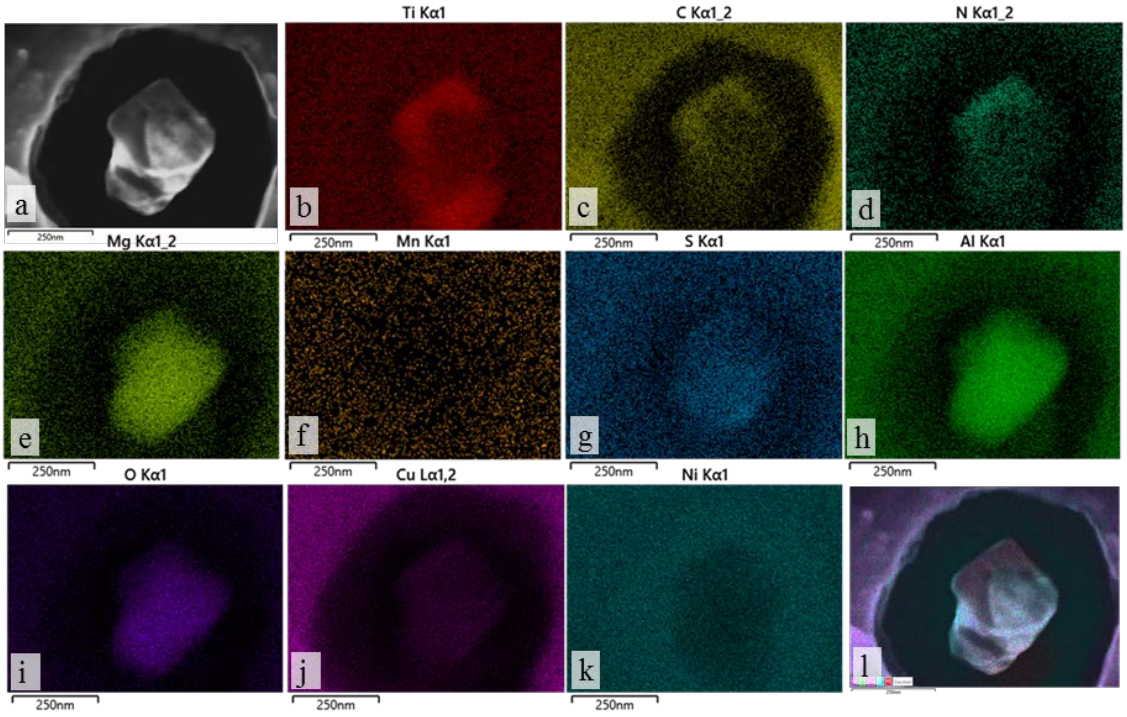

Figure 4.6.9 SEM-EDS elemental maps showing TiCNMgSAlO–rich particles in deposition after annealing and ageing at 610 ºC condition: (a) representative SEM image of a particle; (b-k) EDS maps of Ti, C, N, Mg, Mn, S, Al, O, Cu and Ni, respectively; (l) EDS elemental overlay.

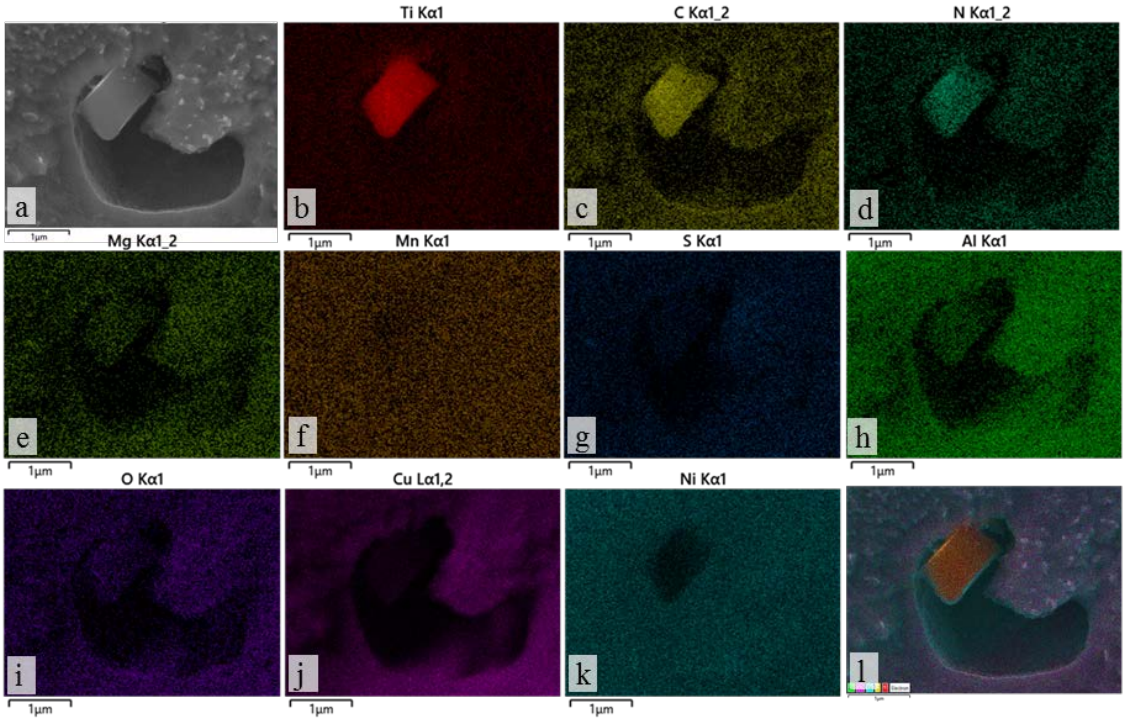

Figure 4.6.10. SEM-EDS elemental maps showing TiCNMgAlO–rich particles in deposition after ageing at 610º C: (a) representative SEM image of a particle; (b-k) EDS maps of Ti, C, N, Mg, Mn, S, Al, O, Cu and Ni, respectively; (l) EDS elemental overlay.

4.6.2 Microstructure characterisation of the component

The microstructure of the as-received Monel K500 component consisted of single phase fcc grains with average size of 48 µm (Figure 4.6.11 and Table 4.6.1). After deposition the grain size in the heat affected zone increased by up to 25 %, the width of heat affected zone was about 0.5 mm. 250-1100 nm particles were distributed in strings along the grain boundaries and across the grains (Figure 4.6.12). The SEM-EDS elemental mapping confirmed the particles to be of TiCN type (Figure 4.6.13).

Annealing followed by ageing has led to the grain growth by 2.5 times, compared to the as-received component (Table 4.6.1). After ageing without annealing, the grain growth was only 35%, compared to the as-received condition, due to a much lower temperature of ageing compared to this of annealing. The particle chemistry did not change during annealing. Although the average particle size and number density both decreased in the annealed + aged condition by 25%, compared to the as-received condition. Obviously, during long

hot processing of the component material the majority of TiC precipitated in the form of large SEM visible particles and the solid solution was depleted in Ti and C. Therefore, no new particles were precipitating in the component during annealing. The average particle size, number density and chemical composition of TiCN particles in the aged only condition did not vary significantly compared to the as-received condition. Although some precipitation of NiAlTi-rich particles is possible during ageing, their sizes would be too small to be visible in SEM.

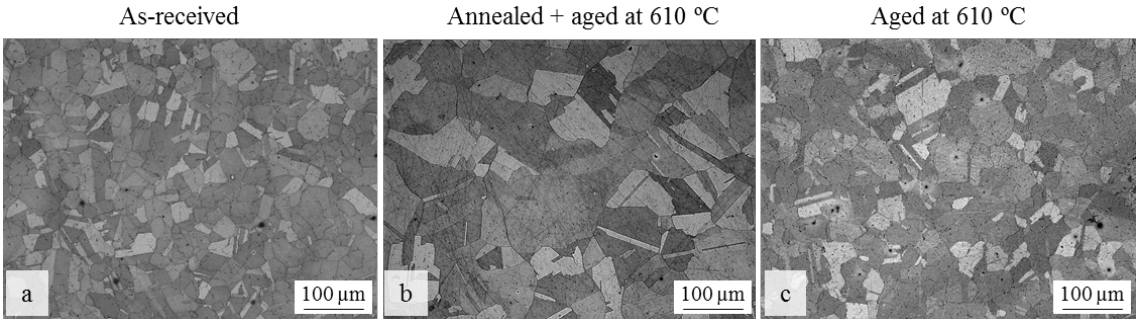

Figure 4.6.11. Optical images showing grain size variation in the component with heat treatment.

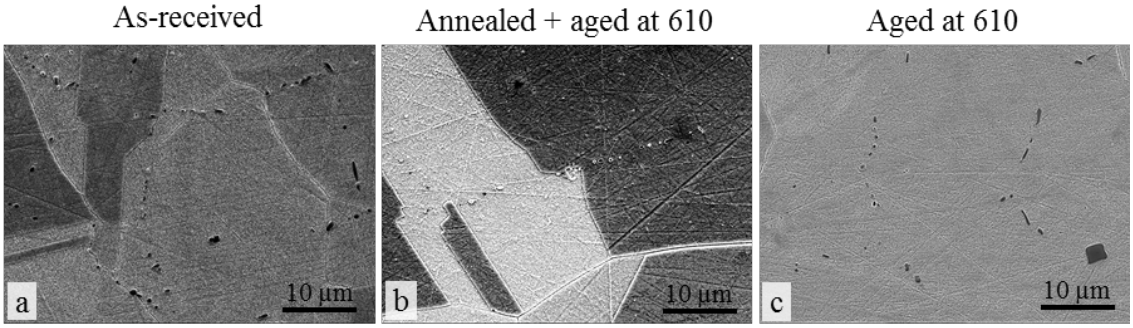

Figure 4.6.12. SEM images showing distribution of particles in the component for various heat treatment conditions.

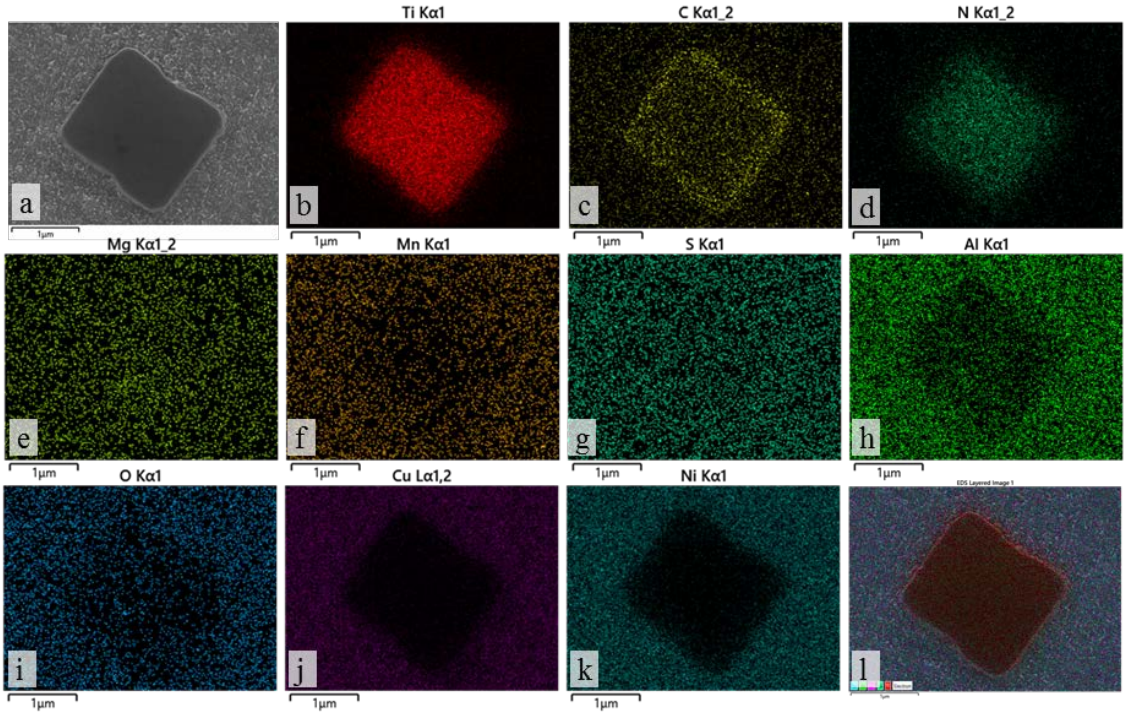

Figure 4.6.13. SEM-EDS elemental maps showing TiCN particle in the as-received component: (a) representative SEM image of a particle; (b-k) EDS maps of Ti, C, N, Mg, Mn, S, Al, O, Cu and Ni, respectively; (l) EDS elemental overlay.

4.6.3 Hardness of deposition and component

The microhardness was measured for deposition and base metal in all heat treatment conditions. The indents were positioned along the line with an interval of 0.5 mm to record the variation in hardness across the bead towards the base metal. Two types of measurement were performed for each condition: perpendicular to the bead, shown in blue arrow in Figure 4.7.14a, and in a place where two neighbouring beads overlap, shown in red arrow in Figure 4.6.14a. The charts in Figure 4.6.14b and c illustrate the hardness variation along the lines shown in Figure 4.6.14a. Both measurements have shown similar hardness profiles. This suggests rather similar properties of the deposition in the component circumference.

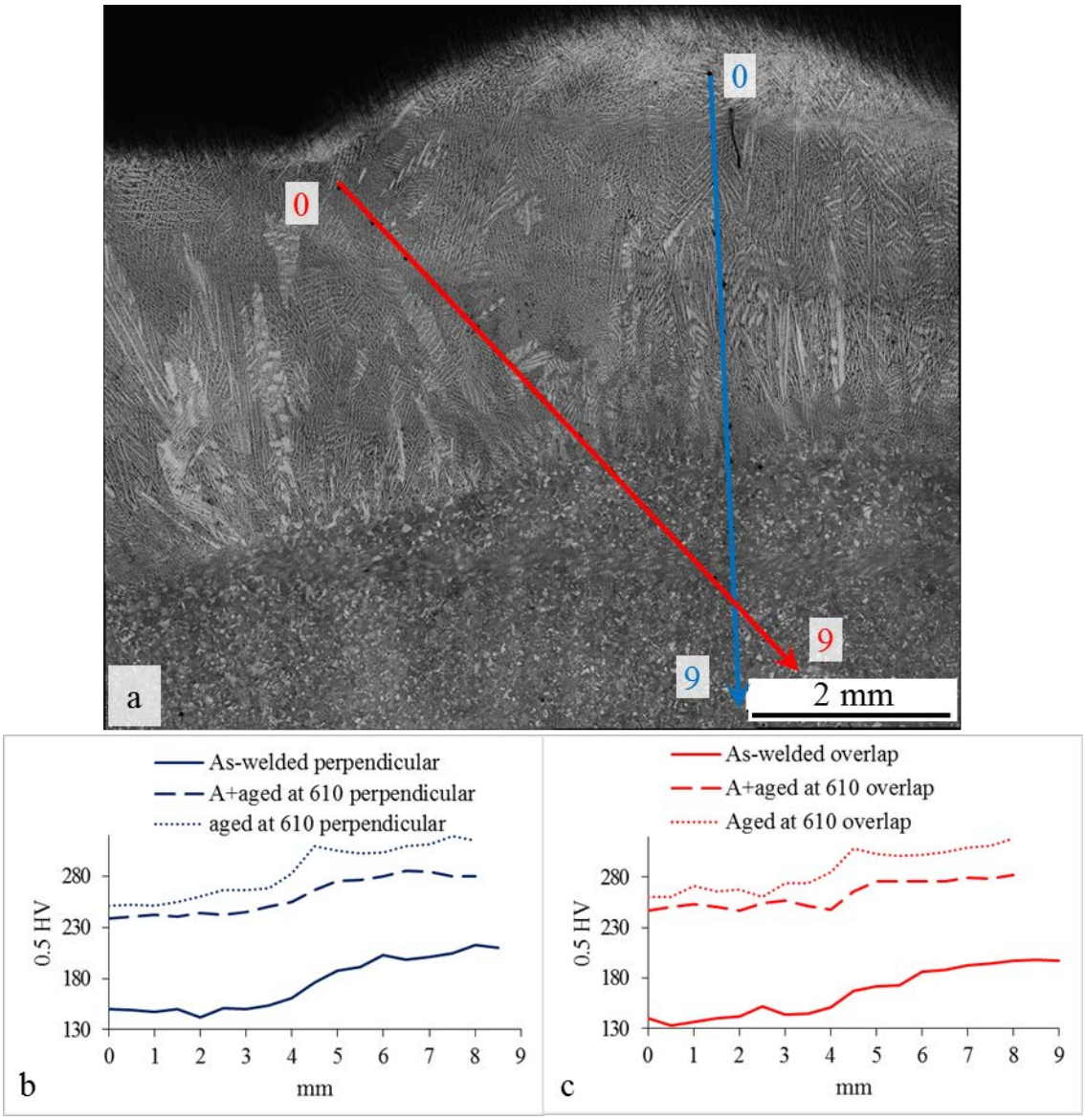

Figure 4.6.14. (a) Hardness variation across welding zones toward the base metal perpendicular to the bead (blue arrow) and in place where two beads overlap (red arrow); hardness variation with heat treatment: (b) perpendicular measurement and (c) bead overlap measurement (the interface deposition-base metal comes to the mark of 4.5 mm).

The average hardness value in the fusion zone of as-welded deposition, 146 HV (Table 4.6.1), is similar to the results obtained previously for the deposition on plate (Table 4.4.1). The hardness of as-received component (198 HV) was higher than this of the deposition, due to the influence of hot deformation on microstructure development in the component. After annealing + ageing the hardness of both deposition and component increased by 65% and 40%, respectively. Although, ageing without annealing resulted in a larger hardness increase compared to the as-welded/as-received

conditions, by 80% and 55% for the deposition and the component, respectively. To a significant extent, this difference originated from a variation in the grain size after annealing+ageing or after aging only. In addition, the fine particle precipitation should be affected by annealing: the <20 nm particle number density (size) may be larger (smaller) after ageing without annealing. The hardness increase after heat treatment most likely resulted from the precipitation of <20 nm TiC and γ′ - $Ni_3(Al,Ti)$ particles.

Table 4.6.1. Microstructural parameters and hardness variation with heat treatment in Monel K500 deposition and component.

Parameter		**Deposition**			**Component**		
		As-welded	Annealed+ aged at 610 ℃	Aged at 610 ℃	As-received	Annealed + aged at 610 ℃	Aged at 610 ℃
SDAS/Grain size, μm		5-15 (avg.* 9)	15-20 (avg. 18)	5-15 (avg. 10)	10-75 (avg. 48)	55-165 (avg. 122)	15-111 (avg. 65)
Particles	size, nm	350-950 (avg. 520)	150-350 (avg. 320)	350-980 (avg. 530)	250-1100 (avg. 560)	140-670 (avg. 450)	250-990 (avg. 550)
	ND* $x10^{-3}$ μm^{-2}	4	3	4	35	28	32
	Chemistry	TiCNMgMnSAlO	TiCNMgSAlO	TiCNMgSAlO	TiCN	TiCN	TiCN
Hardness 0.5HV		146±7	242±4	262±9	198±5	276±7	309±5

*avg. stands for average.

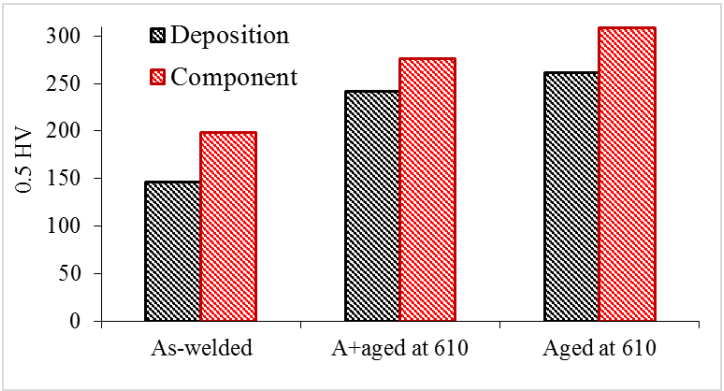

Figure 4.6.15. Difference in hardness between deposition (black) and component (red) for various heat treatment conditions.

The biggest difference in average hardness between the component and deposition was measured to be 52 HV in the as-welded condition (Figure 4.6.15). However, this difference decreased after heat treatment: to 34 HV and 47 HV after annealing + ageing and ageing only, respectively. Due to fast cooling rates during deposition, the matrix in deposition is, probably, more enriched with particle forming elements, compared to the component, which was hot deformed. Therefore, the nano-particle precipitation during heat treatment may be more intensive in the deposition compared to the component, this requires further investigation.

4.6.4 Conclusions to Chapter 4.6

A simulation of repair of a functional component was carried out by WAAM. Monel K500 wire was deposited on top of the machined Monel K500 cylindrical component; after deposition cross sections of the component underwent heat treatment (ageing with and without previous annealing) and the variation of the deposition/base metal microstructure and mechanical properties with heat treatment has been investigated. It has resulted in the following conclusions:

1. In deposited layer, the secondary dendrite arm spacing was by 30% larger in annealed and aged condition, than in as-welded and annealed only conditions, due to grain growth during annealing.

2. Similar size and number density of particles in SEM size range was measured for the as-welded and aged only conditions. Annealing + ageing led to a decrease in the average particle size and number density. However, in our previous investigations, annealing led to a significant increase in particle number density in SEM size range. This could be related to a variation in heat input and cooling rates during solidification when the wire is deposited on either a flat or a cylindrical surface. If during the deposition on a cylindrical component the cooling rate was faster than during deposition on a flat surface, particle nucleation did not occur, thus annealing heat treatment led only to nucleation and slight growth of <15 nm particles, not visible in SEM. A more detailed investigation is required to prove this theory.

3. After wire deposition, a 0.5 mm wide heat affected zone was observed in the component; the grain size in the heat affected zone was up to 25% larger than in the as-received component.

4. Annealing followed by ageing led to the grain growth by 2.5 times, compared to the as-received component. Although after ageing without annealing, the grain growth was only 35%, compared to the as-received condition, due to a much lower temperature of ageing compared to this of annealing.

5. The hardness of both deposition and component increased after annealing + ageing by 65% and 40%, respectively, compared to as-welded/as-received condition. Although, ageing without annealing resulted in a larger hardness increase compared to the as-welded/as-received conditions, by 80% and 55% for the deposition and the component, respectively. The hardness increase after heat treatment most likely resulted from the precipitation of <20 nm TiC and γ′ - Ni3(Al,Ti) particles. The hardness of deposition was by 35%, 14% and 19% lower in the as-welded, annealed + aged and aged only conditions, compared to the base metal of corresponding condition mainly due to the difference in microstructure (cast or deformed).

5. THESIS CONCLUSIONS

Ni-Cu alloys have been fabricated for the first time at the University of Wollongong using wire arc additive manufacturing technology. The technology was tested for two Ni-Cu alloys with various contents of Ti, Mn, Al and C, by depositing them on flat and curved surfaces in shapes of horizontal plates and vertical walls. The wire deposition was carried out using a wide range of welding parameters: torch travel speed from 200 to 500 mm/min, wire feed rate from 5.4 to 10.5 m/min, resulting heat input from 200 to 700 J/mm. To modify solute atom concentrations and particle number density values, the depositions were treated by applying the following procedures: annealing at 1100 °C for 15 min followed by either (i) air cooling to room temperature, (ii) slow cooling to 610 °C, holding for 8 h and air cooling to room temperature, (iii) slow cooling to 610 °C, holding for 8 h, slow cooling to 480 °C, holding for 8 h and air cooling to room temperature or (iv) heating to 610 °C, holding for 8 h and air cooling to room temperature. Microstructure characterisation, in particular a detailed study of the precipitate's parameters (size, number density and chemical composition) and mechanical properties (hardness, tensile testing, wear and corrosion resistance testing) were carried out for as-deposited and heat treated samples.

This research work resulted in the following conclusions:

Depositions on a plate:

1. In the as-welded condition, precipitation of TiC particles in all size ranges was observed in Monel K500, the alloy with a higher C content, rather than in FM60, containing a higher Ti content. In FM60 only minor precipitation of TiC in <10 nm size range took place. The majority of coarse particles in both alloys were TiMnMgAl-rich sulphides and oxides.

2. Heat treatment (annealing followed by age hardening) resulted in a vast precipitation of TiC and Ni_3(Al,Ti) particles in Monel K500. Precipitation of Ni_3(Al,Ti) coincided with substantial (3.0 wt.%) Al content in Monel K500. In contrast, in FM60 age hardening led to only minor increase in the particles number density in all size

ranges. The second ageing at 480 °C could led to the particle coarsening, accompanied by a decrease in the particle number density, in both alloys.

3. Due to precipitation of TiC/TiCN particles and smaller secondary dendrite arm spacing, Monel K500 exhibited a higher hardness, yield stress and tensile strength than FM60 for all the studied conditions. In spite of FM60 elongation being larger in annealed and aged conditions, toughness of Monel K500 was higher due to a higher strength. In accordance with a higher hardness and toughness, the wear resistance of Monel K500 was higher in almost all conditions.

4. In the as-welded condition, the lowest hardness, strength and wear resistance in both alloys were observed for the slowest deposition speed of 300 mm/min. These coincided with the highest particle number density in both alloys. In the annealed and aged conditions, the highest wear resistance (supported by either the highest hardness or strength) in both alloys was obtained at the highest deposition speed of 500 mm/min. These coincided with the low >20 nm particle number density.

5. The strain hardening behaviour of the studied alloys varied with heat treatment condition, and was affected by the dislocation density, size and number density of precipitates, and solid solute concentrations. The lowest strain hardening rate at the end of regime I (following the yield point) was observed in both alloys in annealed condition. This corresponded to the lowest dislocation density after annealing. The highest strain hardening rate was observed after the first ageing in Monel K500, and after the second ageing in FM60. This can be related to the highest number density of <10 nm precipitates, and potentially the highest number of dislocation-particle interaction sites, in Monel K500 and FM60 after the first and second ageing, respectively.

6. Both alloys exhibited ductile fracture behaviour in all studied conditions and decreasing average void size, corresponding to decreasing elongation, with age hardening. This supports transition to a more brittle fracture mode with age hardening in both alloys. However, toughness did not follow the trend for elongation

and void size, i.e. did not decrease with heat treatment, but rather followed the trend for strength.

7. In all heat treatment conditions both Monel K500 and FM60 depositions exhibited passive behaviour with low corrosion rates in 3.5 wt. % NaCl. The value of I_{corr} slightly increased after age hardening, which suggests that these alloys are more susceptible to corrosion in age hardened state.

8. The corrosion behaviour of hot-rolled Monel K500 plate was similar to that observed for both Monel K500 and FM60 depositions in all heat treatment conditions. This indicates that WAAM fabricated parts retain good corrosion resistance typical for conventionally fabricated Monel K500.

Depositions on a cylindrical component:

1. After wire deposition, a 0.5 mm wide heat affected zone was observed in the component; the grain size in the heat affected zone was up to 25% larger than in the as-received component. Annealing followed by ageing led to the grain growth by 2.5 times, compared to the as-received component. Although after ageing without annealing, the grain growth was only 35%, compared to the as-received condition, due to a much lower temperature of ageing compared to this of annealing.

2. In a deposited layer, the secondary dendrite arm spacing was by 30% larger in annealed and aged condition, than in as-welded and annealed only conditions, due to grain growth during annealing.

3. Similar size and number density of particles in SEM size range was measured for the as-welded and aged only depositions. Annealing + ageing led to a decrease in the average particle size and number density. However, in our previous investigations, annealing led to a significant increase in particle number density in SEM size range. This could be related to a variation in heat input and cooling rates during solidification when the wire is deposited on either a flat or a cylindrical surface. If during the deposition on a cylindrical component the cooling rate was faster than

during a deposition on a flat surface, particle nucleation did not occur, thus annealing heat treatment led only to nucleation and slight growth of <15 nm particles, not visible in SEM. A more detailed investigation is required to prove this theory.

4. The hardness of both deposition and component increased after annealing + ageing by 65% and 40%, respectively, compared to as-welded/as-received condition. Although, ageing without annealing resulted in a larger hardness increase compared to the as-welded/as-received conditions, by 80% and 55% for the deposition and the component, respectively. The hardness increase after heat treatment most likely resulted from the precipitation of <20 nm TiC and γ′ - Ni3(Al,Ti) particles. The hardness of deposition was by 35%, 14% and 19% lower in as-welded, annealed + aged and aged only conditions, compared to the base metal of corresponding condition mainly due to the difference in microstructure (cast or deformed).

6. FUTURE WORK

This work present a unique in-depth study of the microstructure and mechanical properties of Ni-Cu alloys, fabricated using wire arc additive manufacturing technology. It also provides recommendations for the optimal welding parameters and subsequent heat treatment. However, this study is only a step forward in understanding the possibilities of wire arc manufacturing technology during fabrication or repair of Ni-Cu alloys and it raises a number of questions and challenges, which need to be answered in the future.

1. The effect of an object shape on thermal history during deposition and mechanical properties of a fabricated component.

It was observed that the value of resulting heat input may be different for different shapes of deposition (single bead, horizontal plate or vertical wall) even when similar welding parameters are used (torch travel speed and wire feed rate). For example, the average heat input during deposition of a plate may be by 50 J/mm and of a wall by 60 J/mm higher than this of a single bead. As a result, the mechanical properties of the fabricated part may be to some extent different depending on the way the part was built up. The variation in properties with the deposition method is likely to be larger in as-deposited condition, although in heat treated components the properties are less dependent on the deposition method. For example, the average hardness in as-deposited wall and plate can be up to 10 HV and 50 HV, respectively, higher than this in a single bead. Although after heat treatment, the hardness of both wall and plate could only be by up to 10 HV higher than this of a single bead. Perhaps a higher heat input during deposition of walls/plates could induce some heat treatment effect leading to precipitation of particles with larger size and number density, than during deposition of beads. However, this effect was not deeply studied here.

2. The effect of a base component shape on thermal history during deposition and mechanical properties of depositions.

It was noticed during the simulation of welding repair procedure (deposition of a wire on a cylindrical surface of the component) that the welding parameters optimised for a wire deposition on a plate did not work for a wire deposition on a cylindrical surface. In order to compensate the fast cooling rate due to the surface curvature of the

component, a lower torch travel speed (higher heat input) was required. Namely, a successful wire deposition on a plate was carried out at a travel speed of 500 mm/min, while for a deposition on a component a travel speed of 200 mm/min was required. Thus, when conducting repair/deposition using WAAM, a base metal surface curvature should be taken into account. A preheat of a component may also be a way to avoid application of a high heat input. This requires further investigation.

3. The effect of annealing stage of heat treatment on microstructure and properties of depositions.

A short investigation of the effect of annealing heat treatment was done during simulation of welding repair of a functional component. The cross section of a component with a deposited layer underwent annealing heat treatment, annealing followed by age hardening and age hardening without annealing. The highest hardness of both depositions and a base metal was observed for the age hardened only sample. The effect of ageing without annealing on other mechanical properties (strength, toughness, wear and corrosion resistance) was not studied here.

4. The effect of heat treatment parameters (holding temperature and time) on microstructure and properties of the studied Ni-Cu alloys.

In this work age hardening at 610 °C for 8 hours showed a positive effect on mechanical properties following precipitation of fine (<10 nm) TiC and Ni_3(Al, Ti) particles. Second age hardening stage at 480 °C for another 8 hours could reduce mechanical properties following the particle coarsening. Optimisation of the heat treatment parameters (holding time during annealing, cooling rate and finish cooling temperature after annealing, age hardening temperature in the 480-610 °C range, and ageing time) to obtain a combination of maximum strength and maximum toughness can be undertaken in the future.

5. Effect of alloying element additions on microstructure and properties of Ni-Cu alloys fabricated using WAAM.

Increased C and Al contents in the studied Ni-Cu alloys have been shown to increase strength via precipitation of TiC and Ni_3(Al, Ti) particles. However, the solution strengthening effect of Ti, Mn and Fe was not studied, although may be significant.

References

[1] Nickel 200 and 201, Special Metals Corporation, SMC-061 (2006), www.specialmetals.com, accessed 15.05.2019.

[2] High-Performance Alloys for Resistance to Aqueous Corrosion, The Monel Ni-Cu products, Special Metals Corporation, SMC-026 (2000).

[3] T.H. Bassford, J. Hosier, Nickel and its Alloys, in: M. Kutz (Ed.), Handbook of materials selection, Wiley, New York (2002).

[4] J.C. Lippold, J. DuPont, and S.D. Kiser, Welding Metallurgy and Weldability of Nickel-Base Alloys, Chapter 1. Introduction, Hoboken, NJ. USA: John Wiley & Sons (2009), p.1-15.

[5] J.R. Davis, Nickel, Cobalt, and Their Alloys. Chapter 1. Introduction to Nickel and Nickel Alloys, Technology & Engineering, ASM Specialty handbook, ASM International, Materials Park, OH 44073, USA (2000).

[6] R.W. Kozar, A. Suzuki, W.W. Milligan, J.J. Schirra, M.F. Savage, and T.M. Pollock, Strengthening Mechanisms in Polycrystalline Multimodal nickel-base alloys, The Minerals, Metals and Materials Society and ASM International, Metallurgical and Materials Transactions A, Vol.40A (2009), p. 1588-1603.

[7] J.C. Lippold, J. DuPont, and S.D. Kiser, Welding Metallurgy and Weldability of Nickel-Base Alloys, Chapter 2. Alloying additions, Phase diagrams and Phase stability, Hoboken, NJ. USA: John Wiley & Sons (2009), p.15-45.

[8] C. Czajkowski, M.Butters, Investigation in hardsurfacing a Nickel-Copper alloy (Monel 400), Formal report, Brookhaven National laboratory, Upton, NY, USA (2001).

[9] R.W. Heckel, J.H. Rickets, and J. Buchwald, Measurement of the degree of segregation in Monel 400 weld metal by X-ray line broadening, Welding Journal, 34(7) (1965), pp. 332-336.

[10] Margot Gayle, David Look, John Waite. Metals in America's Historic Buildings. Washington, DC: National Park Service (1995). Available from: http://www.gsa.gov/portal/content/113038, accessed 21.09.2016.

[11] Product handbook of high performance Ni alloys, published by Special Metals, Copyright © Special Metals Corporation, www.specialmetals.com, accessed 15.05.2019.

[12] All metals and Forge Group, ISO 9001:2008 and AS9100C manufacturer, http://www.steelforge.com, accessed 21.09.2016.

[13] E.W. Ross, C.T. Sims, Nickel-base alloys, Superalloys II – High Temperature Materials for Aerospace and Industrial Power, ASM International, Materials Park, OH, (1987), pp. 97-133.

[14] J.C. Lippold, J. DuPont, and S.D. Kiser, Welding Metallurgy and Weldability of Nickel-Base Alloys, Chapter 4. Precipitation-strengthened Nickel-base alloys, Hoboken, NJ. USA: John Wiley & Sons (2009), p. 157-254.

[15] Henan ZZHN & Steel Co., Ltd, http://www.vankernhem.nl, accessed 05.05.2019.

[16] Monel alloy 400 (UNS N04400). Ni 66.5 Cu 31.5. Description, High Performance Alloys, Inc., 2014, http://www.hpalloy.com/Alloys/descriptions/MONEL400.html, accessed 21.09.2016.

[17] Monel Alloy 400, Special Metals, SMC-053, New Hartford, NY, USA, 2005, www.specialmetals.com, accessed 15.05.2019.

[18] Monel Alloy 401, Special Metals, SMC-084, New Hartford, NY, USA, 2004, www.specialmetals.com, accessed 15.05.2019.

[19] Monel Alloy 404, SMC-059, New Hartford, NY, USA, 2004, www.specialmetals.com, accessed 15.05.2019.

[20] Monel Alloy R-405, Special Metals, SMC-085, New Hartford, NY, USA, 2004, www.specialmetals.com, accessed 15.05.2019.

[21] Monel alloy R-405 (UNS N04405), Description, High Performance Alloys, Inc., 2014, http://www.hpalloy.com/alloys/descriptions/MONELR_405.aspx, accessed 21.09.2016.

[22] Z.X. Wang, S. Liu, S. Yuan, C. Yang, Strength and ductility of Ni-Cu-Base alloy Monel K-500, Transactions of NFsoc 5(1), (1995), p.111-115.

[23] Monel Alloy K-500, Special Metals, SMC-062, New Hartford, NY, USA, (2004), www.specialmetals.com, accessed 15.05.2019.

[24] Monel alloy K-500 (UNS N05500), Description, High Performance Alloys, Inc., 2014, http://www.hpalloy.com/Alloys/descriptions/MONELK_500.aspx, accessed 21.09.2016.

[25] Alloy K-500, Data Sheet, Corrosion Materials, CM022-06, www.corrosionmaterials.com, accessed 21.09.2016.

[26] www.hofmannengineering.com, accessed 21.09.2016.

[27] maritime.org, accessed 21.09.2016.

[28] www.gcc-engr.com, accessed 21.09.2016.

[29] N.S. Stoloff, Wrought and P/M superalloys, ASM Handbook, Volume 1, ASM International, Materials Park, OH, USA (1990), pp. 950-980.

[30] R.B. Brooks, Heat treatment, structure and properties of nonferrous alloys, ASM international, Materials Park, OH (1982), p.145.

[31] C. Barbosa, J.L. Nascimento, I.M.V. Caminha, I.C. Abud, Microstructural aspects of the failure analysis of nickel-base superalloys components, Engineering Failure Analysis 12(3) (2005) 348-361.

[32] L. Krishna Reddy, Principles of Engineering Metallurgy, New Age International, New Delhi, India (2007), p. 260.

[33] G.K. Dey, P. Mukhopadhyay, Precipitation in the Ni-Cu-base alloy Monel K-500, Materials Science and Engineering, 84 (1986) pp. 177-189.

[34] R.W. Breitzing, Forming of Nickel-base alloys, Forming and forging, Vol. 14, ASM Handbook, ASM International (1988), pp. 831-837.

[35] www.forgemag.com, accessed 20.01.2016.

[36] Federal specification, Nickel-Copper-Aluminium Alloy, Wrought (UNS N05500), (2000), p.43.

[37] www.bonpertuis-steel.com, accessed 20.01.2016.

[38] J. D. Hurlbatt, Hot rolling of sheet: nickel-based alloys, Materials Science and technology, Volume 2, Issue 1 (1975), pp. 326-330.

[39] J.R. Davis, Nickel, Cobalt, and Their Alloys, Chapter 3. Fabrication and finishing of Nickel alloys, Heat treating of nickel alloys, Technology & Engineering, ASM Specialty handbook, ASM International, Materials Park, OH, USA (2000).

[40] Fabrication of Nickel alloys, Special Metals Corporation, Huntington, Vest Virginia, USA, www.specialmetals.com, accessed 15.05.2019.

[41] M. di Giovanni, Flat and corrugated diaphragm design handbook, Ametek Controls Division, Feasterville, Pensilvania, Marcel Dekker, Inc., New York (1982).

[42] http://mechanical-engg.com, accessed 20.01.2016.

[43] Ya. S. Gallai, E. G. Karmanova, N. A. Zorina, M. M. Grigor'eva, Cold working and recrystallization of nickel alloys, Metal Science and Heat Treatment, Volume 9, Issue 4, (1967), pp. 323-324.

[44] www.connection-mag.com, accessed 20.01.2016.

[45] Mechanical engineers' handbook by Myer Kutz, Volume 1, Nickel and its alloys, Gaylord D. Smith, Brian A. Baker, Materials and Engineering Mechanics, John Wiley and Sons, Inc., Hoboken, New Jersey, USA (2015).

[46] Heat treating of Nickel and Nickel alloys, Total Materia, http://www.totalmateria.com/Article32.htm, accessed 20.01.2016.

[47] Monel K-500 Material Property Data, Metal Suppliers Online, Inc., http://www.suppliersonline.com/propertypages/monelk500.asp, accessed 20.01.2016.

[48] Machining of Nickel Alloys, bulletin, Special Metals Corporation, Huntington, Vest Virginia, USA.

[49] Machining Nickel and Nickel Alloys (Including Monel, Kovar, Inconel and Incoloy), Rensselaer Hartford Libraries, http://www.ewp.rpi.edu, accessed 20.09.2016.

[50] G.K. Dey, R. Tewari, P. Rao, S.L. Wadekar, P. Mukhopadhyay, Precipitation hardening in nickel-copper base alloy Monel K-500, Metallurgical and materials Transactions A (1993), p. 2709-2719.

[51] A. Guinier, X-ray diffraction in crystals, imperfect crystals, and amorphous bodies, San Francisco (CA), W.H. Freeman, San Francisco, CA, USA, (1963).

[52] J.H.Ai, H. M. Ha, R.P. Gangloff, J.R. Scully, Hydrogen diffusion and trapping in a precipitation-hardened nickel-copper-aluminum alloy Monel K-500 (UNS N05500), Acta Materialia 61 (2013) p. 3186-3199.

[53] C.T. Liu, J.O. Stiegler, F.H. Froes, Ordered intermetallics, ASM Handbook, Vol.2, Properties and selection: nonferrous alloys and special-purpose materials, ASM International, Materials Park, OH (1990), pp. 913-942.

[54] I.M. Lifshitz, V.V. Sloyozov, The kinetics of precipitation from supersaturated solid solutions, Journal of Physical Chemistry of Solids, 19 (1-2) (1961) pp. 35-50.

[55] W.C. Hagel, H.J. Beattie, Jr., High-temperature aging structures in gamma prime-hardened austenitic alloys, Trans. Met. Soc. AIME; Journal Volume: Vol: 215 (1960).

[56] Wrought Nickel-Copper Alloys, Publ. 4236, International Nickel Ltd., London, UK (1970).

[57] C.T. Sims and W.C. Hagel (eds.), The Superalloys, John Wiley & Sons, New York, USA, 1972, pp.145-174.

[58] A.J. Ardell, R.B. Nicholson, J.D. Eshelby, On the modulated structure of aged Ni-Al alloys (with an appendix on the elastic interaction between inclusions), Acta Metallurgica 14 (1966) p. 1295-1309.

[59] D.H. Ben Israel, M.E. Fine, Precipitation studies in Ni-10 at.% Ti, Acta Metallurgica, 11 (1965), p. 1051-1059.

[60] R. F. Dekker, C. T. Sims, in C. T. Sims and W. C. Hagel (eds.), The Superalloys, Wiley, New York, USA (1972), p. 33.

[61] M. Hansen and K. Anderko, Constitution of Binary Alloys, McGraw-Hill, New York, USA (1958).

[62] P.H. Thornton, P.H. Davies, and T.L. Johnston, Temperature dependence of the flow stress of the gamma prime phase based upon Ni_3Al, Metallurgical Transactions A, 1(1) (1970), pp. 207 – 218.

[63] H.Ed. Baker, Alloy phase diagrams, ASM International, Materials Park, OH, USA (1992).

[64] J.N. DuPont, C.V. Robino, A.R. Marder, M.R. Notis, and J.R. Michael, Solidification of Nb-Bearing Superalloys: Part I. Reaction Sequences, Metallurgical and Material Transactions A, 29A (1988), pp. 2785 – 2796.

[65] L.E Murr, P.J. Smith, C.M. Gilmore, Relative interfacial free energies in pure nickel, dispersion hardened nickel and a precipitation-hardened nickel-base alloy, Philosophical Magazine A, 17 (1968), pp. 89-106.

[66] P.C.J. Gallagher, The influence of alloying, temperature, and related effects on the stacking fault energy, Metallurgical Transactions, Vol.1, issue 9 (1970), pp. 2429-2461.

[67] P.S. Kotval, Identification of the strengthening phase in “Inconel” alloy 718, Trans. AIME, Vol. 242 (1968), pp. 1764-1765.

[68] I.L. Dillamore, The stacking fault energy dependence of the mechanisms of deformation in fcc metals, Metallurgical Transactoins, Vol. 1 (1970), pp. 2463-2470.

[69] L. Delehouzce and A. Deruyttere, The stacking fault density in solid solutions based on silver, nickel, aluminium and lead, Acta Metallurgy, Vol. 15 (1967), pp. 727-734.

[70] R. W. Kozar, A. Suzuki, W. W. Milligan, J. J. Schirra, M. F. Savage and T. M. Pollock, Strengthening mechanisms in polycrystalline multimodal nickel-base superalloys, Metallurgical and Materials Transactions 40A (2009), pp 1588-1603.

[71] J.P Hirth, The influence of grain boundaries on mechanical properties, Metallurgical Transactions, Vol. 3 (1972), pp 3047-3067.

[72] G.T. Gray III, Shuh Rong Chen, Kenneth S. Vecchio, Influence of grain size on the constitutive response and substructure evolution of Monel 400, Metallurgical and Materials transactions, 30 A (1999), p. 1235-1247.

[73] E.R. Parker and T.H. Hazlett, Principles of solution hardening. 12th Technical report, University of California, Berkley, CA, USA (1953), p.30.

[74] Lippold, John C., DuPont, John, and Kiser, Samuel D., Welding Metallurgy and Weldability of Nickel-Base Alloys, Chapter 3. Solid-solution strengthened Ni-base alloys, Hoboken, NJ. USA: John Wiley & Sons (2009) p. 45-156.

[75] R.F. Decker and J.R. Mihalisin, Coherency strains in gamma prime hardened nickel alloys, Transactions of ASM quarterly, 62 (1969), p. 481-489.

[76] R.B. Brooks, Heat treatment, structure and properties of nonferrous alloys, ASM International, Materials Park, OH, p. 145, 1982, p.430.

[77] W. Huther and B. Reppich: Z. Metallkd, Interaction of dislocations with coherent, stress-free, ordered particles, Vol. 69 (1978), p. 628-34.

[78] P.H. Thorton, P.H. Davies and T.L. Johnson, Temperature dependence of the flow stress of the gamma prime phase based upon Ni_3Al, Metallurgical Transactions A, 1 (1970), p. 207-218.

[79] V. Biss and D.L. Sponseller, Effect of molybdenum on gamma prime coarsening and on elevated-temperature hardness in some experimental Ni-base superalloys, Metallurgical Transactions A, 4 (1973), p. 1953-1960.

[80] R.W. Guard and J.H. Westbrook, Transactions of the Metallurgical society of AIME, 215 (1959), p. 807-816.

[81] C.R. Brooks, Nickel base alloys, in heat treatment, structure and properties of nonferrous alloys, ASM International, Materials Park, OH, USA (1982).

[82] V. Martens and E. Nembach, Strengthening of the Nimonic alloy PE 16 by ordered particles of Ni_3(Al, Ti), Acta Metallurgica, vol. 23 (1975), p. 149-53.

[83] C.H. Greenall and G.R. Gohn, Fatigue properties of non-ferrous sheet metals, Proceedings of American Society for Testing materials, Vol. 37, 2 (1937), p. 160-194.

[84] S. Kiser, Nickel alloy consumable selection for severe service conditions, Welding Journal, 69(11) (1990), p. 30 – 35.

[85] Review of the wear and galling characteristics of stainless steels, A designers' handbook series, Committee of stainless steel producers. American Iron and steel Institute (1978).

[86] M. Marya, V. Singh, Y. Lu, Transition microstructures and properties in the laser additive manufacturing repair of Monel K-500 (UNS N05500) and Tougmet 3AT (UNS C72900), Annual Meeting Supplemental Proceedings TMS, The Minerals, Metals and Material Society (2015), p.413.

[87] Galling. Wikipedia, https://en.wikipedia.org/wiki/Galling, accessed 21.09.2016.

[88] www.ptonline.com, accessed 21.09.2016.

[89] I. Gibson, D. W. Rosen and B. Stucker, Additive manufacturing technologies: rapid prototyping to direct digital manufacturing, Springer 1, 17 (2010).

[90] D. D. Gu, W. Meiners, K. Wissenbach, R. Poprawe, Laser additive manufacturing of metallic components: materials, processes and mechanisms, Institute of Materials, Minerals and Mining and ASM International. Maney, International Materials Reviews 57(3), (2012).

[91] X. He, G. Yu and J Mazumder, Temperature and composition profile during double-track laser cladding of H13 tool steel, Journal of Physics D: Applied Physics, 43(1), (2010).

[92] A. Manthiram, D.L. Bourell, and H.L. Marcus, Nanophase materials in solid freeform fabrication, Journal of materials science, 45 (11) (1993), p. 66–70.

[93] J. P. Kruth, X. Wang, T. Laoui and L. Froyen, (2003) Lasers and materials in selective laser sintering, Assem. Autom., 23 (2003), p. 357–371.

[94] M. Giacomantonio, S. Gulizia, M. Jahedi, Y. Wong, R. Moore, M. Valimberti, Heat treatment of thermally sprayed Ni-based wear and corrosion coatings, Materials forum volume 35 (2011).

[95] G. Irons et al., Thermal spray alternatives for electroplated chromium, Proceedings of the Ninth National Thermal Spraying Conference (1996), p. 39-48.

[96] J.C. Tan, L. Looney, M.S.J. Hashmi, Component repair using HVOF thermal spraying, Materials Journal of Materials Processing Technology 92-93 (1999), p. 203-208.

[97] D.C. Crawmer et al., Coating development of HVOF process using design of experiments, Proceedings of the 13th International Thermal Spraying Conference, Florida (1992), p. 127-136.

[98] HVOF, http://www.fst.nl/hvof, accessed 21.09.2016.

[99] Brochure of HVOF Spray System, Miller Thermal Inc. (1988).

[100] X.C. Zhang, B.S. Xu, Y.X. Wu, F.Z. Xuan and S.T. Tu, Porosity, mechanical properties, residual stresses of supersonic plasma-sprayed Ni-based alloy coatings prepared at different powder feed rates, Applied surface science, vol. 254 (2008), p.3879-3889.

[101] J. Tuominen, P. Vuoristo, T. Mantyla, S. Ahmaniemi, J. Vihinen and P. Andersson, Corrosion behaviour of HVOF-sprayed and Nd-YAG laser-remelted high-chromium, nickel-chromium coatings, Journal of Thermal spray technology, vol. 11 (2002), p. 233-243.

[102] B. Dutta, V. Singh, H. Natu, J. Choi and J. Mazumder, Direct metal deposition, Advanced Materials Processing, 167 (2009), p. 29–31.

[103] R.P. Mudge and N. R. Wald, Laser engineered net shaping advances additive manufacturing and repair, Welding Journal, 86 (2007), p. 44–48.

[104] http://www.eagle-group.eu/en/laser-deposition, accessed 21.09.2016.

[105] M. Agarwala, D. Bourell, J. Beaman, H. Marcus and J. Barlow, Direct selective laser sintering of metals, Rapid Prototyping Journal, Vol. 1, No. 1 (1995), p. 26–36.

[106] S. Das, M. Wohlert, J. J. Beaman, and D. L. Bourell, Processing of titanium net shapes by SLS/HIP, Materials Design, vol. 20 (1999), p. 115–121.

[107] S. Kumar and J. P. Kruth: Selective laser sintering: a qualitative and objective approach. Journal of materials science, 55 (2003), p. 43–47.

[108] M. L. Griffith, M. E. Schlienger, L. D. Harwell, M. S. Oliver, M. D. Baldwin, M. T. Ensz, M. Essien, J. Brooks, C. V. Robino, J. E. Smugeresky, W. H. Hofmeister, M. J. Wert and D. V. Nelson, Understanding thermal behavior in the LENS process, Materials Design, 20 (1999), p. 107–113.

[109] L. Qian, J. Mei, J. Liang and X. Wu, Influence of position and laser power on thermal history and microstructure of direct laser fabricated Ti-6A1-4V samples, Materials Science and Technology, 21 (2005), p. 597–605.

[110] P. Pratt, S. D. Felicelli, L. Wang and C. R. Hubbard, Residual stress measurement of LENS AISI 410 thin plates using neutron diffraction, Metall. Mater. Trans. A, 39A (2008), p. 3155–3163.

[111] M. Marya, V. Singh, Y.Lu, J.-Y. Hascoet and S. Marya, Transition Microstructures and Properties in the Laser Additive Manufacturing Repair of Monel K-500 (UNS N05500) and Toughmet 3 AT (UNS C72900), The Minerals, Metals & Materials Society, TMS2015 Supplemental Proceedings (2015).

[112] R. Acheson, Automatic welding apparatus for weld build-up and method of achieving weld build-up, US patent no. 4 952 769 (1990).

[113] D. Ding, Z. Pan, D. Cuiuri, H. Li, Wire-feed additive manufacturing of metal components: technologies, developments and future interests, Int. J. Adv. Manuf. Tech., 81 (2015), p. 465-481.

[114] Y. Ma, D. Cuiuri, C. Shen, H. Li, Z. Pan, The effect of location on the microstructure and mechanical properties on in-situ alloying and additive layer manufacturing of titanium aluminides using gas tungsten arc welding, Mater. Sci. Eng. A, 631 (2015), p. 230–240.

[115] D. Ding, Z. Pan, D. Cuirui, H. Li, A practical path planning methodology for additive manufacturing of thin-walled structures. Robot. Com-Int. Manuf., 34 (2015), p. 8–19.

[116] F. Martina, J. Mehnen, S.W. Williams, P.A. Colegrove, F. Wang, Investigation of the benefits of plasma deposition for the additive layer manufacture of Ti–6Al–4V, J. Mater. Process. Technol., 212 (2012), p. 1377–1386.

[117] S. W. Williams, F. Martina, A. C. Addison, J. Ding, G. Pardal, P. Colegrove, Wire + Arc Additive Manufacturing, Materials Science and Technology, 32 (2016), p. 641-647.

[118] Joining of Nickel Alloys, Special Metals Corporation, Huntington, Vest Virginia, USA, www.specialmetals.com, accessed 15.05.2019.

[119] Requirements, Procedure and Inspection for Weld Repair of Copper Alloy Nickel Alloy Castings, Ministry of Defence, Defence Standard 02-771 (NES 771), 1 (2000).

[120] http://www.deloro.de, accessed 21.09.2016.

[121] http://www.stellite.com, accessed 21.09.2016.

[122] Guidelines for the welded fabrication of Nickel alloys for corrosion-resistant service, A Nickel Development Institute Reference book, Series N 11012, (1994).

[123] B. Wu, D. Ding, Z. Pan, D. Cuiuri, H. Li, J. Han, Z. Fei, Effects of heat accumulation on the arc characteristics and metal transfer behavior in Wire Arc Additive Manufacturing of Ti6Al4V, J. Materials Processing Technology, 250 (2017), p. 304-312.

[124] F. Wang, S. Williams, M. Rush, Morphology investigation on direct current pulsed gas tungsten arc welded additive layer manufactured Ti6Al4V alloy, The International Journal of Advanced Manufacturing Technology, 57 (2011), p. 597–603.

[125] C.V. Haden, G. Zeng, F.M. Carter III, C. Ruhl, B.A. Krick, D.G. Harlow, Wire and arc additive manufactured steel: tensile and wear properties. Additive Manufacturing, 16 (2017), p. 115-123.

[126] C. Shen, Z. Pan, D. Cuiuri, D. Ding, H. Li, Influences of deposition current and interpass temperature to the Fe3Al-based iron aluminide fabricated using wire-arc additive manufacturing process, The International Journal of Advanced Manufacturing Technology, 88 (2017), p. 2009-2018.

[127] B. Cong, J. Ding, S. Williams, Effect of arc mode in cold metal transfer process on porosity of additively manufactured Al-6.3%Cu alloy, The International Journal of Advanced Manufacturing Technology, 76 (2015), p. 1593-1606.

[128] D. Ding, Z. Pan, S. van Duin, H. Li, C. Shen, Fabricating superior NiAl Bronze components through wire arc additive manufacturing, Materials, 9 (2016), p.652.

[129] F.J. Xu, Y.H. Lv, B.S. Xu, Y.X. Liu, F.Y. Shu, P.He, Effect of deposition strategy on the microstructure and mechanical properties of Inconel 625 superalloy fabricated by pulsed plasma arc deposition, Materials Design 45 (2013), p. 446-455.

[130] B. Baufeld, Mechanical properties of Inconel 718 parts manufactured by shaped metal deposition (SMD), Journal of Materials Engineering and Performance, 21 (2012), p.1416-1421.

[131] S.J.Kim, K.M.Ryu, M.Oh, Addition of cerium and yttrium to ferritic steel weld metal to improve hydrogen trapping efficiency, International Journal of Minerals, Metallurgy and Materials, Vol. 24:4 (2017), p. 415-422.

[132] L. Karlsson, L.-E. Svensson, K. Hurti, Influence of dilution on properties of high strength steel weld metals, Biuletyn Instytutu Spawalnictwa, 5 (2014), p. 62-71.

[133] J. Strid, K.E. Easterling. On the chemistry and stability of complex carbides and nitrides in microalloyed steels, Acta Metallurgica, 33 (1985), p. 2057-2074.

[134] R.D.K. Misra, H. Nathani, J.E. Hartmann, F. Siciliano, Microstructural evolution in a new 770MPa hot rolled Nb-Ti microallyed steel, Materials Science Engineering A, 394 (2005), p. 339-352.

[135] M. G. Akben, T. Chandra, P. Plassiard, J.J. Jonas, Dynamic precipitation and solute hardening in a titanium microalloyed steel containing three levels of manganese, Acta Metallurgica, 32(4) (1984), p. 591-601.

[136] Z. Wang, X. Sun, Z. Yang, Q. Yong, C. Zhang, Z. Li, Y. Weng, Effect of Mn concentration on the kinetics of strain induced precipitation in Ti microalloyed steels, Materials Science Engineering A, 561 (2013), p. 212-219.

[137] R. Soto, W. Saikaly, X. Bano, C. Issartel, G. Rigaut, A. Charai, Statistical and theoretical analysis of precipitates in dual-phase steels microalloyed with titanium and their effect on mechanical properties, Acta Metallurgica, 47(12) (1999), pp. 3475-3481.

[138] Y. Chen, Y. Wang, A. Zhao, Precipitation of AlN and MnS in low carbon aluminium killed steel, Journal of Iron and Steel Research International, 19(4) (2012), p. 51-56.

[139] https://www.metaltek.com, accessed 15.12.2017.

[140] Z.P. Xiong, A.G. Kostryzhev, A.A. Saleh, L. Chen, E.V. Pereloma. Microstructures and mechanical properties of TRIP steel produced by strip casting simulated in the laboratory, Materials Science Engineering A, 664(2016), p. 26-42.

[141] K. Luo, B. Bai, Microstructure, mechanical properties and high stress abrasive wear behaviour of air-cooled MnCrB cast steels, Materials Design 31 (2010), p. 2510-2516.

[142] W. Wang, R. Song, S. Peng, Z. Pei, Multiphase steel with improved impact-abrasive wear resistance in comparison with conventional Hadfield steel, Materials Design 105 (2016), p. 96-105.

[143] S. Huth, N. Krasokha, W. Theisen, Development of wear and corrosion resistant cold-work tool steels produced by diffusion alloying, Wear 267 (2009), p. 449-457.

[144] M. Lindroos, K. Valtonen, A. Kemppainen, A. Laukkanen, K. Holmberg, V.-T. Kuokkala, Wear behavior and work hardening of high strength steels in high stress abrasion, Wear 322-323 (2015), p. 32-40.

[145] H. Fu, Q. Xiao, H. Fu, Heat treatment of multi-element low alloy wear-resistant steel, Materials Science Engineering A, 396 (2005), p. 206-212.

[146] G. Bregliozzi, A.Di Schino, J.M. Kenny, H. Haefke, The influence of atmospheric humidity and grain size on the friction and wear of AISI 304 austenitic stainless steel, Materials Letters 75 (2003), p. 4505-4508.

[147] https://www.mee-inc.com/hamm/electrochemical-corrosion-testing/, accessed 13.01.2018.

[148] A. Mohamed, J. R. Cahoon, and W. F. Caley, Anodic Polarization Behaviour of Nickel-Based Alloys in Neutral and Very Acidic Solutions, The journal of Corrosion Science and Engineering 15 (2012) p. 37.

[149] Y. S. Lim, H. P. Kim, M. K. Jung, J. S. Kim, Phase analysis of the precipitates in an Alloy 600/182 weld, Solid State Phenomena 119 (2007) pp. 111-114.

[150] V. Ya. Dashevskii, A. A. Aleksandrov, A. G. Kanevskii, M. A. Makarov, Deoxidation Equilibrium of Titanium in the Iron–Nickel Melts, The Iron and Steel Institute of Japan International 50(1) (2010) p. 44–52.

[151] A. V. Karasev, H. Suito, Nitride precipitation on particles in Fe–10mass%Ni alloy deoxidized with Ti, M (M_Mg, Zr and Ce) and Ti/M, The Iron and Steel Institute of Japan International 49(2) (2009) p. 229–238.

[152] B. Garbarz, J. Marcisz, J. Wojtas, TEM analysis of fine sulphides dissolution and precipitation in steel, Material Chemistry and Physics 81 (2003), p. 486 – 489.

[153] G. Angella, R. Donnini, D. Ripamonti, M. Maldini, The role of particle ripening on the creep acceleration of Nimonic 263 superalloy, MATEC Web of Conferences 14 (2014), p. 14001.

[154] A. Baldan, Review: Progress in Ostwald ripening theories and their applications to the γ'-precipitates in nickel-base superalloys, Part II Nickel-base superalloys, Journal of Materials Science 37 (2002) p. 2379 – 2405.

[155] A. Teresiak, H. Kubsch, X-ray investigations of high energy ball milled transition metal carbides, NanoStructured Materials, 6 (1995) p. 671-674.

[156] S. Zhang, C.D. Qin, L.C. Lim, Solid solution extent of WC and TaC in Ti(C,N) as revealed by lattice parameter increase, Int. J. of Refractory Metalls and Hard Materials, 12 (1993-1994) p. 329-333.

[157] A.G. Kostryzhev, P. Mannan, O.O. Marenych, High temperature dislocation structure and NbC precipitation in three Ni-Fe-Nb-C model alloys, Journal of Materials Science 50 (2015) p. 7115-7125.

[158] B.K. Agrawal, Introduction to engineering materials, Tata McGraw-Hill (1988), p. 353.

[159] J. Zhu. A. Wise, T. Nuhfer, G. R. Holcomb, P.D. Jablonski, High-temperature-oxidation-induced ordered structure in Inconel 939 superalloy exposed to oxy-combustion environments, Materials Science & Engineering A, 566 (2013) p. 134-142.

[160] Z.Y. Wang, D. Han, X.W. Li, Competitive effect of stacking fault energy and short-range clustering on the plastic deformation behavior of Cu-Ni alloys, Materials Science & Engineering A 679 (2017) p. 484-492.

[161] A. Shadkam and C.W. Sinclair, The coupled effect of grain size and solute on work hardening of Cu–Ni alloys, Philosophical Magazine Letters 95(12) (2015) p. 555-563.

[162] D. Han, Z.Y. Wang, Y. Yan, F. Shi, X.W. Li, A good strength-ductility match in Cu-Mn alloys with high stacking fault energies: Determinant effect of short range ordering, Scripta Materialia 133 (2017) p. 59-64.

[163] P. Li, S.X. Li, Z.G. Wang, Z.F. Zhang, Fundamental factors on formation mechanism of dislocation arrangements in cyclically deformed fcc crystals, Progress in materials science 56 (2011) p. 328-377.

[164] K. Ankamma, D. V. V. Satyanarayana, R. Sarkar, G. C. M. Reddy, M. Komaraiah, N. Eswara Prasad, Effect of aging on work hardening behaviour of cold rolled Nimonic C-263 alloy, Materials Science and Technology 27(8) (2011) p. 1333-1340.

[165] A. Lavakumar, Ch.V.S.Murthy, D.V.V.Satyanarayana, N. Eswara Prasad, Strain hardening behaviour of a Nickel based superalloy SUPERCAST 247A, International Journal of Scientific & Engineering Research 4(8) (2013) p. 1914-1920.

[166] M.J. Yao, E. Welsch, D. Ponge, S.M.H. Haghighat, S. Sandlobes, P. Choi, M. Herbig, I. Bleskov, T. Hickel, M. Lipinska-Chwalek, P. Shanthraj, C. Scheu, S. Zaefferer, B. Gault, D. Raabe, Strengthening and strain hardening mechanisms in a precipitation hardened high-Mn lightweight steel, Acta Materialia 140 (2017) p. 258-273.

[167] W. Li, S. Lu, Q. Hu, S. K. Kwon, B. Johansson, L. Vitos, Generalized stacking fault energies of alloys, Journal of Physics: Condensed Matter 26 (2014) p. 265005.

[168] M. H. Lewis, J. W. Martin, Yielding and work-hardening in internally oxidised copper alloys, Acta Metallurgica 11 (1963) p. 1207-1214.

[169] D. Caillard, J.L. Martin. Some aspects of cross-slip mechanisms in metals and alloys. Journal de Physique 50 (18) (1989) p. 2455-2473.

[170] W.G. Nohring, Dislocation Cross-Slip in Face-Centered Cubic Solid Solution Alloys, École polytechnique fédérale de Lausanne, Ph.D. thesis (2017), p.137.

[171] V. Gerold and H. P. Karnthaler, On the origin of planar slip in F.C.C. alloys, Acta Metallurgica 37(8) (1989), p. 2177-2183.

[172] A. Weck, D.S. Wilkinson, E. Maire, Observation of void nucleation, growth and coalescence in a model metal matrix composite using X-ray tomography, Materials Science and Engineering A 488 (2008), p. 435–445.